



UNIVERSIDAD DE LOS ANDES

Multimodal X-ray edge illumination imaging for medical applications with polychromatic sources

Author:

Gibran David Jurado Romero

Advisor:

PhD. Carlos Avila

*This thesis is submitted in fulfillment of the requirements for the award of a Master's
degree in Physics at Universidad de los Andes*

High energy physics group
Universidad de los Andes - Physics department

November 15, 2023

Abstract

MSc. in Physics

Multimodal X-ray edge illumination imaging for medical applications with polychromatic sources

by Gibran David Jurado Romero

Conventional X-ray imaging relies on the absorption of X-rays by different tissues, which can result in low-contrast images. A solution to this issue is detecting the phase signal due to interactions of photons with matter, which is highly sensitive for low-attenuating tissues and samples.

The consistent improvement of the quality of optical elements, the incorporation of precision instruments, and the optimization of imaging techniques are responsible for the significant advancement of Phase Contrast Imaging (PCI) methods. Due to limitations in technology and imaging techniques, phase contrast was restricted to using synchrotron X-ray radiation sources. However, in the last two decades, new solutions to the problem of spatial and temporal resolution have allowed the implementation of phase contrast techniques with conventional polychromatic X-ray sources. The In-line propagation, speckle-based, and edge illumination phase contrast X-ray imaging techniques are among the different PCI methods. The latter is of great interest since edge illumination is particularly adapted to visualize details that present low photon absorption, as well as being able to extend spatial resolution by exploiting the dithering process, which is crucial in application areas such as biology and medicine.

Edge illumination PCI consists of illuminating the sample using the collimation of the photon flux through a grating. The sample then deflects the beamlets via photon diffraction; this effect causes beam signals to have positive or negative fringes on detection. The detector lecture of each fringe may be retrieved by exploiting the pixel pitch and grating spatial periodicity, which can lead to the retrieval of absorption, differential phase, and dark-field signals that bring a complementary description of the observed sample. Recent works use two gratings to achieve the edge lighting configuration; one collimates the photon flux, and the other limits the photon counting area

in the detector pixels. However, the second grating can be avoided if the pixel size is sufficiently small to gather the diffraction pattern. This subpixel effect is achieved by slightly de-aligning the detector from the grating, which produces a positive and negative fringe on the signal (50-50) or a fully fringed signal (100-0).

In this work, a readout system for multi-modal X-ray imaging is characterized to study the feasibility of a non-invasive visualization method of biological specimens for medical applications developed using the edge illumination technique. The absorption, phase contrast, and dark field signals are effectively recovered using the proposed imaging system for a *Poecilia reticulata* ex-vivo specimen, with a significant CNR increase by a factor of about 7 as compared to conventional X-ray low-dose radiography signal, while also reducing the absorbed dose per mass unit. Furthermore, a comparative analysis with Speckle-Based X-ray imaging is performed on this specimen, successfully recovering the absorption, phase, and dark field signals.

Declaration

Multimodal X-ray edge illumination imaging for medical applications with polychromatic sources

This thesis project involves the use of animal specimens to advance our understanding in the contrast and resolution of improved ionizing radiation imaging. In compliance with ethical standards and institutional guidelines, this declaration outlines the details of animal use in the project.

Species and State of Animals:

- **Species:** Guppy Fish (*Poecilia reticulata*).
- **Age:** 12 days.
- **State:** Ex vivo.
- **Total Number of Specimens Used:** 3 individuals.

The selection of guppy fish for this project is based on specific criteria pertinent to our research objectives. These include the variability of the tissues present inside the fish and the small size of the 2-week-old alevine guppy fish, which is ideal for the experimental procedures and observations planned in this study.

The guppy fish used in this project were sourced as part of a separate study. They were already in an ex vivo state and had been fixated for purposes unrelated to the current project. This approach ensures no additional animals were sacrificed specifically for this thesis.

This project adheres to the ethical guidelines for the use of animal specimens in research. All procedures involving the animal specimens were conducted in accordance with Uniandes CICUA standards for ethical research. The use of previously fixated specimens minimizes ethical concerns and aligns with the principles of reducing animal use in scientific research. The use of biological samples in this project is crucial for achieving the research objectives while upholding the highest ethical standards in scientific research. The project is committed to transparency and ethical responsibility in all aspects of animal use.

Throughout the development and completion of this thesis, artificial intelligence (AI) tools were employed within the guidelines of permissible use. These tools were primarily utilized for grammar checks, code reviews, and troubleshooting coding issues. It is important to clarify that the AI's role was strictly limited to these auxiliary functions. At no point was AI used for generating content, formulating research conclusions, or influencing the fundamental direction of the thesis. This declaration serves to assure the integrity of the research and to confirm that the core intellectual contributions and decision-making processes remained exclusively human-driven. The use of AI was conducted transparently and ethically, adhering to the principles of academic honesty and the established norms of research conduct within Uniandes.

Acknowledgements

This acknowledgment page is dedicated to those that with their invaluable support, patience, insight and affection had make this work possible; I offer them my most profound gratitude.

To the High Energy Physics Uniandes (HEP) laboratory; especial thanks to Camilo Rueda, for working by my side on the investigation; Steven Cely and Cristian Tibambre for their outstanding support and invaluable advice on the Edge and Speckle technique details.

To Natasha Bloch and Liz Stephany Riveros for providing me with great samples and showing interest on the investigation, to the Biophysics group member Elizabeth Suezca for her invaluable help in preserving the samples and providing help on mounting them, also for providing the tools for microscopic observation.

To Alonso Botero for the guidance on the topics related to information theory and statistics. To Manuel Sanchez and Paula Pardo for the guidance using the MIST software. To the Ecosistema Uniandes team for believing in this project from the start.

To PhD Zayra Garavito for the assessment on identifying the anatomy of the fish on all the images and to Carlos Navarrete, who introduced me in the HEP group and the fascinating world of medical physics.

To the people who supported me when I most needed it, especially my mother. To Juan David Marmolejo for his emotional support and company. To Santiago Henao for providing me with a temporary computer where I could finish this work.

To my companion and partner Julieth Forero, for staying late with me, and for her patience, unconditional support, and her love. I hope I can be at least a fraction of who you were with me.

To my thesis advisor, professor, and mentor, Carlos Avila, for his patience, help, and guidance.

Contents

| | |
|--|------------|
| Abstract | ii |
| Declaration | iv |
| Reader's note | vi |
| Acknowledgements | vi |
| List of figures | xi |
| List of tables | xxi |
| | |
| I State of the Art | 1 |
| 1 Discovery of X-rays | 3 |
| 2 Advancements on early radiology | 7 |
| 3 Phase contrast Imaging | 11 |
| 3.1 Development of phase contrast imaging | 13 |
| 3.2 Phase contrast early methods | 14 |
| 3.3 Diffraction Enhanced Imaging | 15 |
| 3.4 First steps of the propagation-based methods: Holography | 15 |
| 3.5 The study on phase retrieval algorithms | 17 |
| | |
| II Theoretical Foundations | 19 |
| 4 X-Ray fundamentals | 21 |
| 4.1 Wave equations in Vacuum | 21 |
| 4.1.1 Homogenous Helmholtz equation | 23 |
| 4.1.2 Spectral decomposition | 26 |
| 4.1.3 Plane wave formulation and propagation operator | 27 |
| 4.2 X-Ray propagation in matter | 28 |
| 4.2.1 Electromagnetic incidence in conductors and complex refractive index | 31 |

| | | |
|------------|---|------------|
| 4.2.2 | Electromagnetic elastic model for dielectric materials | 34 |
| 4.2.3 | Magnetically dispersive materials | 38 |
| 4.3 | Paraxial and projection approximation | 39 |
| 4.3.1 | Validity of the projection approximation | 43 |
| 4.3.2 | Fresnel Diffraction theory | 44 |
| 4.4 | Multi-slice approximation | 47 |
| 4.5 | Phase signal evolution: The transport-of-intensity equation | 48 |
| 4.5.1 | Linear imaging systems | 51 |
| 5 | X-Ray light-matter interactions | 53 |
| 5.1 | Attenuation: Photon absorption | 55 |
| 5.1.1 | Photoelectric effect | 55 |
| 5.1.2 | Pair production | 57 |
| 5.2 | Scattering | 59 |
| 5.2.1 | Thomson scattering | 59 |
| 5.2.2 | Rayleigh scattering | 61 |
| 5.2.3 | Compton scattering and the Klein-Nishina equation | 63 |
| 6 | X-Ray Imaging Fundamentals | 67 |
| 6.1 | Scattering kinematics | 68 |
| 6.2 | Detector projection | 72 |
| 6.3 | Attenuation contrast | 74 |
| 6.4 | Gradient Contrast | 76 |
| 7 | Phase contrast imaging systems | 79 |
| 7.1 | Propagation-based Imaging | 80 |
| 7.2 | Edge-Illumination Imaging | 82 |
| 7.3 | Illumination curve - Edge position vs intensity | 86 |
| 8 | Phase retrieval | 89 |
| 8.1 | Paganin Algorithm | 89 |
| 8.1.1 | Multimaterial Algorithm | 94 |
| 9 | Dithering Sampling | 97 |
| 9.1 | Dithering theoretical limit | 101 |
| 9.2 | Multimodal imaging of odd and even pixels | 102 |
| 9.3 | Photon statistics interpretation of the multimodal signals | 104 |
| 9.3.1 | n Momenta | 105 |
| III | Preliminaries | 107 |
| 10 | Experimental preliminaries | 109 |
| 10.1 | The source | 110 |
| 10.2 | Diffraction mask | 111 |
| 10.3 | Mask alignment modalities | 113 |
| 10.4 | Medipix detector | 115 |
| 10.5 | Detection mechanism, semiconductor detectors | 116 |

| | |
|---|------------|
| 10.6 XPCI setups | 118 |
| 10.6.1 Experimental Propagation-based Imaging | 119 |
| 10.6.2 Speckle-based Imaging | 120 |
| 10.6.3 Edge Illumination Imaging | 121 |
| 10.7 Imaging artifacts | 122 |
| 11 Computational framework and toolkit | 125 |
| 11.1 AutoAlign | 128 |
| 11.2 Pre-processing | 131 |
| 11.2.1 Dead-pixel interpolation | 131 |
| 11.2.2 Flat-field correction | 132 |
| 12 Poecilia Reticulata | 135 |
| 12.1 Generalities | 135 |
| 12.2 Guppy fish anatomy | 136 |
| 12.2.1 Otoliths | 136 |
| 12.2.2 Nasal sacs | 137 |
| 12.2.3 Fins | 137 |
| 12.2.4 Spine | 138 |
| 12.3 Experimental specifications | 138 |
| IV Results and Remarks | 141 |
| 13 Results and discussion | 143 |
| 13.1 In-line feasibility: conditions over the Fresnel number | 143 |
| 13.1.1 Cylindrical effect of phase contrast imaging | 147 |
| 13.2 Moiré pattern recognition and processing | 151 |
| 13.3 Edge-Illumination: <i>Poecilia Reticulata</i> | 152 |
| 13.4 Reconstruction of dithered attenuation-based imaging | 154 |
| 13.5 Reconstruction of dithered differential phase imaging | 156 |
| 13.6 Reconstruction of dithered phase retrieval imaging | 158 |
| 13.7 Reconstruction of Dark field (scatter) imaging | 159 |
| 13.8 Additional imaging for further momenta: Skewness | 161 |
| 13.9 Automatic segmentation of fish sections | 162 |
| 13.10 Visible structures | 162 |
| 13.11 Figures of merit over ROIs | 163 |
| 13.12 Signal resolution for AT, PH, DF signals | 165 |
| 13.13 Estimation of the Entrance Surface Dose | 166 |
| 13.14 Speckle imaging and retrieval using MIST | 169 |
| 13.15 A first exploration of triple-channel X-ray imaging using colormap representation | 170 |
| 14 Conclusions and further remarks | 173 |
| A Feynman rules for QED | 189 |

| | |
|---|------------|
| B Auto-movement imaging flux diagram | 191 |
|---|------------|

List of Figures

| | | |
|-----|--|----|
| 1.1 | a) Michael Faraday b) Wilhelm Rontgen c) Thomson cathode tubes d) Lenard's design of the cathodic X-ray tube [1] e) Chronological list of renamed physicists on the XXI century [2]. | 4 |
| 1.2 | a) Diagram of an X-ray tube from Dental and Oral Radiography [3]. b) X-ray image of the hand of Röntgen's wife Anna Bertha, taken by Wilhelm Conrad Röntgen [4]. | 5 |
| 2.1 | a) An 1896 advertisement for an x-ray apparatus [5]. b) Early Chest fluoroscopy [5]. c) Equipped X-ray room [5]. d) Patent blueprint for a modern X-ray tube (Coolidge) [6]. | 8 |
| 2.2 | a) Operation mechanism of the anti-scatter grid. A highly absorbing material will stop photons that will not arrive at the detection system to reduce the total dose emitted in the direction of the patient [5]. b) Photosensitive plates patent illustration [7]. c) Muller linear threshold model of radiation and mutation [8]. | 9 |
| 4.1 | Wave-field elements propagating in space over the z direction over time. The region in space that comprises $z = 0$ and $z > 0$ is the region for which the Helmholtz equation holds. The vector $\nabla\phi$ shows the direction of the energy flow, which is constant for each wave-front. This vector $\nabla\phi$ provides the direction to the Poynting vector and is tangent to its associated wave-front. | 25 |
| 4.2 | X-ray imaging representation of a sample with known composition and density (known μ', δ') embedded inside another material with known characteristics μ, δ . The projection approximation remains whenever the maximum transverse deviation effects $\Delta\phi$ can be neglected. Namely when the transverse diffraction spread caused by the embedded object with size d (Given by the Fresnel relation $\lambda z_o/a$) cannot be resolved. . . | 43 |
| 4.3 | Contour map of the relation of the Fresnel number and the propagation distance z_o along with the minimum resolution d with a fixed $\lambda = 10^{-10}$ value for the wavelength in the X-ray regime. a) represents the case of for objects in the range of micro X ray imaging, while b) is presented for even lower resolutions in the range of nanometric distances where the projection approximation lessens. It is clear that for most state-of-art medical imaging devices, the projection approximation holds due to the short distance z_o needed to hold the condition [9]. Both plots also have the specific values for the fresnel number at $N_F = 10, 20, 30$ | 44 |

| | | |
|-----|--|----|
| 4.4 | Plane wave fields traveling along the z direction. in figure b) The scatterer volume lies between the planes $z = z_1$ and $z = z_2$. The unscattered beam is given by the trajectories described at a). The intensity and phase of the wave at the exit-surface $z = z_2$ is given by the projection approximation. Under this approximation, the ray path distribution in the presence of the scatterer is taken to be equal to their unscattered counterparts. Thus the phase and amplitude at z_2 are considered to be accumulated along the wave path. | 46 |
| 4.5 | Coherent X-ray radiation is produced by a point-source s within the optic axis z . Multislice algorithm is applied to a scatterer with size z_o , to be sliced into a number of slabs (8). After passing through all slices of the scatterer, one has the exit-surface wave-function $\psi_\omega(z_c)'$. This exit-surface wave-function then propagates into the half-space downstream of the exit surface of distance z_2 . The resulting signal is the resulting wave-function after interacting with eight different scatters that have a defined depth l and an associated value for the material density in each region given by δ_l, β_l | 47 |
| 4.6 | Representation of wave-object interaction in the in-line imaging modality for a constant wave-field ψ_ω generated from a point-source at distance $z_1 + z_2$ from the detector. X-rays travel across a sample located at z_2 from where X-ray are deflected due to an associated n^2 of the scatterer. For a z_2 large enough, the differential phase is detected as positive and negative fringing on the detector. | 51 |
| 5.1 | Percentage of contribution for the refraction coefficient on real and imaginary parts δ, β over the energy spectrum range commonly used in medical applications for hydroxyapatite $\text{Ca}_5(\text{PO}_4)_3(\text{OH})$ commonly found in bone tissue [10]. | 54 |
| 5.2 | This figure depicts the change of intensity due to the presence of an inhomogeneous sample, according to the trajectory, the exit intensity varies. X-rays are produced by the same source at the same energy. Bottom ray follows a trajectory that travels only through the embedding material with known δ, β in a depth distance z_o . The top ray travels through both the embedding and embedded material producing a contrast difference. The total depth traveled throughout the embedding material is $z_o - w$ while the depth traveled in the embedded with known δ', β' and $\delta' > \delta, \beta', \beta$ is w | 55 |
| 5.3 | a) diagram of a photon going through the process of inducing the photoelectric effect. A photon in between the frequency range of X-ray imaging interacts with an atom and if the energy of the photon is sufficient it ejects an inner core electron. b) Feynman diagram that depicts the photoelectric effect, it is an annihilation of a photon with momentum k_o changing at the same time the momentum of an electron present in a material with N atoms. | 56 |

| | | |
|-----|--|----|
| 5.4 | Total attenuation interactions cross-section contributions due do different light-matter interactions. The black line represents the total attenuation cross-section as the sum of coherent scattering, incoherent scattering, and attenuation. The total attenuation including and excluding coherent scattering effects is also plotted in Figure B) with its respective difference as a subplot. We note that for the energy range used in this work (20kV-40kV) these values are close, hence Thomson and Rayleigh's contributions in the total cross-section can be ignored [10]. | 57 |
| 5.5 | From left-to-right. Diagram showing the process of electron-positron pair production. The produced pair are nearly collinear. Next Feynman diagram describes another process of higher energy in the nucleus field viewpoint, where there is an electric field produced by the presence of the Z charges of a nucleus [11]. | 58 |
| 5.6 | a) diagram description of the Compton scattering, photons interact with a free electron, during the interaction the proton transfers energy to the electron field hence $\hbar\omega' < \hbar\omega$. b) Two low-order Feynman diagrams representations of the Compton scattering, both contribute to the calculation of the total cross-section of this process given by the Klein-Nishina equation | 63 |
| 5.7 | Body tissue attenuation and scattering contributions numerically calculated by simulating $N = 10^6$ photons that cross over four kinds of tissue slabs of $w = 1m$. The attenuation and scattering probability is calculated using the NIST database with the compound mixture proportions for bone, adipose, and fibrous tissue found in medical literature [12, 13]. a) Body weight estimation percentage for an average human male body. b) Weighted dose absorption factored over the total body weight. c) percentage contribution for three interaction types of events. The photon crossing the material slabs may either cross without interacting, be absorbed by the material, or be scattered. The simulation is done for each material slab with a photon energy of $28kV$. As expected, heavy materials such as bone and fibrous tend to attenuate, while adipose and water tend to scatter and cross the material with more ease. | 65 |
| 6.1 | Cauchy path plot to solve the Green integral at 6.7. Paths Γ_3 and Γ_6 enclose the positive and negative poles, respectively. | 69 |
| 6.2 | Diagram of attenuation intensities | 75 |
| 7.1 | Partial illumination system due to the presence of a diffraction slit and a diffractive object. a) it is said that the fringing is positive if the apparent deviation of the ray path is at higher Δy than the path without the refractive sample. b) Conversely, it is said that the fringing is negative if the apparent deviation of the ray path is at lower Δy than the path without the refractive sample. This principle is the main mechanism exploited in edge-illumination imaging. | 83 |
| 7.2 | a) Double mask edge-illumination phase contrast imaging and b) Single mask edge-illumination phase contrast imaging. As the name may imply, the main difference on both techniques are the number of masks present in the optical path. Double mask case requires the double of images to construct the final dithering but has more specificity on the fringed signal. | 85 |

| | | |
|------|--|-----|
| 7.3 | Edge illumination reconstruction of the illumination curve (IC) according to the relative position of the mask and the detector Δx . The mask is said to be aligned on a percentage modality when the total IC (Which is the sum of the total fringing in intensity) meets at the relative intensity distribution spot on the system. $\sim 100\% - 0\%$ are asymptotic values on the tails of the distribution in the illumination curve. However, since the interference pattern is known to be periodic going too far on Δx may result on falling back on the illumination curve due the mask and detector periodicity. Dark field illumination condition is met near $\sim 100\% - 0\%$ while phase contrast is maximized on $\sim 50\% - 50\%$. Several techniques use a full IC scan to retrieve the phase and dark field signals [14]. | 87 |
| 9.1 | Small simulation of how the dithering sample works. Dithering can be interpreted as the addition of multiple quantized signals, when morphing said signals to an analog pattern (interpreted as a continuum), these signals may express a homogeneous pattern instead of large-scale patterns. a) and b) start as a unit cell of randomized colors, this cell is then concatenated n times in each direction to create a dithering pattern, that when the scale is large enough ($n = 8$) the pattern is perceived as a homogeneous color which is the average color of the unit cell. The factor $n = 8$ follows the rule of the sampling frequency and will be important later on as the factor is chosen to dither laboratory images in the edge illumination technique | 98 |
| 9.2 | Region map over the resolution conditions of the system. The region where $r = a$ is constant over all values and is given solely by the aperture size of the mask a . However, several cases are also present whenever the beamlet size follows the Fresnel condition, additionally, the system may also be limited by the nature of the PSF of the system, given by σ . The sweet spot of the region plot may be interpreted as the centre of the rectangle, which corresponds to the case where $I^+ \sim I^- \sim 2\sigma \sim a$ | 101 |
| 9.3 | Sketch of single and double mask edge-illumination systems with the approximate histogram of intensities with and without the sample on the $\sim 50\% - 50\%$ illumination modality. a) Single mask EI flat-field where odd and even pixels meet almost equal illumination, this is represented by how aligned are the histograms from each other. b) Illumination switch of a sinngle mask EI system initially aligned due to the presence of the scatterer sample in the path. c) Double mask EI flat-field. In this case, the second mask takes the role of differentiating positive and negative fringing instead of the illumination percentage. For this reason , at least two scans are necessary to retrieve the same information per dithering frame as in single mask modality d) Double mask EI system with the sample present, the switch of the illumination in the histogram represents the phase difference of the signal. | 104 |
| 10.1 | Illustrative general experimental setup. a) X-ray polychromatic source. b) diffraction mask. c) X-ray detector array (Medipix3RX) | 109 |
| 10.2 | a) Pixel count distribution with a misaligned mask, the skewness at the left is due to non-uniform intensity counts. b) Voltage vs target current in the regimes of small and large focal spots for the Hamamatsu source [15]. c) Source and RS-232C interface [15]. | 110 |

| | | |
|-------|---|-----|
| 10.3 | a) Flat-field image of a perfectly aligned diffraction mask and detector array, captured by a Medipix3RX b) Histogram distribution over pixel values. A slight skewness is present due to the support bars present on the diffraction mask. A bin at zero pixel value is visible due to dead pixels on the detector; the final distribution shows a Gaussian-like behavior, a direct consequence of the central limit theorem due to the sum of multiple Poisson distributions (see chapter 12). | 111 |
| 10.4 | Technological characterization of the diffractive mask. This device is normally made of an attenuating material and manufactured using photolithographic techniques. Additional materials have been explored for the production of these masks [16] as seen in figure 10.5 since the only condition is to be highly attenuating. The dimensions, patterns, and periodicity are not fixed for all systems. However, an effective edge illumination system must preserve the periodicity of the device's grating pattern. | 112 |
| 10.5 | Difference on material attenuation coefficients using in recent works [16] provided by NIST [10]. Although the difference is not significative for these materials as seen in the difference subplot, the cost of Tungsten is 11 times lower than gold, this provides higher scalability for the production of diffracting mask devices. | 113 |
| 10.6 | Diffractive mask degrees of freedom over x, y, z, ϕ which is the transversal angle over the x axis. The minimal step for each of the micromotors used in the movement of the diffractive mask device are also included. | 114 |
| 10.7 | Perspective of a single beamlet for a) $\sim 50\% - 50\%$ illumination and b) $\sim 100\% - 0\%$ over odd and even pixels alike. The even and odd condition is taken over the scanning direction. In this case the x direction where each column of pixels is labelled as either odd or even. c) A different perspective of the illumination projection, where a set of odd and even columns is included for the $\sim 50\% - 50\%$ and $\sim 100\% - 0\%$ illumination alignments. | 114 |
| 10.8 | Alignment process for $\sim 50\% - 50\%$ and $\sim 100\% - 0\%$ configurations. The mask is moved in the coordinates shown in the arrow to change the Moiré interference pattern as seen in the flat-field images right below. Once axial alignment is done, an alignment on the x, y coordinates is performed where the histograms have the same area and same distribution to guarantee a homogeneous scan. | 115 |
| 10.9 | a) Medipix3RX detector [17] b) Different semiconductor materials can be bump-bonded to the ASIC to act as an x-ray detection layer. When a photon is detected, an electron/hole pair is created. The bias voltage applied across the sensor layer drifts one of the charge clouds to the ASIC end. Within the ASIC, the photon is individually analyzed and can be sorted into multiple energy bins. | 117 |
| 10.10 | Set of materials used in semiconductor ceramic detectors for X-ray imaging, the M_n and L_n regimes are labeled. The energy ranges used during this work fall under the L_n region. The subplot represents the detection efficiency of photons by their given energy [18] | 118 |
| 10.11 | In-line configuration for phase contrast X-ray imaging. As seen during the first part of this document, it is crucial to maximize z_2 to amplify the phase effects on the imaging system. | 119 |

| | | |
|-------|---|-----|
| 10.12 | Speckle-based imaging setup. The grating must meet the condition that each speckle occupies at least 2 pixels on the magnified image, along with a total visibility of at least 20% this illustration includes the distances used in the study | 120 |
| 10.13 | Edge illumination imaging setup. | 121 |
| 10.14 | Heel Effect | 123 |
| 11.1 | Flow diagram of the whole imaging process | 126 |
| 11.2 | Simulated Moiré fringes using the Fourier series for Moiré patterns under different parameters of frequency (Which in our EI system may be translated on number of lines) and rotation angle of the pattern as seen on the y axis. These values for the Moiré parameters are used in equation 11.2 and numerically produced using Python. | 129 |
| 11.3 | Iterative align process. a) shows the software communication and feedback of an iterative process whereby the Moiré patterns seen in the detector, the diffractive mask knows it's real-time position on the EI system. b) Process statuses that may be found, REST implies a 2 freedom coordinate movement while GRID uses just one which is Δx . Finally when the algorithm detects uneven illumination in SINGLE, moves only the Δy coordinate. c) Representative histogram evolution over this process. | 130 |
| 11.4 | Recovers one frame per second, 30 frames of 1 second for a series, each series is captured at $10\mu m$ distance. Saves the detector array as a .txt file per frame, which are correctly labeled for later reconstruction. Integrates over the frame files for each dithering step (8 total) giving a total of 8 files one for each integration which corresponds to a whole series | 131 |
| 11.5 | a) Dead-hot pixel interpolation for saturated and zero values, the interpolation is done over the first-like neighbors. b) Mask density interpolation. High values are replaced by the average intensity of the top and bottom pixels. | 132 |
| 12.1 | a) Lateral view of a <i>Poecilia Reticulata</i> alevine fish with it's respective parts. PhD. Zayra Garavito kindly helped with the identification of visible anatomy as well as the estimation of age of the fish (2 weeks). b) Superior view of the fish after X-ray radiation. Otoliths located in the Otic organ are visible but have low contrast due to their distinctive white color | 137 |
| 12.2 | a) Total contribution of the attenuation coefficient given by the three main materials found on the fish' anatomy composition which include $CaCO_3$, Collagen and Hydroxyapatite. Each value labelled is either TA (Total Attenuation), PE (Photoelectric Effect) or SC (Scattering). The red zone represents the range of energies used during the imaging process. b) Gamma value calculated using $CaCO_3$, Collagen and Hydroxyapatite δ, β values found in the subplot [19]. | 138 |

| | | |
|------|---|-----|
| 13.1 | Simulated images for a 0.5mm width PMMA rod at different distances L from the sample and constant source-detector distance of 1m. $z_2 = 1m - L$. At the left the retrieved phase contrast image can be found, the differential phase signal is extracted using the paganin algorithm explored in chapter 8. At the right, the attenuation image directly retrieved from the simulation with no processing can be found. | 144 |
| 13.2 | normalized profile intensity for each raw attenuation image simulation. Each line represents the PMMA rod at a different position in the simulation. Edges on the attenuation image retrieved by the profile plot are sharp. This is mainly due to the effect that propagation-based imaging attenuation image provides also a convoluted phase signal which contributes to the total intensity in the edges and is maximum on places where the structure gradient is also maximum by the TIE equation. . . | 145 |
| 13.3 | normalized profile intensity for each processed phase retrieval image simulation. Each line represents the PMMA rod at a different position in the simulation. Edges on the attenuation image retrieved by the profile plot are smooth mainly due to ignoring the contribution of the attenuation signal. | 145 |
| 13.4 | Profile plot of the gradient for the attenuation images. As expected, the gradient is maximum on the edges and some of the edges present two peaks. The threshold for the automatic segmentation of background noise and signal is chosen to be $Th = 0.06$ on the gradient values. . . . | 146 |
| 13.5 | Profile plot of the gradient for the phase images after phase retrieval algorithm is processed. The gradient is again maximum on the edges and some of the edges present two peaks. The threshold for the automatic segmentation of background noise and signal is chosen to be $Th = 0.06$ on the gradient values. Although the same value was chosen, it is clear that this gradient is more decidable on the edge sections than the gradients seen at figure 13.4. | 146 |
| 13.6 | Ray-tracing geometry of the trajectory of a photon that crosses a cylindrical geometry unabsorbed. Two processes of refraction can be seen due to the entering and exit of the curved geometry. This is expressed as a major concentration of intensity in the edges of this geometry, which is an effect seen in the simulations. | 147 |
| 13.7 | Edge-specific figure of the aligned profiles over the edge. Note how when the Fresnel condition that depends on L and inversely on z_2 is reduced, the sensitivity over the edge regions is lost and the profile adapts a curved nature on this region, hence implying a resolution loss on low Fresnel number conditions as predicted on the phase contrast theory of this work. | 148 |
| 13.8 | Calculated FWHM of the intensity profile given both measured widths. The sub-plot represents the discrepancy of the FWHMS calculated using the different signals. | 149 |
| 13.9 | Contrast-to-Noise ratio and Signal-to-Noise ratio of phase contrast and attenuation images over the reference frame of a) z_2 while the distance between the object and the source varies (Hence a variation of the magnification) b) reference frame of L where the z_2 value increases and magnification remains constant, hence increasing the Fresnel number. . | 149 |

| | | |
|-------|---|-----|
| 13.10 | Signal-to-noise ratio difference between both techniques. As z_2 increases, the difference between the SNRs also increases as a direct consequence of graph 13.9 where attenuation remains constant while phase contrast increases. | 150 |
| 13.11 | a) Moiré pattern flat-fields provided to the algorithm for characterization, each column represents a case where the algorithm is whether decidable and can characterize the pattern (left), undecidable and cannot classify the flat-field as aligned or misaligned (centre), and when the algorithm can decide that the flat-field is aligned (right). b) processed images of the Moiré patterns seen in a), these are the images that are submitted to the binary k-means segmentation. c) Confusion matrix of the total cases where the algorithm could successfully classify the flat-field. This algorithm was tested with a total of 26 flat-fields acquired during this work. | 151 |
| 13.12 | a) Full image road for the scanning of a Guppy fish in a multi-modal setup. This scanning starts with the flat-field of a $\sim 100\% - 0\%$ setup. Each image provided by the flat-field has ten times more time exposure than the sample image. This process is done eight times one for each dithering step where the scan is moved on the $+\Delta x$ direction. After this process finishes, the setup is aligned to $\sim 50\% - 50\%$ to take a second flat-field using this configuration, again for a total of 8 dithering steps. Once the flat-field imaging finishes. The sample is placed on the rod for reverse scanning using the same alignment of $\sim 50\% - 50\%$ as the previous step but in the inverse direction $-\Delta x$ again for the same 8 dithering steps. Once this dithering finishes, the sample is moved outside the field of view by using the $-\Delta z$ direction as seen in c) to align again the system to $\sim 100\% - 0\%$ illumination. Once this is done the sample is moved back to the original position in the $+\Delta z$ direction as seen in b) and the last dithering using the $\sim 100\% - 0\%$ illumination is performed. | 153 |
| 13.13 | Diagram of the dithering integration and the reconstruction of images with augmented resolution, phase contrast, and dark-field. a) The pairs of images that coincide in the x direction and illumination modality are pre-processed by a flat-field correction, which consists of the pixel-wise quotient of intensities. b) a pixel column-wise operation is performed over the images according to the signal that needs to be retrieved. d) Each signal has a pair-wise operation that can be used to retrieve said signal. This however reduces the spatial resolution to half the original resolution in the direction where the dithering was performed. A column-wise concatenation will correct this. c) eight total corrected images are then concatenated in dither order, this means the first column of each image of the eight ordered dithers are concatenated, then the second column until the final resolution of 256×1024 is reached. This is done for the full set of images that were obtained from the column-wise operations. e) The output shows the three (or more) signals retrieved (AT,PH,DF) with the augmented resolution. | 155 |
| 13.14 | Attenuation images for a Guppy fish with differences in the number of dithering steps and alignment system used. Image is re-escalated on the x axis for a better fitting and representation of the actual dimensions of the sample | 156 |

| | | |
|---------|--|-----|
| 13.15 | Differential phase images for a Guppy fish with differences in the number of dithering steps and alignment system used. Image is re-escalated on the x axis for a better fitting and representation of the actual dimensions of the sample | 158 |
| 13.16 | Retrieved phase images for a Guppy fish with differences in the number of dithering steps and alignment system used. Image is re-escalated on the x axis for a better fitting and representation of the actual dimensions of the sample | 159 |
| 13.17 | Dark-field images for a Guppy fish with differences in the number of dithering steps and alignment system used. Image is re-escalated on the x axis for a better fitting and representation of the actual dimensions of the sample | 160 |
| 13.18 | Dark-field images for a Guppy fish with differences in the number of dithering steps and alignment system used. Image is re-escalated on the x axis for a better fitting and representation of the actual dimensions of the sample | 162 |
| 13.19 | Masking process to determine the regions of interest (ROIs) of the Guppy fish. First, the already processed, augmented, and reconstructed image output from 13.13 of the three signals goes through an image processing algorithm. Where the image goes through a re-scale process that ignores pixels on the limit values. Then a ULTRA-CLAHE (See section 12) is performed to the image with a $\sigma = 6$ enhancement parameter. This algorithm will improve the distribution of intensities over the whole image, making a dynamic contrast enhancement. Finally, an image smoothing using Kuwahara kerneling with $k = 4$ is performed. This smooth uses a dynamic window where the kernel changes its size and factors depending on the previous average values of intensity, hence minimizing the gradient loss which translates into less edge smoothing. When the processing is over, a k-means algorithm is performed to extract specific regions of the fish as masks that will be operated later on. The number of kernels used was 12 although multiple kernels correspond to the same region. The four final regions chosen are shown on the last step, this includes the background signal, fins and fish edges, head and body section, and otoliths which are high contrast | 163 |
| 13.20 | Masking result for each of the signals, the masks are directly multiplied to each signal image, giving an intensity distribution on the ROI and zero elsewhere. | 164 |
| 13.21 | Qualitative selection of regions that were enhanced by the phase contrast or dark field signal. The four selected structures are the Otoliths, the neck region where the spine is located, the lateral fin visible on the x-ray images, and the tail. | 164 |
| 13.22a) | Selected region masks that were used to calculate the figures of merit of the profile plot at b). Otoliths are compared to the head to give a more specific contrast metric since otoliths are embedded in the head tissue. b) Profile plot of the three signals, the three curves seen in the profile plot correspond to a specific structure seen also in the images at c) for each signal. Region I, II and III correspond to the left otolith, the neural tubes and the right otolith of the fish respectively. | 165 |

| | | |
|---------|--|-----|
| 13.23 | Compared regions for the CNR and SNR metrics, in some cases three regions were used to compare the total signal to the background. | 166 |
| 13.24a) | Selected region for the resolution numerical result, this region corresponds to the left otolith at the leftmost edge, which in all curves will represent an increase in intensity. The trimmed data is represented in b) where is fitted to an Erf, this Erf is shown with better numeric stepping in c). The derivative of said Erf is a normal distribution given by d) which has an associated FWHM that corresponds to the resolution of that signal in the image. | 167 |
| 13.25a) | Additional flat-field with a modified EI setup. the setup has now a Rhodium filter at the exit of the X-ray source to equalize the energy spectrum as the one used in Roque et. al. b) X ray imaging setup from Roque et. al. with a Rhodium filter and modified distances, along with the dosimetry measurements of the ESD | 168 |
| 13.26 | Estimated ESD on the fish region normalized over the total dose, by the geometrical effects as well as the presence of the mask, the estimated ESD corresponds to 0.388 mGy per dithering frame. For a full imaging set the total estimate is 3.11 mGy per 240 seconds. The subplot is the difference between the 5050 and 0100 alignment systems, as expected, both systems preserve the ESD value | 168 |
| 13.27 | Speckle-based phase contrast, dark-field, Laplacian signal reconstruction, and attenuation images | 169 |
| 13.28a) | An example of normalizing AT-PH-DF channels into R-G-B color channels. These may give more insights about the contrast over the sample using multi-modal signal integration. b) Possible combinations between color channels and signal channels for the integration of single image reading PH/DF/AT imaging, in some of the images there is a clear highlighting of zones that are not visible in the individual signals, such as a better visibility of the spine, a clear visualization of the skull and edge enhancement. | 171 |
| B.1 | Single Flat-Field correction processing a) Flux diagram for alignment pre-condition | 191 |
| B.2 | Image integration process | 192 |

Table index

| | |
|--|-----|
| 13.1 Performance Metrics Derived from the Confusion Matrix | 152 |
| 13.2 X-Ray Capture Specifications | 154 |
| 13.3 Signal Analysis in Different Regions | 165 |
| 13.4 Parameter Fitting and FWHM in Different Regions. OT1 corresponds to the first otolith, while NT corresponds to the neural tube region. NA values are in place where the fitting could not be done | 167 |

Part I

State of the Art

Chapter 1

Discovery of X-rays

The story of X-rays starts with the discovery and study of electromagnetic waves and radiation. In 1836, Faraday began studying the physics of materials by investigating the effects of multicolor light emission. He explored the gas discharge phenomenon by passing electricity through an evacuated glass globe under different conditions, such as high voltage, air pressure, gas type, and temperature. A few years later, Julius Plücker made an observation that hinted that during the electric discharge process, the cathode emits, in addition to the locally bright light, a stream of electric radiation propagating in straight lines to the anode [20]. Plücker began to explore the fluorescent glow at the tube wall near the cathode; in particular, he observed a shift of this multi-color light when applying a magnetic field.

In the 1870s, an English physicist named William Crooke studied the properties of cathode rays. He used a modified Geissler tube evacuated with a modified Sprengel mercury pump. Crooke observed that even under ultrahigh-vacuum conditions, when the glow effects of electric discharge slowly begin to disappear, cathode rays can still hit the anode and the back end of the tube. As a result, they cause material heating and characteristic light emission known as "cathodoluminescence" on the glass.

Similarly, Johann Wilhelm Hittorf, a student of Plücker, found in experiments with Geissler tubes that a shadow image of solid objects placed inside the tube appeared at the fluorescing part of the glass wall. Also, Hittorf found a shift of this shadow image induced by a magnetic field. From these studies, Plücker and Hittorf concluded that the cathode emits a negatively charged particle stream, which Philipp Lenard confirmed in 1888 as cathode rays ("Kathodenstrahlen") [21]. In his studies of cathode rays, Lenard came close to detecting X-rays. He constructed a gas tube with a thin metal foil to determine the range in air, replacing the glass at the end of the tube. By studying the properties of cathode rays, he found that the induced light intensity was

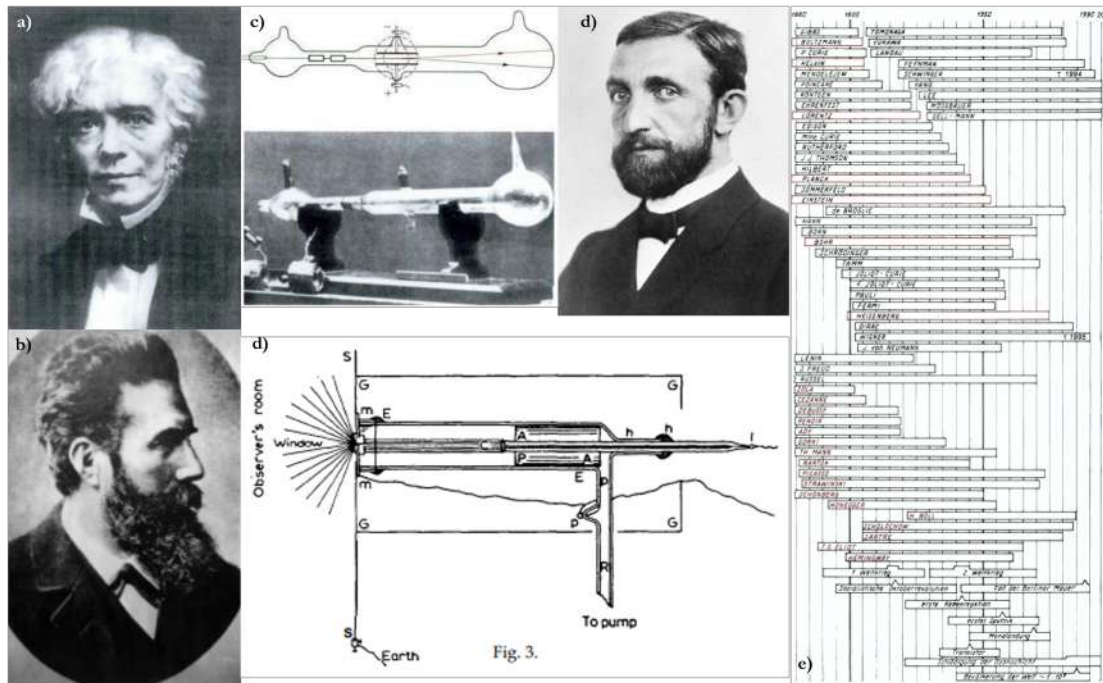


FIGURE 1.1: a) Michael Faraday b) Wilhelm Röntgen c) Thomson cathode tubes d) Lenard's design of the cathodic X-ray tube [1] e) Chronological list of renamed physicists on the XXI century [2].

proportional to the material density, and the range of the cathode rays in the air was a few centimeters [22].

Motivated by observations made by Plücker, Hittorf, and particularly Lenard, Röntgen conducted further experiments to explore the properties of this stream of free electrons created in an electric gas discharge tube. One of these experiments involved repeating Lenard's measurements of the range of the cathode rays outside the tube. Röntgen used a more sensitive technique and recorded the electric discharge with an electrometer, which showed that the effect ranged much further than the few centimeters Lenard had observed with his fluorescent screen [23]. The history of radiology began with the discovery of X-rays by Wilhelm Roentgen in 1895. While experimenting with a cathode-ray tube and glass at the University of Würzburg, he unexpectedly discovered invisible rays that could pass through most substances, leaving shadows that could be recorded on photographic plates. Due to the unknown nature of these rays at the time, Röntgen labeled them "X-rays," a form of electromagnetic radiation that can penetrate through materials that absorb or reflect visible light [23].

In another experiment, Röntgen covered the whole glass tube with cardboard to exclude any light effects coming from inside the tube. In the completely darkened laboratory, he observed by chance a screen fluorescing next to the experimental setup. After excluding artifacts such as external light or cathode ray effects, he wondered

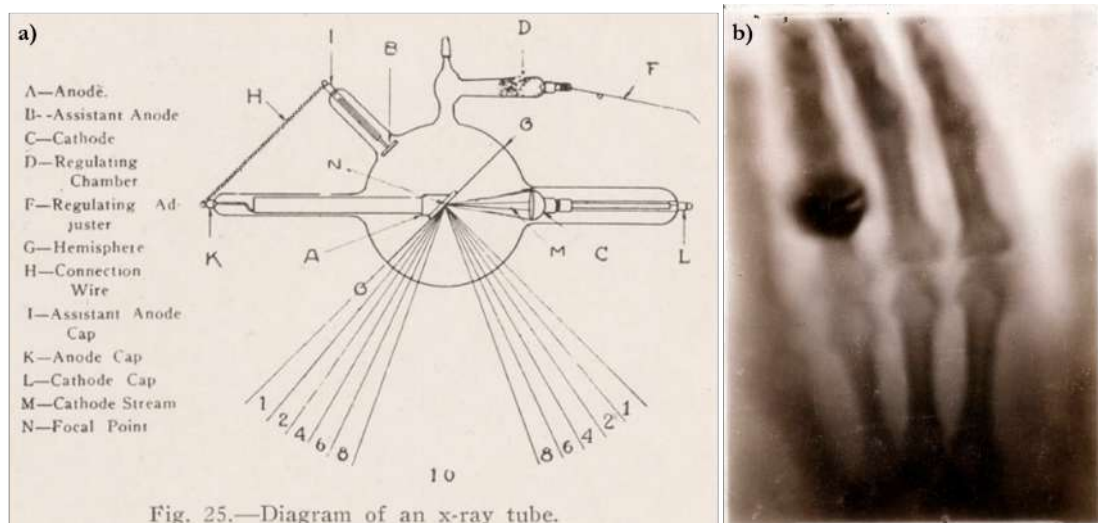


FIGURE 1.2: a) Diagram of an X-ray tube from *Dental and Oral Radiography* [3]. b) X-ray image of the hand of Röntgen's wife Anna Bertha, taken by Wilhelm Conrad Röntgen [4].

why the green light emitted from the crystals of that screen [23]. On 8th November 1895, Rontgen systematically investigated this phenomenon by varying the distance, direction, and absorption of the invisible radiation by different materials. Fascinated by these experiments, Rontgen worked day and night, even ordering his bed to be transferred into his lab. He observed the fluorescing effect at larger distances, which fluctuated with electric tube current, and found the high penetrative power of the radiation when exposing different materials. He also noticed the protective capability of heavy metals like lead and the blackening of films as the first step to radiography [2]. The critical experiment that revolutionized medicine fundamentally and is considered the birthday of radiology was when Rontgen held a small object in the beam between his fingers and recognized the image of his fingers on the cardboard screen. This was the first radiographic image ever. However, still hesitating about what he had observed, he complemented his investigations with several further experiments, including the well-known image of his wife's hand, which he submitted to the Physical-Medical Society in Würzburg on 28th December 1895.

Several applications and technical improvements of the X-ray tube have been reported over the years. One notable case is the first image-guided surgery in Birmingham, England, where surgeons could use X-rays to locate a foreign object in a patient's hand. In February 1896, the first studies were initiated to demonstrate the potential of X-ray imaging in non-bony structures such as the vascular anatomy by injecting a contrast medium and the gastrointestinal tract [24]. Just within the first few months after the discovery of X-rays, fluoroscopes were developed, widely used in medical examinations consisting of a box shielding the ambient light and a high-attenuating screen.

In 1896, substantial technical progress was achieved by industrial developments initiated by Thomas Alva Edison, who improved the technique to focus the X-ray beam better and optimized the fluorescing screen by choosing calcium tungstate. In total, 1044 scientific papers were published on X-rays in 1896 [24], with about 400 referring to medical and less than 200 to physical aspects. The acknowledgment of Röntgen's discovery resulted in 1901 in the first Nobel Prize for Physics ever awarded [25]. In the early 20th century, X-ray imaging became a standard medical diagnostic tool. However, the conventional X-ray imaging method relies on the absorption of X-rays by different tissues, which can result in low-contrast images.

Chapter 2

Advancements on early radiology

This chapter talks about the early developments in X-ray technology, the involvement of manufacturers, the challenges faced by pioneers, and the hazards associated with early X-ray technology. Soon after Rontgen's discovery, the use and application in medical imaging and diagnostics were evident, and using various devices and techniques for visualization and recording of X-ray images brought a widespread and highly increasing new field of study. However, ionizing radiation hazards were not yet fully known and studied. Developing safety regulations and focused techniques would also be crucial in the radiology and medical physics area. Parallel to advancements in X-ray imaging, The first imaging devices used to provide real-time feedback for guiding medical procedures were also invented employing Fluoroscopy in 1900 [26].

The involvement of manufacturers significantly contributed to the development of X-ray technology in the early days of radiology. Manufacturers played a crucial role in advancing the technology by producing and improving the apparatus used for X-ray imaging. This involvement is evident in the advertisements from 1896, which showcased the products and innovations of manufacturers in the field. Additionally, manufacturers were involved in developing regulating devices for X-ray tubes, such as lead aprons and gloves for radiation protection and the self-regulating tube, which further enhanced the safety and efficiency of the technology. Additionally, manufacturers introduced calcium tungstate intensifying screens, which emitted ideal light for sensitivity in X-ray imaging [27].

Furthermore, manufacturers were instrumental in producing sensitive plates and films for capturing X-ray images. They developed plates with higher sensitivity and introduced calcium tungstate intensifying screens, which emitted ideal light for the sensitive emulsions used in X-ray imaging. The way X-rays would propagate from an

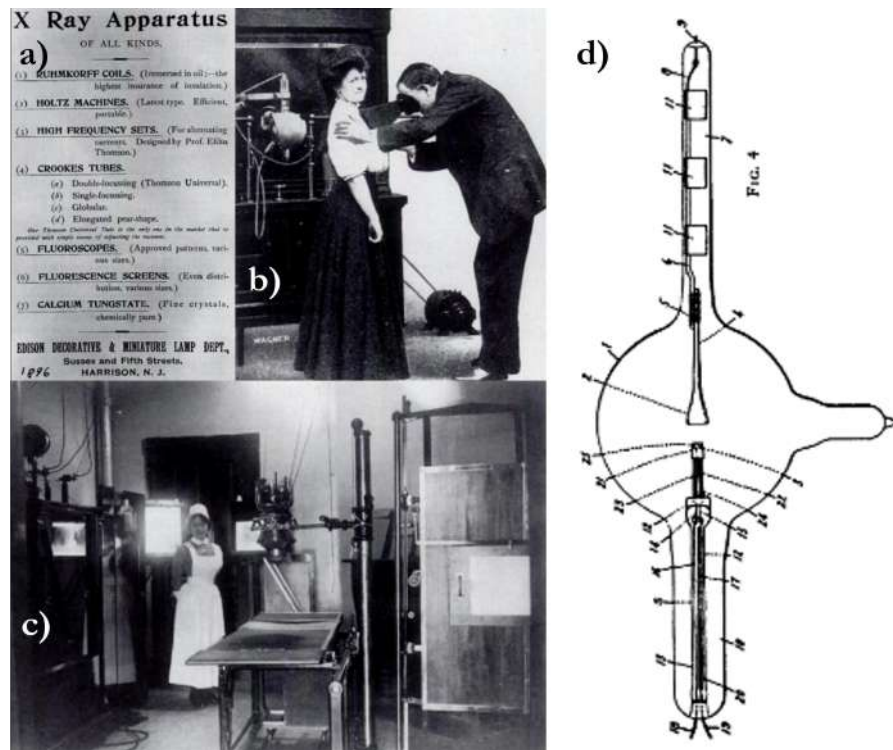


FIGURE 2.1: a) An 1896 advertisement for an x-ray apparatus [5]. b) Early Chest fluoroscopy [5]. c) Equipped X-ray room [5]. d) Patent blueprint for a modern X-ray tube (Coolidge) [6].

X-ray tube was known. Trajectories are almost random and unfocused due to scatter effects on the anode; this resulted in additional ionizing radiation being delivered to the patient [5]. Gustav Bucky invented the first X-ray grid, which solved this problem; the Bucky factor is a measure of the efficiency of a grid as it is the ratio of X-rays that are stopped in the grid to those that pass through the grid [27].

Pioneers in radiology faced several challenges during the late 19th and early 20th centuries. One of the challenges was the uncertainty regarding who would practice radiology, as the earliest x-ray examinations were performed by various individuals, including photographers, electricians, and physicians in the early days. Additionally, the quality of early radiographs was poor by today's standards [28], and there were concerns about radiation hazards and protection. The lack of standardized equipment and materials for imaging posed a challenge, as manufacturers were still developing and improving apparatus, regulating devices, and sensitive imaging materials for X-ray technology [29].

The hazards and risks associated with early X-ray technology were recognized almost immediately after Roentgen discovered X-rays. Pioneers addressed these issues by developing and implementing radiation protection measures. For example, lead aprons and gloves were introduced to shield operators from radiation exposure, and efforts

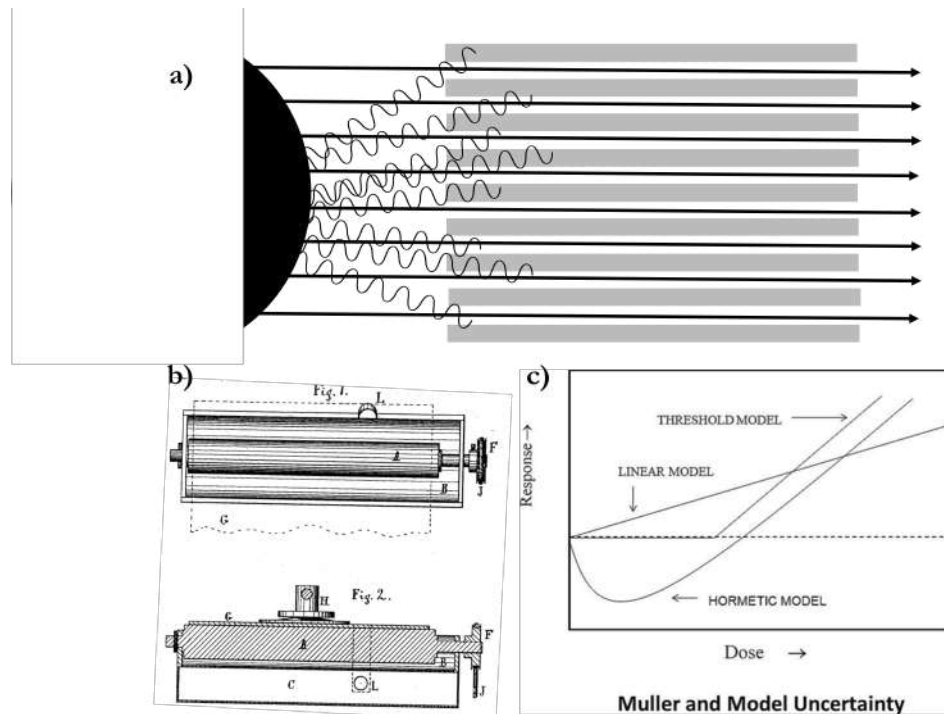


FIGURE 2.2: a) Operation mechanism of the anti-scatter grid. A highly absorbing material will stop photons that will not arrive at the detection system to reduce the total dose emitted in the direction of the patient [5]. b) Photosensitive plates patent illustration [7]. c) Muller linear threshold model of radiation and mutation [8].

were made to improve the safety of x-ray equipment and minimize unnecessary radiation exposure to patients and operators. The development of regulating devices for X-ray tubes contributed to the safety and efficiency of the technology, helping to mitigate the risks associated with radiation exposure. As the understanding of radiation hazards grew, pioneers in radiology worked to establish safety protocols and guidelines to minimize the risks associated with early X-ray technology [30].

X-rays are ionizing radiation that can affect living organisms in various ways. Hermann Joseph Muller conducted studies on fruit flies and discovered a direct correlation between the amount of X-ray exposure and genetic damage. This was the first evidence showing that radiation can cause genetic effects. One observed effect was gene mutations and chromosome reorganization in fruit flies (*Drosophila*) due to X-ray exposure [31]. These mutations were also observed in the somatic cells of *Drosophila melanogaster*.

Studies suggest that X-rays could cause effects similar to radium radiation, another ionizing radiation, on gene mutations. This indicates that the impact of X-rays on biological samples may be similar to those of other ionizing radiation sources. Besides gene mutations, x-rays have also been linked to changes in productivity and sex ratio in *Drosophila melanogaster* [32]. Hence, x-rays can have broader effects on the biology

and genetics of organisms beyond just causing mutations. Muller was awarded the Nobel Prize in Physiology or Medicine in 1946 for his study on the effects of x-ray radiation [33]. Current knowledge on the radiation effects on the human body is way broader, and some of the Muller hypotheses were proven wrong over time, especially how the total dose and the dose rate risks were fundamentally different and do not work as a linear model and how the Genetic load could lead to the risk of species extinction [8].

Chapter 3

Phase contrast Imaging

X-ray phase imaging, including both phase-contrast and phase imaging, offers higher contrast and sensitivity for low-Z materials than traditional absorption imaging. This enhanced contrast aids in distinguishing different compositions within an object. Techniques in X-ray phase imaging include Zernike's X-ray microscopy, X-ray holography, differential X-ray microscopy, coherent diffraction microscopy, crystal and grating interferometers, diffraction-enhanced imaging (DEI), and propagation-based methods. Each technique uses unique methods to manipulate and interpret phase-shifted X-ray light, leading to improved image quality and contrast. This chapter will further discuss these techniques.

X-ray phase contrast imaging took longer to develop compared to X-ray absorption imaging, which was quickly adopted after Röntgen's discovery in 1895. The delay in X-ray phase contrast imaging was due to the need for new monochromatic coherent sources that allowed phase resolution such as synchrotron [34], which were developed later in the 1950s, and advancements in electron microscopy to extract phase information from diffraction experiments. However, the evolution from phase in visible light optics to phase contrast in X-ray imaging was crucial for both optics and quantum mechanics. X-ray phase imaging merges these discoveries and other incremental steps, enhancing medical diagnostics as a complement to absorption imaging since it traces back to Thomas Young's wave theory of light in 1804, based on Huygens' ideas. The interference notion of the wave-like behavior of light is an important principle for the basis of X-ray phase contrast imaging, especially under the field propagation interpretation where the Rayleigh Sommerfeld integrals explain the scattering phenomena on apertures (These are mostly ignored during this work due to their consistency holding only for apertures, while Fresnel-Kirchhoff integrals are more general for scatterers) [35].

The concept of a coherent wave with a well-defined phase, established by Thomas Young's 1804 wave theory of light, significantly influenced optics and physics. Young deduced light's frequency and wavelength by analyzing Newton's data on light paths and incorporating Römer's speed of light estimate. This concept played a vital role in quantum mechanics, contributing to Bohr's quantization of electron orbitals and explaining hydrogen's spectral lines, thus cementing the phase concept in wave mechanics and electromagnetism [36].

Advancements in phase-contrast imaging have led to higher contrast and sensitivity for low-Z materials compared to traditional absorption imaging. Various techniques, such as Zernike's X-ray microscopy, X-ray holography, differential X-ray microscopy, coherent diffraction imaging, crystal and grating interferometers, diffraction-enhanced imaging (DEI), and propagation-based techniques, have been developed to enhance the contrast by phase-shifting undiffracted light or creating interference patterns for image reconstruction. Each technique has its specific advantages and applications, constantly advancing the field of X-ray imaging [37].

In X-ray phase analysis, two key aspects are considered: the phase of incident radiation and the real part of the refractive index decrement of the medium, with the refractive index being less than unity. This results in anomalous dispersion, where the phase is advanced, in contrast to ordinary optical frequencies where n is greater than unity, and the phase is retarded. The absolute phase of the wave through an object isn't directly measurable, but the relative phase delay is proportional to the optical path length, related to the refractive index's real part. As previously stated in this work, The phase ϕ at any point (x, y) on a screen is determined by the real part of the refractive index along the path of a wave vector k . The interaction with a reference wavefield makes the phase shift caused by the object detectable, despite the absolute phase of the wavefield being elusive. For partially coherent sources, time-averaged quantities from a fully coherent source are used, allowing for well-defined behavior similar to that of a fully coherent source [38].

In the early days of studying diffraction, several scientists including Haga, Wind, Walter, Pohl, and Koch attempted to demonstrate it. Their efforts eventually led to the recognition of X-rays as a wave phenomenon. In 1912, Arnold Sommerfeld analyzed these experiments and finally elucidated the nature of X-ray diffraction. However, the spectral range of X-ray wavelengths made interpreting the diffraction patterns a challenging task. By 1911, physicists faced a dilemma as evidence suggested both the corpuscular and wave nature of X-rays. Max von Laue, in 1912 [39], connected the deduced X-ray wavelength with atomic dimensions in crystals, leading to the birth

of X-ray crystallography and demonstrations of diffraction phenomena. This development paralleled medical imaging, which focused on X-rays' particle-like properties. William and Lawrence Bragg further solidified the wave nature of X-rays and leveraged them as a crystallographic tool for analyzing various materials. The wave properties of X-rays were initially explored through slit diffraction experiments and later confirmed via crystal diffraction, leading to their use in characterizing materials from simple to complex structures. Notable achievements include the detailed determination of proteins like myoglobin and hemoglobin by Kendrew and Perutz [40]. This progress paralleled developments in medical imaging. The section connects these advancements to phase contrast in optical microscopy, holography, and coherence, highlighting the intertwined evolution of material characterization and medical imaging technologies.

3.1 Development of phase contrast imaging

Holography can be traced back to the 1920s X-ray crystallography, which aimed to reconstruct crystal structures from diffraction patterns. However, these patterns only provided intensity information, leaving phase details hidden. In 1927, the discovery of electron diffraction confirmed de Broglie's matter-wave hypothesis. In 1930, Fritz Zernike discovered phase contrast which is a new type of contrast that is different from absorption, while working in a dark room. This method focused on phase objects, which do not absorb light but alter their phase.

To make these phase objects visible, Zernike used phase annuli plates, which were initially overlooked until their significance was realized in 1941. This led to the manufacture of phase-contrast microscopes. By 1943, Boersch's observation of Fresnel fringes in electron microscopy demonstrated the wavelike nature of electrons and revealed that phase information was encoded in these fringes.

Dennis Gabor invented holographic imaging in 1948 to overcome the resolution limits of electron microscopy, which was a significant breakthrough. By including a reference wave, Gabor's method captured the elusive phase information, which was expanded in the following years. This led to the development of transmission-type holography, which is now commonly used in X-ray and electron microscopy. Initially, X-ray holography struggled with low spatial coherence but benefited from advancements in synchrotron sources, especially in soft X-ray microscopy. In-line holography, which is effective around the "water window" photon energies, plays a crucial role in biological and materials imaging, using phase retrieval methods for reconstruction. In-line

holography originated as microradiography or point projection radiography, primarily for absorbing objects. Initially, diffraction effects were viewed as unwanted image blurring. Later, the technique's relationship with X-ray phase contrast imaging was explored, demonstrating its evolution from a method for absorbing objects to a tool in phase contrast imaging [41].

Coherence in wave theory is categorized into temporal (longitudinal) and spatial (lateral) coherence, which relates to a source's bandwidth and spatial extent, respectively. In this context, the used polychromatic source lacks temporal coherence but possesses high spatial coherence due to its small size. Spatially coherent waves maintain consistent phase across laterally displaced points on the same wavefront. The wave's behavior, including phase and intensity variations, is described by a complex function, with phase change $\Delta\phi$ revealed through intensity changes after propagation. Interferometry, which combines a wave of interest with a reference wave to deduce phase changes, requires coherence, a challenging aspect for X-ray imaging. Unlike optical microscopy where partial coherence can optimize resolution, X-ray imaging's experimental complexity limits interferometry's applicability. Zernike's "defocusing" technique in phase contrast imaging allows phase-induced intensity contrasts to be detected by propagating radiation over a distance. In conventional radiography, reducing the object-detector distance minimizes blur, but increasing this distance with sufficient source coherence reveals the phase properties of the object, as illustrated in various imaging scenarios.

3.2 Phase contrast early methods

X-ray phase contrast imaging can be achieved through three main methods: interferometry, crystal analyzer imaging, and in-line holography. Interferometry and in-line holography rely on the interference of scattered wavefronts from the sample with a reference wave, examples being multi-energy holography and phase contrast imaging. Crystal analyzer imaging, or diffraction-enhanced imaging, utilizes a crystal analyzer's reflective properties to differentiate the angular distribution of refracted beams. In-line holography is also known as phase propagation imaging or phase-based imaging. The first phase image of a non-crystalline object using interferometric methods was achieved in 1965 with a triple-Laue-case (LLL) interferometer. This device, often made from a monolithic crystal, consists of three parallel lamellas: a splitter, a mirror, and an analyzer. The splitter divides the incident beam, and the mirror further splits and redirects them to interfere at the analyzer. Initially used to detect lattice deformations, it evolved for imaging by placing an object in one beam's path to cause

phase shifts, observable as interference fringes directly associated with the phase shift. Further advancements in this field have been made by Momose [42].

3.3 Diffraction Enhanced Imaging

Diffraction Enhanced Imaging (DEI) is based on the refraction principle. When X-rays transition between materials with different refractive indices (n_1 and n_2), they deviate according to Snell's law. DEI utilizes this refraction, especially noticeable at curved surfaces, with deviations in the order of 10^{-3} radians for typical δ values around 10^{-6} . The technique involves a collimator and analyzer, focusing on measuring the phase gradient rather than the phase itself. This method, first used by Forster et al. in 1980, has found applications in analyzing biological materials, notably by Somenkov and Shil'shtein in 1991. DEI, the contrast is created by slight beam deviations due to refraction when interacting with an object. These deviated rays are then distinguished by the analyzer screen. This technique's sensitivity hinges on the slope of the reflection curve, with maximum contrast at the reflectivity maximum's edge. DEI effectively measures $\Delta\phi$, the differential phase of the object perpendicular to the wavefront. Ingal and Beliaevskaya further extended this method to image non-crystalline objects using Laue diffraction with a transmission-type analyzer crystal. The incident beam is monochromatized using two asymmetrical Bragg diffraction crystals, enabling simultaneous imaging of both reflected and transmitted beams. This technique, termed Phase Dispersion Imaging (PDI), distinguishes between "area contrast" and "boundary contrast." A significant advantage of DEI is its ability to reject incoherent (Compton) scatter, a common issue in conventional radiography. Unlike anti-scatter grids, which have limitations and increase patient dose, DEI uses the analyzer crystal's rocking curve for precise selection of X-ray interactions, effectively rejecting incoherently scattered rays and producing images with excellent scatter rejection, akin to traditional radiographs [43].

3.4 First steps of the propagation-based methods: Holography

Holographic X-ray phase contrast imaging is a technique that requires a specific distance between the object and detector. If the distance is short, the absorption images will be more prominent. But if the distance is increased, it is possible to form Fresnel fringes which can significantly enhance the definition and contrast of the image

compared to traditional absorption images. However, if the distance is too high, excessive fringes can degrade the image quality. Therefore, there is an optimal distance for image capture.

This technique is different from interferometry and does not require complex reconstruction methods. The fringe patterns highlight edge contrasts, which improves image resolution and contrast. High source coherence is essential to achieve effective phase contrast imaging using holographic approach. However, filters, collimators, and monochromators, among other factors, can also influence beam coherence and image quality. Artifacts, such as those from beryllium filter windows, can impact images, as observed by researchers like Carlsson and Cloetens [44].

Two methods are used in X-ray imaging for obtaining phase contrast images: the monochromatic approach and the polychromatic approach. The monochromatic approach uses a monochromator to select the wavelength, and phase shifts in the beam caused by inhomogeneous objects are detectable as intensity variations, particularly in the Fresnel region. This method does not require an analyzer crystal, as opposed to diffraction-based approaches, which have limitations related to crystal resolution and angular acceptance.

On the other hand, the polychromatic approach in in-line holography, used by Pfeiffer et al. and Wilkins et al., utilizes the full spectrum of available wavelengths. This method relies on phase differences caused by the object's varying refractive index [45]. The phase shift for a ray passing through the object is calculated using the object's electron density and the classical electron radius. This approach is particularly effective for light atomic number materials across a wide energy range, with the refractive index dependent on both wavelength and material properties. The technique allows for a detailed understanding of wavefront phase alterations due to the object's structure.

The polychromatic approach in X-ray phase contrast imaging is simpler than crystal-based methods and is similar to conventional radiography. It effectively utilizes a wide photon spectrum, which is particularly beneficial for non-synchrotron sources like microfocus sources. These sources offer the advantage of a divergent X-ray beam, aiding in magnification and making this technique more adaptable to clinical practice due to its high spatial coherence. However, the impact of source size on image quality is a critical factor in this method.

3.5 The study on phase retrieval algorithms

Current detectors lack the sensitivity to detect phase disturbances in complex electromagnetic waves. Phase retrieval is a process that aims to extract phase information from intensity measurements. This is done by using virtual optics in software to extend the optical system. With this approach, complete system knowledge can be obtained by emulating various microscopy modes and replacing physical components like mirrors with software equivalents. Gerchberg and Saxton's 1972 iterative method is notable for using intensity and diffraction patterns to refine phase estimates. These techniques are particularly valuable in fields like electron microscopy, where objects exhibit primarily phase information [46].

In X-ray imaging, especially with synchrotron sources, phase retrieval methods are essential to address beam optic and window imperfections. These methods, categorized into direct and indirect (iterative) approaches, are summarized by Nugent. Direct methods like Guigay's, transport of intensity, multi-wavelength, homogeneous sample, and phase-only approaches use two data sets for real and imaginary object parts. Each method has unique assumptions, such as weak interaction with radiation or material homogeneity. These techniques vary in their stability, noise handling, and uniqueness of solutions, offering diverse applications in imaging [47].

Indirect or iterative phase retrieval methods are used when direct analytical relationships are not feasible. These methods incorporate a priori information and handle experimental uncertainties like noise. Originating in electron microscopy, these methods involve taking multiple-intensity measurements along the optic axis to create a wave consistent with all measured data. Far-field methods, such as the Gerchberg-Saxton algorithm and its variations, use far-field images and a priori object shape information. Ptychography and astigmatic diffraction are other variations, the former involving multiple diffraction patterns from localized specimen illumination, and the latter controlling the illuminating wave's phase structure. Each method varies in uniqueness, stability, and experimental complexity.

In medical applications, phase contrast imaging focuses on optimizing image quality while minimizing patient dose. Non-synchrotron sources like gratings or microfocus sources are practical for high coherence. In medical imaging, particularly mammography, the optimal X-ray energy window is 15-50 keV. Phase contrast imaging enhances soft tissue differentiation, which is crucial in cancer detection. Contrast agents, commonly used in angiography, enhance visibility of structures but pose risks, highlighting phase contrast imaging's potential for safer and clearer diagnostic imaging.

Part II

Theoretical Foundations

Chapter 4

X-Ray fundamentals

In this section, we explore a complete explanation of the interaction mechanisms of X-ray imaging. We begin by deriving the paraxial equation from Maxwell equations. We then delve into the light-matter interactions between photons and objects and, finally, the detection mechanisms of light interactions with detectors.

X-ray fundamentals can be derived from the electromagnetic theory of radiation, which involves studying how this radiation propagates over space and time and how electromagnetic waves may shift due to light-matter interactions.

Phase contrast imaging is a principle that can be derived using two main approaches. The first approach suggests using photons as individual entities with defined and predictable trajectories (the ray-tracing approach). However, for this part, we use wave kinematics formulation using wave-field elements, which is more convenient to explain direct observable phenomena in medical imaging and more intuitive.

Maxwell equations follow the wave equation, and the space of solutions of this wave equation forms wave-field elements containing all the electromagnetic field information. This approach helps us to understand how spatial coherence may create variations in how electromagnetic radiation may be represented in detection systems. It also helps us see how phase detection and phase contrast can be powerful tools in medical imaging.

4.1 Wave equations in Vacuum

The basis for developing a full view of the X-ray diffraction theory is understanding the free-space diffraction theory of classical electromagnetic (EM) waves. Obtaining

the vacuum wave equations is possible by taking the Maxwell equations as a starting point. It is also possible to get a separate description of the time and space of the vacuum wave equation for different energies using spectral decomposition, starting from the Maxwell Equations.

$$\nabla \cdot \mathbf{E}(x, y, z, t) = \frac{\rho}{\epsilon_0} \quad (4.1)$$

$$\nabla \cdot \mathbf{B}(x, y, z, t) = 0 \quad (4.2)$$

$$\nabla \times \mathbf{E}(x, y, z, t) = -\frac{\partial}{\partial t} \mathbf{B}(x, y, z, t) \quad (4.3)$$

$$\nabla \times \mathbf{B}(x, y, z, t) = \mu_0 \mathbf{J} + \mu_0 \epsilon_0 \frac{\partial}{\partial t} \mathbf{E}(x, y, z, t) \quad (4.4)$$

Using Faraday's law (equation 4.3) and the vector potential $\mathbf{B} = \nabla \times \mathbf{A}$

$$\nabla \times \mathbf{E}(x, y, z, t) + \nabla \times \frac{\partial}{\partial t} \mathbf{A}(x, y, z, t) = 0 \quad (4.5)$$

Hence

$$\nabla \times \left(\mathbf{E}(x, y, z, t) + \frac{\partial \mathbf{A}(x, y, z, t)}{\partial t} \right) = 0 \quad (4.6)$$

Since the curl of $\mathbf{E} + \frac{\partial \mathbf{A}}{\partial t}$ must be zero, the inner part follows

$$\mathbf{E}(x, y, z, t) = -\nabla V - \frac{\partial \mathbf{A}(x, y, z, t)}{\partial t} \quad (4.7)$$

Where V is a scalar potential, and using Gauss' law (equation 4.1)

$$\nabla \cdot \mathbf{E}(x, y, z, t) = \frac{\rho}{\epsilon_0} \quad (4.8)$$

Hence

$$\nabla \cdot \left(-\nabla V - \frac{\partial \mathbf{A}}{\partial t} \right) = \frac{\rho}{\epsilon_0} \quad (4.9)$$

$$\nabla^2 V + \frac{\partial(\nabla \cdot \mathbf{A})}{\partial t} = -\frac{\rho}{\epsilon_0} \quad (4.10)$$

Using now Ampere-Maxwell's law (equation 4.4) by applying $\mathbf{B} = \nabla \times \mathbf{A}$ following is derived

$$\nabla \times (\nabla \times \mathbf{A}) = \mu_0 \mathbf{J} + \mu_0 \epsilon_0 \frac{\partial}{\partial t} \mathbf{E} \quad (4.11)$$

Since $\nabla \times (\nabla \times \mathbf{A}) = \nabla(\nabla \cdot \mathbf{A}) - \nabla^2 \mathbf{A}$, using the equation 4.7 the following is true.

$$\nabla(\nabla \cdot \mathbf{A}) - \nabla^2 \mathbf{A} = \mu_o \mathbf{J} + \mu_o \epsilon_o \frac{\partial}{\partial t} \left(-\mu_o \epsilon_o \nabla V - \frac{\partial \mathbf{A}}{\partial t} \right) \quad (4.12)$$

$$= \mu_o \mathbf{J} - \mu_o \epsilon_o \nabla \frac{\partial V}{\partial t} - \frac{\partial^2 \mathbf{A}}{\partial t^2} \quad (4.13)$$

$$\nabla \left(\nabla \cdot \mathbf{A} + \mu_o \epsilon_o \frac{\partial V}{\partial t} \right) - \nabla^2 \mathbf{A} + \mu_o \epsilon_o \frac{\partial^2 \mathbf{A}}{\partial t^2} = \mu_o \mathbf{J} \quad (4.14)$$

To make a relativistic description of the model. The Lorenz gauge is picked, where the Lorenz gauge follows

$$\nabla \cdot \mathbf{A} = -\mu_o \epsilon_o \frac{\partial V}{\partial t} \quad (4.15)$$

Using 4.15 on equation 4.14 is clear that.

$$\nabla \left(-\cancel{\mu_o \epsilon_o} \frac{\partial V}{\partial t} + \cancel{\mu_o \epsilon_o} \frac{\partial V}{\partial t} \right) - \nabla^2 \mathbf{A} + \mu_o \epsilon_o \frac{\partial^2 \mathbf{A}}{\partial t^2} = -\mu_o \mathbf{J} \quad (4.16)$$

$$- \left(\nabla^2 - \mu_o \epsilon_o \frac{\partial^2}{\partial t^2} \right) \mathbf{A} = -\mu_o \mathbf{J} \quad (4.17)$$

Equation 4.17 is an inhomogeneous wave equation and is regarded as a 4th-dimensional Poisson's equation [48]. Similarly, going back to 4.10 using 4.15.

$$\nabla^2 V + \frac{\partial(\nabla \cdot \mathbf{A})}{\partial t} = -\frac{\rho}{\epsilon_o} \quad (4.18)$$

$$\nabla^2 V - \mu_o \epsilon_o \frac{\partial^2 V}{\partial t^2} = -\frac{\rho}{\epsilon_o} \quad (4.19)$$

$$\left(\nabla^2 - \mu_o \epsilon_o \frac{\partial^2}{\partial t^2} \right) V = -\frac{\rho}{\epsilon_o} \quad (4.20)$$

Using the D'Alembert operator, equations 4.17 and 4.20 can be rewritten as.

$$\boxed{\begin{aligned} \square^2 V &= -\frac{\rho}{\epsilon_o} \\ \square^2 \mathbf{A} &= -\mu_o \mathbf{J} \end{aligned}} \quad (4.21)$$

4.1.1 Homogenous Helmholtz equation

When the EM waves travel in a vacuum, they follow a transport transformation in the propagation direction. In the paraxial approximation, said EM wave does not show a change in the wavefront; this can be then expressed classically as the wave in an initial point in space ($z = z_i$) transformed by a displacement operator \mathcal{D}_{z_f} . Starting from the

homogeneous case of equations 4.21, set $\rho(x, y, z) = 0$ and $\mathbf{J}(x, y, z) = 0$ such that.

$$\begin{aligned}\square^2 V &= 0 \\ \square^2 \mathbf{A} &= 0\end{aligned}\tag{4.22}$$

Which also follows the free-wave propagation equations for \mathbf{E} and \mathbf{B}

$$\begin{aligned}\left(\frac{1}{c^2} \frac{\partial^2}{\partial t^2} - \nabla^2\right) \mathbf{E} &= 0 \\ \left(\frac{1}{c^2} \frac{\partial^2}{\partial t^2} - \nabla^2\right) \mathbf{B} &= 0\end{aligned}\tag{4.23}$$

Let $\Psi(x, y, z, t)$ a scalar field such that it contains the information given by \mathbf{E} and \mathbf{B} . When shifting from a vector-wave representation to a scalar-wave representation of the X-ray field, the consideration of polarization is implicitly neglected. It is further assumed that \mathbf{E} is linearly polarized in the \hat{x} direction. This assumption does not cause any information loss for the case study here since polarization effects are primarily significant in the magnetic scattering of circularly polarized X-rays and dynamical diffraction of crystals, which are cases outside this work's approach. The set of equations 4.2 can be written.

$$\frac{1}{c^2} \left(\frac{\partial^2 \Psi}{\partial t^2} \right) = \nabla^2 \Psi\tag{4.24}$$

Which follows the complex solution

$$\Psi(x, y, z, t) = \sqrt{I(x, y, z, t)} e^{i\phi(x, y, z, t)}\tag{4.25}$$

Such that I is the intensity of the field and follows

$$|\Psi(x, y, z, t)|^2 = I(x, y, z, t)\tag{4.26}$$

And ϕ is the phase of the field. Using \mathbf{E} and \mathbf{B} to get the Poynting vector. It follows

$$\mathbf{S} = \frac{\mathbf{E} \times \mathbf{B}}{\mu_0} = \frac{||\mathbf{B}|| ||\mathbf{E}||}{\mu_0} \hat{n} = \frac{1}{\mu_0 c} ||\mathbf{E}||^2 \hat{n}\tag{4.27}$$

This holds due to the orthonormal nature of \mathbf{E} and \mathbf{B} where $||\mathbf{B}|| = ||\mathbf{E}||/c$. It is also straightforward that the propagation direction \hat{n} must be the same as the phase gradient $\nabla\phi$ since the phase gradient is, by definition, parallel to the field ϕ and the phase surface. Figure 4.1 represents how this vector is orthonormal to the wavefronts. Then, it can be written as $\hat{n} = A \nabla\phi$. Hence

$$\mathbf{S} = \frac{1}{\mu_0 c} ||\mathbf{E}||^2 A \nabla\phi = \tilde{I} \nabla\phi\tag{4.28}$$

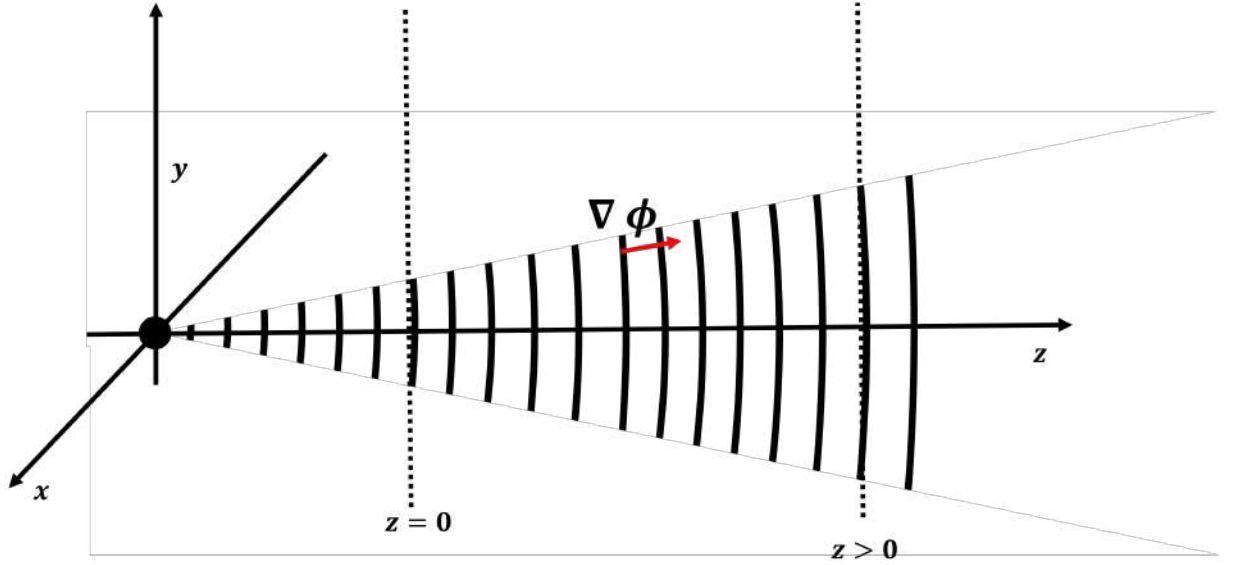


FIGURE 4.1: Wave-field elements propagating in space over the z direction over time. The region in space that comprises $z = 0$ and $z > 0$ is the region for which the Helmholtz equation holds. The vector $\nabla\phi$ shows the direction of the energy flow, which is constant for each wave-front. This vector $\nabla\phi$ provides the direction to the Poynting vector and is tangent to its associated wave-front.

Where \tilde{I} is the normalized intensity and $\tilde{I} = ||\mathbf{E}||^2 A / \mu_0 c$ is a constant. This result will be used later on, taking now the solution 4.25, assuming the solution for a monochromatic field (therefore strictly coherent) such that.

$$\Psi(x, y, z, t) = \psi_\omega(x, y, z)e^{-i\omega t} \quad (4.29)$$

Such that by definition $\omega = ck$ and going back to 4.24 then

$$\left(\frac{1}{c^2} \frac{\partial^2}{\partial t^2} - \nabla^2 \right) \psi_\omega(x, y, z)e^{-i\omega t} = 0 \quad (4.30)$$

$$\frac{1}{c^2} \left[\ddot{\psi}_\omega e^{-i\omega t} - i^2 \omega^2 e^{-i\omega t} \psi_\omega \right] - \nabla^2 \psi_\omega e^{-i\omega t} = 0 \quad (4.31)$$

$$- \left(\frac{i\omega}{c} \right)^2 \psi_\omega + \nabla^2 \psi_\omega = 0 \quad (4.32)$$

$$\boxed{(\nabla^2 + k^2) \psi_\omega(x, y, z) = 0} \quad (4.33)$$

The last equation at 4.33 is the Helmholtz equation, a central equation in diffraction theory. This equation is mathematically identical in form to the time-independent free-space Schrödinger equation for spinless non-relativistic particles [49]. It may be relevant for the reader that free-space potentials that follow scattering properties are also used in other contexts of optic physics and electrodynamics. Aside from the obvious applications in visible spectrum optics, due to its similitude to the time-independent Schrödinger equation, some of the deductions in this section are analogous to electron

optics principles in electron microscopy. In fact, in-line holography as an application in electronic microscopy was developed before X-ray phase contrast imaging and also exploits the phase switch of an electron beam under the field propagation [50] [51].

4.1.2 Spectral decomposition

Section 4.1.1 shows the derivation of the Helmholtz equation in the free-space propagation case with a monochromatic X-ray source, which can be the case of synchrotron sources in medical applications. However, this section demonstrates a more general case where the energy spectrum encloses multiple energies, like medical devices such as mammograms and CT scanners [52]. The total energy description of a polychromatic source can be written as the superposition of monochromatic fields of photons with energy $\hbar\omega$. This decomposition can be expressed as a Fourier integral over the energy spectrum [53].

$$\Psi(x, y, z, t) = \frac{1}{\sqrt{2\pi}} \int_{-\infty}^{\infty} \psi_{\omega}(x, y, z) e^{-i\omega t} d\omega \approx \frac{1}{\sqrt{2\pi}} \int_0^{\infty} \psi_{\omega}(x, y, z) e^{-i\omega t} d\omega \quad (4.34)$$

Replacing this solution in equation 4.24.

$$\left(\frac{1}{c^2} \frac{\partial^2}{\partial t^2} - \nabla^2 \right) \frac{1}{\sqrt{2\pi}} \int_0^{\infty} \psi_{\omega}(x, y, z) e^{-i\omega t} d\omega = 0 \quad (4.35)$$

Hence

$$\frac{1}{\sqrt{2\pi}} \int_0^{\infty} \left(\frac{1}{c^2} \frac{\partial^2}{\partial t^2} - \nabla^2 \right) \psi_{\omega}(x, y, z) e^{-i\omega t} d\omega = 0 \quad (4.36)$$

$$\int_0^{\infty} ([k^2 + \nabla^2] \psi_{\omega}(x, y, z)) e^{-i\omega t} d\omega = 0 \quad (4.37)$$

Integral 4.37 leads to the condition for ψ_{ω} .

$$\boxed{[k^2 + \nabla^2] \psi_{\omega}(x, y, z) = 0} \quad (4.38)$$

This arrives again at the same Helmholtz equation as in 4.33. It is concluded that solving the diffraction problem brought by the Helmholtz equation for non-monochromatic fields is possible by solving for each monochromatic component $\psi_{\omega}(x, y, z)$. This conclusion makes sense since there is no interaction between photons, and the effective diffraction is not affected by the simultaneous presence of photons with different energies. An important remark is that most of the conventional X-ray imaging systems work with polychromatic sources, these sources are known for being the standard in medical imaging and are widely available in hospitals and clinics. As well as less expensive to produce and maintain than monochromatic X-ray sources. The impact

of polychromatic X-ray sources in image quality and radiation dose will be further discussed in later sections.

4.1.3 Plane wave formulation and propagation operator

Starting from the supposition that the wave-field equation acts as a plane wave propagating forward and considering the propagation over the z axis and defining two parallel planes ($z = 0$), ($z = \Delta$) where $\Delta > 0$ with a vacuum in between, then the Helmholtz equation deduced at 4.33 applies. Using the plane wave definition then ψ_ω takes the shape

$$\psi_\omega(x, y, z) = \exp [i(k_x x + k_y y + k_z z)] \quad (4.39)$$

Where the wave vector follows $\mathbf{k}^2 = k_x^2 + k_y^2 + k_z^2$. And by definition $|\mathbf{k}| = 2\pi/\lambda$. Take now the component $k_z = \sqrt{\mathbf{k}^2 - k_x^2 - k_y^2}$ such that the plane wave has the following shape

$$\psi_\omega(x, y, z) = e^{i(k_x x + k_y y)} e^{iz\sqrt{\mathbf{k}^2 - k_x^2 - k_y^2}} \quad (4.40)$$

Setting $z = 0$ as in the first parallel plane, the initial condition is given by $\psi_\omega(x, y, =)$.

$$\psi_\omega(x, y, z = 0) = e^{i(k_x x + k_y y)} \quad (4.41)$$

From here, it is clear that the z term plays the role of the displacement over the optical axis. Taking the expression on the 2D Fourier space, the inverse transform is given by ($\psi_\omega(x, y, z = 0) = \psi_\omega[0]$).

$$\psi_\omega[0] = \frac{1}{2\pi} \iint_{\mathbb{R}^2} \tilde{\psi}_\omega[0] e^{i(k_x x + k_y y)} dx dy \quad (4.42)$$

$$= \mathcal{F}^{-1} \{ \tilde{\psi}_\omega[0] \} \quad (4.43)$$

We define the free-space propagator for $z = \Delta$ as seen in equation 4.44.

$$\mathcal{D}(\Delta) = e^{i\Delta\sqrt{\mathbf{k}^2 - k_x^2 - k_y^2}} \quad (4.44)$$

So the field expression for a propagated wave between the parallel z planes is given by ($\psi_\omega(x, y, z = \Delta) = \psi_\omega[\Delta]$)

$$\psi_\omega[\Delta] = \frac{1}{2\pi} \iint \tilde{\psi}_\omega[0] e^{i(k_x x + k_y y)} e^{i\Delta\sqrt{\mathbf{k}^2 - k_x^2 - k_y^2}} dx dy \quad (4.45)$$

$$= \mathcal{F}^{-1} \{ \mathcal{D}(\Delta) \tilde{\psi}_\omega[0] \} \quad (4.46)$$

$$= \mathcal{F}^{-1} \{ \mathcal{D}(\Delta) \mathcal{F} \{ \psi_\omega[0] \} \} \quad (4.47)$$

This expression is the angular-spectrum representation for the propagated wave-field. It solves the boundary value problem of determining the propagated field for $z = \Delta$ by operating the forward-propagating field from $z = 0$ on the free space. Now it is possible to obtain the free-space diffraction operator from the angular spectrum representation in 4.47, denoting free space propagation as

$$\psi_\omega[\Delta] = \Phi(\Delta)\psi_\omega[0] \quad (4.48)$$

In this fashion, it is possible to write $\Phi(\Delta)$ by combining 4.47 and 4.48.

$$\Phi(\Delta)\psi_\omega[0] = \mathcal{F}^{-1} \{ \mathcal{D}(\Delta) \mathcal{F} \{ \psi_\omega[0] \} \} \quad (4.49)$$

Hence

$$\Phi(\Delta) = \mathcal{F}^{-1} \mathcal{D}(\Delta) \mathcal{F} \quad (4.50)$$

$$= \mathcal{F}^{-1} e^{i\Delta \sqrt{k^2 - k_x^2 - k_y^2}} \mathcal{F} \quad (4.51)$$

These operators act from left to right to keep commutativity rules. For cases where the scalar wave field's components have a slight angle on their trajectory regarding the optical axis (paraxial wave fields), the Fresnel diffraction theory describes the dynamics and interaction of the wave-field with vacuum. The operator formulation is treated later on in section 4.195.

4.2 X-Ray propagation in matter

The previous section provided a full description of the X-ray propagation process in a vacuum space. A review of the inhomogeneous case for the Maxwell equations provides the wave field propagation of X-rays in matter. Starting from the Maxwell equations in matter.

$$\nabla \cdot \mathbf{D}(x, y, z, t) = \rho(x, y, z, t) \quad (4.52)$$

$$\nabla \cdot \mathbf{B}(x, y, z, t) = 0 \quad (4.53)$$

$$\nabla \times \mathbf{E}(x, y, z, t) = -\frac{\partial}{\partial t} \mathbf{B}(x, y, z, t) \quad (4.54)$$

$$\nabla \times \mathbf{H}(x, y, z, t) = \mathbf{J} + \frac{\partial}{\partial t} \mathbf{D}(x, y, z, t) \quad (4.55)$$

Here, the materials are restricted to be linear and isotropic. However, this assertion covers most of the materials present in medical physics. Cases such as ferroelectric and ferromagnetic materials require ϵ, μ time dependence and are not covered in this

section. Given this restriction, fields follow $\mathbf{D} = \epsilon \mathbf{E}$ and $\mathbf{B} = \mu \mathbf{H}$. Rewriting in this fashion the Maxwell equations.

$$\nabla \cdot [\epsilon(x, y, z) \mathbf{E}(x, y, z, t)] = \rho(x, y, z, t) \quad (4.56)$$

$$\nabla \cdot \mathbf{B}(x, y, z, t) = 0 \quad (4.57)$$

$$\nabla \times \mathbf{E}(x, y, z, t) = -\frac{\partial}{\partial t} \mathbf{B}(x, y, z, t) \quad (4.58)$$

$$\nabla \times \left[\frac{\mathbf{B}(x, y, z, t)}{\mu(x, y, z)} \right] = \mathbf{J}(x, y, z, t) + \frac{\partial}{\partial t} [\epsilon(x, y, z) \mathbf{E}(x, y, z, t)] \quad (4.59)$$

Just like in the vacuum case, to deduce the wave equation for the electric field by taking the curl of the equation and using the property to compute $\nabla \times [\nabla \times \mathbf{E}]$ it follows

$$\nabla(\nabla \cdot \mathbf{E}) - \nabla^2 \mathbf{E} + \frac{\partial}{\partial t}(\nabla \times \mathbf{B}) = 0 \quad (4.60)$$

Now recall the vector identity $\nabla \times \left(\frac{1}{\mu} \mathbf{B} \right) = \frac{1}{\mu}(\nabla \times \mathbf{B}) + \left(\nabla \frac{1}{\mu} \right) \times \mathbf{B}$ So the equation 4.59 becomes.

$$\mu^{-1}(\nabla \times \mathbf{B}) + (\nabla \mu^{-1}) \times \mathbf{B} - \frac{\partial}{\partial t} [\epsilon \mathbf{E}] = \mathbf{J} \quad (4.61)$$

$$\nabla \times \mathbf{B} = \mu \left[\mathbf{J} - (\nabla \mu^{-1}) \times \mathbf{B} + \frac{\partial}{\partial t} [\epsilon \mathbf{E}] \right] \quad (4.62)$$

Introducing the result 4.2 at 4.60

$$0 = \nabla(\nabla \cdot \mathbf{E}) - \nabla^2 \mathbf{E} + \frac{\partial}{\partial t} \mu \left[\mathbf{J} - (\nabla \mu^{-1}) \times \mathbf{B} + \frac{\partial}{\partial t} [\epsilon \mathbf{E}] \right] \quad (4.63)$$

$$= \nabla(\nabla \cdot \mathbf{E}) - \nabla^2 \mathbf{E} + \left[\mu \frac{\partial}{\partial t} \mathbf{J} - (\mu \nabla \mu^{-1}) \times \frac{\partial}{\partial t} \mathbf{B} + \mu \epsilon \frac{\partial^2}{\partial t^2} \mathbf{E} \right] \quad (4.64)$$

Using the fact that

$$\mu \nabla \mu^{-1} = -\mu \frac{1}{\mu^2} = -\frac{1}{\mu} = -\nabla \ln \mu \quad (4.65)$$

Recall also $\partial \mathbf{B} / \partial t = -\nabla \times \mathbf{E}$

$$0 = \nabla(\nabla \cdot \mathbf{E}) - \nabla^2 \mathbf{E} + \left[\mu \frac{\partial}{\partial t} \mathbf{J} - \nabla \ln \mu \times (\nabla \times \mathbf{E}) + \mu \epsilon \frac{\partial^2}{\partial t^2} \mathbf{E} \right] \quad (4.66)$$

Factorizing the D'alembert factor

$$\nabla(\nabla \cdot \mathbf{E}) + \mu \frac{\partial}{\partial t} \mathbf{J} = \nabla \ln \mu \times (\nabla \times \mathbf{E}) - \left(\mu \epsilon \frac{\partial^2}{\partial t^2} - \nabla^2 \right) \mathbf{E} \quad (4.67)$$

Similarly, for $\mathbf{B} = \mu\mathbf{H}$ an analogous process can be derived by using the curl and 4.59.

$$\left(\mu\varepsilon\frac{\partial^2}{\partial t^2} - \nabla^2\right)\mathbf{H} = \nabla \times \mathbf{J} - \nabla(\nabla \cdot \mathbf{H}) + \frac{1}{\varepsilon}\nabla\varepsilon \times [(\nabla \times \mathbf{H}) - \mathbf{J}] \quad (4.68)$$

For and it is clear that when $\rho = 0, \mathbf{J} = 0, \varepsilon = \varepsilon_0, \mu = \mu_0$ these equations take the homogeneous D'alambert form for vacuum deducted in . To uncouple equations and , set the case of non-magnetic materials where $\mu = \mu_0$. Furthermore, take $\rho = 0, \mathbf{J} = 0$ for a wave propagating inside a material without charges or currents.

$$\nabla(\nabla \cdot \mathbf{E}) + \mu\frac{\partial}{\partial t}\mathbf{J} = \nabla\ln\mu \times (\nabla \times \mathbf{E}) - \left(\mu_0\varepsilon\frac{\partial^2}{\partial t^2} - \nabla^2\right)\mathbf{E} \quad (4.69)$$

$$\nabla(\nabla \cdot \mathbf{E}) = -\left(\mu_0\varepsilon\frac{\partial^2}{\partial t^2} - \nabla^2\right)\mathbf{E} \quad (4.70)$$

And for 4.2.

$$\left(\mu\varepsilon\frac{\partial^2}{\partial t^2} - \nabla^2\right)\mathbf{H} = \frac{1}{\varepsilon}\nabla\varepsilon \times [(\nabla \times \mathbf{H})] \quad (4.71)$$

Now, a final assumption is made where the scattering medium is slowly varying over space compared to the wavelength in the energy spectrum $\nabla\varepsilon \gg \lambda$ Again, since 4.70 and 4.71 are non-coupled equations, the general follows a scalar form equal to any single electromagnetic field component. From said condition and using the Maxwell equations, the right side of both equations is neglected

$$\nabla \cdot (\nabla \times \mathbf{H}) = \frac{\partial}{\partial t} \nabla \cdot \mathbf{E} \quad (4.72)$$

$$C = \nabla \cdot \mathbf{E} \quad (4.73)$$

Where C is a constant, so $\nabla C = 0$. Similarly to $\nabla \times \mathbf{H}$. Hence, the following is true

$$\left(\mu_0\varepsilon(x, y, z)\frac{\partial^2}{\partial t^2} - \nabla^2\right)\mathbf{E} = 0 \quad (4.74)$$

$$\left(\mu_0\varepsilon(x, y, z)\frac{\partial^2}{\partial t^2} - \nabla^2\right)\mathbf{H} = 0 \quad (4.75)$$

Since equations 4.74 and 4.75 are uncoupled, both equations can be expressed as a scalar field once again, like in section 4.1. Hence.

$$\left(\varepsilon(x, y, z)\mu_0\frac{\partial^2}{\partial t^2} - \nabla^2\right)\Psi(x, y, z, t) = 0 \quad (4.76)$$

Using the spectral decomposition shown at 4.34.

$$\left(\varepsilon(x, y, z) \mu_o \frac{\partial^2}{\partial t^2} - \nabla^2 \right) \frac{1}{\sqrt{2\pi}} \int_{-\infty}^{\infty} \psi_{\omega}(x, y, z) e^{-i\omega t} d\omega = 0 \quad (4.77)$$

Distributing the D'alambertian operator and commuting the integral

$$\frac{1}{\sqrt{2\pi}} \int_{-\infty}^{\infty} \left(\varepsilon(x, y, z) \mu_o \frac{\partial^2}{\partial t^2} [\psi_{\omega}(x, y, z) e^{-i\omega t}] - \nabla^2 [\psi_{\omega}(x, y, z) e^{-i\omega t}] \right) d\omega = 0 \quad (4.78)$$

$$\int_{-\infty}^{\infty} \left(\varepsilon(x, y, z) \mu_o (i\omega)^2 e^{-i\omega t} \psi_{\omega}(x, y, z) - e^{-i\omega t} \nabla^2 [\psi_{\omega}(x, y, z)] \right) d\omega = 0 \quad (4.79)$$

$$- \left[\int_{-\infty}^{\infty} (\varepsilon(x, y, z) \mu_o \omega^2 + \nabla^2) \psi_{\omega}(x, y, z) d\omega \right] = 0 \quad (4.80)$$

using $k = \omega/c$ and the refraction index definition $n^2 = c^2/v^2 = \frac{\mu_o \varepsilon_{\omega}(x, y, z)}{\mu_o \varepsilon_o} = \frac{\varepsilon_{\omega}(x, y, z)}{\varepsilon_o}$ where v is the velocity propagation in the material. The condition for the integral to be zero follows.

$$(n_{\omega}^2(x, y, z) k^2 + \nabla^2) \psi_{\omega}(x, y, z) = 0 \quad (4.81)$$

And

$$\left(\left(\frac{2\pi}{\lambda/c\mu_o\sqrt{\varepsilon}} \right)^2 k^2 + \nabla^2 \right) \psi_{\omega}(x, y, z) = 0 \quad (4.82)$$

Recall that the treatment for the refraction index $n_{\omega}(x, y, z)$ is complex. The following sub-section shows why this factor takes a complex form and contains all the information in the wave-field element ψ_{ω} .

4.2.1 Electromagnetic incidence in conductors and complex refractive index

The treatment of conductor materials now assumes the existence of free currents in the material, which follows Ohm's law.

$$\mathbf{J}_{free} = \sigma \mathbf{E} \quad (4.83)$$

Where σ is the resistivity of the material. In this case, Maxwell equations do not have a homogeneous treatment and instead follow (by taking 4.56 derivative over time and divergence of 4.59),

$$\frac{\partial}{\partial t} \nabla \cdot \mathbf{D} = \frac{\partial}{\partial t} \rho_{free} \quad (4.84)$$

$$\cancel{\nabla \cdot (\nabla \times \mathbf{H})} = \nabla \cdot \mathbf{J} + \nabla \cdot \frac{\partial}{\partial t} \mathbf{D} \quad (4.85)$$

$$-\nabla \cdot \mathbf{J} = \frac{\partial \rho_{free}}{\partial t} \quad (4.86)$$

Using Gauss' law, we also have the condition

$$\frac{\partial \rho_{free}}{\partial t} = -\frac{\sigma}{\epsilon} \rho_{free} \quad (4.87)$$

This differential equation has a simple solution and has an exponential behavior, such

$$\rho_{free} = \rho_0 e^{-\frac{\sigma}{\epsilon} t} \quad (4.88)$$

This behavior can be interpreted as any free-charge density will eventually vanish in an exponential decay; the temporal factor $\tau = \epsilon/\sigma$ depends on the characteristics of the conductor. Exploring the behavior for $t \gg \tau$ Following an analogous derivation of taking the curl for Ampere-Maxwell's law and Faraday's law

$$\nabla \cdot \mathbf{D} = 0 \quad (4.89)$$

$$\nabla \cdot \mathbf{H} = 0 \quad (4.90)$$

$$\nabla \times \mathbf{D} = -\frac{\partial \mathbf{B}}{\partial t} \quad (4.91)$$

$$\nabla \times \mathbf{H} = \frac{\partial \mathbf{D}}{\partial t} + \sigma \mathbf{E} \quad (4.92)$$

Hence, the wave equation in a conductor material is given by the coupled equations

$$\nabla^2 \mathbf{E} = \mu\epsilon \frac{\partial^2 \mathbf{E}}{\partial t^2} + \mu\sigma \frac{\partial \mathbf{E}}{\partial t} \quad (4.93)$$

$$\nabla^2 \mathbf{B} = \mu\epsilon \frac{\partial^2 \mathbf{B}}{\partial t^2} + \mu\sigma \frac{\partial \mathbf{B}}{\partial t} \quad (4.94)$$

Where the solution has the general form for Ψ

$$\Psi = \Psi_0 e^{i(\kappa z - \omega t)} \quad (4.95)$$

Where $\kappa = \omega/v$. Using the orthonormal condition of the electric and magnetic fields on the plane wave $\kappa \cdot \mathbf{E} = \kappa \cdot \mathbf{B} = 0$ and $B_0 = \frac{|\kappa|}{\omega} E_0$ Hence, computing the curl

$$\nabla \times \mathbf{E} = \hat{k} \left(\frac{\partial}{\partial y} E_0 e^{i(\kappa z - \omega t)} \right) = i\omega \mathbf{B} \quad (4.96)$$

$$\nabla \times \mathbf{B} = \hat{i} \left(-\frac{\partial}{\partial x} \frac{\kappa}{\omega} E_0 e^{i(\kappa z - \omega t)} \right) = -i\omega\epsilon\mu \mathbf{E} + \mu\sigma \mathbf{E} \quad (4.97)$$

From here

$$-\frac{i\kappa^2}{\omega} \mathbf{E} = (-i\omega\epsilon\mu + \mu\sigma) \mathbf{E} \quad (4.98)$$

Hence

$$\kappa^2 = \omega^2 \epsilon \mu + i \mu \sigma \omega = \mu \omega^2 \left(\epsilon + i \frac{\sigma}{\omega} \right) \quad (4.99)$$

Recall the definition for the refraction coefficient $\kappa^2 = \frac{\omega^2}{c^2} n^2$ then the imaginary and real part dependency is clear

$$n^2 = \frac{c^2}{\omega^2} \mu \omega^2 \left(\epsilon + i \frac{\sigma}{\omega} \right) = c^2 \mu \left(\epsilon + i \frac{\sigma}{\omega} \right) \quad (4.100)$$

Finally

$$n^2 = \frac{\mu \epsilon}{\mu_o \epsilon_o} + i \mu c^2 \frac{\sigma}{\omega} \quad (4.101)$$

This result emphasizes how the complex refractive index is composed. Recall that, for the wave-field solution on the plane wave case under the paraxial approximation, aside from the oscillatory behavior of the wave, there is also an exponential decay envelope. This exponential decay represents the attenuation factor given by the complex part of the refractive index, and the real part shows the diffracting behavior of the wave. For a direct analogy, compute n instead of n^2 so $n = a + ib$ by considering the complex wave number $k = q + ip$. Hence

$$k^2 = q^2 - p^2 + 2iqp = \mu \epsilon \omega^2 + i \mu \sigma \omega \quad (4.102)$$

Such that the real and imaginary part

$$q^2 - p^2 = \mu \epsilon \omega^2 \quad 2iqp = i \mu \sigma \omega \quad (4.103)$$

Here, a quadratic expression appears

$$q^4 - q^2 \mu \epsilon \omega^2 - \left(\frac{\mu \sigma \omega}{2} \right)^2 = 0 \quad (4.104)$$

With the solution for q^2 as

$$q^2 = \frac{\mu \epsilon \omega^2}{2} \pm \frac{\mu \omega}{2} \sqrt{\epsilon^2 \omega^2 + \sigma^2} \quad (4.105)$$

Simplifying

$$q^2 = \frac{\mu \epsilon \omega^2}{2} \left(1 + \sqrt{1 + \left(\frac{\sigma}{\epsilon \omega} \right)^2} \right) \quad (4.106)$$

and

$$p^2 = \frac{\mu \epsilon \omega^2}{2} \left(-1 + \sqrt{1 + \left(\frac{\sigma}{\epsilon \omega} \right)^2} \right) \quad (4.107)$$

Following the first reasoning for n

$$n = \frac{c}{2v} \left(\sqrt{\left(1 + \sqrt{1 + \left(\frac{\sigma}{\varepsilon\omega}\right)^2}\right)} + i \sqrt{\left(-1 + \sqrt{1 + \left(\frac{\sigma}{\varepsilon\omega}\right)^2}\right)} \right) \quad (4.108)$$

In a simpler fashion

$$n = \frac{c}{\omega} (q + ip) \quad (4.109)$$

Which expresses the complex form of the refractive index. Some remarks can be noted in equation 4.149. First note how the elastic factor (real part) is the ratio of velocity propagation, which shows the momentum conservation of the light-matter interaction. Secondly, the inelastic factor (imaginary part) depends on the material magnetization and the material conductivity. But most important is how this factor is inversely proportional to the photon frequency. This is a direct consequence of the Beer-Lambert law and how high-energy photons interact less with matter.

4.2.2 Electromagnetic elastic model for dielectric materials

In the last subsection, the case of conductor materials was explored under the boundaries of the electromagnetic theory using Ohm's law of transport relation solely. However, when the refractive index n_ω has a dependency on the photon energy, the material where the wave travels has dispersive properties. Dielectric materials, however, can be modeled using the Lorentz formulation. Starting from the mechanical model.

$$M \frac{\partial^2 l}{\partial t^2} = F_{EM} - F_{Att} - F_{Bond} \quad (4.110)$$

Where F_{EM} is the electromagnetic force over the atom and F_{Att} is a damping force related to the electron's velocity and loss of kinetic energy throughout the material, this is described with the following equation

$$M \frac{\partial^2 l}{\partial t^2} = QE(t) - M\gamma \frac{dl}{dt} - M\omega_o^2 l \quad (4.111)$$

Changing to the frequency domain

$$M(i\omega)^2 \hat{l}(\omega) + M\gamma(i\omega) \hat{l}(\omega) + M\omega_o^2 \hat{l}(\omega) = Q\hat{E}(\omega) \quad (4.112)$$

So, the total displacement can be expressed as

$$\hat{l}(\omega) = -\frac{Q}{M(\omega_o^2 - \omega^2 + i\gamma\omega)} \hat{E}(\omega) \quad (4.113)$$

And since, by definition, the polarization vector is given by the dipole moment of individual charges, then the polarization vector per unit volume is given by

$$\hat{P} = NQ\hat{l} = \frac{N}{M} \frac{Q^2}{(\omega_o^2 - \omega^2 + i\gamma\omega)} \hat{E}(\omega) \quad (4.114)$$

For the electric field of the plane wave $\hat{E}(\omega) = E_o e^{i\omega t}$ and electron charge $Q = -e$

$$\hat{P} = \frac{N}{M} \frac{e^2 E_o}{(\omega_o^2 - \omega^2 + i\gamma\omega)} e^{i\omega t} \quad (4.115)$$

Moreover, if the material does not have a uniform inter-molecular force, the expression 4.115 becomes

$$\hat{P} = \frac{Ne^2}{M} E_o \sum_k \frac{n_k}{(\omega_k^2 - \omega^2 + i\gamma_k\omega)} e^{i\omega t} \quad (4.116)$$

where n_k is the number of electrons with natural frequency ω_k , furthermore with $\rho_e = Ne^2/M$

$$\hat{P} = \rho_e E_o \sum_k \frac{n_k}{\omega_k^2 - \omega^2 + i\gamma_k\omega} e^{i\omega t} \quad (4.117)$$

Similarly, since $\hat{P} = \epsilon_o \chi_e \hat{E}$, the electric susceptibility may be written as

$$\chi_e(\omega) = \frac{\rho_e}{\epsilon_o} \sum_k \frac{n_k}{\omega_k^2 - \omega^2 + i\gamma_k\omega} \quad (4.118)$$

From here, the χ_e for the time domain can also be derived

$$\chi_e(t) = \frac{\rho_e}{\epsilon_o} \sum_k \frac{n_k}{\sqrt{\omega_k^2 - \gamma_k^2}} e^{-\gamma_k t} \sin\left(t \sqrt{\omega_k^2 - \gamma_k^2}\right) u(t) \quad (4.119)$$

And the electric permittivity

$$\epsilon = \epsilon_o (1 + \chi_e) = \epsilon_o + \rho_e \sum_k \frac{n_k}{\omega_k^2 - \omega^2 + i\gamma_k\omega} e^{i\omega t} \quad (4.120)$$

This exact path can also be used with the Drude model and Debye model for materials; such models describe the constitutive relations for dispersive materials, which is the case of the dielectric media, one can prove for a Drude material (which is a simpler case of the model already shown where $F_{Bond} = 0$) that.

$$\chi_e(\omega) = \frac{\rho_e}{\epsilon_o} \sum_k \frac{n_k}{\omega_k^2 - i\gamma_k\omega} \quad (4.121)$$

Similarly, for the Debye model, which is analogous to an RC circuit, one can find

$$\chi_e(\omega) = \frac{\epsilon_r}{1 + i\omega\tau_r} \quad (4.122)$$

Where ε_r is the relative permittivity to the material and τ_r is a time constant. Now recall equation 4.98 where the wave number may be written as

$$\kappa = \sqrt{\mu\varepsilon}\omega = \omega c_{medium} \quad (4.123)$$

Then, by the electric permittivity

$$\kappa = \omega\sqrt{\mu\varepsilon_o} \left[1 + \frac{\rho_e}{\varepsilon_o} \left(\sum_k \frac{n_k}{\omega_k^2 - \omega^2 + i\gamma_k\omega} \right) \right]^{1/2} \quad (4.124)$$

By the binomial expansion

$$\kappa \approx \omega\sqrt{\mu\varepsilon_o} \left[1 + \frac{\rho_e}{2\varepsilon_o} \left(\sum_k \frac{n_k}{\omega_k^2 - \omega^2 + i\gamma_k\omega} \right) \right] \quad (4.125)$$

Recall that the attenuation of a plane wave is most directly expressed in terms of the real and imaginary parts of the wave number. Hence, as in the previous section, κ takes the form

$$\kappa = \phi + i\frac{\beta}{2} \quad (4.126)$$

Where

$$\phi^2 - \frac{\beta^2}{4} = \frac{\omega^2}{c^2} \mathbf{Re}(\varepsilon/\varepsilon_o) \quad (4.127)$$

$$\phi\beta = \frac{\omega^2}{c^2} \mathbf{Im}(\varepsilon/\varepsilon_o) \quad (4.128)$$

$$(4.129)$$

In the case of X-ray attenuation and phase signal, the case where $\beta \ll \phi$ comprehends the model of low attenuation contrast for medical imaging. Under this model, the relation becomes.

$$\beta \approx \frac{\mathbf{Im}[\varepsilon(\omega)]}{\mathbf{Re}[\varepsilon(\omega)]} \phi \quad (4.130)$$

In the limit of low-frequency waves $\omega \rightarrow 0$ there is a clear difference in the medium's response related to the lowest resonant frequency. This feature depends exclusively on the structure and phase of the material. Say for a fraction f_o of free electrons present in the material, the permittivity is now given by

$$\frac{\varepsilon(\omega)}{\varepsilon_o} = 1 + \frac{\rho_e}{\varepsilon_o} \sum_k \frac{n_k}{\omega_k^2 - \omega^2 + i\gamma_k\omega} \quad (4.131)$$

$$= 1 + \frac{\rho_e}{\varepsilon_o} \frac{f_o}{\omega(\gamma_o - i\omega)} \quad (4.132)$$

Which represents the individual contribution of the dipoles. Each singular behavior of the dipoles can be understood by computing the Ampere-Maxwell equation 4.59 assuming \mathbf{J} follows Ohm's law.

$$\nabla \times \mathbf{H} = -i\omega \left(\epsilon_0 + i \frac{\sigma}{\omega} \right) \mathbf{E} \quad (4.133)$$

Where the conductivity is given by

$$\sigma = \frac{\rho_e f_0}{\sigma_0 - i\omega} \quad (4.134)$$

This result is directly related to the Drude conductivity model, which shows a clear connection between dielectrics and conductors, where if the medium possesses free electrons, it behaves as a conductor at low frequencies (ignoring quantum-mechanical effects). And at non-zero frequencies, the contribution to $\epsilon(\omega)$ appears as a resonant amplitude. Next, the high-frequency limit is explored by taking the limit of frequencies much greater than the highest resonant frequency, such that $\omega_k^2 \gg \omega^2 + i\gamma_k\omega$. Then

$$\frac{\epsilon(\omega)}{\epsilon_0} = 1 - \frac{\rho_e}{\epsilon_0} \sum_k \frac{n_k}{\omega_k^2 - \omega^2 + i\gamma_k\omega} \quad (4.135)$$

$$\approx 1 - \frac{\rho_e}{\epsilon_0} \sum_k \frac{n_k}{\omega_k^2} \quad (4.136)$$

Since the atomic number is related to the number of particles with a certain natural frequency ω_k , the oscillator strengths of the model follow the sum rule $\sum_k f_k = Z$. Hence

$$\frac{\epsilon(\omega)}{\epsilon_0} = 1 - \frac{\rho_e}{\epsilon_0} \frac{Z}{\omega^2} \quad (4.137)$$

It may be written as

$$\frac{\epsilon(\omega)}{\epsilon_0} = 1 - \frac{\omega_p^2}{\omega^2} \quad (4.138)$$

Where $\omega_p^2 = NZe^2/\epsilon_0 M$ is the plasma frequency of the medium, the effect of electromagnetic radiation is apparent, where it can penetrate a short distance into the material, and it is almost entirely reflected; however when the frequency is increased into the domain where $\epsilon(\omega) > 0$ the reflectivity changes drastically.

4.2.3 Magnetically dispersive materials

Starting from Faraday's law for materials in 4.2, it is possible to write the frequency domain for this equation by considering the Fourier transform [54]; hence

$$\nabla \times \hat{\mathbf{E}} = -i\omega \hat{\mathbf{B}} - \sigma_m \hat{\mathbf{H}} \quad (4.139)$$

Recall that in the frequency domain for linearly-behaved magnetic materials, the definition of the auxiliary field $\hat{\mathbf{H}}$ follows

$$\hat{\mathbf{B}}(\omega) = \mu_o \hat{\mathbf{H}}(\omega) + \mu_o \hat{\chi}_m(\omega) \hat{\mathbf{H}}(\omega) \quad (4.140)$$

Then, the permeability may be written as

$$\hat{\mu}(\omega) = \mu_o \hat{\mu}_r(\omega) = \mu_o (\mu_\infty + \hat{\chi}_m(\omega)) \quad (4.141)$$

Where μ_∞ is the permeability at high frequencies. Following 4.140.

$$\nabla \times \hat{\mathbf{E}} = -i\omega \mu_o \mu_\infty \hat{\mathbf{H}} - \sigma_m \hat{\mathbf{H}} - \hat{\mathbf{J}}_m \quad (4.142)$$

Where $\hat{\mathbf{J}}_m = j\omega \mu_o \hat{\chi}_m(\omega) \hat{\mathbf{H}}(\omega)$ is the magnetization current. Consider the case of Lorentz dispersion, where [55].

$$\hat{\mathbf{J}}_m = i\omega \mu_o \hat{\chi}_m(\omega) \hat{\mathbf{H}}(\omega) = i\omega \mu_o \frac{\rho_e}{\epsilon_o} \sum_k \frac{n_k}{\omega_k^2 - \omega^2 + i\gamma_k \omega} \hat{\mathbf{H}}(\omega) \quad (4.143)$$

Then

$$\nabla \times \hat{\mathbf{E}} = -i\omega \mu_o \mu_\infty \hat{\mathbf{H}} - \sigma_m \hat{\mathbf{H}} - i\omega \mu_o \frac{\rho_e}{\epsilon_o} \sum_k \frac{n_k}{\omega_k^2 - \omega^2 + i\gamma_k \omega} \hat{\mathbf{H}} \quad (4.144)$$

$$= \left[-i\omega \mu_o \mu_\infty - \sigma_m - i\omega \mu_o \frac{\rho_e}{\epsilon_o} \sum_k \frac{n_k}{\omega_k^2 - \omega^2 + i\gamma_k \omega} \right] \hat{\mathbf{H}} \quad (4.145)$$

By taking $\nabla \cdot (\nabla \times \hat{\mathbf{E}}) = 0$ The following grants the condition for the frequency

$$0 = \left[-i\omega \mu_o \mu_\infty - \sigma_m - i\omega \mu_o \frac{\rho_e}{\epsilon_o} \sum_k \frac{n_k}{\omega_k^2 - \omega^2 + i\gamma_k \omega} \right] (\nabla \cdot \hat{\mathbf{H}}) \quad (4.146)$$

And by 4.141

$$\frac{\mu(\omega)}{\mu_o} = \mu_\infty (i\omega + 1) - (i\omega + 1) \frac{\rho_e}{\epsilon_o} \sum_k \frac{n_k}{\omega_k^2 - \omega^2 + i\gamma_k \omega} - \frac{\sigma_m - \mu_o \mu_r}{\mu_o} \quad (4.147)$$

4.3 Paraxial and projection approximation

Recall equation 4.81 and how the refractive index has a real and imaginary part. The paraxial field is a particular case of the propagating field, where all wavefronts can be obtained by slightly deforming planar surfaces perpendicular to the optical axis. Under this approximation, the monochromatic scalar X-ray field can be written as the composite of a z-directed plane wave ψ_d and a perturbing envelope $\tilde{\psi}$. Hence

$$\psi_\omega(x, y, z) = \tilde{\psi}_\omega(x, y, z)\psi_{d\omega}(z) = \tilde{\psi}_\omega(x, y, z)e^{ikz} \quad (4.148)$$

Recall the form of the complex refractive index at 4.149.

$$n^2 = \frac{\mu\epsilon}{\mu_o\epsilon_o} + i\mu c^2 \frac{\sigma}{\omega} \quad (4.149)$$

And by introducing the paraxial plane wave solution, which conveniently follows that $|\tilde{\psi}_\omega(x, y, z)|^2 = I_\omega(x, y, z)$. Replacing into the matter Helmholtz equation previously deduced at 4.81.

$$(n_\omega^2(x, y, z)k^2 + \nabla^2) \tilde{\psi}_\omega(x, y, z)e^{ikz} = 0 \quad (4.150)$$

Using the fact that $\nabla^2[AB] = A\nabla^2B + B\nabla^2A + 2\nabla A \cdot \nabla B$.

$$e^{ikz}\nabla^2\tilde{\psi}_\omega - \tilde{\psi}_\omega e^{ikz}k^2 + 2\nabla\tilde{\psi}_\omega \cdot ik e^{ikz} + k_\omega^2 n_\omega^2 \tilde{\psi}_\omega e^{ikz} = 0 \quad (4.151)$$

$$\nabla^2\tilde{\psi}_\omega - k^2\tilde{\psi}_\omega + 2ik\nabla\tilde{\psi}_\omega + k^2n^2\tilde{\psi}_\omega = 0 \quad (4.152)$$

$$(\nabla^2 - k^2 + 2ik\nabla + k^2n^2) \tilde{\psi}_\omega = 0 \quad (4.153)$$

$$\left(\left(\frac{\partial^2}{\partial x^2} + \frac{\partial^2}{\partial y^2} + \frac{\partial^2}{\partial z^2}\right) - k^2 + 2ik\left(\frac{\partial}{\partial x} + \frac{\partial}{\partial y} + \frac{\partial}{\partial z}\right) + k^2n^2\right) \tilde{\psi}_\omega = 0 \quad (4.154)$$

Taking the trasverse laplacian

$$\nabla_\perp = \left(\frac{\partial}{\partial x} + \frac{\partial}{\partial y}\right) \quad (4.155)$$

And by the paraxial approximation, the wavefront change on the propagation axis plane is negligible for $\Delta \gg \lambda$. then $\partial^2/\partial z^2\tilde{\psi}_\omega = 0$. Applying first the paraxial approximation.

$$\left[\left(\nabla_\perp^2 + \frac{\partial^2}{\partial z^2}\right) - k^2 + 2ik\left(\nabla_\perp + \frac{\partial}{\partial z}\right) + k^2n^2\right] \tilde{\psi}_\omega = 0 \quad (4.156)$$

$$\left[2ik\frac{\partial}{\partial z} + \nabla_\perp^2 + k^2(n^2 - 1)\right] \tilde{\psi}_\omega = 0 \quad (4.157)$$

Note that for $n = 1$ equation 4.157 reduces to the homogeneous paraxial equation

$$\left[2ik \frac{\partial}{\partial z} + \nabla_{\perp}^2 \right] \tilde{\psi}_{\omega} = 0 \quad (4.158)$$

On the other hand, the projection approximation assumes that the scatters are sufficiently weak to negligibly perturb the ray paths inside the material so that the ray path inside the material follows the trajectory as if said volume were a vacuum. Henceforth, since the wave has a normal incidence on the z -directed plane, the transversal Laplacian is also neglected

$$\left(\frac{\partial}{\partial z} \right) \tilde{\psi}_{\omega} = -\frac{k}{2i} (n^2 - 1) \tilde{\psi}_{\omega} \quad (4.159)$$

Integrating over the material volume distribution on z

$$\tilde{\psi}_{\omega}(x, y, z_0) = \exp \left[\frac{k}{2i} \int_{z=0}^{z=z_0} (1 - n_{\omega}^2(x, y, z)) dz \right] \tilde{\psi}_{\omega}(x, y, 0) \quad (4.160)$$

Recall the complex refractive index expressed as

$$n_{\omega} = 1 - \delta_{\omega} + i\beta_{\omega} \quad (4.161)$$

By approximating to the first order term of the refractive index n^2

$$n^2 = 1 - 2\delta_{\omega} + 2i\beta_{\omega} - i\delta_{\omega}\beta_{\omega} + \delta_{\omega}^2 - \beta_{\omega}^2 \approx 1 - 2(\delta_{\omega} - i\beta_{\omega}) \quad (4.162)$$

Using this approximation, integral at equation 4.163 becomes.

$$\tilde{\psi}_{\omega}(x, y, z_0) = \exp \left[-ki \int_{z=0}^{z=z_0} (\delta_{\omega}(x, y, z) - i\beta_{\omega}(x, y, z)) dz \right] \tilde{\psi}_{\omega}(x, y, 0) \quad (4.163)$$

The latter expression is called the projection approximation. Now, by separating the integral, the phase and amplitude shift contributions become clear

$$\tilde{\psi}_{\omega}(x, y, z_0) = \exp \left[-ki \int_{z=0}^{z=z_0} \delta_{\omega}(x, y, z) dz \right] \exp \left[ki \int_{z=0}^{z=z_0} \beta_{\omega}(x, y, z) dz \right] \tilde{\psi}_{\omega}(x, y, 0) \quad (4.164)$$

This model shows how the initial wave-field is transformed upon the interaction with matter that is placed in space from $z = 0$ to $z = z_0$ and acquires the shape of the exit wave-field $\tilde{\psi}_{\omega}(x, y, z_0)$. Some references call the integrating factor that interacts with the initial wave-field the "transmission function" \mathcal{T}_{ω} .

$$\mathcal{T}_{\omega}(x, y) = \exp \left[-ki \int_{z=0}^{z=z_0} \delta_{\omega}(x, y, z) dz \right] \exp \left[ki \int_{z=0}^{z=z_0} \beta_{\omega}(x, y, z) dz \right] \quad (4.165)$$

Under this definition, the position-dependent phase shift may be written as the argument of the complex transmission function.

$$\arg [\mathcal{T}_\omega] = \Delta\phi_\omega(x, y) = -k \int \delta_\omega(x, y, z) dz \quad (4.166)$$

By squaring both sides and recalling the I definition, this equation follows

$$I_{z_0} = \exp \left[-2ki \int_{z=0}^{z=z_0} \delta_\omega(x, y, z) dz \right] \exp \left[2ki \int_{z=0}^{z=z_0} i\beta_\omega(x, y, z) dz \right] I_0 \quad (4.167)$$

Define $\iota(x, y, z) = I_{z_0} / I_0$ the normalized intensity transmitted over the material; it is immediate that the logarithmic expression follows

$$\log [\iota(x, y, z)] = -2ki \int_{z=0}^{z=z_0} (\delta_\omega) dz + 2ki \int_{z=0}^{z=z_0} (i\beta_\omega) dz \quad (4.168)$$

Now, by taking the modulus of the expression 4.168, the Beer-Lambert law is obtained for the normalized intensity, where

$$\log [\iota(x, y, z)] = -2k \int_{z=0}^{z=z_0} \beta_\omega dz \quad (4.169)$$

As stated before, the imaginary part of the refractive index is related to the attenuation signal. Where $\mu_\omega(x, y, z) = 2k\beta_\omega(x, y, z)$ and may take the more-familiar shape of

$$I_\omega(x, y, z = z_0) = \exp \left[- \int \mu_\omega(x, y, z) dz \right] I_\omega(x, y, z = 0) \quad (4.170)$$

It is important to clarify that the absolute phase is not directly measurable. However, measuring the relative phase delay to the reference wave is possible. For a defined projected thickness over a x, y plane in the same fashion as a flat detector reconstruction, define the projected thickness function over the z direction as $T(x, y)$. So, for a single material, the phase shift may be written as

$$\Delta\phi(x, y) = -k\delta_\omega T(x, y) \quad (4.171)$$

For the simple case of a single-material scatterer, the Beer-Lambert law of absorption may be written as

$$I_\omega(x, y, z = z_0) = \exp [-\mu_\omega T(x, y)] I_\omega(x, y, z = 0) \quad (4.172)$$

An important remark is how the projection function $T(x, y)$ is acquired for both signals. The attenuation case shows that the projection function is simply the detector response of a projection from a 3D volume to a 2D discrete array (The z value is preserved on the value of the function). However, for the phase signal, the projection

may be deviated by the deflection of photons that arrive at the detector. This process is called phase retrieval, an inverse problem where phase-contrast images are viewed as encrypted images of the desired phase distribution. The concept of the phase problem and the phase retrieval algorithms will be later explored in chapter 8. Recall the definition at 4.44. The solution to the free-space propagation under the paraxial approximation can be written as

$$\psi_\omega(x, y, z = \Delta) = \mathcal{D}(\Delta)\psi_\omega(x, y, z = 0) \quad (4.173)$$

Where again the squared magnitude of this field element is the intensity of the propagated field, and the evolution of the field throughout space is rather proportional to the intensity and phase of the unpropagated field $\psi_\omega(x, y, z = 0)$. This also implies that the Fresnel diffraction operator provides the phase contrast signal information. In this fashion, it is possible to express the total phase with the projection function, which provides the thickness information $T(x, y)$. The accumulated phase signal is given by the total wavelengths that fit into the projected thickness $T(x, y)$.

$$\phi_{\text{material}} = \int_0^{\lambda_{\text{max}}} 2\pi \frac{\text{Re}(n_\omega)T(x_t, y_t)}{\lambda} d\lambda \quad (4.174)$$

Where x_t, y_t are the coordinates in between the trajectory. Similarly, for the same trajectory, the vacuum phase is propagated as

$$\phi_{\text{vacuum}} = \int_0^{\lambda_{\text{max}}} 2\pi \frac{z_o - T(x_t, y_t)}{\lambda} d\lambda \quad (4.175)$$

Therefore, the total phase signal that comprehends the full trajectory from the source to the detector for a single trajectory may be expressed as

$$\phi_{x_t, y_t} = \phi_{\text{vacuum}} + \phi_{\text{material}} = \int_0^{\lambda_{\text{max}}} 2\pi \frac{\text{Re}(n_\omega)T(x_t, y_t)}{\lambda} d\lambda + \int_0^{\lambda_{\text{max}}} 2\pi \frac{z_o - T(x_t, y_t)}{\lambda} d\lambda \quad (4.176)$$

$$= \int_0^{\lambda_{\text{max}}} \frac{2\pi}{\lambda} T(x_t, y_t) \left[\text{Re}(n_\omega) + \frac{z_o - 1}{T(x_t, y_t)} \right] d\lambda \quad (4.177)$$

This can be further simplified using the fact that $\text{Re}(n_\omega) = 1 - \delta_\omega$

$$\phi_{x_t, y_t} = \int_0^{\lambda_{\text{max}}} \frac{2\pi}{\lambda} [z_o - T(x_t, y_t)\delta_\omega] d\lambda \quad (4.178)$$

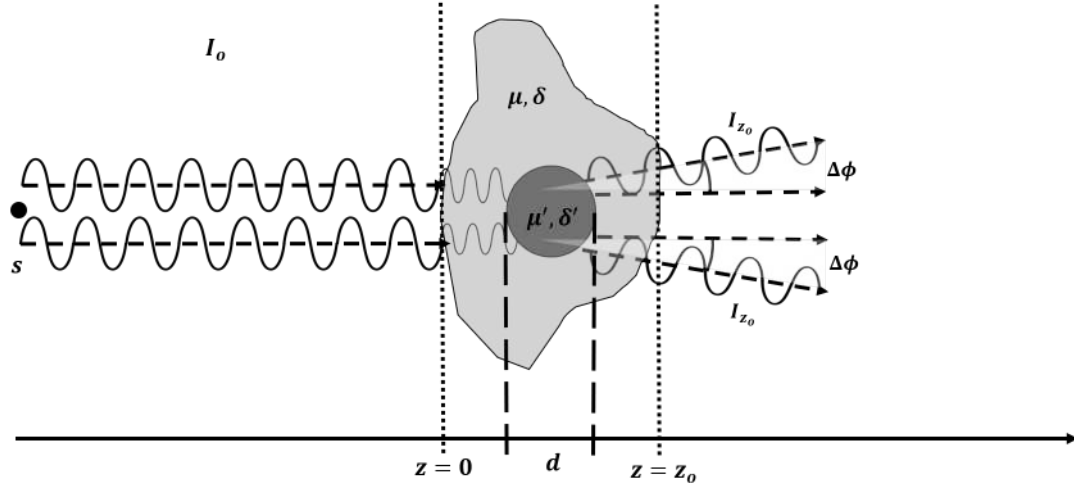


FIGURE 4.2: X-ray imaging representation of a sample with known composition and density (known μ', δ') embedded inside another material with known characteristics μ, δ . The projection approximation remains whenever the maximum transverse deviation effects $\Delta\phi$ can be neglected. Namely when the transverse diffraction spread caused by the embedded object with size d (Given by the Fresnel relation $\lambda z_o/a$) cannot be resolved.

4.3.1 Validity of the projection approximation

Recall that the primary assumption to apply the projection approximation is that the X-ray diffraction effects within the sample are negligible. The projection approximation is then valid if we assume that X-rays propagate along straight lines within the volume occupied by the sample. This implies that the diffraction from features embedded in the sufficiently small material can be neglected. To put the consequences of this assumption into perspective, take the following example. Modern mammograph devices have detectors with a spatial resolution of less than $100 \mu\text{m}$, and early-stage cancer microcalcifications have sizes between $50 \mu\text{m}$ and $400 \mu\text{m}$; the capability of resolving microcalcifications is crucial for an adequate diagnosis. However, if the projection approximation is considered, the phase signal from such objects is neglected. This section will evaluate the validity of this approximation by weighing the setup constraints and the relation of the projection approximation with the Fresnel number. Starting from the geometry already proposed, take a sample which is extended from $z = 0$ to $z = z_o$, at $z = z_d$ an embedded spherical sub-sample is present where $0 < z_d < z_o$ and with $\delta'_\omega \neq \delta_\omega$ and $\mu'_\omega \neq \mu_\omega$, the sub-sample has a depth and diameter d which is fully embedded on the sample medium. The primary constraint to resolve the sub-sample is that $d < l_{px}\sqrt{2}$ where l_{px} is the detector's pixel size. Following the Fresnel diffraction principle, the maximum diffraction angle for photons with wavelength λ scattered by the sub-sample is [?].

$$\Delta\theta = \frac{\lambda}{d} \quad (4.179)$$

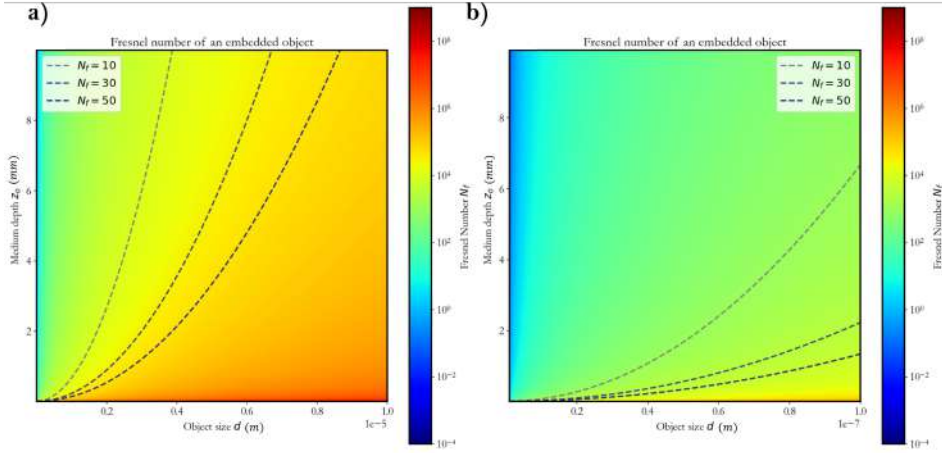


FIGURE 4.3: Contour map of the relation of the Fresnel number and the propagation distance z_0 along with the minimum resolution d with a fixed $\lambda = 10^{-10}$ value for the wavelength in the X-ray regime. a) represents the case of for objects in the range of micro X ray imaging, while b) is presented for even lower resolutions in the range of nanometric distances where the projection approximation lessens. It is clear that for most state-of-art medical imaging devices, the projection approximation holds due to the short distance z_0 needed to hold the condition [9]. Both plots also have the specific values for the fresnel number at $N_F = 10, 20, 30$

Henceforth, the sample depth gives the maximum spread that the detector perceives and the projection of the scattered signal on the detector, which is $\Delta\theta z_0$ for small θ . Then, the main condition for the projection approximation is given by the limit when $\frac{\lambda}{d} z_0 \gg d$. The fresnel number for a diffractive optical element is defined as

$$N_F = \frac{d^2}{\lambda z_0} \quad (4.180)$$

Then, the same condition for the projection approximation may be written as

$$\frac{d^2}{\lambda z_0} \gg 1 \quad (4.181)$$

Figure 4.3 shows the dependency of the geometry for a fixed energy value with the Fresnel number, which is related to the geometric distortion caused by the diffraction of the sub-sample. This approximation may not hold for ultra-high resolution X-ray systems, for which a fully dynamic model called the multi-slice approximation is applied and is developed in section 4.4. Both approximations may not hold for even higher resolution since magnetic and polarization effects become relevant.

4.3.2 Fresnel Diffraction theory

The Fresnel Diffraction theory seeks to determine how wave fields evolve throughout space when they propagate further from their source. Starting from the operator

defined in equation 4.51 and with the paraxial approximation for a monochromatic component of the wave field $\psi_\omega(x, y, z)$ propagating over the vacuum in the range previously defined ($0 \leq z \leq \Delta$). The paraxial approximation for the z chosen direction implies

$$|k_z| \gg |k_x| \quad |k_z| \gg |k_y| \quad |k_z| \gg |k_x| + |k_y| \quad (4.182)$$

Hence

$$\sqrt{k^2 - k_x^2 - k_y^2} = k \sqrt{1 - \left(\frac{k_x^2 + k_y^2}{k^2} \right)} \approx k \left(1 - \frac{1}{2} \left(\frac{k_x^2 + k_y^2}{k^2} \right) \right) \quad (4.183)$$

$$\approx k - \frac{k_x^2 + k_y^2}{2k} \quad (4.184)$$

So the diffraction operator in equation 4.51 becomes

$$\Phi(\Delta) = \mathcal{F}^{-1} e^{i\Delta \left(k - \frac{k_x^2 + k_y^2}{2k} \right)} \mathcal{F} \quad (4.185)$$

$$= e^{i\Delta k} \mathcal{F}^{-1} e^{-\frac{i\Delta(k_x^2 + k_y^2)}{2k}} \mathcal{F} \quad (4.186)$$

This operator corresponds to the Fresnel diffraction operator. Substituting this result into equation 4.48

$$\psi_\omega[\Delta] = e^{i\Delta k} \mathcal{F}^{-1} e^{-\frac{i\Delta(k_x^2 + k_y^2)}{2k}} \mathcal{F} \psi_\omega[0] \quad (4.187)$$

$$= \boxed{e^{i\Delta k} \frac{1}{2\pi} \iint_{\mathbb{R}^2} dk_x dk_y \left[e^{-\frac{i\Delta(k_x^2 + k_y^2)}{2k}} \tilde{\psi}_\omega[0] \right]} \quad (4.188)$$

Which is the operator form of the Fresnel diffraction integral [?]. And can be written as.

$$\mathcal{D}_\Delta^{(F)} = e^{ik\Delta} \mathcal{F}^{-1} e^{-i\frac{\Delta(k_x^2 + k_y^2)}{2k}} \mathcal{F} \quad (4.189)$$

Now, the solution to the diffraction problem under the paraxial formulation may be written as may be written as 4.48 by using the Fresnel diffraction integral operator.

$$\psi_\omega(x, y, z = \Delta) = \mathcal{D}_\Delta \psi_\omega(x, y, z = 0) \quad (4.190)$$

Taking the squared magnitude of this term, it shows that the intensity of the propagated field depends on both the intensity and the phase of the unpropagated field since it implies that the Fresnel diffraction pattern given by the propagated wave field in the region $z > 0$ provides the phase contrast information mainly that is not acquired

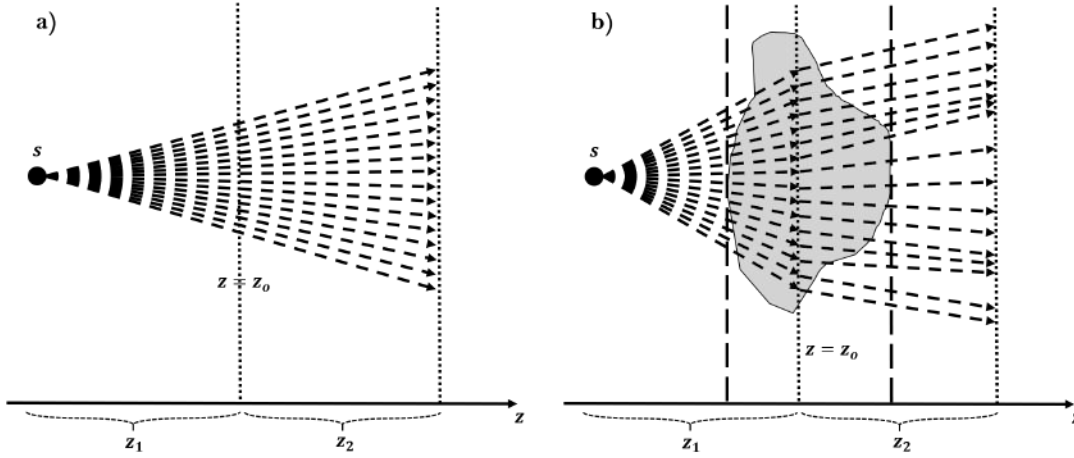


FIGURE 4.4: Plane wave fields traveling along the z direction. in figure b) The scatterer volume lies between the planes $z = z_1$ and $z = z_2$. The unscattered beam is given by the trajectories described at a). The intensity and phase of the wave at the exit-surface $z = z_2$ is given by the projection approximation. Under this approximation, the ray path distribution in the presence of the scatterer is taken to be equal to their unscattered counterparts. Thus the phase and amplitude at z_2 are considered to be accumulated along the wave path.

on the intensity on arrival. This is the main mechanism of operation for propagation-based phase contrast imaging techniques, which will be further explored throughout this work.

Finally, a more intuitive description of what happens with the wave-field signal can be introduced using the system's geometry. Figure 4.4 shows how this system is modeled. A point source S located at a l distance from the sample object emits at a constant rate wave field elements that propagate through z_1 until they reach the object, with a finite d depth extending on the optical plane axis. The right-most section of the object has a distance z_2 to the detector, where deflected wave-field elements propagate until they reach the detector. The distance z_2 is assumed to be large enough that the propagation-based phase contrast effects are relevant but not significantly sufficient for interference effects to be present as Fresnel diffraction fringes. Taking the object as a slit-type diffractor, the Fresnel number may be written as.

$$N_f = \frac{z_1 + z_2}{z_1} \frac{d^2}{\lambda z_2} \quad (4.191)$$

In frequency form

$$N_f = \frac{z_1 + z_2}{z_1 z_2} \frac{\omega d^2}{c} \quad (4.192)$$

Where the term $z_1 + z_2/z_1$ is the geometric magnification. This term and the Fresnel number N_F have a major role when the projection approximation of X-ray wave fields interacting with matter is further developed in section 4.3.

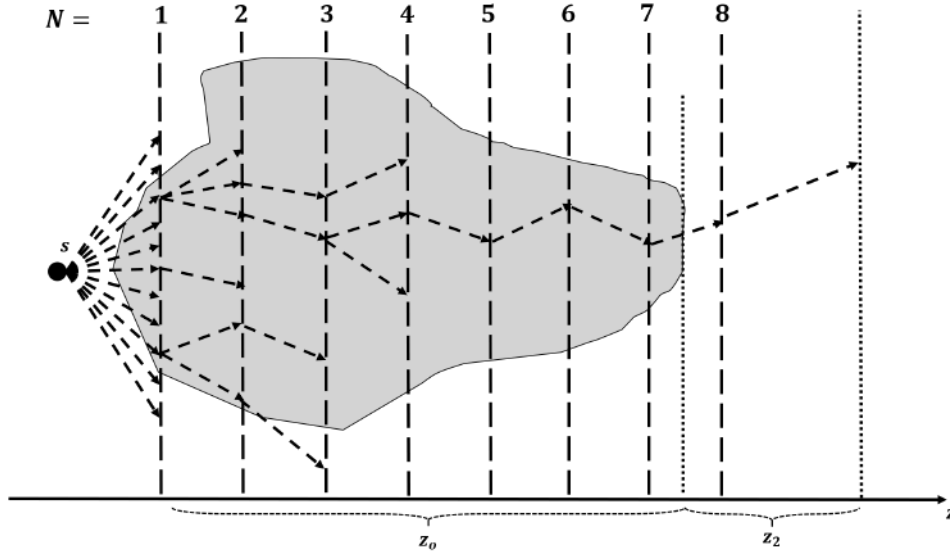


FIGURE 4.5: Coherent X-ray radiation is produced by a point-source s within the optic axis z . Multislice algorithm is applied to a scatterer with size z_0 , to be sliced into a number of slabs (8). After passing through all slices of the scatterer, one has the exit-surface wave-function $\psi_\omega(z_c)'$. This exit-surface wave-function then propagates into the half-space downstream of the exit surface of distance z_2 . The resulting signal is the resulting wave-function after interacting with eight different scatters that have a defined depth l and an associated value for the material density in each region given by δ_l, β_l .

4.4 Multi-slice approximation

Since this work also includes high-resolution X-ray optics, it is essential to fulfill the geometrical limitations of the projection approximation. The multi-slice approximation was proposed in electron microscopy and later used in high resolution by X-ray optics. This approach mainly consists of decomposing a thick sample into a fixed number of slices that can hold the condition of the projection approximation for the Fresnel number $N_f \gg 1$. Say a sample of thickness D can be decomposed on multiple thickness samples $d_i = D/N$. Figure 4.5 illustrates this process.

Since the wave field interacting with the first slice is known, its propagation can be calculated using the Fresnel diffraction until it reaches the second slice. It becomes an iterative process until it arrives at the last slice, which may be propagated in the vacuum space between the sample and the detector. The squared magnitude of the propagated wave-field that reaches the sensor is then interpreted as the intensity distribution alongside the sample. Considering the abovementioned considerations, we may write the transmission function for the j -th slice as the wave-field propagation of a material with a complex refractive index $n_{(\omega)j}$.

$$T_j(x, y) = \exp [ik(n_j(x, y) - 1)(z_j - z_{j-1})] \quad (4.193)$$

Such that the next wave-field propagated for the next slice is given by

$$\psi_{j+1}(x, y) = \mathcal{D}_{(z_j - z_{j-1})} [\psi_j(x, y) T_j(x, y)] \quad (4.194)$$

Figure 4.5 shows this iterative process. Now suppose that crossing over each j -th step is infinitesimal, where $\delta z = (z_j - z_{j-1})$. Equation 4.195 may be re-written as

$$\psi_{j+1}(x, y) = \mathcal{D}_{\delta z} [\psi_j(x, y) \exp [ik(N_j(x, y) - 1)\delta z]] \quad (4.195)$$

4.5 Phase signal evolution: The transport-of-intensity equation

The phase contrast propagation in time and space may be modeled as a forward problem; phase contrast images can be particularly modeled following the fundamentals explored in the last sections. Nonetheless, extending the notion of wave-fields to experimental imaging systems that consider the non-stationary nature of wavefronts detected in X-ray imaging is essential. This model is called the transport-of-intensity (TOI) equation and has been explored deeply by several authors in the X-ray imaging field. To extend the space evolution of the propagated wave-field, recall equation 4.158 but now using the wave-field definition at 4.25.

$$\left(2ik \frac{\partial}{\partial z} + \nabla_{\perp}^2 \right) \sqrt{I(\mathbf{r})} \exp(i\phi\mathbf{r}) = 0 \quad (4.196)$$

Under the Teague deduction [56], take the matter paraxial approximation for material with $n = 0$. Then it becomes

$$\left(i \frac{\partial}{\partial z} + \frac{\nabla_{\perp}^2}{2k} + k \right) \psi_{\omega} = 0 \quad (4.197)$$

Also, recall the wave-field element that contains the amplitude information and phase.

$$\psi_{\omega} = \sqrt{I(\mathbf{r})} \exp(i\phi\mathbf{r}) \quad (4.198)$$

It becomes by multiplying the paraxial approximation for the complex conjugate of the wave-field element.

$$\left(i \frac{\partial}{\partial z} + \frac{\nabla_{\perp}^2}{2k} + k \right) |\psi_{\omega}|^2 = 0 \quad (4.199)$$

Now take the complex conjugate of equation 4.197 and multiplying it by ψ_ω the subtraction with 4.199

$$\frac{2\pi}{\lambda} \frac{\partial}{\partial z} I = -\nabla_\perp \cdot I \nabla_\perp \phi \quad (4.200)$$

Rewriting the equation

$$\nabla_\perp \cdot [I(\mathbf{r}) \nabla_\perp \phi(\mathbf{r})] = -k \frac{\partial I(\mathbf{r})}{\partial z} \quad (4.201)$$

Recall equation 4.28 where a relation between the transverse divergence and the Poynting vector is established. The transverse energy flow is directly related to the expansion or contraction of the local paraxial field. So if the energy flow is positive, energy would be moving away from the optical axis; hence, the longitudinal derivative of intensity would become negative, and then the convergence of the transverse Poynting vector is proportional to the rate of change of intensity along the propagation direction [57]. Figure 4.1 depicts this relation in a better fashion. To solve this expression, it is necessary to introduce an auxiliary equation Y that satisfies.

$$Y = I \nabla \phi \quad (4.202)$$

Then

$$\nabla_\perp^2 Y = \frac{-2\pi}{\lambda} \frac{\partial}{\partial z} I \quad (4.203)$$

Which is the two-dimensional Poisson equation and can be deduced by finding the Green function that satisfies

$$Y(\mathbf{r}) = \iint_\Gamma d\mathbf{r}' G(\mathbf{r}, \mathbf{r}') \frac{\partial}{\partial z} I(\mathbf{r}') - \int_{\Gamma'} ds' \left[G(\mathbf{r}, \mathbf{r}') \frac{\partial Y(\mathbf{r}')}{\partial n'} G(\mathbf{r}, \mathbf{r}') \right] \quad (4.204)$$

And by integrating the infinitesimal auxiliar equation $\psi = I_o(\phi + C)$, the Dirichlet boundary conditions and with $\mathbf{r}' = a\hat{r}'$

$$G(\mathbf{r}, \mathbf{r}') = \frac{1}{4\pi} \ln \left(\frac{\mathbf{r}^2 + \mathbf{r}'^2 - 2\mathbf{r} \cdot \mathbf{r}'}{\frac{r^2 r'^2}{a^2} + a^2 - 2\mathbf{r} \cdot \mathbf{r}'} \right) \quad (4.205)$$

it is possible to deduce the propagation of phase inside a material over the region as

$$\phi_o(\mathbf{r}) = \iint_\Gamma d\mathbf{r}' G(\mathbf{r}, \mathbf{r}') \left[\frac{-2\pi}{\lambda I_o} \frac{\partial I_o(\mathbf{r})}{\partial z} \right] + \int_{\Gamma'} ds' \phi_o(\mathbf{r}') \frac{\partial G}{\partial n'}(\mathbf{r}, \mathbf{r}') \quad (4.206)$$

Since the gradient of the irradiance detected has to be approximated by measured values, the first-order finite-difference approximation is used.

$$\frac{\partial I_o(\mathbf{r}')}{\partial z} \approx \frac{I_{\partial z}(\mathbf{r}') - I_o}{\delta z} \quad (4.207)$$

By the conditions previously mentioned, 4.201 can take the following form under the finite difference approximation.

$$I_{\delta z} \approx I - \frac{\delta z}{k} \nabla_{\perp} \cdot [I \nabla_{\perp} \phi] \quad (4.208)$$

An additional approximation can be made whenever the transversal phase gradient or intensity gradient fulfills $\ll I(x, y, z)$ so equation 4.208 becomes

$$I(x, y, z + \delta z) \approx I - \frac{\delta z}{k} I \nabla_{\perp}^2 \phi \quad (4.209)$$

An approximate description for propagation-based phase contrast X-ray imaging is obtained in the regime of sufficiently small propagation distances δz at equation 4.208. More about the methods for phase contrast imaging can be further developed in chapter 7. On the other hand, it is analogous to equation 4.210 using the finite differences approximation.

$$\phi_o(\mathbf{r}) = \int_{-a}^a dx' G(\mathbf{r}, \mathbf{r}') \left[\frac{-2\pi}{\lambda I_o} \frac{\partial I_o(x')}{\partial z} \right] + \left(\frac{x+a}{2a} \right) \phi_o(a) - \left(\frac{x-a}{2a} \right) \phi_o(-a) \quad (4.210)$$

Where the green function follows

$$G(\mathbf{r}, \mathbf{r}') = \frac{1}{2} |x - x'| - \frac{1}{2} \left| \frac{xx'}{a} - a \right| \quad (4.211)$$

A general symbolic solution for the Poisson equation at 4.203 can also be found by applying the inverse perpendicular gradient

$$Y = k \nabla_{\perp}^{-2} \frac{\partial}{\partial z} I \quad (4.212)$$

Now by applying the operator ∇_{\perp} again, it follows

$$Y = -k \nabla_{\perp} \left[\nabla_{\perp}^{-2} \frac{\partial I}{\partial z} \right] \quad (4.213)$$

Then dividing by I and applying the divergency operator, it follows

$$\nabla_{\perp}^2 \phi = -k \nabla_{\perp} \cdot \left\{ \frac{1}{I} \nabla_{\perp} \left[\nabla_{\perp}^{-2} \frac{\partial I}{\partial z} \right] \right\} \quad (4.214)$$

By using the Fourier derivative theorem, it is possible to deduce the following relation

$$\left(\frac{\partial^m}{\partial x^m} + \frac{\partial^n}{\partial y^n} \right)^p g(x, y) = \frac{1}{2\pi} \iint_S [(ik_x)^m + (ik_y)^n]^p \tilde{g}(k_x, k_y) e^{i(k_x x + k_y y)} dk_x dk_y \quad (4.215)$$

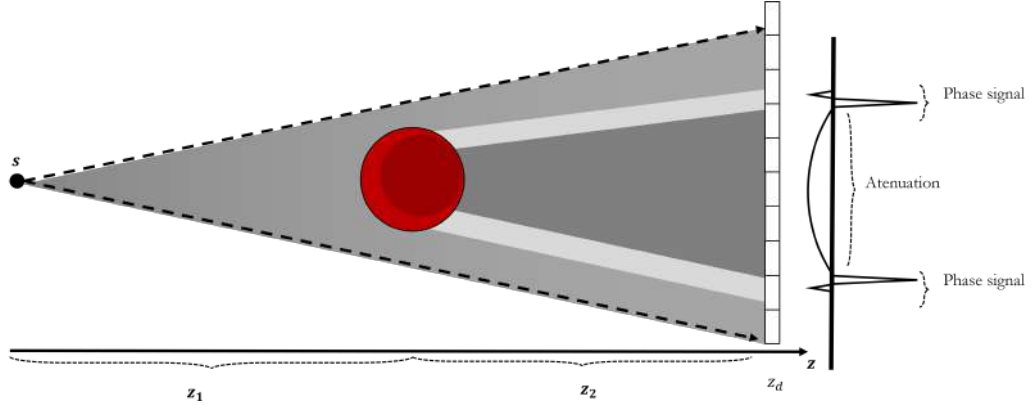


FIGURE 4.6: Representation of wave-object interaction in the in-line imaging modality for a constant wave-field ψ_ω generated from a point-source at distance $z_1 + z_2$ from the detector. X-rays travel across a sample located at z_2 from where X-ray are deflected due to an associated n^2 of the scatterer. For a z_2 large enough, the differential phase is detected as positive and negative fringing on the detector.

where $\tilde{g}(k_x, k_y)$ is the Fourier transform of $g(x, y)$. This result describes that the p -th gradient for a two-dimensional function may be calculated by taking the Fourier transform of the function, multiplied by the polynomial $[(ik_x)^m + (ik_y)^n]^p$ and then get the inverse Fourier transform. In this way it is possible to calculate the operator ∇_\perp^{-2} where in general

$$\nabla_\perp^{-p} = \mathcal{F} \left(\frac{1}{k_x^n + k_y^m} \right)^{(p-1)} \mathcal{F} \quad \text{Particularly} \quad \nabla_\perp^{-2} = -\mathcal{F} \frac{1}{k_x^2 + k_y^2} \mathcal{F} \quad (4.216)$$

Finally, the transport-of-intensity equation by this formalism

$$\nabla_\perp^2 \phi = -k \nabla_\perp \cdot \left\{ \frac{1}{I} \nabla_\perp \left[-\mathcal{F} \frac{1}{k_x^2 + k_y^2} \mathcal{F} \frac{\partial I}{\partial z} \right] \right\} \quad (4.217)$$

The principle of free-space propagating imaging systems achieving phase contrast is called propagation-based phase contrast imaging. This phase contrast, according to equation 4.201, is achieved because the propagated image has a transverse intensity distribution that depends on the phase shifts on the transverse X-ray upstream plane. With this generalized version, we can explore more complex optical imaging systems that may enhance the acquisition of phase signals by interposing an optical imaging system.

4.5.1 Linear imaging systems

Now that the tools to interpret phase contrast imaging systems have been explored, a linear imaging system can be described by a linear transform that follows a continuous

matrix multiplication form.

$$\Psi_{out} = \iint dx' dy' G(x, y, x', y', \tau) \Psi_{in} \quad (4.218)$$

Where τ is a set of control parameters of the optical system and G is its corresponding Green function. Such a system could be modeled with an integral that transforms one function by assuming shift invariance over space (which holds for a homogeneous illumination imaging system). The Green function depends only on coordinate differences in this approximation because the system's action does not change under transverse translation. Then, the system may be written as.

$$\Psi_{out}(x, y, \tau) = \iint dx' dy' G(x - x', y - y', \tau) \Psi_{in}(x', y') \quad (4.219)$$

Which is a two-dimensional convolution integral

$$\Psi_{out}(x, y, \tau) = \Psi_{in}(x, y) * G(x, y, \tau) \quad (4.220)$$

Now, we can connect the diffraction operator notion with this interpretation. Consider the transfer function to be the Fourier transform to be .

$$T(k_x, k_y, \tau) = 2\pi \mathcal{F}[G(x, y, \tau)] \quad (4.221)$$

Then, the diffraction operator quantifying our imaging system is the Fourier-space filtration

$$\mathcal{D}(\tau) = \mathcal{F}^{-1} T(k_x, k_y, \tau) \mathcal{F} \quad (4.222)$$

Linear systems can then be described as the product of the input wave in Fourier space with the system's Transfer function, which contains enough optical parameters τ to model the real system. A generalization for \mathcal{D} can be made by taking the derivative Fourier theorem (eq. 4.215) and applying it to the convolution case. Elements in τ may then be written as a set of complex aberration coefficients $\tau = \{\alpha_{m,n}\}$ which, following a Taylor series expansion, may be written as

$$\mathcal{D}(\{\alpha_{m,n}\}) = \mathcal{F}^{-1} \exp \left[i \sum_{m,n} \alpha_{m,n} k_x^m k_y^n \right] \mathcal{F} \quad (4.223)$$

Note that if all aberration coefficients $\alpha_{m,n}$ are zero, $\mathcal{D} = 1$, Which implies that the wave-field element does not show phase signal shifts. This is critical since it means that perfect imaging systems with no aberrations present do not replicate phase phenomena. It makes sense to examine how the space-propagated phase contrast effects are amplified when aberration effects due to distance are also amplified.

Chapter 5

X-Ray light-matter interactions

The process of diffraction, which is the main focus in phase contrast X-ray imaging convolution of a diffraction operator with the wave-field element defined in the propagation field, phenomena can be reflected as the consequence of scattering and interference. This chapter aims to explain the fundamentals of the imaging formation process and contextualize it within the broader scattering framework. Previously, the complex index of refraction, $n = 1 - \delta + i\beta$, was used to characterize how x-rays interacted with matter, but little was said about the nature of δ and β and how were they obtained. We do know, however, that both parts of the refractive index are necessarily associated with absorption and angular scattering phenomena, which in a mesoscopic scale the junction of these phenomena is interpreted as light refraction.

Further development of our understanding in the phase contrast imaging theory leads to the necessity of discussing the interaction between X-rays and matter and scattering theory for the conventional medical X-ray source potentials in the range of $21 - 100\text{kVp}$. Three interactions of particular interest are present in medical imaging: photoelectric absorption, coherent and incoherent scattering. Additionally, pair-production interactions will be shallowly discussed as a way of contextualization, although they are not present at low energy range.

Photons can undergo two types of interactions when passing through an absorbing medium. The first type involves interactions with atomic nuclei, such as pair production, which requires very high photon energy, far beyond that used in radiology. The second type involves interactions between photons and orbital electrons, specifically those lightly bound, where their binding energy E_B is much less than the photon energy $h\nu$. The interactions relevant in this case are the Compton Effect and Thomson scattering.

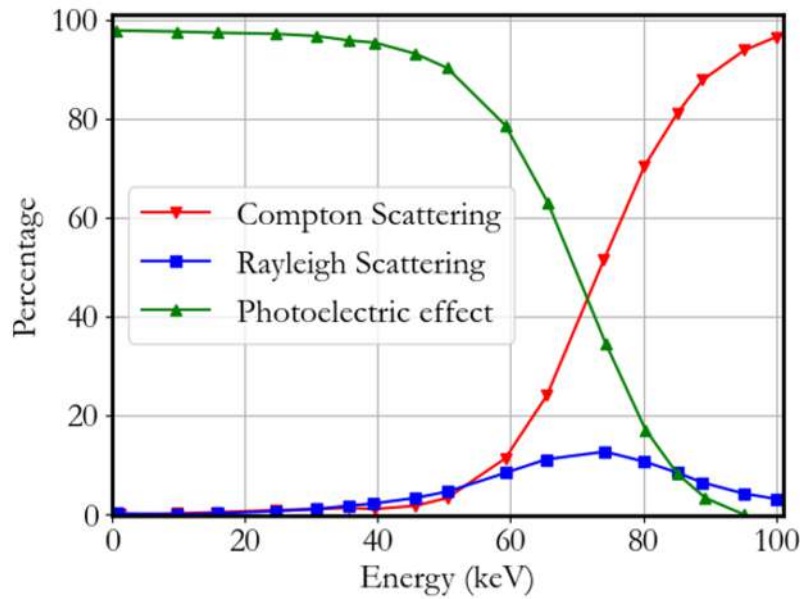


FIGURE 5.1: Percentage of contribution for the refraction coefficient on real and imaginary parts δ, β over the energy spectrum range commonly used in medical applications for hydroxyapatite $\text{Ca}_5(\text{PO}_4)_3(\text{OH})$ commonly found in bone tissue [10].

Additionally, interactions can occur with strongly bound electrons whose binding energy E_B is approximately equal to or less than the photon energy $h\nu$. In this case, the interactions encompass the photoelectric effect and Rayleigh scattering [58] and minimal photon absorption due to pair production. Quantitatively, the absorption is described by the Beer-Lambert law, which, in this case, can be denoted as the magnitude of the wave-field element in the z direction.

$$|\psi(x, y, z_0)|^2 = |\psi(x, y, 0)e^{ikz}T(x, y)|^2 \quad (5.1)$$

By the form of equation 4.170 the Transmission function and the Fourier term take the form of equation 5.2.

$$I(z_0; x, y) = I(0; x, y) \exp \left[- \int \mu(x, y, z) dz \right] \quad (5.2)$$

The imaginary part of the refraction coefficient previously defined β is related to the attenuation coefficient μ in the form $\mu = 2k\beta$. This phenomenon is depicted in figure 5.2. In the polychromatic case as it applies to conventional medical imaging devices, the relation between the attenuation coefficient μ and β refraction coefficient is not linear and the Beer-Lambert law takes the form.

$$I(z_0) = I_0 \int S(\omega) \exp \left[- \int \mu(z, \omega) dz \right] d\omega \quad (5.3)$$

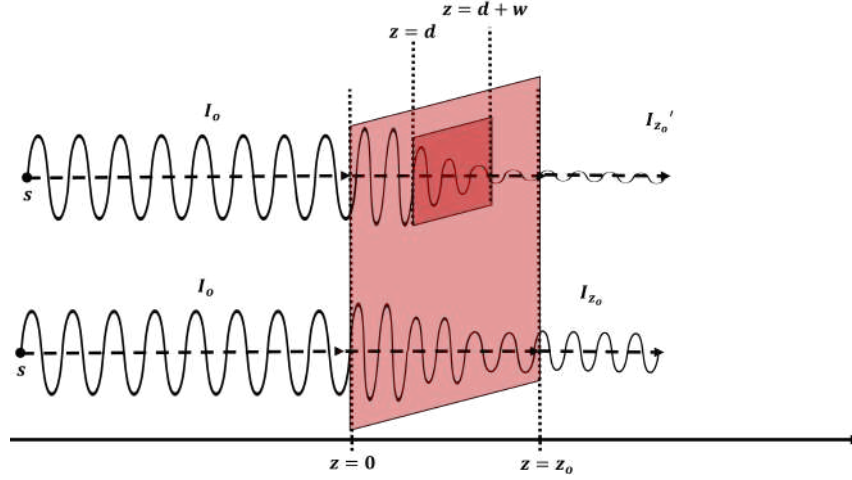


FIGURE 5.2: This figure depicts the change of intensity due to the presence of an inhomogeneous sample, according to the trajectory, the exit intensity varies. X-rays are produced by the same source at the same energy. Bottom ray follows a trajectory that travels only through the embedding material with known δ, β in a depth distance z_o . The top ray travels through both the embedding and embedded material producing a contrast difference. The total depth traveled throughout the embedding material is $z_o - w$ while the depth traveled in the embedded with known δ', β' and $\delta' > \delta, \beta', \beta$ is w .

5.1 Attenuation: Photon absorption

Absorption and attenuation are terms often used interchangeably to describe the reduction of X-rays as they pass through matter [59]. It is also employed in astronomy to define the combined processes of absorption and scattering of electromagnetic radiation by materials such as dust and gas between an emitting object and an observer [59].

In the realm of infrared optics, the extinction coefficient κ forms a part of the complex refractive index, denoted as $\hat{n} = n - i\kappa$, and the absorption coefficient is related to it by $\alpha = 2\kappa/\lambda$ [60]. Absorption is defined as the conversion of photon energy into different forms of energy and matter, such as heat, inelastic scattering, and pair-production, which are the processes that represent a net energy shift in the incident photons. The photoelectric effect is the primary absorber process in the low-energy X-ray ($< 30\text{keV}$) realm [61].

5.1.1 Photoelectric effect

The photoelectric effect is the predominant interaction between light and matter for energies below 30 keV, where the photon is completely absorbed, and its energy is transferred to the electron [62]. Figure 5.3 depicts this case. The result is the ejection

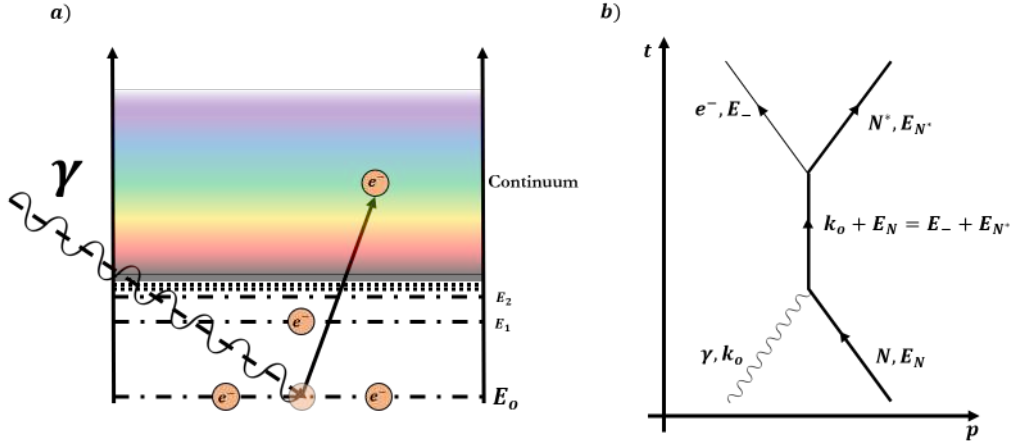


FIGURE 5.3: a) diagram of a photon going through the process of inducing the photoelectric effect. A photon in between the frequency range of X-ray imaging interacts with an atom and if the energy of the photon is sufficient it ejects an inner core electron. b) Feynman diagram that depicts the photoelectric effect, it is an annihilation of a photon with momentum k_0 changing at the same time the momentum of an electron present in a material with N atoms.

of an electron from the inner shell with a kinetic energy of $h\nu - E_B$, and this electron loses that energy by exciting other atoms. Since no scattered photons are produced, and the material mainly absorbs the energy, this effect primarily contributes to the measurement of deposited dose [63]. The probability of interaction in the photoelectric effect increases rapidly with the atomic number Z , and this measurement depends on the attenuation coefficient μ . The total cross-section shown in appendix A for the Feynmann diagram in figure 5.3.b is proportional to.

$$\sigma_{pe} = \begin{cases} \sim Z^4 / (\hbar\omega)^3 & \text{low energy } < 100\text{keV} \\ \sim Z^5 / \hbar\omega & \text{high energy } > 100\text{keV} \end{cases} \quad (5.4)$$

The cross-section highly depends on the atomic number Z , which quickly interprets why heavy materials in an X-ray imaging system are visible while lighter materials are invisible. Fluorescence effects, Croster-Kronig effect, and Auger emission take part after the photoelectric effect occurs mainly because of atom ionization. However, they are deficient in energy and intensity, ergo, for practical purposes, negligible.

By the explicit dependence on Z , we can say that their elemental and chemical compositions determine X-rays' attenuation by different body tissue types. In medical X-ray imaging, the three tissue types of interest are adipose tissue (fat), glandular/fibrous tissue (soft), and bone [64]. Soft tissues include muscle and body fluids, comprising 75% to 90% water. For simulation and numerical purposes, they may be treated as equivalent to water with an adequate atomic number $Z_{eff} = 7.4$ and an electron density of 3.34×10^{26} electrons per gram [65]. Some imaging techniques take advantage

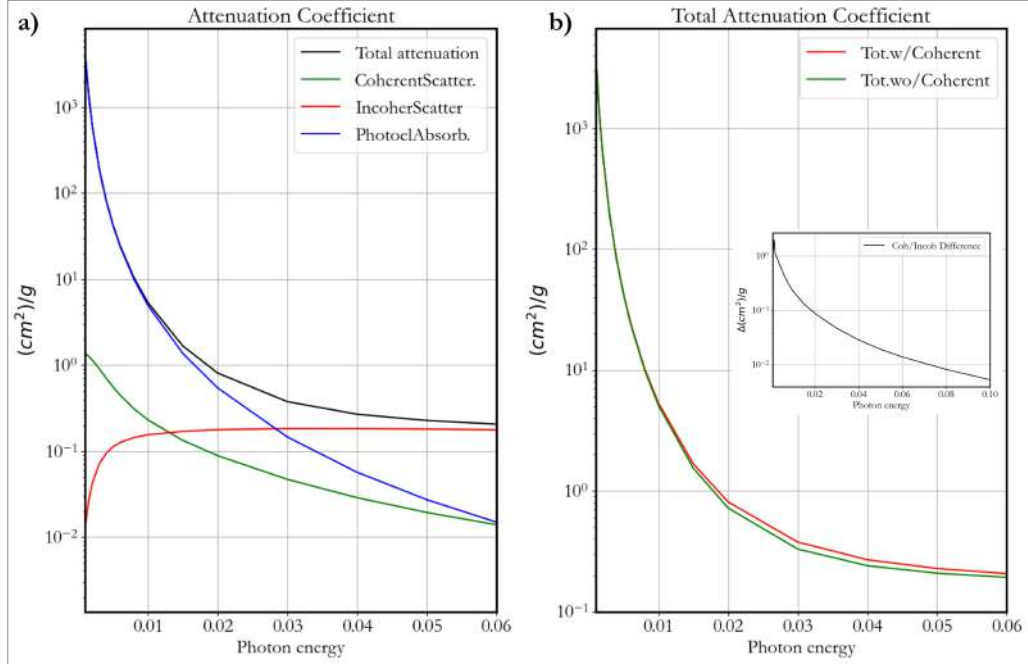


FIGURE 5.4: Total attenuation interactions cross-section contributions due do different light-matter interactions. The black line represents the total attenuation cross-section as the sum of coherent scattering, incoherent scattering, and attenuation. The total attenuation including and excluding coherent scattering effects is also plotted in Figure B) with its respective difference as a subplot. We note that for the energy range used in this work (20kV-40kV) these values are close, hence Thomson and Rayleigh's contributions in the total cross-section can be ignored [10].

of this fact by using contrast agents for specific organs and tissues. However, phase contrast imaging has an advantage in resolving internal structures that absorption techniques may not be able to, eliminating the need for a chemical contrast agent.

5.1.2 Pair production

Pair production is not a significant occurrence in diagnostic X-ray imaging, as it necessitates extremely high energies for activation. However, some occurrences are possible in the radiotherapy energy regime. Specifically, the minimum energy needed for pair production is 1.02 MeV. In this process, an X-ray photon engages with the electric field of an atom's nucleus, causing a transformation of the photon's energy into an electron-positron pair. Notably, each electron carries a rest mass energy equivalent of 0.511 MeV, which underscores the 1.02 MeV energy requirement for this reaction to happen.

In this process, a photon interacts with the nucleus of an atom. During this interaction, the photon transfers its energy to the nucleus, forming a pair comprising positively and negatively charged electrons. The positron ionizes until it combines with a free

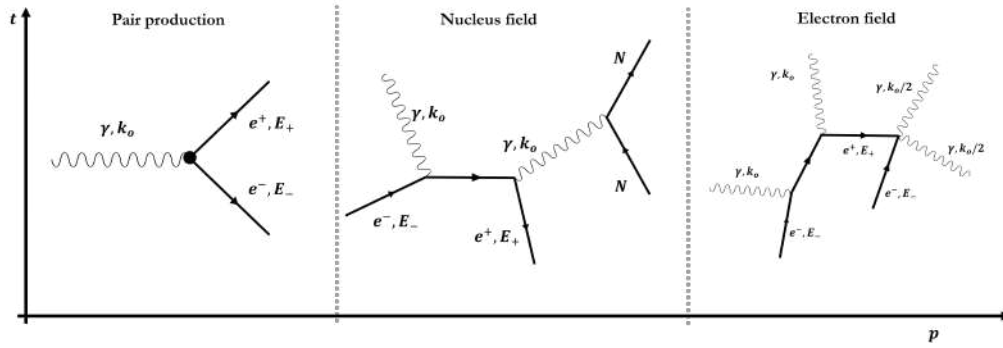


FIGURE 5.5: From left-to-right. Diagram showing the process of electron–positron pair production. The produced pair are nearly collinear. Next Feynman diagram describes another process of higher energy in the nucleus field viewpoint, where there is an electric field produced by the presence of the Z charges of a nucleus [11].

electron in the material, yielding two photons of less energy that disperse in opposite directions. If the photon is near an atomic nucleus, the energy of a photon can be converted into an electron–positron pair as depicted in equation 5.5. Since the photon must be near a nucleus to satisfy the conservation of momentum and the electron–positron pair produced in free space cannot satisfy said condition, The atomic nucleus receives some recoil. The free positron may annihilate with an external electron to produce two photons, each with an energy of 0.511 MeV. Equation 5.6 shows this process

$$(Z)\gamma \longrightarrow e^+ + e^- \quad (5.5)$$

$$e^+ + e^- \longrightarrow \gamma + \gamma \quad (5.6)$$

The likelihood of pair production is directly related to the logarithm of the photon's energy and is proportional to the material's atomic number. The energy spectrum where pair production predominates is $\geq 25\text{MeV}$, far above radiology and radiotherapy regimes. To a certain extent, this interaction occurs in routine radiation therapy utilizing high-energy photon beams. The effective cross-section for the process expressed in Feynman's diagram at figure 5.5.b of pair production is given by equation 5.7 for lower energies.

$$\sigma_{pp} = Z^2 \alpha r_e^2 \frac{2\pi}{3} \left(1 - \frac{2E_e}{E_\gamma}\right) \Lambda(\rho)_4 \quad (5.7)$$

$\Lambda(\rho)$ is the Maximon equation expansion to fourth order, α is the fine structure constant and E_e is the electron rest mass energy. For higher energies, when $E_\gamma \gg E_e$, the cross-section is also still proportional to Z^2 , but the Maximon equation follows a zeta-Riemann additional term.

5.2 Scattering

Another mechanism of interaction aside from photon absorption by atoms and free electrons present in the sample is the photon trajectory deflection produced by scattering effects. Since X-ray photons work at a higher energy regime, scattering effects are considerably more present than reflection effects from common objects. The model presents the scattering process via two components: An elastic component, where photons have no energy loss, and a modified inelastic component, where an energy fraction of the photons is not preserved. Classical effects only predict the elastic component using Thomson scattering and Rayleigh (coherent) scattering.

5.2.1 Thomson scattering

As we know from the classical electrodynamic theory, an accelerated charged particle irradiates electromagnetic fields employing the Maxwell equations and the Lorenz gauge in four-vector covariant form (see A). For a particle with a defined trajectory takes the form

$$\partial_\mu F^{\mu\nu} = \mu_0 j^\nu \rightarrow \partial_\nu (\partial^\mu A^\nu - \partial^\nu A^\mu) = \mu_0 j^\nu \quad (5.8)$$

$$\partial_\mu \partial^\mu A^\nu - \partial^\nu (\partial_\mu A^\mu) = \mu_0 j^\nu \rightarrow \partial_\mu \partial^\mu A^\nu = \mu_0 j^\nu \quad (5.9)$$

By this formulation, it may be clear that A^ν satisfies the wave equation. By solving the Green equation for a retarded potential of the form.

$$\partial_\mu \partial^\mu G_R(x, x') = \delta^{(4)}(x - x') \quad (5.10)$$

It is then possible to solve the wave equation through the equation under the presence of electromagnetic sources.

$$A^\nu(x) = \int d^4x' G_R(x - x') j^\nu(x') \quad (5.11)$$

Applying the retarded Green function and integrating over the four-space poles at τ_0 , we then arrive at the Liénard-Wiechert potential equation

$$A_\mu(x) = q \frac{u^\mu(\tau_0)}{u^\mu \cdot (x - r(\tau_0))} \quad (5.12)$$

The scalar and vector potential field information is included using the light cone boundary conditions on τ_0 . The radiated electric field can then be deduced using

the potential, hence

$$\mathbf{E}(t, \mathbf{r}) = \frac{q}{R} \frac{\mathbf{n} \times ((\mathbf{n} - \mathbf{v}/c) \times \dot{\mathbf{v}})}{c^2 (1 - \frac{1}{c} \mathbf{v} \cdot \mathbf{n})^3} \quad (5.13)$$

Now by 4.28, a relation between the electromagnetic radiation of moving charges and their radiation intensity may be deduced, where in the non-relativistic limit, this becomes the Larmor formula

$$\mathbf{S} = \frac{1}{\mu_o} ||\mathbf{E}||^2 \mathbf{n} = \frac{q^2}{4\pi\epsilon_o c^2} \left| \frac{\mathbf{n} \times (\mathbf{n} \times \dot{\mathbf{v}})}{R} \right| \mathbf{n} = \frac{q^2 \mu_o}{4\pi} \left| \frac{\mathbf{n} \times (\mathbf{n} \times \dot{\mathbf{v}})}{R} \right| \mathbf{n} \quad (5.14)$$

The differential radiated power as a spherical expansive wave may be written as.

$$dP = \mathbf{S} \cdot d\mathbf{A} = \frac{1}{\mu_o} R^2 d\Omega ||\mathbf{E}||^2 \quad (5.15)$$

With the result above at 5.14

$$\frac{dP}{d\Omega} = \left(\frac{q^2}{mc^2} \right)^2 \sin^2 \theta \quad (5.16)$$

And for the cross-section $\sigma = \langle P \rangle / \langle \mathbf{S} \rangle$ it follows.

$$\sigma_T = \int \left(\frac{q^2}{mc^2} \right)^2 \sin^2 \theta d\Omega = \frac{8\pi}{3} \left(\frac{q^2}{mc^2} \right)^2 \quad (5.17)$$

The important feature is that the cross-section is independent of x-ray energy, and it mostly depends on the impact object parameter, which is proportional to the square of the classical radius of a point particle of mass m and charge q , namely $r_e = e^2/mc^2$.

$$\sigma_T = \frac{8\pi}{3} r_e^2 = \frac{8\pi}{3} \left(\frac{\alpha \lambda_c}{2\pi} \right)^2 \quad (5.18)$$

Where α is the fine structure constant and λ_c is the Compton wavelength for the mass at rest. Since Thomson scattering process does not rely on photon energy but rather on moving charged particles density, the intensity of Thomson scattering for one particle with mass m and elementary charge q is

$$I_o = I_e \left(\frac{q^2}{mc^2} \right)^2 \sin^2 \theta = I_e \left(\frac{q^4}{m^2 c^4} \right) \frac{1 + \cos^2 2\theta}{2} \quad (5.19)$$

Since the atomic nuclei, which are much heavier than an electron, contribute negligibly to the scattered X-rays, the coherent scattering detected from an atom can be accurately approximated by analyzing the collective scattering from the electrons in the system. This is the main mechanism of X-ray crystallography techniques.

5.2.2 Rayleigh scattering

Coherent or Rayleigh scattering is a scattering interaction between a single-bound electron and a photon. Because of the great mass of an atom, very little energy is absorbed by the electron under the bound force. The photon is, therefore, deflected with essentially no loss of energy. Coherent scattering is essential only at relatively low energies ($\ll 50$ keV), and it is significant in precise photon transmission measurements, i.e., in x-ray computed tomographic scanning. Using a damping oscillatory classical model shown at 5.20.

$$m\ddot{\mathbf{x}} + m\gamma\dot{\mathbf{x}} + m\omega_s^2\mathbf{x} = -q(\mathbf{E} + \mathbf{v} \times \mathbf{B}) \quad (5.20)$$

Where ω_s is the discrete binding energy of the photon and γ is the damping coefficient. One can finally arrive using the incident and radiated power to an expression for the cross-section.

$$\sigma_b(\omega) = \frac{8\pi}{3} \left(\frac{q^2}{mc^2} \right)^2 \frac{\omega^4}{(\omega^2 - \omega_s^2)^2 + (\gamma\omega)^2} \quad (5.21)$$

Note how this final expression, unlike Thomson scattering, is dependent on the photon energy and has a resonance frequency maximum at

$$\omega_{rs} = \frac{\omega_s}{\sqrt{1 - \frac{1}{2} \left(\frac{\gamma}{\omega_s} \right)}} \quad (5.22)$$

Such that the cross-section

$$\sigma_b(\omega) = \sigma_T \left(\frac{\omega_s}{\gamma} \right)^2 \quad (5.23)$$

However, the Thomson scattering cross-section is also included in this equation for the limit case when the photon energy is much greater than the binding energy ($\omega \gg \omega_s$). On the other hand, the limit when the binding energy is much greater than the photon energy ($\omega \ll \omega_s$), the cross-section reduces to the following expression.

$$\sigma_b(\omega) = \frac{8\pi}{3} \left(\frac{q^2}{mc^2} \right)^2 \left(\frac{\omega}{\omega_s} \right)^4 \quad (5.24)$$

Rayleigh scattering may be generalized for the multi-electron atom by introducing the complex scattering factor

$$f(\Delta\mathbf{s}, \omega) = \sum_{j=1}^Z \frac{\omega^2 e^{-i\Delta\mathbf{s} \cdot \Delta\mathbf{r}_j}}{\omega^2 - \omega_s^2 + i\gamma\omega} \quad (5.25)$$

Where $\Delta \mathbf{s} = \mathbf{k} - \mathbf{k}_i$ is defined as the scattering vector for the i -th electron. In this case, the differential cross-section may also be written as

$$\frac{d\sigma}{d\Omega} = \left(\frac{q^2}{mc^2} \right)^2 |f(\Delta \mathbf{s}, \omega)|^2 \sin^2 \Theta \quad (5.26)$$

$$\sigma(\omega) = \frac{8\pi}{3} \left(\frac{q^2}{mc^2} \right)^2 |f(\Delta \mathbf{s}, \omega)|^2 \quad (5.27)$$

We may connect the role of the complex scattering factor, and the complex refractive index explored at 4.2.2 under the elastic solid theory of light for multiple oscillators. Defining the refractive index as.

$$n^2 = 1 + \frac{e^2}{\pi m} \sum_j \frac{N_j}{\omega_{o,j}^2 - \omega^2} \quad (5.28)$$

Where N is the number of electrons per unit volume and $\omega_{o,j}$ are the natural frequencies, by using the transverse wave equation for a polarized electric field traveling across a material with these features, we may arrive again to a homogeneous Helmholtz equation of the form.

$$\left[\frac{\partial^2}{\partial t^2} - c^2 n^2(\omega) \nabla^2 \right] \mathbf{E}_t(\mathbf{r}, t) = 0 \quad (5.29)$$

Where the refractive index function $n(\omega)$ follows.

$$n(\omega) = 1 - \frac{e^2 n_a}{\epsilon_o m} \sum_j \frac{g_j}{(\omega^2 - \omega_j^2) + i\gamma\omega} \quad (5.30)$$

Where g_j is the j -th oscillator bind strength. By taking the shape of the complex refractive index $n = 1 - \delta + i\beta$ and separating the real and imaginary part of the sum.

$$n(\omega) = 1 - \frac{n_a}{2\pi} \left(\frac{q^2}{mc^2} \right)^2 \frac{c^2}{\omega^2} (f(\omega) + ig(\omega)) \quad (5.31)$$

Where f, g are strictly real sums. From here, a direct relationship can be done

$$\delta = \frac{n_a}{2\pi} \frac{c^2}{\omega^2} r_e^2 f(\omega) \quad (5.32)$$

$$\beta = \frac{n_a}{2\pi} \frac{c^2}{\omega^2} r_e^2 g(\omega) \quad (5.33)$$

As expected, the values of f, g are normally obtained numerically. Some references provide the values of atomic scattering factors based on photoabsorption measurements of elements in their elemental state. At higher energies (above 1keV) $f(\omega) \approx N$, and $g(\omega) \approx \sigma_e$.

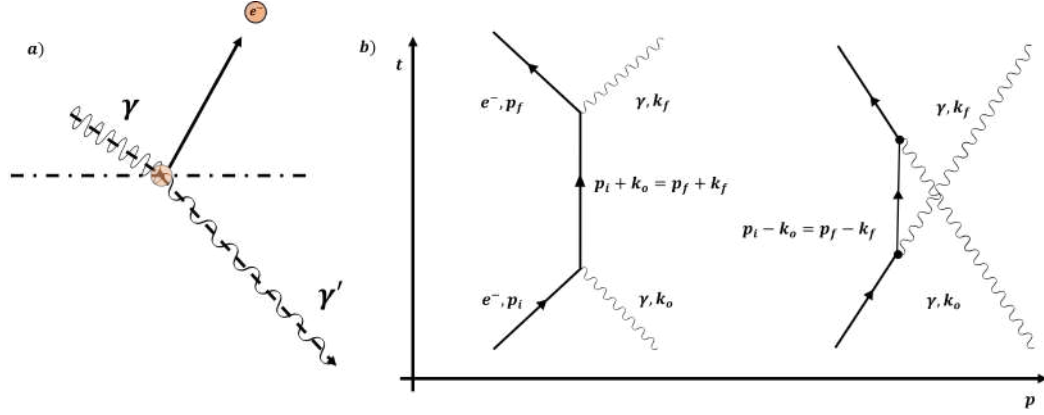


FIGURE 5.6: a) diagram description of the Compton scattering, photons interact with a free electron, during the interaction the proton transfers energy to the electron field hence $\hbar\omega' < \hbar\omega$. b) Two low-order Feynman diagrams representations of the Compton scattering, both contribute to the calculation of the total cross-section of this process given by the Klein-Nishina equation

5.2.3 Compton scattering and the Klein-Nishina equation

Compton scattering is a process that occurs when X-rays or gamma rays interact with free electrons or loosely bound valence shell electrons in an atom. The incident photon is scattered and imparts energy to the electron, which recoils and changes direction. Compton scattering is a partial absorption process, and the original photon loses energy (inelastic scattering), which implies that the scattered photon has a longer wavelength than the incident photon, and the wavelength change can be determined by

$$\Delta\lambda = \frac{h}{m_e c} (1 - \cos \theta) \quad (5.34)$$

Where θ is the scattered photon angle, the energy of the scattered photon decreases with increasing scattered photon angle. Compton scattering is the second dominant effect in X-ray imaging, contributing to images' artifacts. The likelihood of Compton scattering doesn't depend on the material's atomic number; it is rather directly proportional to the number of outer shell electrons, the density of the absorbing medium, and the photon energy. Compton scattering is a direct consequence of quantum mechanical effects in light-matter interactions. The original expression derived independently by Compton and Debye follows the wavelength shift expression at 5.34

$$E_f = \frac{E_i}{1 + \frac{E_i}{mc^2} (1 - \cos \theta)} \quad (5.35)$$

However, the energy shift and angle do not have a direct correspondence mainly due to relativistic quantum effects still not being considered. Klein and Nishina proposed

a full description of photon electron interactions by calculating the differential cross-section of this process. Figure 5.6 shows the two-level Feynman diagrams contributing to the Compton scattering process matrix element. Using the Feynman rules from A, it is possible to write the matrix elements of the diagrams, where.

$$\mathcal{M}_1 = e^2 \bar{u}^{(s')}(p_f) \epsilon'_\nu \gamma^\nu \left[\frac{\not{p} + \not{k} + m}{(p+k)^2 - m^2} \right] \epsilon_\mu \gamma^\mu u^{(s)}(p) \quad (5.36)$$

$$\mathcal{M}_2 = e^2 \bar{u}^{(s')}(p_f) \epsilon_\nu \gamma^\nu \left[\frac{\not{p} - \not{k} + m}{(p-k)^2 - m^2} \right] \epsilon'_\mu \gamma^\mu u^{(s)}(p) \quad (5.37)$$

The sum of these two matrix elements gives the total matrix element $\mathcal{M} = \mathcal{M}_1 + \mathcal{M}_2$. By expressing $|\mathcal{M}|^2$ into the lorentz-invariant variables s, t, u . It is possible to calculate the cross section for the matrix elements using.

$$\sigma = \prod_{i=1}^n \int \frac{d^4 q_i}{(2\pi)^3} \delta(q_i^2 - m_i^2) \Theta(q_i^0) (2\pi)^4 \delta\left(\sum_{i=1}^n q_i - p - k\right) \frac{|\mathcal{M}|^2}{F} \quad (5.38)$$

Where F is the Moller flux factor given by $F = E_1 E_2 v_{12} = 2(s - m_e^2)$ and $|\mathcal{M}|$ is expressed in the s, t, u variable system (See A for the full expression for $|\mathcal{M}|^2$). For the lab frame, the expression may be reduced to the form.

$$\frac{d\sigma}{d\cos\theta} = \frac{1}{32\pi} \frac{\omega'}{m_e^2 \omega - m_e \omega^2 (1 - \cos\theta)} |\mathcal{M}_1 + \mathcal{M}_2|^2 \quad (5.39)$$

By using $m_e \omega' = \frac{1}{2}(m_e^2 - u)$ and replacing s, t, u for the explicit dependencies, we arrive at the Klein Nishina equation.

$$\frac{d\sigma}{d\cos\theta} = \frac{g_e^4}{16\pi m^2} \left(\frac{\omega'}{\omega}\right)^2 \left(\frac{\omega'}{\omega} + \frac{\omega}{\omega'} - \sin^2\theta\right) \quad (5.40)$$

Equivalently

$$\frac{d\sigma}{d\Omega} = \frac{r_e^2}{2} \left(\frac{E_f}{E_i}\right)^2 \left(\frac{E_f}{E_i} + \frac{E_i}{E_f} - \sin^2\theta\right) \quad (5.41)$$

Note how this equation reduces to the Thomson scattering cross-section for the case where $E_f \approx E_i = E$ (The photon energy remains unchanged).

$$\frac{d\sigma}{d\Omega} = \frac{r_e^2}{2} (2 - \sin^2\theta) \quad (5.42)$$

Water-density tissues (e.g., muscle, blood, and solid organs) create the body's most scattered radiation. Tissues of greater density (e.g., bone) tend toward higher absorption of X-rays. Low-density tissues that contain air (e.g., lung and large bowel) allow greater penetration of X-rays. Higher-energy X-rays tend toward greater penetration,

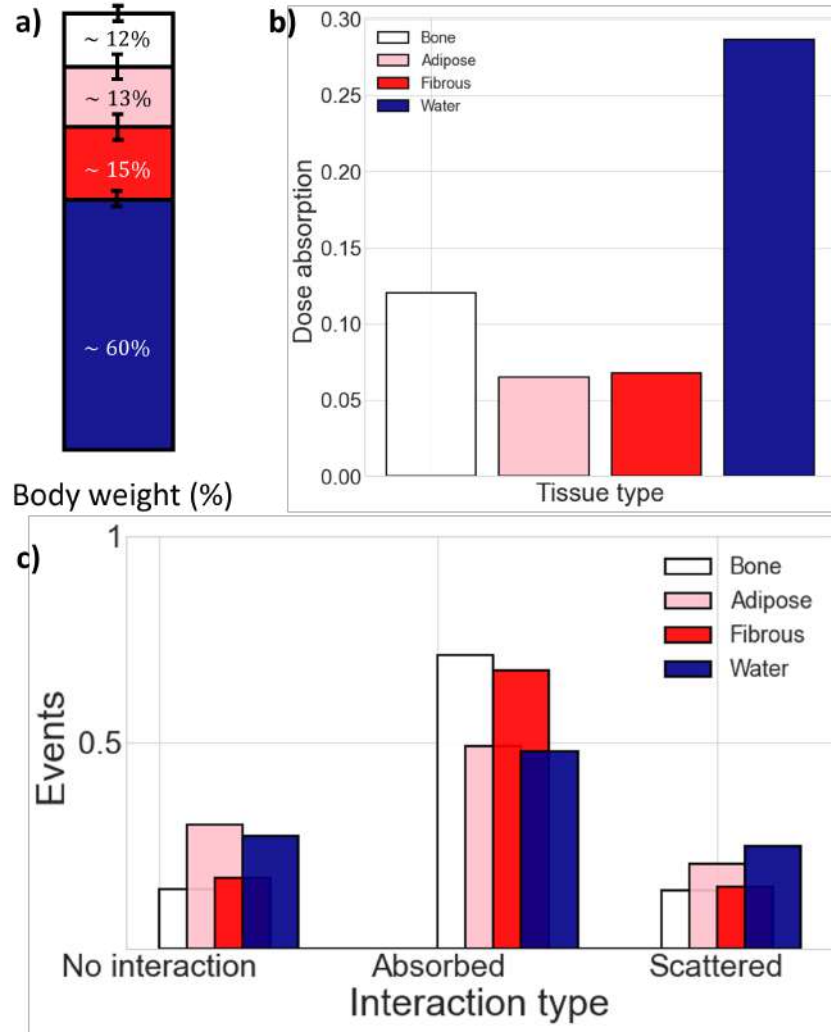


FIGURE 5.7: Body tissue attenuation and scattering contributions numerically calculated by simulating $N = 10^6$ photons that cross over four kinds of tissue slabs of $w = 1m$. The attenuation and scattering probability is calculated using the NIST database with the compound mixture proportions for bone, adipose, and fibrous tissue found in medical literature [12, 13]. a) Body weight estimation percentage for an average human male body. b) Weighted dose absorption factored over the total body weight. c) percentage contribution for three interaction types of events. The photon crossing the material slabs may either cross without interacting, be absorbed by the material, or be scattered. The simulation is done for each material slab with a photon energy of $28kV$. As expected, heavy materials such as bone and fibrous tend to attenuate, while adipose and water tend to scatter and cross the material with more ease.

medium-energy X-rays tend toward partial absorption (scatter), and lower-energy X-rays tend toward total absorption. A simulation for each material mixture composition for the total interaction at a fixed number of photons is performed in figure 5.7.

Chapter 6

X-Ray Imaging Fundamentals

With the fundamental physics of light-matter interaction covered in the preceding sections, it is now appropriate to delve into the underlying physics phenomena of X-ray imaging. The background we have established will serve as the foundation for advancing our understanding of the theory and applications of X-ray imaging. It is worth noting that this section will focus on attenuation X-ray imaging, X-ray phase contrast imaging, and the different techniques imaging systems can exploit to achieve phase contrast X-ray imaging. As previously mentioned, phase-contrast imaging holds great promise for distinguishing soft tissues with limited attenuation contrast. Consequently, conventional X-ray techniques often struggle to detect subtle details within a soft tissue background.

In X-ray imaging modalities, such as Angiography, bone densitometry, Computed Tomography (CT), C-arm Fluoroscopy, Tomosynthesis, and conventional radiography, both inelastic and elastic scattering phenomena can disrupt diagnostic accuracy. They do so by altering spatial information, modifying the energy of the X-ray beam, or introducing unwanted noise. Preferably for absorption-based imaging systems, X-ray photons would either be entirely absorbed through the photoelectric effect or pass through without interaction rather than being diverted from their intended path. The extent of scatter increases with the X-ray beam's size and the target material's thickness. For instance, in chest radiographs, scatter radiation can account for as much as 90 percent of the radiation detected, significantly affecting image quality and diagnostic precision. Using scatter reduction grids may decrease residual scattered radiation to $\sim 50\%$; additional preventive and corrective methods exist to reduce scatter within the patient and the detector.

6.1 Scattering kinematics

With this in mind, the study and relevance of scattering in X-ray imaging is still present and, for the most part, the primary mechanism of phase contrast imaging. By the processes studied in the last chapter, photons may be absorbed via the photoelectric effect or scattered using coherent and incoherent scattering, which, summed up, we can also interpret these phenomena as the refraction and diffraction of waves that interact with matter. However, a more straightforward formulation has been proposed under the Transport of Intensity Equation (TIE) approach established at equation 4.201. Both interpretations, while valid, have a different formalism and are referred to as the ray-tracing formulation and the TIE approach. Here, retaking the ray tracing approach, an interpretation of scatterers and how scatterers are represented as a wave field shift. Intuitively, this shift can be decomposed as the sum of two fields, which would exist without the scatter and the scattered field. With this in mind, we can use a Green function to formulate the outgoing scattered field. Let a point scatterer located at (x', y', z') at a distance $z' - z_o$ from a point source. Recall the inhomogeneous Helmholtz equation.

$$(\nabla^2 + k^2)\psi_\omega(x, y, z) = k^2 [1 - n_\omega^2(x, y, z)] \psi_\omega(x, y, z) \quad (6.1)$$

A point scatterer's case will be represented as a Dirac delta in space $\delta(x - x', y - y', z - z')$. So, the Green function must obey the equation.

$$(\nabla^2 + k^2)G_\omega(\mathbf{r}, \mathbf{r}') = -4\pi\delta(\mathbf{r} - \mathbf{r}') \quad (6.2)$$

Where $\mathbf{r} = (x, y, z)$, $\mathbf{r}' = (x', y', z')$ and $4\pi\delta$ is the normalization factor for the plane wave. Knowing that the free propagation space is homogeneous and isotropic can simplify the above expression to the form.

$$(\nabla^2 + k^2)G_\omega(\mathbf{r}) = -4\pi\delta(\mathbf{r}) \quad (6.3)$$

By using the three-dimensional spherical Laplacian and switching to spherical coordinate representation, we arrive at the Green function of the Fourier integral form.

$$G_\omega(\rho, \theta, \phi) = \frac{1}{2\pi^2} \int_{k_\rho}^{\infty} \int_{k_\theta}^{\pi} \int_{k_\phi}^{2\pi} \frac{e^{ik_\rho \rho \cos k_\theta}}{k_\rho^2 - k^2} k_\rho^2 \sin k_\theta dk_\rho dk_\theta dk_\phi \quad (6.4)$$

We obtain this by using the function parity extending the lower limit of the integral for the radius ρ and evaluating the angular integrals.

$$G_\omega(r, \theta, \phi) = -\frac{1}{\pi\rho} \frac{d}{d\rho} \int_{-\infty}^{\infty} \frac{e^{ik_\rho \rho}}{(k_\rho - k)(k_\rho + k)} dk_\rho \quad (6.5)$$

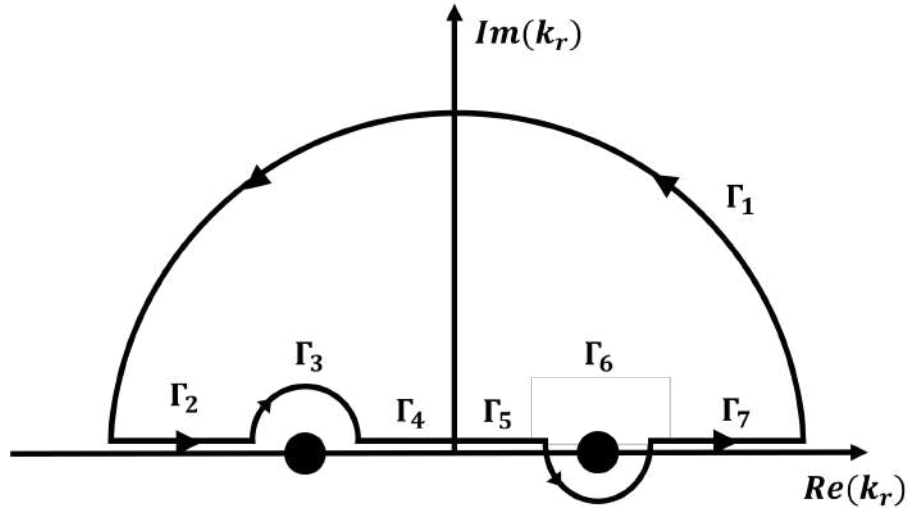


FIGURE 6.1: Cauchy path plot to solve the Green integral at 6.7. Paths Γ_3 and Γ_6 enclose the positive and negative poles, respectively.

Which can finally be evaluated as a Cauchy integral over the poles $k_\rho = \pm k$ using the Cauchy integral over the closed loop path shown in figure 6.1. Thus, we obtain the Green function in spherical and cartesian spatial coordinates.

$$G_\omega(\rho, \theta, \phi) = \frac{e^{ik\rho}}{\rho} \quad (6.6)$$

$$G_\omega(x, y, z) = \frac{e^{ik|\mathbf{r}|}}{|\mathbf{r}|} \quad (6.7)$$

This is the basis for a formulation of scattering. As previously stated, the Green function represents the scattered spherical wave given a point scatterer. We can now re-write the inhomogeneous Helmholtz equation that we stated at the beginning of this chapter at 6.1 in terms of the point scatterer Green function; hence, the integral equation must follow.

$$(\nabla^2 + k^2)\psi_\omega(\mathbf{r}) = \psi_\omega^o(\mathbf{r}) - \frac{k^2}{4\pi} \iiint G_\omega(\mathbf{r} - \mathbf{r}') [1 - n_\omega^2(\mathbf{r}')] \psi(\mathbf{r}') d\mathbf{r}' \quad (6.8)$$

Distributing the operator, we may find the definition at 6.3 on the right side, and then we can reduce the integral using the properties of the Dirac delta under integration.

$$(\nabla^2 + k^2)\psi_\omega(\mathbf{r}) = k^2 [1 - n_\omega^2(\mathbf{r})] \psi_\omega(\mathbf{r}) \quad (6.9)$$

Note how this form is less general than the Helmholtz nonhomogeneous equation since now, we guarantee that the scattered field represents an outgoing wave far away from the scatters under the paraxial approximation by using a Green function instead. By the nature of the refractive index distribution function n_ω the integrated will be

non-zero within the volume of the scatterer; this implies that we can take the incident field in place of the total field as the driving field at each point in the scatterer as long as the X-ray disturbance inside the scattering volume is only slightly different from the disturbance that would have existed at the point \mathbf{r}' in the absence of the scatterer. This is known as the First Born approximation, and it is a simpler way to calculate the scattering amplitude of classical and quantum systems. Now, by using the Green function obtained at 6.7 on 6.8 under the first Born approximation, we may obtain

$$\psi_\omega(\mathbf{r}) = e^{ik_0 \cdot \mathbf{r}} - \frac{k^2}{4\pi} \iiint \frac{e^{ik|\mathbf{r}-\mathbf{r}'|}}{|\mathbf{r}-\mathbf{r}'|} [1 - n_\omega^2(\mathbf{r}')] e^{ik_0 \cdot \mathbf{r}'} d\mathbf{r}' \quad (6.10)$$

This form of the first Born approximation considers the solution for the Green function of a point scatterer, which means we can now describe a whole scatterer volume in which each point of the scatterer is taken to produce free-space outgoing Green functions isomorphic to spherical wave Green functions. An additional approximation is now made to reach an analytical expression for the first Born approximation of the point scatterer, assuming the scattered radiation is detected far away from the scatterer, it follows the condition of far field, where now $|\mathbf{r}| \gg |\mathbf{r}'|$. Hence the Green function follows

$$\frac{e^{ik|\mathbf{r}-\mathbf{r}'|}}{|\mathbf{r}-\mathbf{r}'|} \approx \frac{\exp \left[ik \sqrt{|\mathbf{r}|^2 - 2\mathbf{r} \cdot \mathbf{r}'} \right]}{|\mathbf{r}-\mathbf{r}'|} = \frac{\exp \left[ikr \sqrt{1 - 2\frac{\mathbf{r} \cdot \mathbf{r}'}{r^2}} \right]}{r} \quad (6.11)$$

By the binomial approximation over the root term, we arrive at the following expression

$$G'_\omega = \frac{\exp \left[ikr \sqrt{1 - 2\frac{\mathbf{r} \cdot \mathbf{r}'}{r^2}} \right]}{r} \approx \frac{\exp \left[ikr \left(1 - \frac{\mathbf{r} \cdot \mathbf{r}'}{r^2} \right) \right]}{r} \quad (6.12)$$

With this new Green function, the integral equation has the form.

$$\psi_\omega(\mathbf{r}) = e^{ik_0 \cdot \mathbf{r}} - \frac{k^2 e^{ikr}}{4\pi r} \iiint \exp \left[-ik \frac{\mathbf{r} \cdot \mathbf{r}'}{r} \right] [1 - n_\omega^2(\mathbf{r}')] e^{ik_0 \cdot \mathbf{r}'} d\mathbf{r}' \quad (6.13)$$

That may be solved to arrive at the condition

$$\psi_\omega(\mathbf{r}) = e^{ik_0 \cdot \mathbf{r}} + \frac{e^{ikr}}{r} \mathbf{f}(\Delta \mathbf{k}) \quad (6.14)$$

Where

$$\mathbf{f}(\Delta \mathbf{k}) = \frac{k^2}{4\pi} \iiint [n_\omega^2(\mathbf{r}') - 1] \exp [-i\Delta \mathbf{k} \cdot \mathbf{r}'] d\mathbf{r}' \quad \Delta \mathbf{k} = k\hat{\mathbf{r}} - k_0 \quad (6.15)$$

Finally, we have described the wave field in the presence of the scattering potential under the first Born approximation. The scattered radiation is then given by a

“perturbed” spherical wave that originates at the point where the scatterer is located. The function \mathbf{f} is the wave envelope or scattering amplitude, which multiplies the unperturbed wave given by the term $\exp(ik)/r$. Meanwhile, the function \mathbf{f} is the Fourier transform of the scatterer. Finally, the term $\Delta\mathbf{k} = (k_x, k_y, k_z)$ refers to the vector difference between the incident wave-vector \mathbf{k}_o and the scattered wave-vector $k\hat{\mathbf{r}}$. Henceforth, the evaluation of the function $\mathbf{f}(\Delta\mathbf{k})$ represents the value that takes the perturbed wave in the far field condition for a scatterer $[n_\omega^2(\mathbf{r}') - 1]$ with an incident wave-vector \mathbf{k}_o . We may also relate this result to the Fraunhofer diffraction integral by assuming all scatterers have an incident wave vector k_o . By also using the complex refractive index definition and approximation seen at 4.162, we arrive at [66].

$$\mathbf{f}(\Delta\mathbf{k}) = \frac{-k^2}{2\pi} \int_{-\infty}^{\infty} \int_{-\infty}^{\infty} \exp[-i(\Delta k_x x' + \Delta k_y y')] \quad (6.16)$$

$$\times \left[\int_0^{z_o} \delta_\omega(x', y', z') - i\beta_\omega(x', y', z') \right] \exp(-i\Delta k_z z') dz' dx' dy' \quad (6.17)$$

Now, it is necessary to study how the first Born approximation presents the propagated field over the scattering volume and not just the free space; this will be done using the Weyl expansion, which is the integral representation of the spherical wave. Starting with the Green function representation in the real space as the inverse Fourier transform.

$$G_\omega(x, y, z) = \frac{1}{2\pi^2} \iiint \frac{\exp[i(k_x x + k_y y + k_z z)]}{k_x^2 + k_y^2 + k_z^2 - k^2} dk_x dk_y dk_z \quad (6.18)$$

$$G_\omega(x, y, z) = \frac{1}{2\pi^2} \iint \exp(i(k_x x + k_y y)) dk_x dk_y \int \frac{\exp[ik_z z]}{k_z^2 - (k^2 - k_x^2 - k_y^2)} dk_z \quad (6.19)$$

From where the dk_z integral is similar to the Fresnel diffraction operator seen in the last chapter.

$$G_\omega(x, y, z) = \frac{1}{2\pi^2} \iint \exp(i(k_x x + k_y y)) dk_x dk_y \frac{\exp\left(iz\sqrt{k^2 - k_x^2 - k_y^2}\right)}{\sqrt{k^2 - k_x^2 - k_y^2}} \quad (6.20)$$

By substituting this new Green function in 6.8.

$$\psi_\omega(\mathbf{r}) = e^{ik_o \cdot \mathbf{r}} - \frac{ik^2}{8\pi^2} \iint \frac{dk_x dk_y \exp\left[i\left(k_x x + k_y y + z\sqrt{k^2 - k_x^2 - k_y^2}\right)\right]}{\sqrt{k^2 - k_x^2 - k_y^2}} \quad (6.21)$$

$$\iiint [1 - n_\omega^2(\mathbf{r}')] e^{i\mathbf{k}_o \cdot \mathbf{r}'} \times \exp\left[-i\left(k_x x' + k_y y' + z'\sqrt{k^2 - k_x^2 - k_y^2}\right)\right] dx' dy' dz' \quad (6.22)$$

This expression examines the scattered field over any optical plane. Note that the triple integral term gathers the information of the scatterer by being the Fourier transform of the refraction term over the space, and the double integral term is the Wye spherical wave. As a closing remark, one can use the Ewald sphere to model the elastic scattering of incident plane waves under the Born approximation. This is especially useful in cases where the scattering potential is periodic. i.e., crystal scatterers following the Bragg law are specifically useful in crystallography. Additionally, the Born approximation may be expanded to a Born series for further study of dynamical scattering. In this case, the Green function acts like a Green operator under the same constraints but with time dependency.

6.2 Detector projection

Returning to the geometric model considered for the propagation of X-rays due to a point source in the z plane, if the photon interacts with an object at a position (x_o, y_o, z_o) whenever the dimension of the object is small compared to the distance of the screen (Paraxial approximation condition) then the incident intensity can be denoted as $I(x_o, y_o) = I_o$. As a consequence of angular deviation by the object, the ray position at the screen z_d , the object may be projected at a position

$$x_d \approx x_o + z_d \frac{\lambda}{2\pi} \frac{\partial \phi(x_o, y_o)}{\partial x_o} \quad (6.23)$$

$$y_d \approx y_o + z_d \frac{\lambda}{2\pi} \frac{\partial \phi(x_o, y_o)}{\partial y_o} \quad (6.24)$$

$$(6.25)$$

This is then the Jacobian that fulfills the following relation.

$$I(x_d, y_d) = I(x_o, y_o) J = I(x_o, y_o) \frac{\lambda}{2\pi} \begin{vmatrix} 1 + z_d \frac{\partial}{\partial x_o} \frac{\partial \phi(x_o, y_o)}{\partial x_o} & z_d \frac{\partial}{\partial y_o} \frac{\partial \phi(x_o, y_o)}{\partial x_o} \\ z_d \frac{\partial}{\partial x_o} \frac{\partial \phi(x_o, y_o)}{\partial y_o} & 1 + z_d \frac{\partial}{\partial y_o} \frac{\partial \phi(x_o, y_o)}{\partial y_o} \end{vmatrix}^{-1} \quad (6.26)$$

This approximates to

$$I(x_d, y_d) \approx I(x_o, y_o) \left[1 - \frac{z_d \lambda}{2\pi} \nabla^2 \phi(x_o, y_o) \right] \quad (6.27)$$

Given a geometric magnification term that follows.

$$M = \frac{r_o + r_d}{r_o} \quad (6.28)$$

This modifies the Jacobian to

$$I(x_d, y_d) \approx \frac{I(x_o, y_o)}{M^2} \left[1 - \frac{z_d \lambda}{2\pi M} \nabla^2 \phi(x_o, y_o) \right] \quad (6.29)$$

This expression establishes the basis for calculating image formation based on geometric optics. This shows the main hypothesis that phase contrast varies with the distance, the wavelength λ , and the variation in phase across the object given by $\nabla^2 \phi$. The attenuation can also be included by using the Beer-Lambert law.

$$I(x_d, y_d; M; \lambda) \approx \frac{I(x_o, y_o) e^{-\mu(x_o, y_o; \lambda) \cdot z}}{M^2} \left[1 - \frac{z_d \lambda}{2\pi M} \nabla^2 \phi(x_o, y_o; \lambda) \right] \quad (6.30)$$

This expression is the basis for formulating propagation-based phase contrast imaging (PBXPC), which will be explored in the next chapter. The last chapter's formulation for the Fraunhofer integral gives the basis for the Fresnel-Kirchhoff equation. Starting from Green's theorem for a wave field element ψ_ω that follows the homogeneous Helmholtz equation and has an eigensolution of the form $\psi'_\omega = \psi_\omega e^{-i\omega t}$ there must exist a relationship between the volume and surface integrals for a function ϕ_ω that also satisfies the same condition.

$$\int_v (\psi_\omega \nabla^2 \phi_\omega - \phi_\omega \nabla^2 \psi_\omega) dv = - \int_A \left(\psi_\omega \frac{\partial \phi_\omega}{\partial n} - \phi_\omega \frac{\partial \psi_\omega}{\partial n} \right) dA \quad (6.31)$$

This leads to the equation

$$\psi_\omega(x, y, z) = -\frac{Aik}{4\pi} \iint_A \frac{e^{ik(z_o+z_d)}}{z_o z_d} [\cos(n, z_o) - \cos(n, z_d)] dA \quad (6.32)$$

Here the factor $\frac{ik}{4\pi} [\cos(n, z_o) - \cos(n, z_d)]$ represents the obliquity factor of the X-ray incidence and (n, z) is the angle between the normal vector of the detector and the distance to the sample and detector. Of course, in the case of perfect alignment with the z-axis, this term becomes 1; consider the projection approximation where a large distance from the aperture will change slowly. Hence

$$\psi_\omega(x, y, z) \approx \frac{Aik}{\lambda z_o z_d} \iint_A e^{ik(z_o+z_d)} dA \quad (6.33)$$

This is the Fresnel-Kirchhoff equation, which has an operator representation already deduced in the previous chapter. Using the integral form for the following theory remarks is essential, which will build the edge illumination phase contrast imaging fundamentals. Take z_o, z_d as distances representing a series expansion of the projection

of x, y coordinates in space with the form.

$$z'_o = z_o - \frac{x_o \Delta x + y_o \Delta y}{z_o} + \frac{\Delta x^2 + \Delta y^2}{2z_o} - \dots \quad (6.34)$$

$$z'_d = z_d - \frac{x_o \Delta x + y_o \Delta y}{z_d} + \frac{\Delta x^2 + \Delta y^2}{2z_d} - \dots \quad (6.35)$$

In the second order, this expansion leads to the Fresnel-Kirchhoff equation applied to an unpropagated wave-field

$$\psi_\omega(x, y, z) \approx \frac{ie^{ikz}}{\lambda z} \iint_A \psi_\omega(\Delta x, \Delta y, 0) e^{\frac{ik}{2z}[(x-\Delta x)^2 + (y-\Delta y)^2]} d\Delta x d\Delta y \quad (6.36)$$

This may also be written as a convolution integral with the function

$$h(x, y) = \frac{i}{\lambda} e^{i\frac{\pi}{\lambda z}(x^2 + y^2)} \quad (6.37)$$

Hence

$$\psi_\omega(x, y, z) = \frac{e^{ikz}}{z} \psi_\omega(x, y, 0) * h(x, y) \quad (6.38)$$

Here, we have established the basis for the edge illumination theory and the basis for other phase detection techniques, such as field propagation and speckle-based phase contrast imaging. Further talk about the theoretical considerations of the methods themselves will be done in the next chapter. Generally, a phase object is considered to have a component of absorption and a part (or multiple components) of scattering, so there is a mixture of phase and amplitude contrast. Plenty of material structures, especially biological systems, can be considered pure phase objects as a reasonable approximation, where it is understood that the object is thin enough so that phase contrast dominates the amplitude contrast over attenuation.

6.3 Attenuation contrast

Attenuation contrast in X-rays works under the principles of the already described Beer-Lambert law. For distinguishing two media with different optical paths and different attenuation coefficients, medical imaging especially in traumatology and mammography strongly relies on the high contrast of high-attenuating tissue and fibrous-adipose tissue. However, the application of X-ray imaging to other diagnostics like angiography requires the use of invasive contrast agents such as sodium methylglucamine diatrizoate and metrizamide [67].

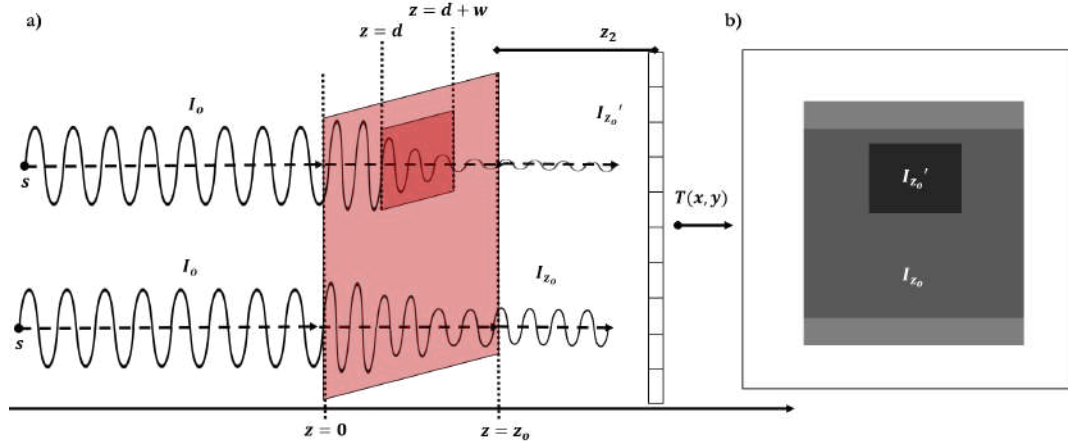


FIGURE 6.2: Diagram of intensities crossing over different attenuation coefficients, where $\mu' > \mu$, $I_{z_0}' < I_{z_0} < I_0$ and there is a measurable contrast in the medium.

Where μ' and μ are densities of two different attenuation coefficients, such that μ' is found in a medium μ , and the intensities I_{z_0}' and I_{z_0} are intensities attenuated by different optical paths, while the intensity I_0 is the emission intensity of the source. Figure 6.2 shows a situation where a material immersed in another represents a change in intensity that follows equation 6.44. Now the contrast between two media is defined as the quantity [68]:

$$C = \frac{I_1 - I_2}{I_1} \quad (6.39)$$

Taking the values of the Beer-Lambert law for each of the intensity values, we have that:

$$I_1 = I_0 \exp(-\mu_1 l_1) \quad (6.40)$$

$$I_2 = I_0 \exp[-\mu_2 l_2] \exp[\mu_1(l_2 - l_1)] \quad (6.41)$$

$$I_2 = I_0 \exp[l_2(\mu_1 - \mu_2) - \mu_1 l_1] \quad (6.42)$$

Now, using these values in equation 6.39, we find that the contrast measured over the two objects is given by:

$$C = 1 - I_0 \exp[l_2(\mu_1 - \mu_2)] \quad (6.43)$$

This result quantifies the distinction of an object embedded in a medium, which is the case study in medical imaging. Note also that this contrast does not depend on the

optical path over the immersion medium l_1 . Still, this contrast disappears when the embedded object is very small ($l_2 \approx 0$) or when the attenuation coefficients are similar ($\mu_1 \approx \mu_2$). This is a simplified way to understand the formation of contrast from intensities in space, however, a spatial model is required for the case study of image formation and event detection. Now defining a coordinate system where the propagation of X-rays is given over the Z-axis [69], we then have that for a polychromatic source that encompasses a range of energies $\Delta\lambda$, the intensity that reaches a detector is given by:

$$I(x, y) = \int I_o(x, y, \lambda) e^{-(\mu'^\lambda - \mu^\lambda) T_o(x, y)} D(\lambda) d\lambda \quad (6.44)$$

Where $T_o(x, y)$ is the projected thickness of the object on the plane (x, y) corresponding to the detector, and $D(\lambda)$ corresponds to the detector's response for an energy λ . The superscripts μ^λ appear due to the dependence of attenuation on energy. For the monochromatic case, this equation becomes:

$$I(x, y) = I_o(x, y) e^{-(\mu_1^\lambda - \mu_2^\lambda) T_o(x, y)} \quad (6.45)$$

6.4 Gradient Contrast

Recall the transmission function discussed in the last chapter at 4.165. Under a phase-dominant object transmission, this function may be written as $T(z) = e^{i\phi(z) - \mu(z)}$ where each function has the form seen in the last chapter.

$$\mu(x, y) = \frac{2\pi}{\lambda} \int \beta(x, y, z) dz \quad (6.46)$$

$$\phi(x, y) = \frac{2\pi}{\lambda} \int 1 - \delta(x, y, z) dz \quad (6.47)$$

If the wave passes through an object that may have a different refractive index n_ω , the phase shift will be equivalent to the refraction difference and the object thickness. This may also be interpreted as a change in the wavenumber proportional to the wave velocity in the refractive medium. With this in mind, we may model the difference at the boundary.

$$i \frac{2\pi v}{\lambda c} \Delta z - \frac{2\pi}{\lambda} \Delta z = -\Delta z (ik\delta + k\beta) \quad (6.48)$$

Then, the transmission function for an edge located on the axis at a position z_o as shown in figure 6.2 is given by the step function $T(z_o) = e^{-\Delta z (ik\delta + k\beta)}$ inside the material

and $T(z_o) = 1$ otherwise. The edge then partially transmits the amplitude of the wavefield, where the wavefield is proportional to.

$$\psi_\omega(x, y) \propto 1 + \phi \left[\int_0^{z_o} \sin(t^2) - \cos(t^2) dt \right] - \mu \left[\int_0^{z_o} \sin(t^2) - \cos(t^2) dt \right] \quad (6.49)$$

$$\propto 1 + (\phi - \mu) \left[\int_0^{z_o} \sin(t^2) - \cos(t^2) dt \right] \quad (6.50)$$

The integrals in this formulation by Margaritondo and Tromba [70] are Fresnel integrals and consider the near-field Fresnel diffraction phenomenon. Here the contrast has an additional contribution due to the phase gradient of the material and depends on the travel path parametrization given by the integrand t and the scatter shift term ϕ which is phase-sensitive. This result shows two important remarks for the scattering model. First is how the wave-field intensity $|\psi(x, y)|^2$ is sensitive to the inelastic interactions of the photons with the material. Second, the propagation path described by the integral limits amplifies the contrast due this effect, which is the main mechanism for holography-based phase contrast techniques. The next chapter will focus on the several techniques to exploit the contrast given by these effects.

Chapter 7

Phase contrast imaging systems

Now that most of the theoretical basis of Phase Contrast X-ray Imaging (PCXI) is fully covered, we will focus on the theoretical modeling of imaging systems that exploit different PCXI techniques, each with its advantages and limitations. Most currently state-of-the-art methods in PCXI use that the object induces a phase shift, a detectable physical quantity. However, they vary in optical principles, devices in the optical path, and illumination-based detector techniques to directly detect the differential or phase signals. PCXI techniques can be divided into two groups, namely interferometric and non-interferometric. Most PCXI techniques also require a crucial processing step called phase retrieval, which consists of a set of algorithms that will use the detector signal (that sometimes is illegible) to a fully processed phase signal; this step will be explored in chapter 8.

Following the wave field interpretation to formulate further complex imaging systems is also convenient. Starting from the Fresnel-Kirchoff integral as in equation 4.189. We recall the general case where z is the optical axis and \mathbf{r} is the direction vector of propagation.

$$\psi_\omega(x, y, z_o) = \iint_{-\infty}^{\infty} \psi_\lambda(x', y', z') \frac{k \exp ik|\mathbf{r}|}{i2\pi|\mathbf{r}|} \cos \theta dx' dy' \quad (7.1)$$

For the Fresnel approximation, when z is sufficiently large, the angle between z direction and the propagation vector is near zero, then $\cos \theta \approx 1$. It is helpful then to write $|\mathbf{r}|$ as

$$|\mathbf{r}| = \Delta z \sqrt{1 + \left(\frac{x - x'}{\Delta z}\right)^2 + \left(\frac{y - y'}{\Delta z}\right)^2} \approx \Delta z \left[1 + \left(\frac{x - x'}{4\Delta z}\right)^2 + \left(\frac{y - y'}{4\Delta z}\right)^2 \right] \quad (7.2)$$

Hence, the full expression for the Fresnel-Kirchhoff integral over the space can be written using the spatial coordinates instead of the operator form shown before.

$$\psi_\omega(x, y, z_o) = \iint_{-\infty}^{\infty} \psi_\omega(x', y', z') \frac{k \exp(ik\Delta z)}{i2\pi\Delta z} \exp \left[ik \left(\frac{(x - x')^2 + (y - y')^2}{2\Delta z} \right) \right] dx' dy' \quad (7.3)$$

This expression is the convolution of the wave field with the Fresnel propagator seen in the previous chapter.

$$H_{\Delta z}(x, y) = \frac{k \exp(ik\Delta z)}{i2\pi\Delta z} \exp \left[ik \left(\frac{x^2 + y^2}{2\Delta z} \right) \right] dx' dy' \quad (7.4)$$

Then, we may write 7.3 in its convolution representation.

$$\psi_\omega(x, y, z_o) = \psi_\omega(x, y, 0) * H_{\Delta z}(x, y) \quad (7.5)$$

Meanwhile, in the presence of a scattering and attenuating object, the paraxial approximation is incorporated by introducing a complex transfer function $T_s(x, y)$ as follows

$$\psi_\omega(x, y, z_{out}) = T_s(x, y) \psi_\omega(x, y, z_{in}) \quad (7.6)$$

The transfer function has complete information on the interaction of the wave with the object by using the complex refractive index 4.149. Hence, the transfer function may be written as.

$$T_s(x, y) = \exp \left[-k \left(\int_{\Delta z} i\delta(x, y, z) + \beta(x, y, z) \right) \right] \quad (7.7)$$

7.1 Propagation-based Imaging

Propagation-Based X-Ray Phase Contrast Imaging (PBXPC), also known as in-line holography and free-space propagation, is the most straightforward non-interferometric phase-sensitive implemented technique. It consists of distancing the detector from the sample at a distance far enough that the perturbed wavefront will express the phase difference as a measurable signal on the detector. This goes along with the projection approximation condition over the Fresnel for a scatterer at a distance d as seen in section 4.3.1. Phase contrast is then formed as a perturbed projection where the phase shift is proportional to the deflection angle (See 6.2). Hence.

$$x_d \propto x + z_d \alpha_x \quad (7.8)$$

$$y_d \propto y + z_d \alpha_y \quad (7.9)$$

Where $\alpha_{x,y} = \frac{1}{k} \frac{\partial \phi(x,y)}{\partial x,y}$. Solving for the Jacobian matrix for x_d, y_d we already got the main result at 6.30, for a magnification of $M \approx 1$ this result follows.

$$I(x_d, y_d; \lambda) \approx I(x, y) e^{-\mu(x,y;\lambda) \cdot z} \left[1 - \frac{z_d \lambda}{2\pi} \nabla^2 \phi(x, y; \lambda) \right] \quad (7.10)$$

This, of course, is the case where the distance between the sample and detector is null and no magnification is present in the system. Hence, the distance $z_d = 0$ and there are no detectable phase effects. Then equation 7.10 reduces to the Beer-Lambert law. However when $M \gg 1$ phase effects start to contribute to the change on the illumination term $I(x, y)$. Let the point source located at the origin be characterized by a spatial intensity distribution and the detector be discrete and finitely distributed at z_d .

$$I(x_d, y_d; \lambda) \approx \frac{I(x, y) e^{-\mu(x,y;\lambda) \cdot z}}{M^2} \left[1 - \frac{z_d \lambda}{2\pi M} \nabla^2 \phi(x, y; \lambda) \right] \quad (7.11)$$

Now, the illumination term will be described with the following convolution relation.

$$I(x_d, y_d; \lambda) = I(x, y; \lambda) * \left[\text{PSF}_s \left(\frac{x_d}{M-1}, \frac{y_d}{M-1} \right) * \text{PSF}_d(x_d, y_d) \right] \quad (7.12)$$

Where $\text{PSF}_{s,d}$ represents the point-spread function of the source and the detector, respectively. As the reader might recall, one of the most important remarks in chapter 4 is how perfect continuous systems without illumination artifacts do not account for phase density change. This implies that the illumination distribution detected under the convolution formulation of this system is a blurred discrete version of the image that would be obtained under ideal conditions. This blurring effect will depend on the source distribution, detector response, and geometry of the system, which at the same time translates into the width of the PSF_{sys} distribution, defining PSF_{sys} as.

$$\text{PSF}_{sys}(x_d, y_d) = \left[\text{PSF}_s \left(\frac{x_d}{M-1}, \frac{y_d}{M-1} \right) * \text{PSF}_d(x_d, y_d) \right] \quad (7.13)$$

The width of the PSF_{sys} distribution is proportional to $\sqrt{s^2(M-1)^2 + d^2}$ Where s describes the source size and d the detector resolution width. This is the main limitation of the PBXPC since most conventional X-ray sources operate with a big source size that dominates over the detector resolution; hence, any improvement in this matter will not affect the visibility of phase effects; there is no feasibility of the use of this technique in medical systems due to the geometrical and technical limitations []. By accounting for the imperfections of the optical systems using $\text{PSF}_{sys}(x_d, y_d)$. It is possible to model the optical path of free-space propagation systems using the transmission

function and the free-space Fresnel-Kirchhoff phase propagation operator.

$$I(x_d, y_d; \lambda) = [(|\psi(x, y, 0; M)|^2 * H_{z_0}) T_s(x, y) * H_{z_d}] * \text{PSF}_{\text{sys}}(x_d, y_d) \quad (7.14)$$

Lastly, the polychromatic source treatment requires integration over the energy spectrum that may also be expressed as a distribution over an energy range. This energy range will normally be between 10keV and $\sim 100\text{keV}$ for conventional sources. Hence, the final treatment that models free-propagation imaging can be expressed as.

$$I(x_d, y_d) = \int_{\omega_{\min}}^{\omega_{\max}} [(|\psi(x, y, 0; M)|^2 * H_{z_0}) T_s(x, y) * H_{z_d}] * \text{PSF}_{\text{sys}}(x_d, y_d) G(\omega') d\omega' \quad (7.15)$$

We now close this section by highlighting the fact that the function $\text{PSF}_{\text{sys}}(x_d, y_d)$ will be the distinctive part in between imaging systems. Additional elements, such as interferometers, analyzers, filters, and collimators, can be added without directly altering how X-rays interact with matter and vacuum. Hence, just changing the geometry by contributing directly to the term $\text{PSF}_{\text{sys}}(x_d, y_d)$.

7.2 Edge-Illumination Imaging

Edge Illumination EIXPCI was first developed using a synchrotron monochromatic X-ray source, first thought to be a combination of analyzer-based X-ray imaging methods and grating interferometry methods. This set of techniques works by projecting X-ray beams onto the edge of sensitive detection regions. Hence, the detection array now operates under a partial illumination setting instead of fully illuminated pixels as in conventional imaging. Although similar to grating interferometry, EIXPCI does not employ Talbot's self-imaging phenomenon; rather, the pixel edge creates sensitivity to the angle of photon refraction. As the reader might already think, this also implies a net loss on the system resolution; since less information is collected by each pixel and the quantitative measurement of deflection effects requires two adjacent pixels to be measured, this spatial-resolution issue can be solved by using a spatial scanning of the sample by the dithering method to retrieve the original or even to increase the original resolution.

Starting over the same outline as in the propagation-based XPCI, we may write the transmission function as 7.7. For simplicity and without loss of generality, the system for now will consist on a single pixel and a single fringe, as well as a monochromatic ideal source of X-ray radiation, refer to figure 7.1. This toy model is sufficient to show the positive and negative fringe effects present in edge illumination, which is the principle of pixel edge illumination [71]. The illumination for the positive and

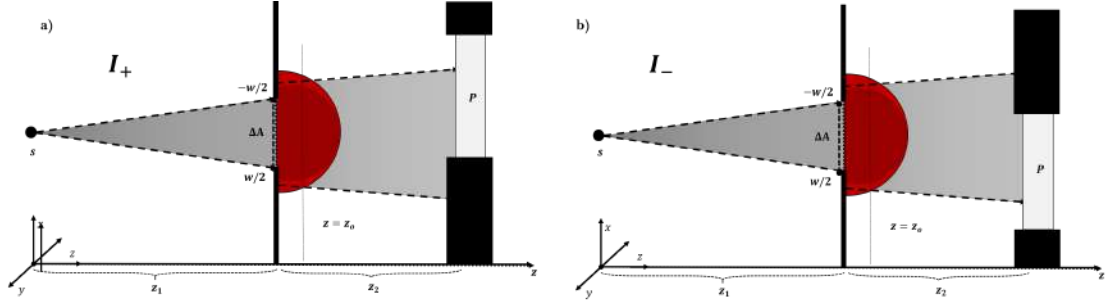


FIGURE 7.1: Partial illumination system due to the presence of a diffraction slit and a diffractive object. a) it is said that the fringing is positive if the apparent deviation of the ray path is at higher Δy than the path without the refractive sample. b) Conversely, it is said that the fringing is negative if the apparent deviation of the ray path is at lower Δy than the path without the refractive sample. This principle is the main mechanism exploited in edge-illumination imaging.

negative fringes is then given by the wave field element that arrives at the single detector area provided by.

$$I_- = \iint_{A_-} |\psi(x, y)|^2 dx dy \quad I_+ = \iint_{A_+} |\psi(x, y)|^2 dx dy \quad (7.16)$$

$$I_- = \int_0^P \int_{-M \cdot w}^0 |\psi(x, y)|^2 dx dy \quad I_+ = \int_0^P \int_0^{M \cdot w} |\psi(x, y)|^2 dx dy \quad (7.17)$$

By using the transmission function, we may assume without loss of generality that the phase and absorption functions may be described locally by a linear function as a Taylor series expansion around the object frame at x'

$$T(x' + x'_s; x_0) = \exp \left[-i\phi(x'_s) - i \left. \frac{\partial \phi}{\partial x'} \right|_{x'_s} (x' - x_0) - \mu(x'_s) - \left. \frac{\partial \mu}{\partial x'} \right|_{x'_s} (x' - x_0) \right] \quad (7.18)$$

Hence, by expanding, we can write $\psi(x)$ as the Fresnel-Kirchhoff operator of the propagation over the full field.

$$\psi(x) = \psi(x_0) \frac{\exp \left(ik(z_1 + z_2) + ik \frac{x^2}{2z_2} \right)}{iz_1 z_2^2 \lambda M^2} \int_{-w/2}^{w/2} T(x' + x'_s; x_0) \exp \left[ikx'^2 \frac{M}{2z_2} - ikx' \frac{x}{z_2} \right] dx' \quad (7.19)$$

Where $M = (z_1 + z_2)/z_2$ is the system's magnification. The first asymptotic solution for this equation can be written as.

$$\begin{aligned} \psi(x)^{(0)} = & \frac{\exp ik \left((z_1 + z_2) + \frac{x^2}{2z_2} \right)}{iz_1 z_2^2 \lambda M^2} \exp \left[i \left(\left. \frac{\partial \phi}{\partial x'} \right|_{x'_s} x_0 - \phi(x'_s) \right) \right] \exp \left[i \left(\left. \frac{\partial \mu}{\partial x'} \right|_{x'_s} x_0 - \mu(x'_s) \right) \right] \\ & \sqrt{\frac{i\lambda z_1}{M}} \exp \left[- \left. \frac{\partial \mu}{\partial x'} \right|_{x'_s} \frac{z_1}{M} \left(\frac{x}{z_2} + \frac{1}{k} \left. \frac{\partial \phi}{\partial x'} \right|_{x'_s} \right)^2 \right] \exp \left[- \frac{ik z_1}{2 M} \left(\frac{x}{z_2} + \frac{1}{k} \left. \frac{\partial \phi}{\partial x'} \right|_{x'_s} \right)^2 \right] \end{aligned}$$

We get this by substituting this whole equation into the integral at 7.17 and integrating over the spatial coordinates.

$$I_- = P|\psi_o|^2 F\left(\frac{\partial\mu}{\partial x'}, \mu\right) \left[\exp\left(\frac{\partial\mu}{\partial x'}\bigg|_{x'_s} w\right) - G\left(\frac{\partial\phi}{\partial x'}, \frac{\partial\mu}{\partial x'}\right) \right] \quad (7.20)$$

$$I_+ = P|\psi_o|^2 F\left(\frac{\partial\mu}{\partial x'}, \mu\right) \left[-\exp\left(-\frac{\partial\mu}{\partial x'}\bigg|_{x'_s} w\right) + G\left(\frac{\partial\phi}{\partial x'}, \frac{\partial\mu}{\partial x'}\right) \right] \quad (7.21)$$

We may now define the two quantities used later on for the phase retrieval. Since any photon that arrives to the diffractor at z_1 will be read at I_+ or I_- . This principle is used to reconstruct the original absorption image, which is the one obtained if no slit diffractor mask would be present. Hence

$$I_+ + I_- = 2P|\psi_o|^2 F\left(\frac{\partial\mu}{\partial x'}, \mu\right) \sinh\left(\frac{\partial\mu}{\partial x'}\bigg|_{x'_s} w\right) \quad (7.22)$$

$$I_+ - I_- = 2P|\psi_o|^2 F\left(\frac{\partial\mu}{\partial x'}, \mu\right) \left[G\left(\frac{\partial\phi}{\partial x'}, \frac{\partial\mu}{\partial x'}\right) - \cosh\left(\frac{\partial\mu}{\partial x'}\bigg|_{x'_s} w\right) \right] \quad (7.23)$$

Where P is the pixel size and F, G are functions that contain the absorption and phase shift over the x' coordinate on the object's reference frame. The result $I_+ + I_-$ can also be obtained by integrating the intensity over the TIE approach over the sample aperture. This reduces to the case where there is no sample to a free propagation of the wave field intensity, which has the geometrical effect of the mask and the detection system.

$$I_0 = \frac{|\psi_o|^2 M w P}{(z_1 + z_2)^2} \quad (7.24)$$

As seen on the deduction, this method uses the periodic aperture of the mask A_1 . Here, it is necessary to make a distinction on Edge Illumination systems, which modulate the illumination that arrives to the detection systems using different mechanisms.

- **Double mask edge illumination** (Figure 7.2 a), as the name suggests, use two masks. The first mask, A_1 called the sample mask, is placed immediately before the sample (mostly to reduce magnification effects). It has the role of shaping the incoming beam into beamlets to create a partial illumination pattern that will arrive at the sample. The second mask, A_2 , also called the detector mask, is placed in front of the detector, and its role is to create shadowed regions over the pixel plane between adjacent pixels. To retrieve a full-phase image, the apertures should be aligned so that the beamlets hit both edges of the detector aperture using a second mask A_2 , which requires moving A_2 to get both positive and negative fringing directions. This system requires two acquisitions to obtain full-phase and reconstructed absorption images.

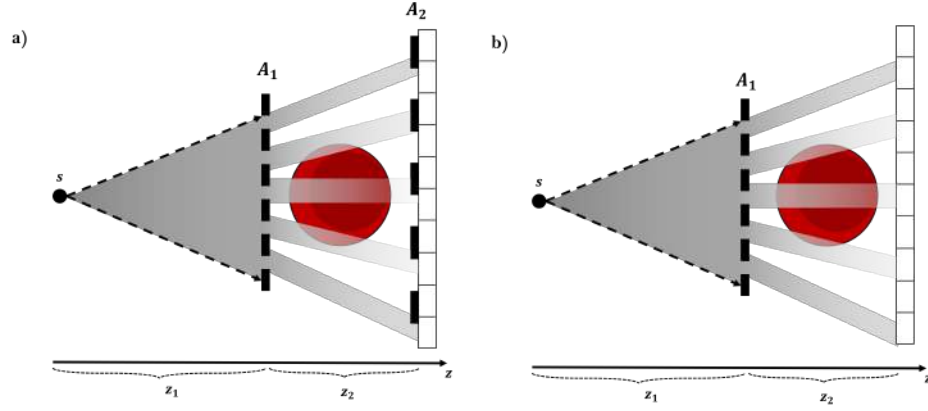


FIGURE 7.2: a) Double mask edge-illumination phase contrast imaging and b) Single mask edge-illumination phase contrast imaging. As the name may imply, the main difference on both techniques are the number of masks present in the optical path. Double mask case requires the double of images to construct the final dithering but has more specificity on the fringed signal.

- **Single mask edge illumination** (Figure 7.2 b)) systems, On the other hand, take advantage of the pixel pitch periodicity to create the positive and negative fringing on odd and even pixels. However, single mask systems require a precise alignment protocol and more magnification distances for the illumination periods to match. This illumination condition allows the complete phase and absorption images to be reconstructed with a single acquisition, representing a significant advantage on time exposure and dose reduction.

Notice how in both systems rely on the relative distinction between positive and negative fringing. This may be seen as a form of data compression that is, however, impossible to retrieve. The final acquisition will necessarily have half of the original resolution on the direction the mask is diffracting. Here, an additional and crucial component of this technique takes importance, which is the Dithering process that will be developed in the next chapter. By applying the convolution deduction for the edge illumination system. Start from the free-propagation form seen in 7.14. For the double-mask EIXPCI method we need to add the effect of both masks over the transmission in the propagating wave [72]. This means that the total amplitude may now be written as.

$$I(x_d, y_d; \lambda) = [(|\psi(x, y, 0; M)|^2 * H_{z_0}) T_s(x, y) * T_{A_1} * H_{z_d}] * \text{PSF}_{\text{sys(SM)}}(x_d, y_d) \quad (7.25)$$

Where the term $\text{PSF}_{\text{sys(SM)}}$ is also modified due to the detector mask presence. Where.

$$\text{PSF}_{\text{sys(SM)}} = \left[\text{PSF}_s \left(\frac{x_d}{M-1}, \frac{y_d}{M-1} \right) * (\text{PSF}_d(x_d, y_d) * T_{A_2}) \right] \quad (7.26)$$

On the other hand. Single mask EIXPCI preserves the point-spread function of the system by not interfering directly with the detection system but rather the illumination over the sample. Where for the single mask we may write.

$$I(x_d, y_d; \lambda) = [(|\psi(x, y, 0; M)|^2 * H_{z_o}) T_s(x, y) * T_{A_1} * H_{z_d}] * \text{PSF}_{\text{sys}}(x_d, y_d) \quad (7.27)$$

Here, we conclude this section by proposing the following hypotheses. Due to less exposure time, alignment consistency, unaffected by mechanical noise, high phase sensitivity compared to other techniques, and a more cost-effective setup of the single mask EIXPCI compared to the double mask EIXPCI setup. Single-mask EIXPCI has increased potential for medical imaging, and the use of double-mask EIXPCI can be justified by the impact of these advantages in commercial use. The next section will focus on how the intensity on the detector without an object is solely a function of the edge position, which is an important principle since this mechanism allows different alignment setups that will bring important scanning signals for multi-modal purposes, such as Dark-field XPCI.

7.3 Illumination curve - Edge position vs intensity

Current EIXPCI methods allow the extraction of three different sample properties (multi-modal imaging): absorption, refraction, and scattering. In the last section, we developed the theory behind edge illumination. We found out that the intensity on the detector without an object is a function of the relative position of the edge and the mask w (See equation 7.23 and 7.22). The intensity recorded with the EI set up by a single detector pixel can be described by equation . This may be simplified by introducing the notion of the Illumination curve (IC) and the Sample Scatter Distribution (SD). Rewriting we have [73].

$$I(x_d, y_d; \lambda) = I_o(IC * SD)(x - \Delta x')t \quad (7.28)$$

Where $T_{A_1} * \text{PSF}_{\text{sys}}(x_d, y_d)$ is the representation of the illumination curve, and $H_{z_o} * T_s(x, y) * H_{z_d}$ has the object scattering information SD . $(x - \Delta x')t$ is the commutator factor $[T_{A_1}, H_{z_d}]$ [74]. Which is the relative position of the mask and object distribution and the fraction of transmitted intensity. The distribution representation for IC and SD will be further explored in chapter 9; changing the illumination curve will be translated in the imaging as switching the histogram intensity distribution of pixels in the flat-field for odd and even pixel, an analytical perspective using the results of odd/even pixels using the fact that the distance to the detector z_2 is much greater

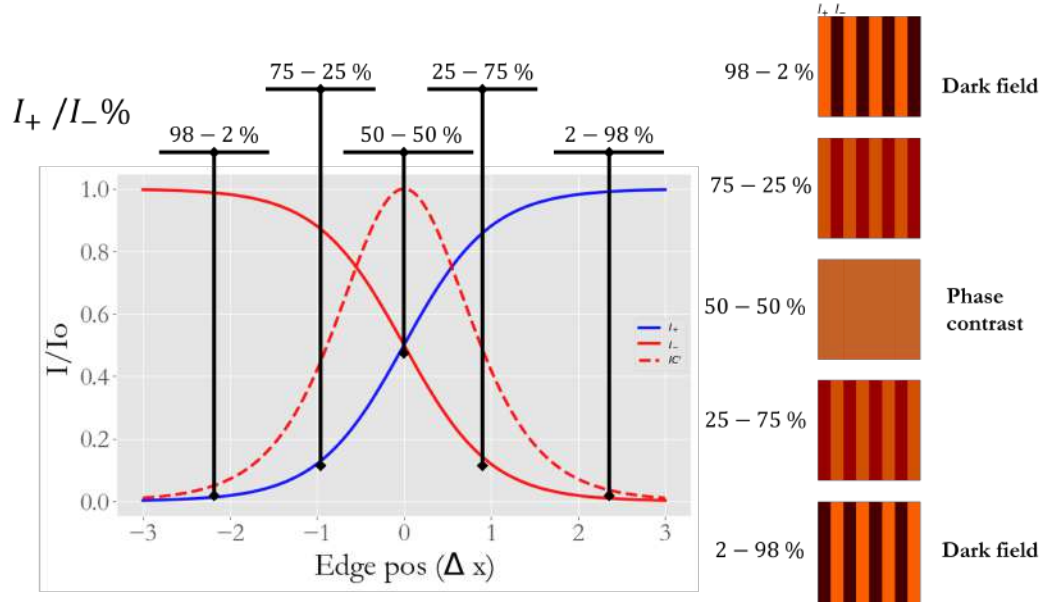


FIGURE 7.3: Edge illumination reconstruction of the illumination curve (IC) according to the relative position of the mask and the detector Δx . The mask is said to be aligned on a percentage modality when the total IC (Which is the sum of the total fringing in intensity) meets at the relative intensity distribution spot on the system. $\sim 100\% - 0\%$ are asymptotic values on the tails of the distribution in the illumination curve. However, since the interference pattern is known to be periodic going too far on Δx may result on falling back on the illumination curve due the mask and detector periodicity. Dark field illumination condition is met near $\sim 100\% - 0\%$ while phase contrast is maximized on $\sim 50\% - 50\%$. Several techniques use a full IC scan to retrieve the phase and dark field signals [14].

than the projected refraction of the sample $\Delta x'$ the Taylor expansion of the normalized illumination curve may be described as [75].

$$IC' / IC = \frac{I_- * I_+}{I_- + I_+} \approx -\frac{z_2}{M} \frac{\partial \phi}{\partial x'} \tanh T(x, y) w \quad (7.29)$$

This last result will be crucial to define the operations that follow the interpretation of combining positive and negative fringing on a composite image that went through the process of dithering. Although the interpretation of the fringing remains, the way of retrieving the composite signals (Attenuation, phase and dark-field) will be mathematically treated under a different formalism in chapter 9.

Figure 7.3 shows how the relation between the relative position of the mask and edge and the illumination curve, as well as the illumination of positive and negative fringing. Given the nature of the pixel intensity distributions, a more straight-forward interpretation can be done for which the illumination curve is a distribution which follows a maximum-likelihood estimation.

Chapter 8

Phase retrieval

X-ray imaging primarily allows for the visualization of high-density tissues like bones. X-ray phase contrast imaging, however, leverages the phase shift and attenuation properties of electromagnetic waves as they pass through a sample. This technique produces images where tissues of varying densities are more distinguishable. Phase retrieval algorithms, which focus on the phase shifts of electromagnetic waves, further enhance this capability. This section details these algorithms, referencing theoretical foundations laid earlier in this thesis. We will explore the Paganin algorithm for uniform materials, and delve into multimaterial algorithms, including the Beltran approximation, linear algorithm, and CTF and Born approximation.

8.1 Paganin Algorithm

For this phase retrieval algorithm, the author [76] assumes the phase retrieval for a single material, uniform and homogeneous sample. This sample will have a constant value for δ and β . which under the paraxial and projection approximation yields

$$\delta_\omega(x, y, z) = \delta_\omega \quad (8.1)$$

$$\beta_\omega(x, y, z) = \beta_\omega \quad (8.2)$$

The transport-of-intensity equation (TIE) plays a crucial role in understanding the intensity evolution of a paraxial monochromatic scalar electromagnetic or matter wave as it propagates and it is the starting point

$$\nabla_\perp \cdot (I(\mathbf{r}_\perp, z) \nabla_\perp \phi(\mathbf{r}_\perp, z)) = -\frac{2\pi}{\lambda} \frac{\delta}{\delta z} I(\mathbf{r}_\perp, z) \quad (8.3)$$

Where the intensity and phase are measured perpendicular to the propagation plane, this equation has been extensively utilized for quantitative non-interferometric phase imaging. Such applications span a diverse range including adaptive optics, visible-light microscopy [77], electron microscopy [78], neutron microscopy, and predominantly hard-X-ray imaging [79]. In order to streamline the derivation of the algorithm for quantitative phase extraction from a single image, an initial assumption is made that the point-source of X-rays is infinitely distant (i.e., $z_1 \rightarrow \infty$). This assumption leads to the conditions of collimated illumination and unit magnification. Subsequent to the primary derivation, modifications are incorporated to accommodate scenarios where z_1 is finite. Under the condition of the homogeneous sample material. For normally incident plane-wave radiation of uniform intensity over the area occupied by the sample, the intensity of the radiation over the plane at the exit surface of the object is assumed to be well approximated by Beer's Law of absorption

$$\Delta\phi(x, y, z_0) = -k\delta_\omega z_0(x, y) \quad (8.4)$$

$$I_\omega(x, y, z_0) = I_\omega(x, y, 0)\exp[-\mu_\omega T(x, y)] = I_\omega(x, y, 0)e^{-\mu_\omega z_0(x, y)} \quad (8.5)$$

Where intensity $I_\omega(x, y, z)$ is related with the squared magnitude of spatial part of an incident component of the electromagnetic field: $I_\omega(x, y, z) = |\vartheta_\omega(x, y, z)|^2 = |\psi_\omega(x, y, z)|^2$, therefore, as it was previously stated:

$$|\vartheta_\omega(x, y, z_0)|^2 = |\vartheta_\omega(x, y, 0)|^2 e^{[-2k \int_0^{z_0} \beta_\omega(x, y, z) dz]} \quad (8.6)$$

$$I_\omega(x, y, z_0) = I_\omega(x, y, 0)\exp\left[-2k \int_0^{z_0} \beta_\omega(x, y, z) dz\right] \quad (8.7)$$

Taking these aspects in consideration, equations 8.4 and 8.5 can be replaced on the TIE equation, in consequence:

$$\begin{aligned} & \frac{k}{R_2} \left[I_\omega(x, y, z) - I_\omega(x, y, 0)e^{-\mu_\omega z_0(x, y)} \right] \\ & + \vec{\nabla} \perp \cdot \left[I_\omega(x, y, 0)e^{-\mu_\omega z_0(x, y)} \vec{\nabla} \perp (-k\delta_\omega z_0(x, y)) \right] = 0 \end{aligned} \quad (8.8)$$

Operating $\vec{\nabla} \perp$ on the right side of 8.8:

$$\begin{aligned} & \frac{k}{R_2} \left[I_\omega(x, y, z) - I_\omega(x, y, 0) e^{-\mu_\omega z_0(x, y)} \right] \\ & - k \delta_\omega I_\omega(x, y, 0) \vec{\nabla}_\perp \cdot \left[e^{-\mu_\omega z_0(x, y)} \vec{\nabla}_\perp (z_0(x, y)) \right] = 0 \end{aligned} \quad (8.9)$$

And due to the fact that: $\vec{\nabla}_\perp \left(e^{-\mu_\omega z_0(x, y)} \right) = -\mu_\omega e^{-\mu_\omega z_0(x, y)} \vec{\nabla}_\perp (z_0(x, y))$, then, $\vec{\nabla}_\perp (z_0(x, y)) = -\frac{1}{\mu_\omega} \vec{\nabla}_\perp \left(e^{-\mu_\omega z_0(x, y)} \right) e^{\mu_\omega z_0(x, y)}$ equation 8.9 turns into:

$$\begin{aligned} & \frac{k}{R_2} \left[I_\omega(x, y, z) - I_\omega(x, y, 0) e^{-\mu_\omega z_0(x, y)} \right] \\ & - k \delta_\omega I_\omega(x, y, 0) \vec{\nabla}_\perp \cdot \left[e^{-\mu_\omega z_0(x, y)} \left(-\frac{1}{\mu_\omega} \vec{\nabla}_\perp \left(e^{-\mu_\omega z_0(x, y)} \right) e^{\mu_\omega z_0(x, y)} \right) \right] = 0 \end{aligned} \quad (8.10)$$

Which becomes:

$$\frac{k}{R_2} \left[I_\omega(x, y, z) - I_\omega(x, y, 0) e^{-\mu_\omega z_0(x, y)} \right] + \frac{k \delta_\omega}{\mu_\omega} I_\omega(x, y, 0) \vec{\nabla}_\perp \cdot \left[\left(\vec{\nabla}_\perp \left(e^{-\mu_\omega z_0(x, y)} \right) \right) \right] = 0 \quad (8.11)$$

Then:

$$\frac{k}{R_2} \left[I_\omega(x, y, z) - I_\omega(x, y, 0) e^{-\mu_\omega z_0(x, y)} \right] + \frac{k \delta_\omega}{\mu_\omega} I_\omega(x, y, 0) \nabla_\perp^2 \left[e^{-\mu_\omega z_0(x, y)} \right] = 0 \quad (8.12)$$

Taking this into consideration, intensity $I_\omega(x, y, z)$ can be expressed as:

$$\boxed{\frac{I_\omega(x, y, z)}{I_\omega(x, y, 0)} = e^{-\mu_\omega z_0(x, y)} - \frac{\delta_\omega R_2}{\mu_\omega} \nabla_\perp^2 \left[e^{-\mu_\omega z_0(x, y)} \right]} \quad (8.13)$$

At this juncture, the Fourier transform becomes integral to the deduction. Consider $F(u, v)$ as the Fourier transform of $f(x, y)$, which is mathematically denoted as $F(u, v) = \mathcal{F}\{f(x, y)\}$. Integrating the concept of Fourier transformation, we have:

$$f(x, y) = \frac{1}{2\pi} \int \int F(u, v) e^{i(ux)} e^{i(vy)} du dv \quad (8.14)$$

Subsequently, each term of equation 8.13 can be represented via Fourier transformations, as illustrated in equations 8.15 and 8.16. Accordingly, the transverse Laplacian applied to $e^{-\mu_\omega z_0(x,y)}$ is also portrayed through a Fourier transformation, as depicted in equation 8.17.

$$\frac{I_\omega(x, y, z)}{I_\omega(x, y, 0)} = \frac{1}{2\pi} \int \int_{-\infty}^{\infty} \mathcal{F} \left\{ \frac{I_\omega(x, y, z)}{I_\omega(x, y, 0)} \right\} (u, v) e^{i(ux+vy)} du dv \quad (8.15)$$

$$e^{-\mu_\omega z_0(x,y)} = \frac{1}{2\pi} \int \int_{-\infty}^{\infty} \mathcal{F} \left\{ e^{-\mu_\omega z_0(x,y)} \right\} (u, v) e^{i(ux+vy)} du dv \quad (8.16)$$

$$\begin{aligned} \nabla_\perp^2 e^{-\mu_\omega z_0(x,y)} &= \left(\frac{\partial^2}{\partial x^2} + \frac{\partial^2}{\partial y^2} \right) e^{-\mu_\omega z_0(x,y)} = -\frac{1}{2\pi} \int \int_{-\infty}^{\infty} (u^2 + v^2) \\ &\quad \times \mathcal{F} \left\{ e^{-\mu_\omega z_0(x,y)} \right\} (u, v) e^{i(ux+vy)} du dv \end{aligned} \quad (8.17)$$

Reintegrating these into expression 8.13 yields:

$$\begin{aligned} &\frac{1}{2\pi} \int \int_{-\infty}^{\infty} \mathcal{F} \left\{ \frac{I_\omega(x, y, z)}{I_\omega(x, y, 0)} \right\} (u, v) e^{i(ux+vy)} du dv = \\ &\frac{1}{2\pi} \int \int_{-\infty}^{\infty} \mathcal{F} \left\{ e^{-\mu_\omega z_0(x,y)} \right\} (u, v) e^{i(ux+vy)} du dv \\ &+ \left(\frac{\delta_\omega R_2}{\mu_\omega} \right) \frac{1}{2\pi} \int \int_{-\infty}^{\infty} (u^2 + v^2) \mathcal{F} \left\{ e^{-\mu_\omega z_0(x,y)} \right\} (u, v) e^{i(ux+vy)} du dv \end{aligned} \quad (8.18)$$

This can be simplified to:

$$\begin{aligned} &\int \int_{-\infty}^{\infty} \mathcal{F} \left\{ \frac{I_\omega(x, y, z)}{I_\omega(x, y, 0)} \right\} (u, v) e^{i(ux+vy)} du dv = \\ &\int \int_{-\infty}^{\infty} \left[\left(1 + \frac{\delta_\omega R_2}{\mu_\omega} (u^2 + v^2) \right) \mathcal{F} \left\{ e^{-\mu_\omega z_0(x,y)} \right\} (u, v) \right] \\ &\quad \times e^{i(ux+vy)} du dv \end{aligned} \quad (8.19)$$

Given the integration is consistent across both sides, we can rewrite the expression as:

$$\mathcal{F} \left\{ \frac{I_\omega(x, y, z)}{I_\omega(x, y, 0)} \right\} (u, v) = \left[1 + \frac{\delta_\omega R_2}{\mu_\omega} (u^2 + v^2) \right] \mathcal{F} \left\{ e^{-\mu_\omega z_0(x,y)} \right\} (u, v) \quad (8.20)$$

From which $\mathcal{F}\left\{e^{-\mu_\omega z_0(x,y)}\right\}$ can be extracted:

$$\mathcal{F}\left\{e^{-\mu_\omega z_0(x,y)}\right\}(u,v) = \frac{\mathcal{F}\left\{\frac{I_\omega(x,y,z)}{I_\omega(x,y,0)}\right\}(u,v)}{1 + \frac{\delta_\omega R_2}{\mu_\omega}(u^2 + v^2)} \quad (8.21)$$

Applying the inverse Fourier transform on both sides:

$$e^{-\mu_\omega z_0(x,y)} = \mathcal{F}^{-1}\left\{\frac{\mathcal{F}\left\{\frac{I_\omega(x,y,z)}{I_\omega(x,y,0)}\right\}(u,v)}{1 + \frac{\delta_\omega R_2}{\mu_\omega}(u^2 + v^2)}\right\} \quad (8.22)$$

$$e^{-\mu_\omega z_0(x,y)} = \frac{1}{2\pi} \int \int_{-\infty}^{\infty} \left[\frac{\mathcal{F}\left\{\frac{I_\omega(x,y,z)}{I_\omega(x,y,0)}\right\}(u,v)}{1 + \frac{\delta_\omega R_2}{\mu_\omega}(u^2 + v^2)} \right] e^{i(ux+vy)} du dv \quad (8.23)$$

Leading to:

$$z_0(x,y) = -\frac{1}{\mu_\omega} \ln \left[\frac{1}{2\pi} \int \int_{-\infty}^{\infty} \left[\frac{\mathcal{F}\left\{\frac{I_\omega(x,y,z)}{I_\omega(x,y,0)}\right\}(u,v)}{1 + \frac{\delta_\omega R_2}{\mu_\omega}(u^2 + v^2)} \right] e^{i(ux+vy)} du dv \right] \quad (8.24)$$

Thus, possessing the Fourier transform of $\frac{I_\omega(x,y,z)}{I_\omega(x,y,0)}$ and initial information about the sample (i.e., δ_ω and β_ω), and acknowledging that equation 8.4 is contingent on z_0 , the phase information of the image can be retrieved:

$$\Delta\phi = \frac{k\delta_\omega}{\mu_\omega} \ln \left[\frac{1}{2\pi} \int \int_{-\infty}^{\infty} \left[\frac{\mathcal{F}\left\{\frac{I_\omega(x,y,z)}{I_\omega(x,y,0)}\right\}(u,v)}{1 + \frac{\delta_\omega R_2}{\mu_\omega}(u^2 + v^2)} \right] e^{i(ux+vy)} du dv \right] \quad (8.25)$$

Consequently, one can define the parameter γ as $\delta_\omega / \mu_\omega$, which physically represents the ratio between the phase associated parameter and the attenuation related parameter. This lead to a small change on 8.25, but, at the same time will represent bigger consequences further:

$$\boxed{\Delta\phi = k\gamma \ln \left[\frac{1}{2\pi} \int \int_{-\infty}^{\infty} \left[\frac{\mathcal{F}\left\{\frac{I_\omega(x,y,z)}{I_\omega(x,y,0)}\right\}(u,v)}{1 + \gamma R_2(u^2 + v^2)} \right] e^{i(ux+vy)} du dv \right]} \quad (8.26)$$

This final equation is known as the Paganin algorithm of phase retrieval. Which can be interpreted as the weighted gradient of the signal over the effective energies of the material used. Thus, the use of the Fourier transform and the inverse Fourier

transform pretends to move the wave-field element to the frequency space, weight the gradient over the effective energies under the material where $\gamma = \delta/\beta$ and returning to the field space with the inverse Fourier transform (expressed as a double integral).

8.1.1 Multimaterial Algorithm

This algorithm takes the premise that the material can be divided in multiple slabs wach with a defined and constant δ, β as defined in section 4.4. If a sample in which multiple material are contained in it, the multimaterial approximation can be used. With this purpose, j materials, each with a z_j thickness, within an encapsulating material with a z_0 thickness. Taking this into consideration, the total thickness $A(x, y)$ for the j - object in conjunction with the encapsulating object can be expressed as:

$$A(x, y) = z_0(x, y) + z_j(x, y) \quad (8.27)$$

Given this, the refractive index for the encapsulating material denoted by z_0 can be described as equation 8.28 suggests, whilst equation 8.29 illustrates the refractive index for every j -esim material. It is important to state that these refractive index will be constant through every material, as well as they will be null for a different material.

$$n_{\omega,j} = 1 - \delta_{\omega,j} + i\beta_{\omega,j} \quad (8.28)$$

$$n_{\omega,0} = 1 - \delta_{\omega,0} + i\beta_{\omega,0} \quad (8.29)$$

Keeping this in mind, intensity variation through a distance z_k (according to equation 8.5) might be expressed as follows:

$$I_{\omega}(x, y, z_k) = I_{\omega}(x, y, 0)e^{[-2k \int_0^{z_k} \beta_{\omega}(x, y, z')dz']} = I_{\omega}(x, y, 0)e^{[- \int_0^{z_k} \mu_{\omega}(x, y, z')dz']} \quad (8.30)$$

$$I_{\omega}(x, y, z_k) = I_{\omega}(x, y, 0)e^{- \int_0^{z_0} \mu_{0,\omega}dz' - \int_0^{z_j} \mu_{j,\omega}dz'} \quad (8.31)$$

$$= I_{\omega}(x, y, 0)e^{-\mu_{0,\omega}z_0(x,y) - \mu_{j,\omega}z_j(x,y)} \quad (8.32)$$

$$= I_{\omega}(x, y, 0)e^{-\mu_{0,\omega}z_0(x,y) - \mu_{j,\omega}z_j(x,y) - \mu_{0,\omega}z_j(x,y)\mu_{0,\omega}z_j(x,y)} \quad (8.33)$$

$$= I_{\omega}(x, y, 0)e^{-\mu_{0,\omega}z_0(x,y) - \mu_{j,\omega}z_j(x,y) - \mu_{0,\omega}z_j(x,y)\mu_{0,\omega}z_j(x,y)} \quad (8.34)$$

$$(8.35)$$

This approximation has been widely use especially in CT applications where the depth resolution takes an important role, this application can also be extended to the dark-field angle estimation for reconstructions [80].

Chapter 9

Dithering Sampling

Dithering is an intentionally applied noise used to randomize quantization error, which results from digital sampling of analogical signals, preventing large-scale patterns such as color banding in images. In physics, dithering can improve measurement resolution and diminish the total measurement uncertainty [81]. Lawrence G. Roberts first applied the concept of dithering to reduce quantization patterns in 1961 [82]. Dithering normally can be used in over-sampled systems following the Nyquist–Shannon sampling theorem with a sampling frequency significantly higher than the Nyquist rate. In X-ray imaging, dithering is used to improve the quality of the images. This technique involves acquiring multiple images per scan as the object is moved over sub-pixel distances [83]. Dithering in X-ray imaging helps to reduce artifacts and improve the signal-to-noise ratio by shifting the pointing direction of the telescope in random directions between each exposure. This process allows for the isolation of the signal from fixed pattern noise, resulting in images with improved quality and reduced noise. Most importantly, dithering enables an increase in the original resolution of the image over the sampling direction. For most applications, dithering effectiveness usually is evident after 6 dithering steps. However, the rule of thumb for dithering enhancement is 8 dithering sampling. In this section, we explore the theoretical dithering effects in radiation image resolution and image enhancement.

Recall under the projection approximation that the angle of refraction in the presence of a sample for an X-ray beamlet is given by

$$\alpha(x, y) = \frac{1}{k} \frac{\partial \phi}{\partial x}(x, y) \quad (9.1)$$

where the phase shift is given by

$$\phi(x, y) = k \int_{\Gamma} \delta d\Gamma \quad (9.2)$$

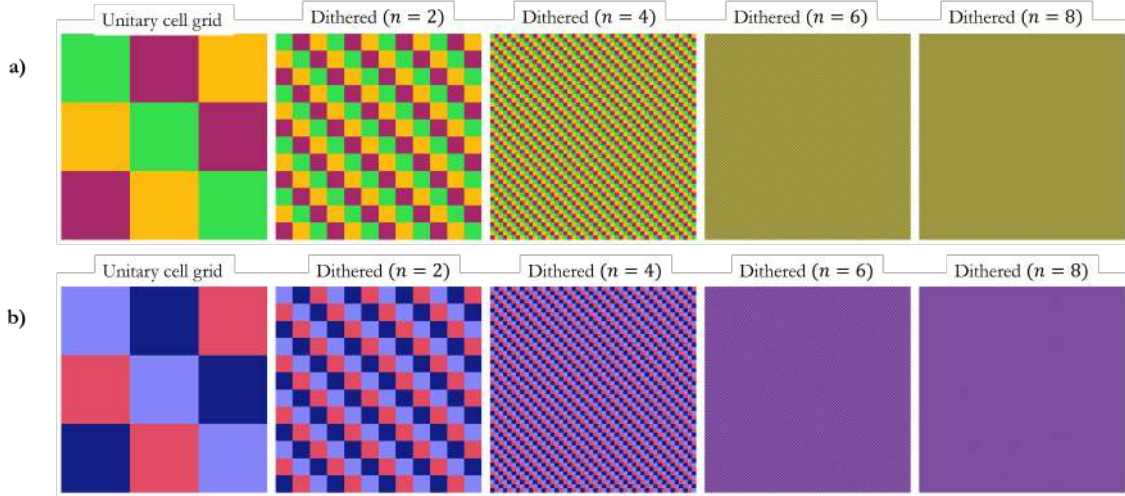


FIGURE 9.1: Small simulation of how the dithering sample works. Dithering can be interpreted as the addition of multiple quantized signals, when morphing said signals to an analog pattern (interpreted as a continuum), these signals may express a homogeneous pattern instead of large-scale patterns. a) and b) start as a unit cell of randomized colors, this cell is then concatenated n times in each direction to create a dithering pattern, that when the scale is large enough ($n = 8$) the pattern is perceived as a homogeneous color which is the average color of the unit cell. The factor $n = 8$ follows the rule of the sampling frequency and will be important later on as the factor is chosen to dither laboratory images in the edge illumination technique

Where Γ is the photon trajectory. This is done for different trajectories where the total dithered signal for the differential phase is given.

$$\frac{1}{k}\phi(x, y) = \int_{\Gamma} \delta d\Gamma \quad (9.3)$$

When the signal is discretized, and the detector has a discrete spatial resolution, the coordinates $(x, y) \rightarrow (i, j)$. Hence.

$$\frac{1}{k}\phi(i_N, j) = \Delta s \sum_{i=1}^{i_N} \alpha(i, j) \quad (9.4)$$

Where Δs is the sampling dithering interval, this can be interpreted as the dithering displacement distance. i_N is the total displaced distance on the detector. Then the total intensity projection due to the movement of the sample in the frame of reference of the setup is.

$$I(x, y, \Delta x, \Delta y) = \exp\left(-\frac{4\pi}{\lambda}\beta(x, y)\right) \cdot \left[IC(\Delta x) - \frac{z_1}{M}IC(\Delta x)\delta(x, y)\right] \quad (9.5)$$

Where $M = (z_1 + z_2)/z_2$. Again, discretizing this system and explicitly writing the dependency on β and δ

$$|I(\beta, \delta)|^2 = \exp\left(-\frac{4\pi}{\lambda}\beta(x, y)\right) \cdot \left[IC(\Delta x) - \frac{z_1}{M}IC(\Delta x)\delta(x, y)\right] \quad (9.6)$$

Recall the wave field equation of the last section for the edge illumination case. Where (Assuming $M=1$) $m(y)$ is the wavelet shape and H is the Fresnel-Kirchhoff operator.

$$I_{det} = |\phi(x, y, \lambda) \cdot m(y) * H_{z_2}(x, y, \lambda)|^2 * G(x, y) \quad (9.7)$$

This is a separable equation and $G(x, y)$ is the intensity distribution of the detection system $IC * O = G$ which follows a 2D Gaussian distribution. Due to the isotropic nature of the wave elements in the field, we may separate the x, y propagated behavior where.

$$I_{det} = |\phi(x, \lambda) * h_{z_2}(x, \lambda)|^2 * g(x) \cdot |\psi(y, \lambda) \cdot m(y) * h_{z_2}(y, \lambda)|^2 * g(y) \quad (9.8)$$

Where $g(x), g(y)$ are 1D Gaussian distributions. This leads to the equation system

$$k_1(x, \lambda) = |\phi(x, \lambda) * h_{z_2}(x, \lambda)|^2 * g(x) \quad (9.9)$$

$$k_2(y, \lambda) = |\psi(y, \lambda) \cdot m(y) * h_{z_2}(y, \lambda)|^2 * g(y) \quad (9.10)$$

The total signal is the integral over the detector area. For an n dither step is given by

$$S(x; y) = \left[\int_{x_0}^{x_d} dx k_1(x, \lambda) \right] \cdot \left[\int_{y_0}^{y_d} dy k_2(y, \lambda) \right] \quad (9.11)$$

Recall that x is the direction parallel to the mask apertures, and y is perpendicular. For the direction parallel to mask lines, the expression for k_1 follows the transport-of-intensity equation [84] .

$$k_1(x, \lambda) = T(x; \lambda) \left[1 - \frac{z_2}{Mk} \frac{\partial \phi}{\partial x} \right] * g(x) \quad (9.12)$$

The resolution is then in the near-field regime where $N_f \gg 1$.

$$r_{near} = \sqrt{(4\sigma_x)^2 + \left(\frac{\Delta x}{M}\right)^2} \quad (9.13)$$

And in the Fresnel diffraction regime condition where $N_F \approx 1$

$$r_{dif} = \sqrt{(2 \cdot \max[\sigma_x, \sqrt{\lambda z_2 / M}])^2 + \left(\frac{\Delta x}{M}\right)^2} \quad (9.14)$$

Of course $r_{near} \leq r_{dif}$. But note how in both cases the resolution does not depend on the dithering displacement Δs and follows the same principle as in-line propagation. Then an important remark, although trivial, might be done. Resolution in a direction where no dithering is done remains constant. On the other hand, the resolution on the perpendicular direction of the displacement may be given by the following signal expression.

$$S(n, \Delta y, \lambda) = \frac{x_p}{M} \left(a - \frac{\Delta y}{M} \right) + \frac{x_p}{M} \cdot \frac{\Delta y}{M} [\Delta \theta * g] \left(\frac{\Delta y}{M} - ny_p \right) \quad (9.15)$$

Where θ is the diffraction angle x_p, y_p is the pixel size of the detector in each direction and a is the beamlet width given by the beamlet shape function $m(y)$. This equation has different regimes of solutions for the resolution given in equations 9.17 to 9.20. Define the coordinate system

$$I^+ = a - \Delta y / M \quad I^- = \Delta y / M \quad (9.16)$$

Then, as described in [85].

$$\text{if } 2\sigma < \min [I^+, I^-] \quad r = 4\sigma \quad (9.17)$$

$$\text{if } I^- < 2\sigma < I^+ \quad r = 2\sigma + I^- \quad (9.18)$$

$$\text{if } I^+ < 2\sigma < I^- \quad r = 2\sigma + I^+ \quad (9.19)$$

$$\text{if } \max [I^+, I^-] < 2\sigma \quad r = a \quad (9.20)$$

$$(9.21)$$

For a fixed grid size a , the important take on this result for the reader is that the spatial resolution in an edge-illumination phase contrast x ray imaging system depends on plenty conditions over the imaging system. Namely it is not just the convolution of the PSF of the source within the detector resolution, but instead it mostly depends on the geometrical shape of the fringes and the dispersive nature of the beamlets after the interaction with the diffractive slits and the sample given by σ . If the reader is familiar to the characterization of optical systems, the resolution is normally given by the Full-Width Half-Maximum (FWHM) of the Point-Spread-Function (PSF) of the system. Which is equivalent by taking the modified PSF of the system evaluated in 7.28

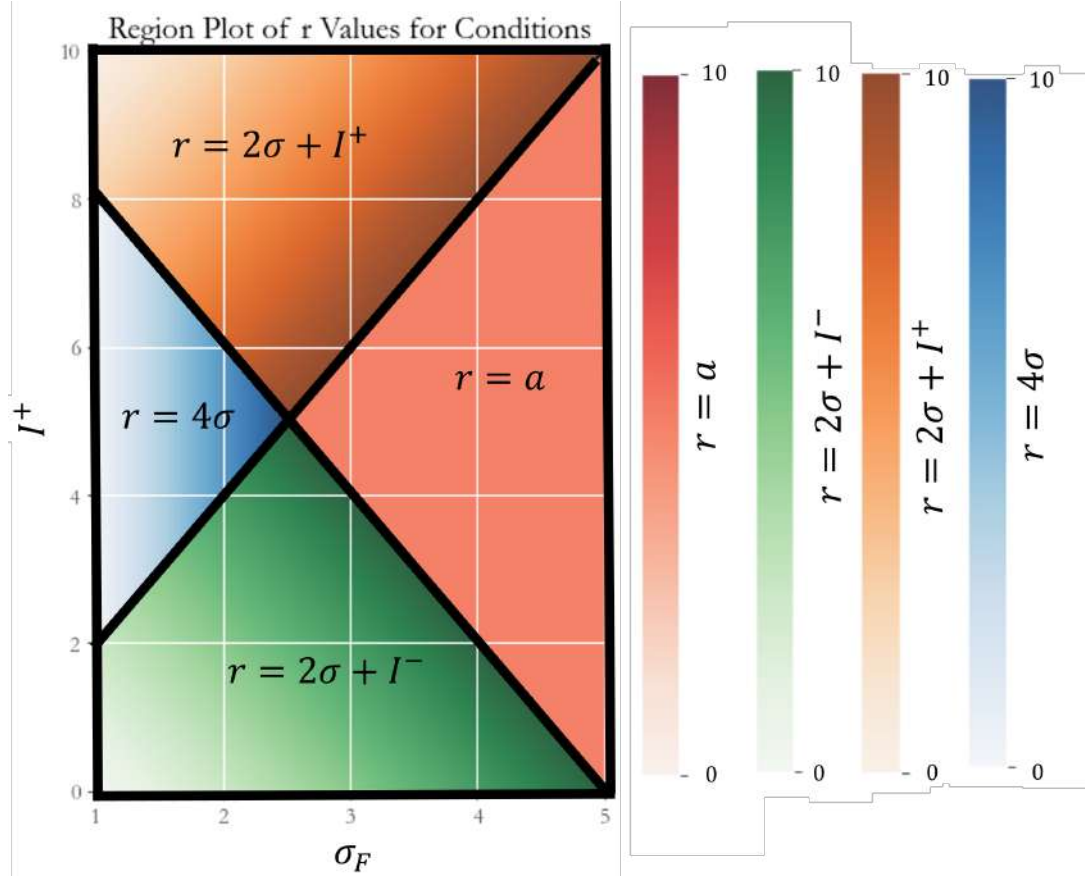


FIGURE 9.2: Region map over the resolution conditions of the system. The region where $r = a$ is constant over all values and is given solely by the aperture size of the mask a . However, several cases are also present whenever the beamlet size follows the Fresnel condition, additionally, the system may also be limited by the nature of the PSF of the system, given by σ . The sweet spot of the region plot may be interpreted as the centre of the rectangle, which corresponds to the case where $I^+ \sim I^- \sim 2\sigma \sim a$

9.1 Dithering theoretical limit

The resolution cases seen in last section, although applicable to the edge illumination imaging system, can be violated by adding additional dithering steps. The reader at this point might think dithering can be indefinitely applicable to the imaging sequence with the only drawback of time-resolution loss. However, dithering also has a theoretical limit that follows the rules of information theory on whether new information may be redundant. Some works have been performed in the realm of X-ray imaging about this theoretical limit [86] but most of the focus on this topic goes to the realm of quantum metrology [87]. To go further in this topic, take the equation that represents the total intensity of the signal as a convolution between the IC and the object scattering curve SD displaced by a factor $(x - \Delta x)$.

$$I(x_d, y_d; \lambda) = I_o(IC * SD)(x - \Delta x')t \quad (9.22)$$

By taking separately distributed functions for IC and SD we may write.

$$IC_n(x) = \sum_{n=1}^N \frac{A_n}{\sqrt{2\pi\sigma_n^2}} \exp\left(-\frac{(x-\mu_n)^2}{2\sigma_n^2}\right) \quad (9.23)$$

And

$$SD_m(x) = \sum_{m=1}^N \frac{A_m}{\sqrt{2\pi\sigma_m^2}} \exp\left(-\frac{(x-\mu_m)^2}{2\sigma_m^2}\right) \quad (9.24)$$

Then the convolution is presented as the joint integration of the distributions in the Fourier, which going back to equation 9.22.

$$\frac{I}{I_0} = \sum_{m=1}^M \sum_{n=1}^N \frac{A_{mn}}{\sqrt{2\pi\sigma_n^2}} \exp\left(-\frac{(x-\mu_n)^2}{2\sigma_n^2}\right) \quad (9.25)$$

Dithering is the joint iteration of m, n values due to the discrete nature of the problem. For each dither step what we are really doing is a parameter estimation that fits the joint probability $IC * SD$. This is maximizing the likelihood of a distribution to meet the parametric joint values μ_{mn}, σ_{mn}^2 . It is known a priori that the distribution will follow a gaussian-like shape, hence $f(\cdot; \theta_0)$, under certain conditions, the maximum likelihood estimator converges in distribution to a normal distribution. It is \sqrt{n} -consistent and asymptotically efficient, meaning that it reaches the Cramér–Rao bound. Specifically,

$$\sqrt{n}(\hat{\theta}_{\text{mle}} - \theta_0) \xrightarrow{d} \mathcal{N}(0, I^{-1}), \quad (9.26)$$

where I is the Fisher information matrix:

$$I_{jk} = \mathbb{E} \left[-\frac{\partial^2 \ln f_{\theta}(X_t)}{\partial \theta_j \partial \theta_k} \right]. \quad (9.27)$$

In particular, it means that the bias of the maximum likelihood estimator is equal to zero up to the order $\frac{1}{\sqrt{n}}$. What this means is that the number of dithering steps has an asymptotic limit where additional steps on the information provided about the IC will not add further resolution. this limit is given by the Cramer-Rao bound of the joint distribution, and as seen in results on [88, 89] .

9.2 Multimodal imaging of odd and even pixels

The phase and dark field signals are reconstructed using the total distribution of fringing concerning the original illumination distribution. Previous works on edge illumination with a double mask system used illumination with and without the sample to compare the fringing. However, in this case, the single mask permits a relative

measurement between odd and even pixels, as depicted in figure 10.7. The distinction between odd and even pixel distribution indicates how the distribution of the illumination and sample curves may be represented as a correlated distribution in space. Articles on edge illumination XPCI fit these curves as Gaussian distributions. Then, the comparison of the illumination and sample curves allows extraction of the attenuation, refraction, and dark-field characteristics of the sample on a pixel-by-pixel basis [90]. In particular, the Gaussian representation is given by.

$$I_{IC}(x) = \frac{t_{IC}}{\sqrt{2\pi\sigma_{IC}^2}} \exp \left[-\frac{(x - \mu_{IC})^2}{2\sigma_{IC}^2} \right] + I_o \quad (9.28)$$

And for the sample curve.

$$I_O(x) = t_O \left[\frac{t_{IC}}{\sqrt{2\pi\sigma_O^2}} \exp \left[-\frac{(x - \mu_O)^2}{2\sigma_O^2} \right] + I_o \right] \quad (9.29)$$

In this case, a total switch of the illumination curve is measured due to the object's presence in the field of view. This switch is the positive and negative fringing of the illumination due to the refraction and scattering effects of the object. However, the odd and even pixel statistics are completely analogous to this case (see figure 9.3), where the relative position of spatial coherence is now resolved as the positive and negative illumination fringing. One can generalize this fact by cutting the IC and O distributions as odd and even pixels too. This, however, is also a Gaussian distribution with two distinguishable detection systems, each with half the resolution (half the amplitude) of the original detection system. Multiplied by an spatial correlation function Γ which can be interpreted as the illumination percentage values.

$$I_{IC}(x : \text{Odd, Even}) = \Gamma(\text{Odd} : \text{Even}) \frac{t_{IC}}{\sqrt{2\pi(\sigma_{IC} - \sigma_{rel})^2}} \exp \left[-\frac{(x - \mu_{IC} - \Delta x_{rel})^2}{2(\sigma_{IC} - \sigma_{rel})^2} \right] + I_o \quad (9.30)$$

Where the Δx_{rel} and σ_{rel} And for the object,

$$I_{(\text{Even:Odd})}(x) = \Gamma(\text{Odd} : \text{Even}) t_O \left[\frac{t_{IC}}{\sqrt{2\pi(\sigma_O + \sigma_{rel})^2}} \exp \left[-\frac{(x - \mu_O - \Delta x_{rel})^2}{2(\sigma_O + \sigma_{rel})^2} \right] + I_o \right] \quad (9.31)$$

However, due to properties of the Gaussian distributions, the metric difference over the expected value can be re-written as a distribution over spacing values using the coordinates $x_{odd} = x - \Delta x_{rel}$ and $x_{even} = x + \Delta x_{rel}$. Expanding and using the resulting square difference.

$$I_{IC}(x : \text{Even} : \text{Odd}) = \Gamma(\text{Odd} : \text{Even}) \left[A \exp \left[-\frac{(x_{E,O} - \mu_{E,O})^2}{2(\sigma_{E,O})^2} \right] + t_O I_o \right] \quad (9.32)$$

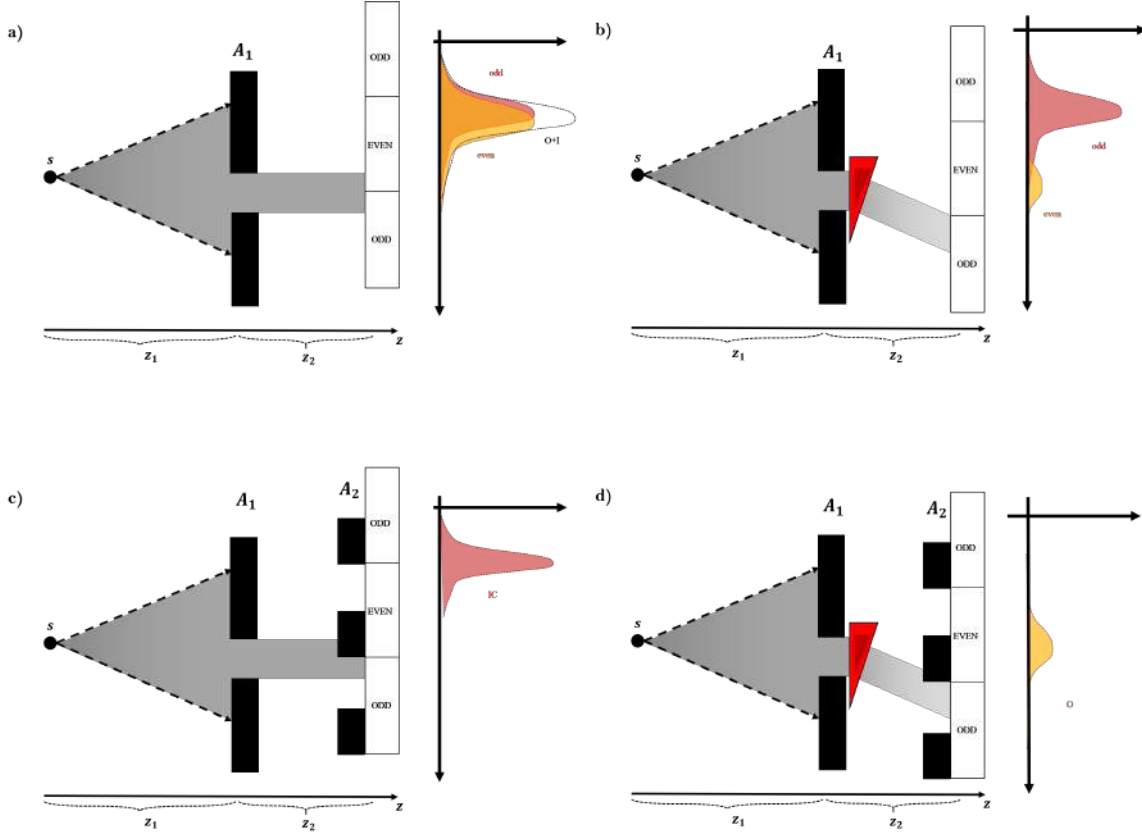


FIGURE 9.3: Sketch of single and double mask edge-illumination systems with the approximate histogram of intensities with and without the sample on the $\sim 50\% - 50\%$ illumination modality. a) Single mask EI flat-field where odd and even pixels meet almost equal illumination, this is represented by how aligned are the histograms from each other. b) Illumination switch of a single mask EI system initially aligned due to the presence of the scatterer sample in the path. c) Double mask EI flat-field. In this case, the second mask takes the role of differentiating positive and negative fringing instead of the illumination percentage. For this reason, at least two scans are necessary to retrieve the same information per dithering frame as in single mask modality d) Double mask EI system with the sample present, the switch of the illumination in the histogram represents the phase difference of the signal.

Where $A = t_O \frac{t_{IC}}{\sqrt{2\pi(\sigma_{E,O})^2}}$

9.3 Photon statistics interpretation of the multimodal signals

The photon statistics for an individual pixel may be interpreted as a Poisson distribution with a parameter of counting time λ . First take a single pixel (scintillator) with ideal zero dead time. The characteristic function for the distribution that counts the probability of detecting x photons is.

$$G(k) = e^{-\lambda} \sum_{\lambda=0}^{\infty} \frac{\lambda^x}{x!} e^{ik} = e^{-\lambda + \lambda e^{ik}} \quad (9.33)$$

Where the i momenta can be calculated.

$$\langle x \rangle = \lambda \quad \langle \Delta x^2 \rangle = \lambda \quad \dots \quad (9.34)$$

Now take, for instance, the multi-pixel case for the random aggregated variable $X = x_1 + x_2 + \dots + x_{255 \times 255}$. This is in fact the same characteristic function, hence

$$P_X(X = n\bar{x}) = e^{-n\lambda} \frac{(n\lambda)^X}{X!} \quad (9.35)$$

And the cramer function is given by

$$s(\bar{x}) = -\bar{x} \frac{\bar{x}}{\lambda} + (\bar{x} - \lambda) \quad (9.36)$$

Which is the inverse Legendre transform of the momentum-generating function. By the central limit theorem (CLT), we state that the large deviation principle collapses fast enough for the distribution tails to be light. Then for large λ which is at least 20 times the minimum detector time-capture. $\mu \approx \lambda, \sigma \approx \sqrt{\lambda}$ is also true for discriminating odd and even pixels.

$$I_{O,E}(x) = \frac{T}{\sqrt{2\pi\sigma_{O,E}^2}} \exp \left[-\frac{(x - \mu_{O,E})^2}{2\sigma_{O,E}^2} \right] \quad (9.37)$$

9.3.1 n Momenta

This distribution's ergodic theorem of time average follows the wiener-Kinchin discrete process for finite pixel size. Take, for instance, the first 4 momenta for a distribution over the odd and even pixels. Where

$$M_O(0) = x_o \quad M_E(0) = x_e \quad (9.38)$$

$$M_O(1) = \mu_o \quad M_E(1) = \mu_e \quad (9.39)$$

$$M_O(2) = \sigma_o^2 \quad M_E(2) = \sigma_e^2 \quad (9.40)$$

$$M_O(3) = E \left[\left(\frac{x_o - \mu_o}{\sigma_o} \right)^3 \right] \quad M_E(3) = E \left[\left(\frac{x_e - \mu_e}{\sigma_e} \right)^3 \right] \quad (9.41)$$

$$M_O(4) = \frac{\mu_o^4}{\sigma_o^4} \quad M_E(4) = \frac{\mu_e^4}{\sigma_e^4} \quad (9.42)$$

However, the 3rd and 4th momenta are constant for a Gaussian distribution. The assumption of the signal being perfectly distributed as normal may not give further information on the subsequent signals. Nevertheless, in a real imaging system, further momenta may produce de-noising signals that will be explored in further work. The

next section uses the momenta representation of illumination distributions to reconstruct absorption, phase, and dark-field signals.

Part III

Preliminaries

Chapter 10

Experimental preliminaries

This section details the experimental setup and preliminary experimental characterizations of the system. It includes information on the image capture source, detectors, diffraction mask, system movement, the input/output relationship necessary for reproducibility purposes, and the specific procedures for sample handling, optical system alignment, and image quality control.

The general setup used is the X-ray radiation chamber of the High-energy Physics (HEP) Laboratory at Universidad de los Andes. It consists of a polychromatic micro-focus experimental X-ray source, a semiconductor detector array, a sample placement platform, and a diffraction sample mask, each with a set of step motors with their coordinate system. The step motors and detector capture systems are managed from a control station computer with the necessary software. The specifics of each component will be further explored in the following sections. Figure 10.1 shows a general description of the system.

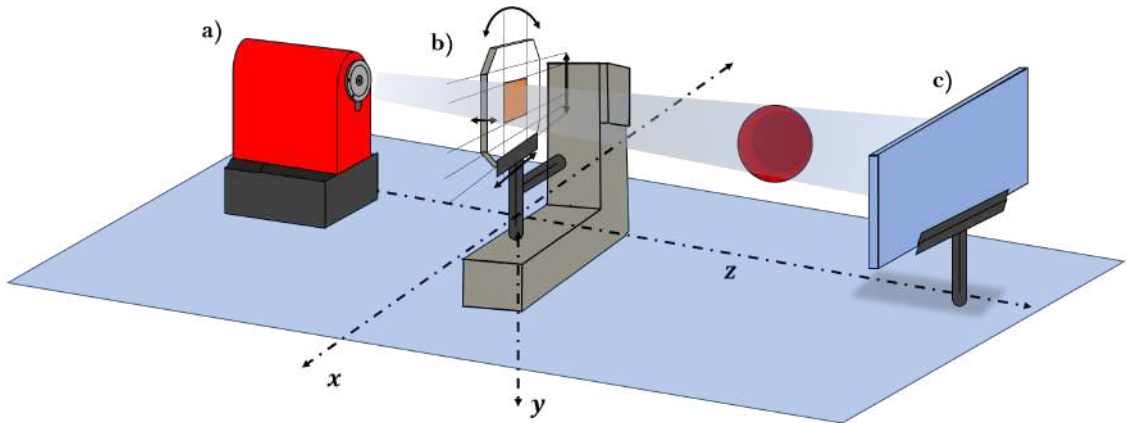


FIGURE 10.1: Illustrative general experimental setup. a) X-ray polychromatic source. b) diffraction mask. c) X-ray detector array (Medipix3RX)

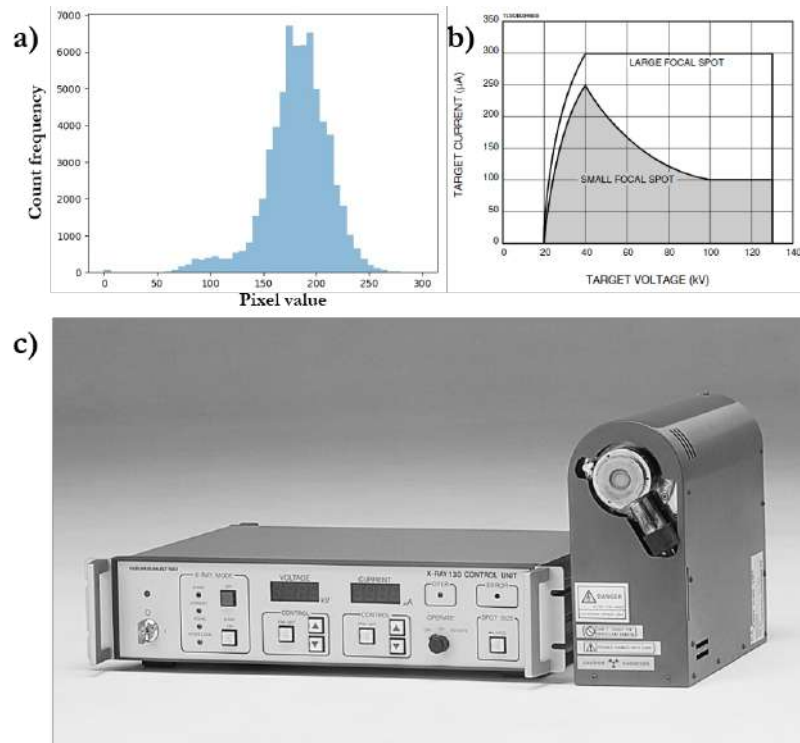


FIGURE 10.2: a) Pixel count distribution with a misaligned mask, the skewness at the left is due to non-uniform intensity counts. b) Voltage vs target current in the regimes of small and large focal spots for the Hamamatsu source [15]. c) Source and RS-232C interface [15].

Besides distance, the main change between systems will be the replacement or removal of the system's diffraction mask for speckle-based and in-line PCI. Later sections will develop further on the specifics of different PCI setups.

10.1 The source

The source used in this work is a Hamamatsu L6622-01 micro-focus polychromatic x-ray source equipped with a Tungsten target and a Beryllium window of $200\ \mu\text{m}$. The operational range of the source was $20 - 130\ \text{kV}$ tube voltage and $10 - 300\ \mu\text{A}$ tube current [15]. The anode had a wide exit angle with a cone amplitude of 43° , which may represent a higher risk to other elements inside the cabinet and can produce noise detection due to scattering effects. A $2.5\ \text{mm}$ Pb collimator was used to fix this issue.

The nominal focal spot size was $5\ \mu\text{m}$ at $4\ \text{W}$, but it could increase up to $30\ \mu\text{m}$ with the tube power. Intensity is approximately normally distributed (see figure 10.3) along the solid angle of the emitted X-rays. The cone aperture with the collimator switches to 2° , the value used for further simulation results. The device includes an RS-232C interface for automatic operability from external control systems.

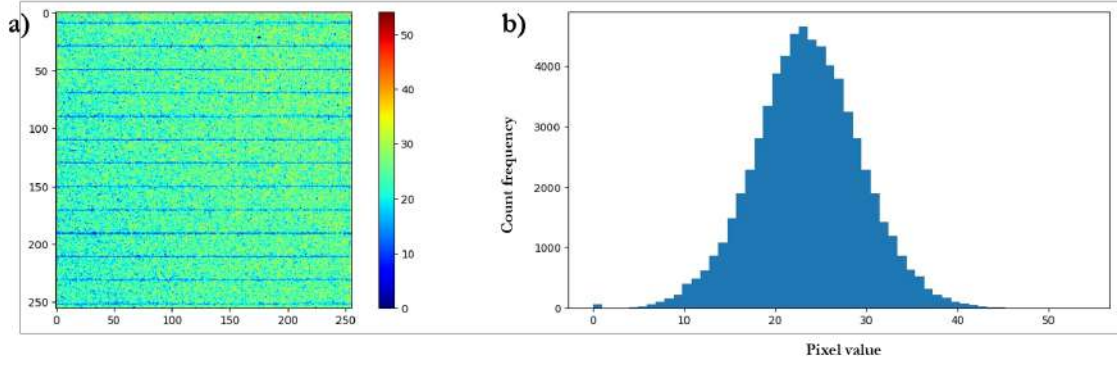


FIGURE 10.3: a) Flat-field image of a perfectly aligned diffraction mask and detector array, captured by a Medipix3RX b) Histogram distribution over pixel values. A slight skewness is present due to the support bars present on the diffraction mask. A bin at zero pixel value is visible due to dead pixels on the detector; the final distribution shows a Gaussian-like behavior, a direct consequence of the central limit theorem due to the sum of multiple Poisson distributions (see chapter 12).

By these specs, this source may be used for X-ray Non-destructive tests such as inspecting printed circuits, electronic components, semiconductor devices, and other non-biological samples. It also can be used in advanced imaging systems for biological ex-vivo tissue at a low energy regime. However, low kV limits the total current operation range (See figure 10.3). Previous works done in the laboratory required a characterization of the source and detector system [91]. This is necessary for direct phase retrieval and calculations. As well as quality control of the images and dosimetry security checks. The nominal value of the Full-Width Half-Maximum at the energy range used in this project was $7.27\mu m$ with a source voltage of $30kV$ and $60\mu A$ current.

10.2 Diffraction mask

The diffraction mask is an optical element that consists of a defined array of highly attenuating material with different distributions depending on the application. Take, for instance, the equation for the propagation field after the mask. Convoluting the mask over the wave field for the intensity equation can be expressed as.

$$I_{A_1}(x, y; p) = \frac{I_o}{M} | [T(x, y) \cdot m(x, y)] * H_z(x, y) |^2 \quad (10.1)$$

Where $T(x, y)$ is the transmission function and $m(x, y)$ is the re-shaped wave function. In the specific case of a 1D mask like the one shown in figure 10.4, the expression follows.

$$I_{A_1}(y; p) = \frac{I_o}{M} | [T(y) \cdot rect_a(y)] * H_z(x, y) |^2 \quad (10.2)$$

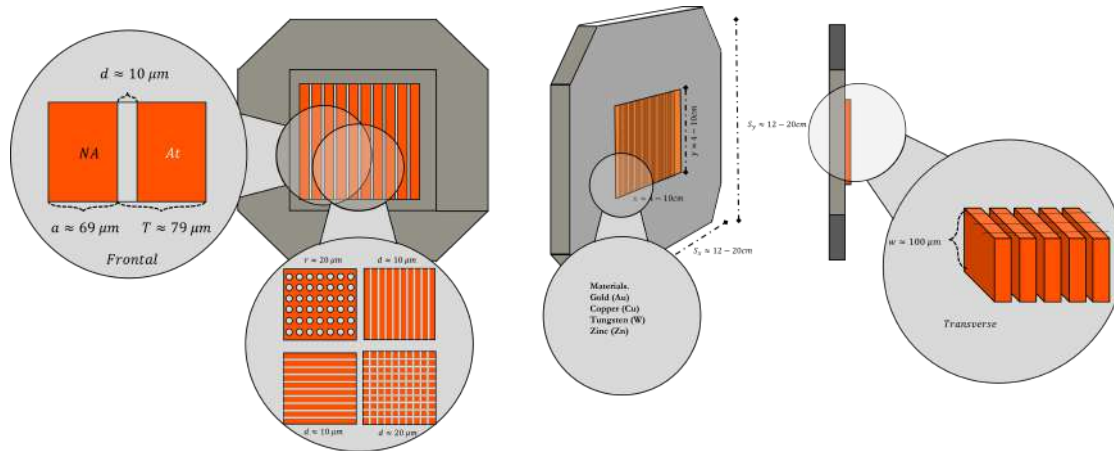


FIGURE 10.4: Technological characterization of the diffractive mask. This device is normally made of an attenuating material and manufactured using photolithographic techniques. Additional materials have been explored for the production of these masks [16] as seen in figure 10.5 since the only condition is to be highly attenuating. The dimensions, patterns, and periodicity are not fixed for all systems. However, an effective edge illumination system must preserve the periodicity of the device's grating pattern.

Where $m(x,y) = \text{rect}_a(y)$ follows the rectangular shape of the masked beams with an aperture $[-a/2, a/2]$. Hence, this step function is 1 in this range and 0 elsewhere (For an ideal fully attenuating material). Diffraction masks are not limited to vertical lines or unidimensionality; several works use grating patterns to address less time exposure and increased resolution on multiple axes [92].

Professor Alessandro Olivo from University College London kindly provided the diffraction mask. which has a period of $79 \mu\text{m}$ and an aperture size of $10 \mu\text{m}$, with a septa thickness of approximately $100 \mu\text{m}$ of gold electroplated on $500 \mu\text{m}$ of graphite. While the septa thickness is nominal, electroplating issues may lead to regions where the mask has less attenuation. This may also be partially corrected by using hot-pixel interpolation and flat-field correction. Figure 10.5 compares the attenuation constant with and without scattering effects for gold and tungsten on the same energy regime for medical and biological use [16]. The set of motors plays a crucial role in matching the mask and detector periods and aligning the outgoing beams of the mask with the pixel columns. These motors, manufactured by Optimal Engineering Systems, Inc., consist of a motorized linear stage with a full step of approximately $5 \mu\text{m}$ for aligning the beams with the detector columns along the y -axis and a motorized goniometer stage with a full step of approximately 7.14 millidegrees for adjusting the mask rotation over the propagation axis. The motor can be modified to different step sizes, reaching $1/32$ step size, where full steps have a $1.25 \mu\text{m}$ displacement. High movement resolution is critical to achieve specific illumination fringing in the alignment process.

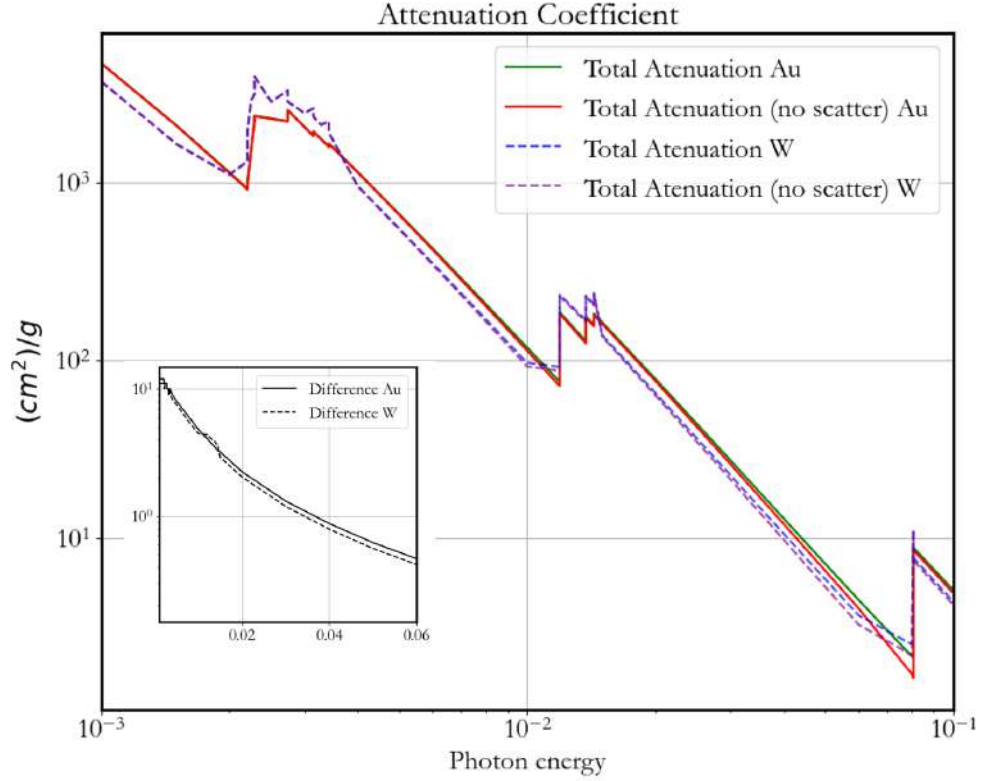


FIGURE 10.5: Difference on material attenuation coefficients using in recent works [16] provided by NIST [10]. Although the difference is not significative for these materials as seen in the difference subplot, the cost of Tungsten is 11 times lower than gold, this provides higher scalability for the production of diffracting mask devices.

10.3 Mask alignment modalities

As reviewed in chapter 7, when the beam is slightly thicker than a detector pixel, it can reach outside the pixel, creating positive signals when it hits the opposite edge of the sample. This results in positive fringes on one side of the sample and negative fringes on the other, effectively doubling the detected signal. The modulation of projected illumination in Edge Illumination imaging follows a distribution function called the Illumination Curve (IC). This IC is the total intensity retrieved by the detector and behaves as a Gaussian distribution or a Poisson distribution whether the dose is measured over time. The IC maps refraction in terms of variation in detected intensity. When a sample refracts a beamlet, the detector perceives it as displacing the illumination point on the IC. Therefore, the IC can be used for phase retrieval by mathematically inverting it by the Paganin method reviewed in chapter 8. For multi-modal imaging that successfully retrieves the three signals of interest, it is necessary to set the system at 50% – 50% illumination fringing and $\sim 100\% - 0\%$. Figure 10.7 illustrates both cases. The $\sim 100\% - 0\%$ system is mainly used to retrieve the dark-field signal, while the $\sim 50\% - 50\%$ illumination setup is primarily used to retrieve phase contrast

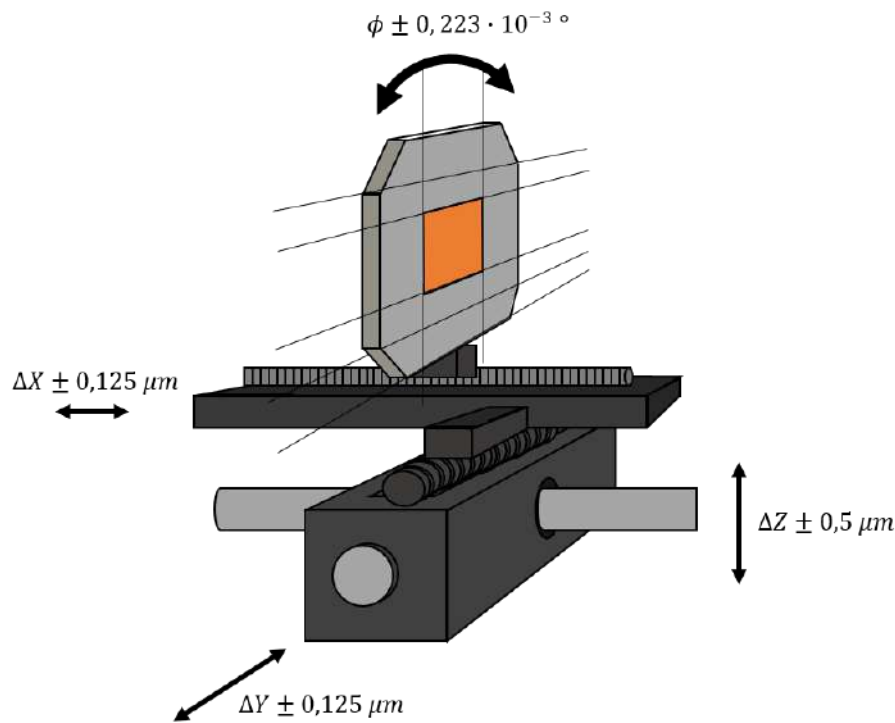


FIGURE 10.6: Diffractive mask degrees of freedom over x, y, z, ϕ which is the transversal angle over the x axis. The minimal step for each of the micromotors used in the movement of the diffractive mask device are also included.

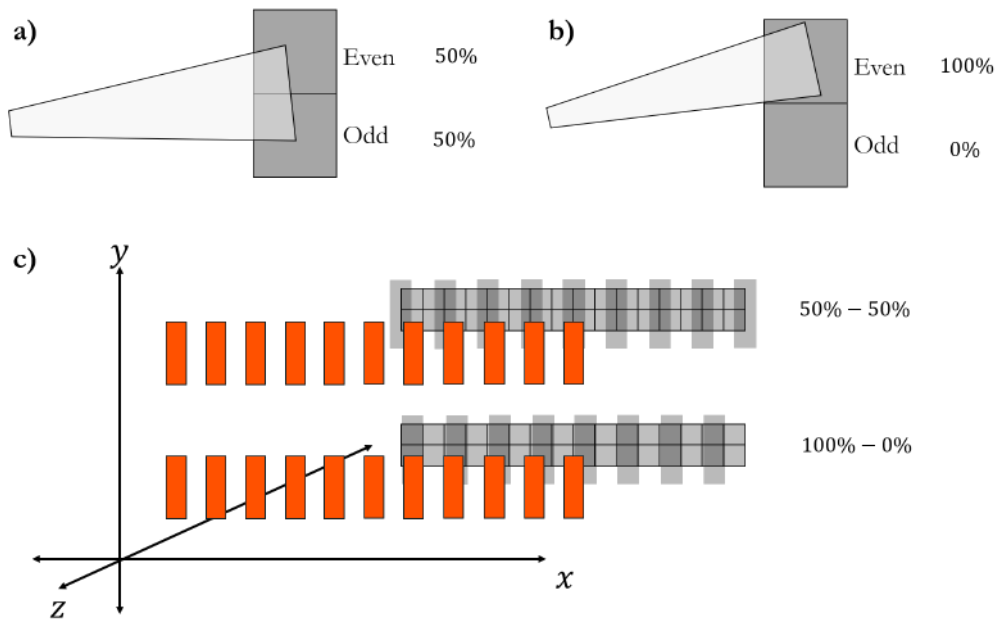


FIGURE 10.7: Perspective of a single beamlet for a) $\sim 50\% - 50\%$ illumination and b) $\sim 100\% - 0\%$ over odd and even pixels alike. The even and odd condition is taken over the scanning direction. In this case the x direction where each column of pixels is labelled as either odd or even. c) A different perspective of the illumination projection, where a set of odd and even columns is included for the $\sim 50\% - 50\%$ and $\sim 100\% - 0\%$ illumination alignments.

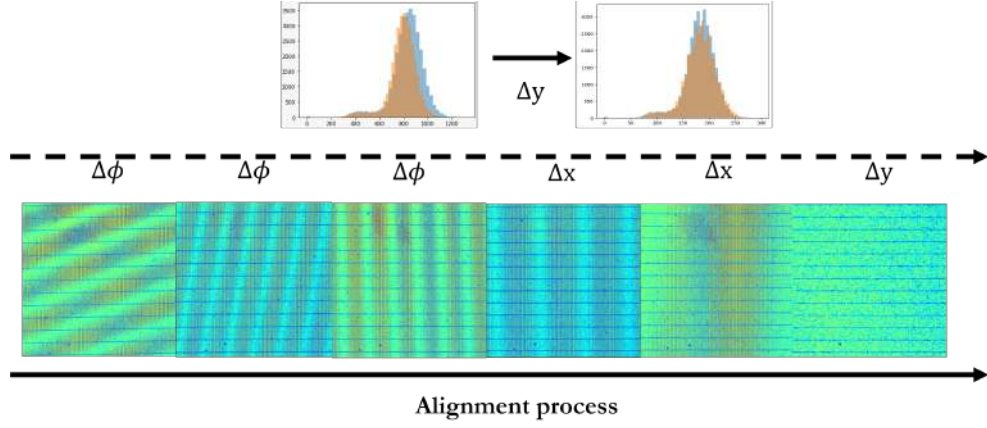


FIGURE 10.8: Alignment process for $\sim 50\% - 50\%$ and $\sim 100\% - 0\%$ configurations. The mask is moved in the coordinates shown in the arrow to change the Moiré interference pattern as seen in the flat-field images right below. Once axial alignment is done, an alignment on the x, y coordinates is performed where the histograms have the same area and same distribution to guarantee a homogeneous scan.

signal with better quality. Nonetheless, it is possible to retrieve each signal with either illumination setup. The alignment process works as a gradient descent with variable step size. The algorithmic process followed to get a fully aligned system is explained in figure 10.8, and the next chapter describes the computational preliminaries for a fully automated alignment system and the Moiré interferometric principles used for this purpose.

Similarly, the $\sim 100\% - 0\%$ case can be aligned with the same iterative processes but with an extra caveat, where the user wants to separate as much as possible the intensity histograms of odd and even pixels, hence odd pixels will have $\sim 100\%$ and even pixels will have $\sim 0\%$ total illumination. This process is assessed with a Python code that can extract the illumination intensities of odd and even pixels of a flat-field.

10.4 Medipix detector

Semiconductor materials are commonly used for radiation detection purposes because they require a small amount of energy to create an electron-hole pair, which is high enough to avoid the generation of thermally induced charge carriers that produce a continuous dark current. Using a solid medium for detection allows for compact designs and high detection efficiencies. Drift describes the movement of charge carriers in the semiconductor caused by an applied electric field. In semiconductor detectors, if drift is the only transport mechanism present, the charges generated in the semiconductor will travel to the collection electrodes following the field lines. However, the

effect of diffusion is to broaden the distribution of charges over time. The Medipix3 addresses the influence of diffusion in the pixel spectrum [93].

By the time of this work, the Medipix collaboration is reviewing the Medipix4 technology for medical spectroscopy applications and the Medipix3 is ready for licensing. The Medipix3RX is an amorphous silicon CdTe pixel readout chip designed to be connected to a segmented semiconductor sensor. Including semiconductor materials intends to address the effects of charge-sharing and beam-hardening artifacts. CdTe detectors also provide a detection efficiency of 100% for X-ray energies up to 60keV with a 1 mm thick sensor [94]. Its efficiency across an X-ray energy spectrum proves highly beneficial, especially considering that diagnostic X-ray imaging covers energy spectra ranging from approximately 10 keV to nearly 150 keV, varying based on tissue requirements.

The detector comprises a $300\mu\text{m}$ thick silicon pixel array sensor of 256×256 pixels bump-bonded to the photon counting Medipix3RX ASIC. Thanks to its high efficiency, CdTe material effectively shields the pixel electronics within the utilized spectrum, safeguarding them against radiation-induced damage over time. Yet, the predominant challenge associated with CdTe sensors currently lies in the complexities of producing high-quality material. Within the Medipix ASIC, the pulse created by the photon detection event is individually analyzed. The detector only records photons higher than a preset threshold, allowing it to sort photons into user-programmable energy bins. This feature is critical for spectral CT applications, where material separation is achieved by analyzing the energy information of transmitted photons. The Modulation Transfer Function (MTF) has been previously characterized under members of the Medipix Collaboration [95].

The Medipix3RX CdTe detector exhibits promising capabilities for high-quality, low-dose imaging, surpassing conventional flat panel mammography imaging technology. It demonstrates a notably sharp increase in CNR (Contrast-to-Noise Ratio) for low ESD (Exposure Setting Detector). The enhanced performance of the CdTe detector is attributed to several factors: a smaller pixel size, a highly efficient sensor material, and an improved data acquisition scheme, collectively contributing to its superior performance [96].

10.5 Detection mechanism, semiconductor detectors

Semiconductor sensor layers in semiconductor detectors, like the Medipix detector, work based on the principles of photoelectric effect which must happen for a photon

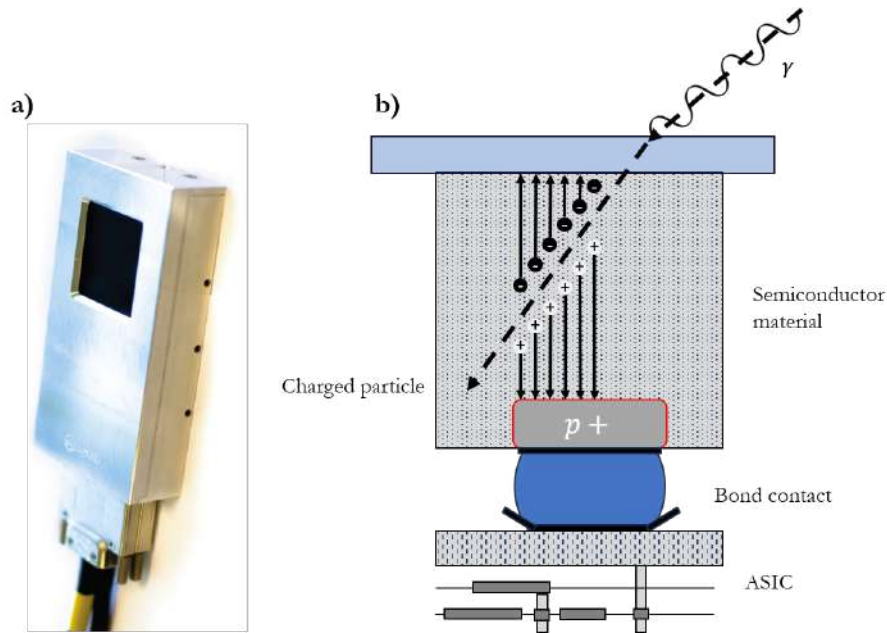


FIGURE 10.9: a) Medipix3RX detector [17] b) Different semiconductor materials can be bump-bonded to the ASIC to act as an x-ray detection layer. When a photon is detected, an electron/hole pair is created. The bias voltage applied across the sensor layer drifts one of the charge clouds to the ASIC end. Within the ASIC, the photon is individually analyzed and can be sorted into multiple energy bins.

to be detected in the material. Semiconductor detectors use materials like silicon (Si), germanium (Ge), cadmium telluride (CdTe), or gallium arsenide (GaAs). It's worth noting that materials with a band gap energy between conductors and insulators are sensitive to energy changes caused by incoming radiation. When a photon or any ionizing radiation with sufficient energy hits the semiconductor material, it can transfer enough energy to an electron in the valence band to overcome the band gap. This energy transfer elevates the electron to the conduction band, creating a free electron and a positively charged "hole" in the valence band. This process is known as the creation of electron-hole pairs.

The semiconductor detector is typically biased with an electric field. When an electron-hole pair is created by an incident photon, the electric field causes the electron to move toward the positively charged electrode and the hole toward the negatively charged electrode. This movement of charges creates a detectable current or a voltage pulse, proportional to the energy of the absorbed photon. The resulting electrical signal is typically very small and requires amplification. This is done using electronic components like field-effect transistors (FETs) which are often integrated into the detector. The amount of charge generated is directly proportional to the energy of the incident photon. This property allows semiconductor detectors not only to detect the presence of radiation but also to measure its energy. This energy resolution is one of the key advantages of semiconductor detectors [18].

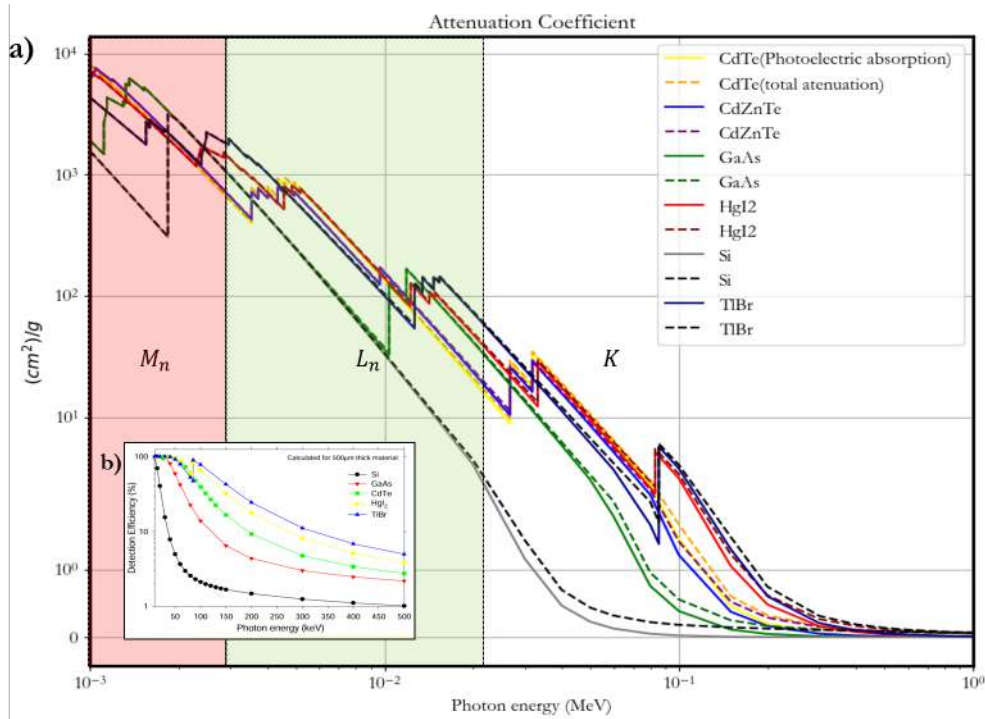


FIGURE 10.10: Set of materials used in semiconductor ceramic detectors for X-ray imaging, the M_n and L_n regimes are labeled. The energy ranges used during this work fall under the L_n region. The subplot represents the detection efficiency of photons by their given energy [18]

All this accounts for high energy resolution due to the relatively small energy required to create an electron-hole pair. Also, detectors can be made compact and portable due to this mechanism being at an atomic scale. Semiconductor detectors also directly convert the energy of the incident radiation into an electrical signal, unlike other detectors which may require a scintillation process. However, their performance can be affected by temperature, as temperature changes can affect the band gap and the mobility of charge carriers. In the case of the Medipix detector, this semiconductor sensor layer is crucial for its functionality in spectral imaging, as it allows for the direct conversion of X-ray photons into an electrical signal.

10.6 XPCI setups

The theoretical principles of phase contrast imaging explained in chapter 7 can be fully implemented in the laboratory. For this work, three main imaging systems will be reviewed as a qualitative comparison and to justify the use of Edge Illumination over other systems for potential use in medical imaging.

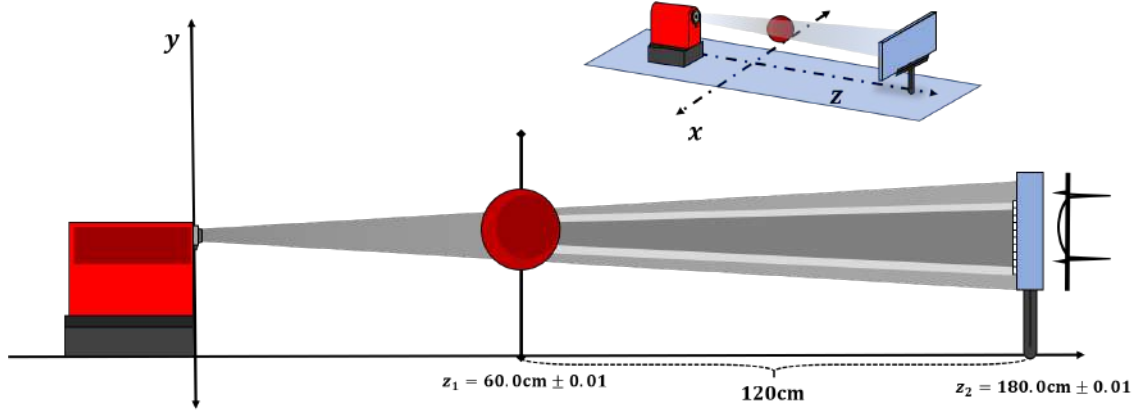


FIGURE 10.11: In-line configuration for phase contrast X-ray imaging. As seen during the first part of this document, it is crucial to maximize z_2 to amplify the phase effects on the imaging system.

10.6.1 Experimental Propagation-based Imaging

Propagation-based Imaging also known as in-line phase contrast imaging is a phase-sensitive non-interferometric technique that works under the deduction of the TIE over free space after the X-ray wave elements shift due to light-matter interactions. Figure 10.10 shows the experimental setup of in-line xPCI and distances z_1, z_2 used. Recall from chapter 12 that to measure the transverse phase gradient it is necessary to introduce the transverse intensity gradient $\nabla_{\perp} I$ by means of the TIE equation. Typically single-image methods such as in-line PCI or single-image grating interferometry are quicker and enable lower X-ray dose, while multi-image methods such as Edge Illumination and speckle-based XPCI can attain better spatial resolution. In this case, the intensity measured by the detector is given by the projected thickness of the transmission function where

$$I(x, y, z_1) = I_o \exp [-\mu T(x, y)] \quad (10.3)$$

The explicit form of the projected thickness can be solved by means of the paganin phase retrieval algorithm, where

$$T(x, y) = -\frac{1}{\mu} \log \left(\mathcal{F}^{-1} \left[\frac{\mathcal{F}(I(x, y, z + d) / I_o)}{1 + (\delta d / \mu)(k_x^2 + k_y^2)} \right] \right) \quad (10.4)$$

At first glance, this method seems practical due to the absence of the complex alignment step and the requirement to dither over the sample. However, some drawbacks can already be noted. For example, the phase retrieval dependency on a single δ, μ value when a multi-material sample, i.e. a biological sample, is present may result in a biased phase signal [97]. Multiple phase retrieval algorithms have been proposed

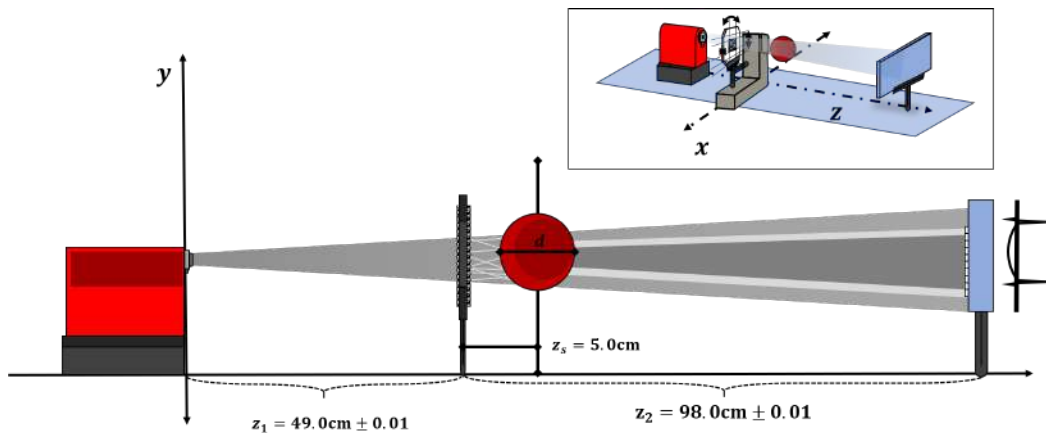


FIGURE 10.12: Speckle-based imaging setup. The grating must meet the condition that each speckle occupies at least 2 pixels on the magnified image, along with a total visibility of at least 20% this illustration includes the distances used in the study

to address this issue [98]. the high dependency on z_2 distance is also a drawback in implementing such a system on existing medical devices Chapter 13 discusses the dependency on this parameter for consistent phase retrieval.

10.6.2 Speckle-based Imaging

Speckle-based X-ray phase contrast imaging is a technique that utilizes X-ray speckles as markers to gather information about a sample. Speckle patterns are formed when partially coherent X-rays interact with randomly distributed scatterers. The size and visibility of these speckles depend on the scattering features and the size of the scatterers [99]. Speckle-based makes use of a diffuser, as an X-ray beam passes through a sample, it causes distortions in the wavefront, observable as modulations in the speckle pattern. These modulations can provide differential phase shift, transmission, and small-angle scattering information about the sample. This process involves analyzing changes in the speckle pattern's position, intensity, and visibility, leading to the reconstruction of the sample's refractive, absorptive, and scattering properties [100].

In this case, speckles are produced using abrasive paper to create random speckle patterns using a lab-based X-ray microfocus source, the speckle patterns arise due to interference of randomly scattered radiation when a partially coherent X-ray beam passes through the abrasive paper. Figure 13.27 shows the magnification used for the speckles to be visible and the moving process. Similar to the dithering process, the abrasive paper is moved in micromillimetrical steps to track these speckle patterns. This scan can be done in one dimension or two dimensions by moving the speckles in $\Delta x, \Delta y$. The distance between the diffuser and the sample intends to be minimal to

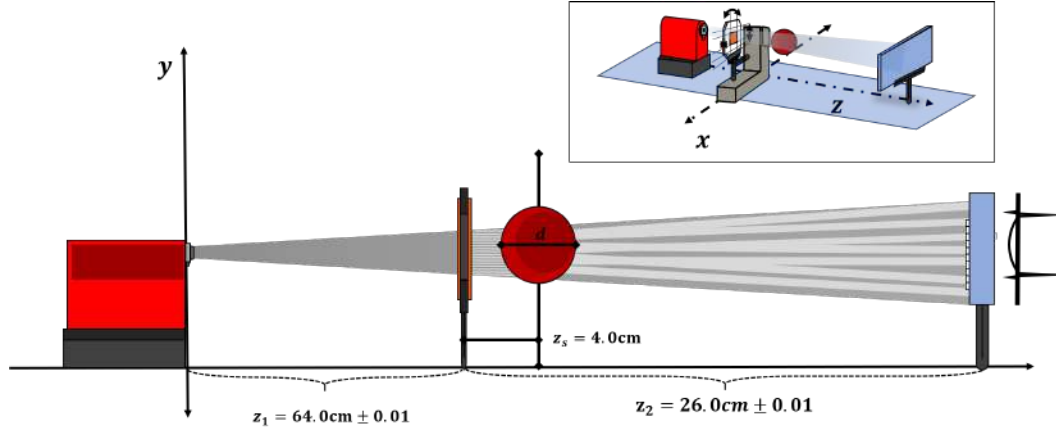


FIGURE 10.13: Edge illumination imaging setup.

avoid magnification effects.

$$\mathcal{V} = \frac{I_{spec}}{\sigma_{bg}} \quad (10.5)$$

A series of two images are taken following the same movement pattern, similar to a flat-field imaging process, first an image of only the abrasive paper is taken. Speckle visibility must be at least 20% for an effective phase retrieval process. Speckle visibility is calculated following the equation 10.5.

$$\mathcal{V} = \frac{I_B - I_O}{I_B} \quad (10.6)$$

After the set of images is obtained, each pair of images is input in the software MIST, which shows the differential phase in x, y directions, the dark field signal, and the Laplacian signal as shown in the results section.

10.6.3 Edge Illumination Imaging

Edge Illumination XPCI is the main technique studied in this work. As stated previously, edge illumination uses a diffracting mask that produces periodical beamlets that can be deflected by the sample (See section 10.2). Producing a positive or negative fringing measured regarding an initial illumination distribution (Section 10.3). Just like in speckle-based imaging, the distance between the diffraction mask and the sample intends to be minimal to avoid magnification effects. Figure 10.13 shows the specific distances of this setup.

For multimodal imaging under different alignments. This process follows the steps depicted in figure 13.12. Flat-field images are captured with ten times the exposure

time more than sample images, which guarantees a consistent correction for detector, mask and source artifacts, uneven illumination regions and

10.7 Imaging artifacts

Artifacts are unusual signals received by the detector which do not provide valuable information about diagnostic and evaluation processes. It is important to be able to identify and classify these artifacts for their treatment and correction, thus improving the quality of the images that are affected.

Beam Hardening occurs when lower energy photons are absorbed more than higher energy photons as the X-ray beam passes through an object. This results in a hardening of the beam spectrum and can lead to artifacts in the reconstructed image, such as streaks or false inhomogeneities. This artifact is more frequent on non-coherent polychromatic X-ray sources at low energy and in TlBr semiconductor detectors

Scatter Radiation is a major concern in medical imaging mainly for the emission of untraceable ionizing radiation dose that is deposited on the sample. This also may interfere with the direct X-ray beam, causing noise and reducing image contrast. This is particularly challenging in holography, where coherence and interference patterns are crucial. This is mostly reduced with X-ray collimation and EI systems that use a diffraction mask.

Motion Artifacts Are a major drawback especially in EI systems. The movement of the object during image acquisition can blur the interference patterns, leading to distorted images, time-resolving solutions for motion artifacts and lower exposure times are proposed in the results and remarks section. An example of motion artifacts can be seen in figure [10.14](#).

Heel Effect: The heel effect is an artifact produced in X-ray tubes emitted by the anode and is observed as variations of intensities on the detector. These variations are due to the direction of emission concerning the axis between the cathode and the anode, which are produced by the geometry of the anode. This is because there can be absorption of some photons by the anode or target itself as shown in figure [10.14](#), then the more anode material there is in the photon's path, the greater the probability that it will be absorbed.

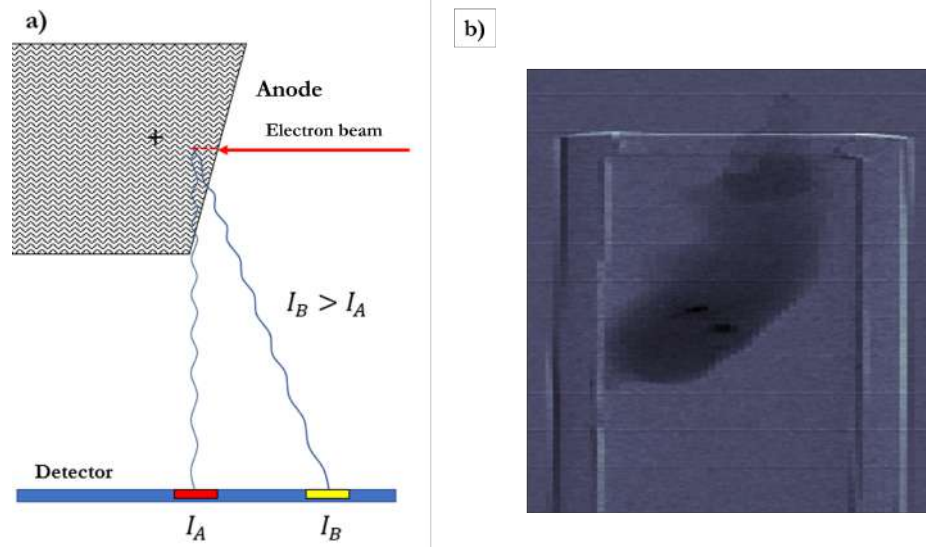


FIGURE 10.14: The Heel effect is an artifact that occurs due to the absorption of photons on the anode that produces them. **a)** The number of counts on the detector at I_A is less than the number of counts received at I_B because the photons on the I_A path are more likely to be absorbed on the anode, this also depends on the anode's absorption coefficient [101]. **b)** Motion detection artifact slightly moves the capilar of the original position.

Low Exposure: Low exposure manifests as a grainy and noisy signal image. This can be due to the exposure time being too low for the used energy range, so very few photons reach the detector, but it can also be due to the energy of the photons being too low and few managing to reach the detector. The opposite case of this artifact is image overexposure or saturation. In both cases, it is recommended to retake the shot with corrected time and energy parameters [102].

Ghosting is an artifact that may occur when a latent previous image can be observed on the new image because a previous exposure overlaps the new image. To correct this error, it is necessary to recalibrate the mammogram so that the memory of the previous shot is removed.

Horizontal Lines: This artifact is attributed to a defective pixel line or incorrect reading of data reaching the detector. It is important to recognize this artifact, as a portion of the diagnosis corresponding to the pixels of the artifact has to be removed. This artifact can also appear as an inclined line. Generally, this artifact represents direct damage to the detector [102].

Chapter 11

Computational framework and toolkit

The software component is crucial for a complete and consistent EIXPCI system. One of the primary needs is to optimize temporal resolution, image quality, and energy/-dose efficiency. System auto-align, Image pre-processing, phase retrieval algorithms, dithering reconstruction, image post-processing, and automatic detection of regions of interest are the main components of this software toolkit provisionally named *PyEdge*. This software component is primarily developed as a back-end Python environment focused on image lecture and processing. Most importantly, the phase retrieval algorithm is also fully implemented in this software, which is vital for the phase signal assessment and quality control for future results in this work. Ph.D. student Steven Cely kindly provided the first version of the phase retrieval algorithm. The flow diagram in figure [11.1](#) shows the algorithmic road for the software implementation and communication with the experimental system.

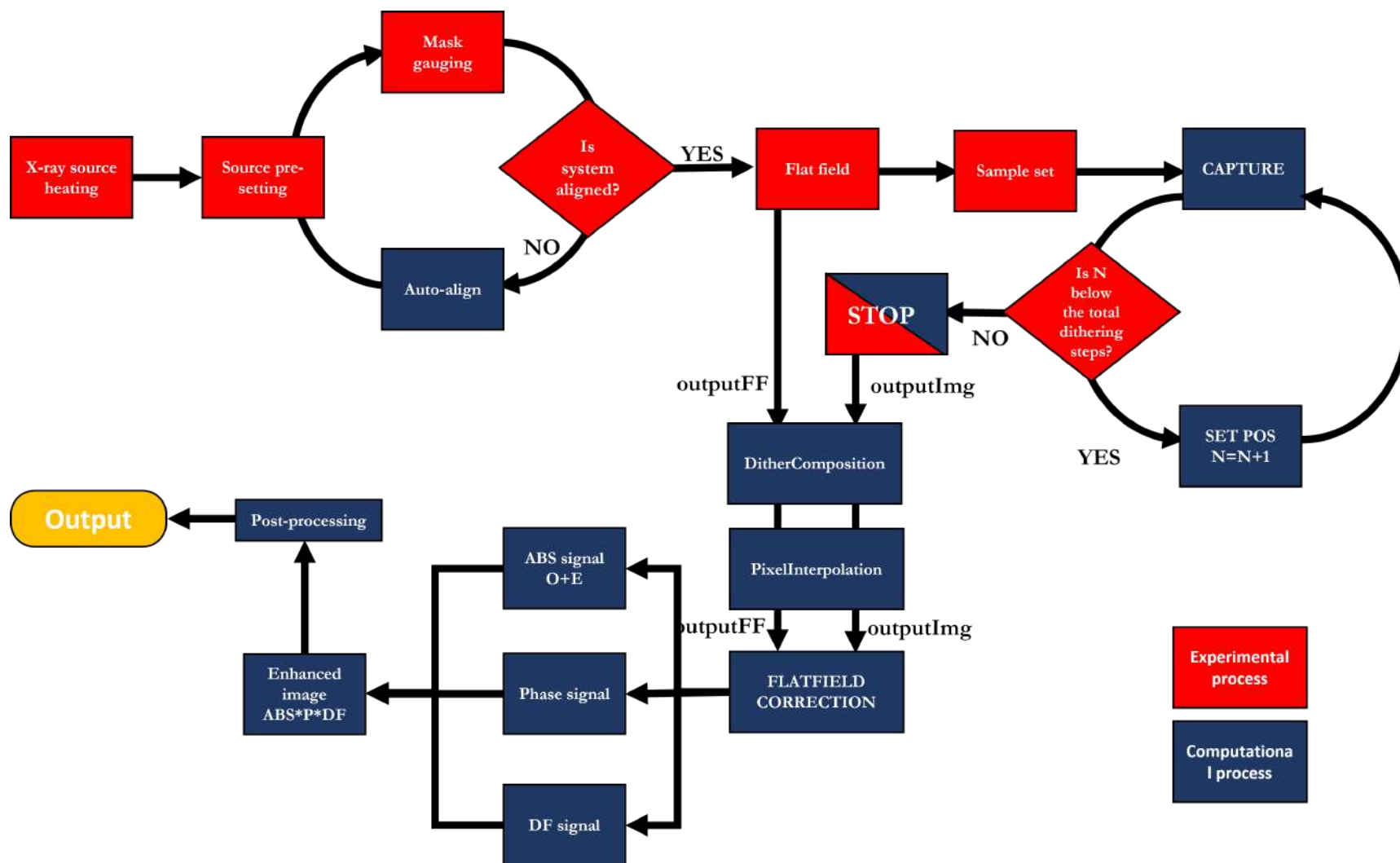


FIGURE 11.1: Flow diagram of the whole imaging process

All the processes shown in this section were implemented using Python version 3.11. The libraries can be checked on the GitHub project repository [103]. The computational essential processes done over the process of imaging, phase retrieval, and processing are as follows:

1. **AutoAlign:** An image of the flat-field illumination with the mask at the correct magnification is provided to the algorithm, Which contains the characteristic Moire fringes inherent in a misaligned setup. With the Moire fringe, the algorithm calculates the total steps on the $\Delta\phi$ and Δx direction to straighten the pattern and homogenize the illumination. Figure 11.3 shows this process in further detail.
2. **Imaging:** Imaging consists of two main parts. CAPTURE, where the detector reads and counts signal events, and SET POSITION, where the dithering scan moves the sample position to a fixed distance. This dithering movement must preserve the direction, and all steps must be of the same distance for a successful resolution amplification. Figure 11.4 shows this process in more detail.
3. **Dither Composition:** for each illumination scan done on the dithering imaging process, odd and even pixels must be concatenated in an imaging array, which is $(R_y/2 \cdot D_y) \times (R_x/2 \cdot D_x)$ where D_x, D_y are the total dithering steps on each direction. Recall that the masking process of odd and even pixels does affect the resolution to half of the original value; it is necessary to dither at least two steps in the mask direction to preserve the original resolution.
4. **Pixel interpolation:** Due to the detector panel imperfections that may lead to singularities on direct calculations of pixel values, it is necessary to perform interpolation on intensity values for dead pixels where the intensity is always zero or *hot* pixels where the intensity value is always the maximum saturation count value (For Medipix3RX this value is 4096)
5. **Flat-Field correction:** With the new image array of reconstructed dithers and corrected pixel values, a flat-field correction is performed. This flat-field correction is done to correct uneven source and detector effects on the final image that may lead to inhomogeneous illumination on the detector plane, optical artifacts, and residual mask signals and shadows.
6. **Phase retrieval and multi-modal signal production:** This part of the algorithm exploits the edge illumination system illumination of odd and even pixels to reconstruct the differential phase and the dark field signals by operations on both sets of pixels. Phase-sensitive methods rely on phase retrieval algorithms to

recover the output signals that may be illegible on raw conditions; an advantage of EIXPCI is mainly its multi-modal nature that allows multiple illumination configurations to recover numerous signals with a single take.

7. **Enhanced image production:** To make the system more intuitive and feasible to implement as a diagnostic technique, a final enhanced image operation is proposed; this enhanced image will contain the three modal signals in a single output, which is expected to be of better quality, have additional information of soft tissue and more sensitive to additional diagnostics.
8. **Post-processing:** This final phase consists of a set of algorithms and techniques that enhance the final image product; this phase is coupled with computer vision algorithms, contrast enhancement, and artificial intelligence to detect objects of interest and low contrast warning signals automatically.

The next sections will go more in-depth on each of the steps suggested here. Additional post-processing algorithms tested in this work may be found in the Appendix [B](#).

11.1 AutoAlign

Moire fringes are expected interference patterns formed due to the superposition of light by networks of lines. Such a pattern is created whenever a repetitive structure, such as a mesh, overlaps another structure. Single mask and double mask edge illumination systems, grating-based electron microscopy, and Talbot-Lau analyzer-based systems present such phenomena due to misalignment on the optical path, mainly amplified in systems that use diffractive masks or pattern-based optical elements. Single mask edge illumination Moire patterns are generated following the Fourier model.

$$E(x, y) = E_1(x, y)E_2(x, y) = \sum_{m=-\infty}^{+\infty} \sum_{n=-\infty}^{+\infty} a_n b_m \exp [i2\pi(mf_2 T_2(x, y) + nf_1 T_1(x, y))] \quad (11.1)$$

Where $a_n b_m$ are the Fourier amplitude of the mask and detector periodicity and T_1, T_2 are the transmission functions discussed in chapter 7. The two-mask edge illumination Moiré patterns work similarly, where the three Fourier series can be reduced into two by the relative shift between the total mask pattern and the detector. Suppose that the Moire pattern is solely generated in one dimension as expected in the laboratory setup (since the diffraction mask pattern is one-dimensional and so is the scanning

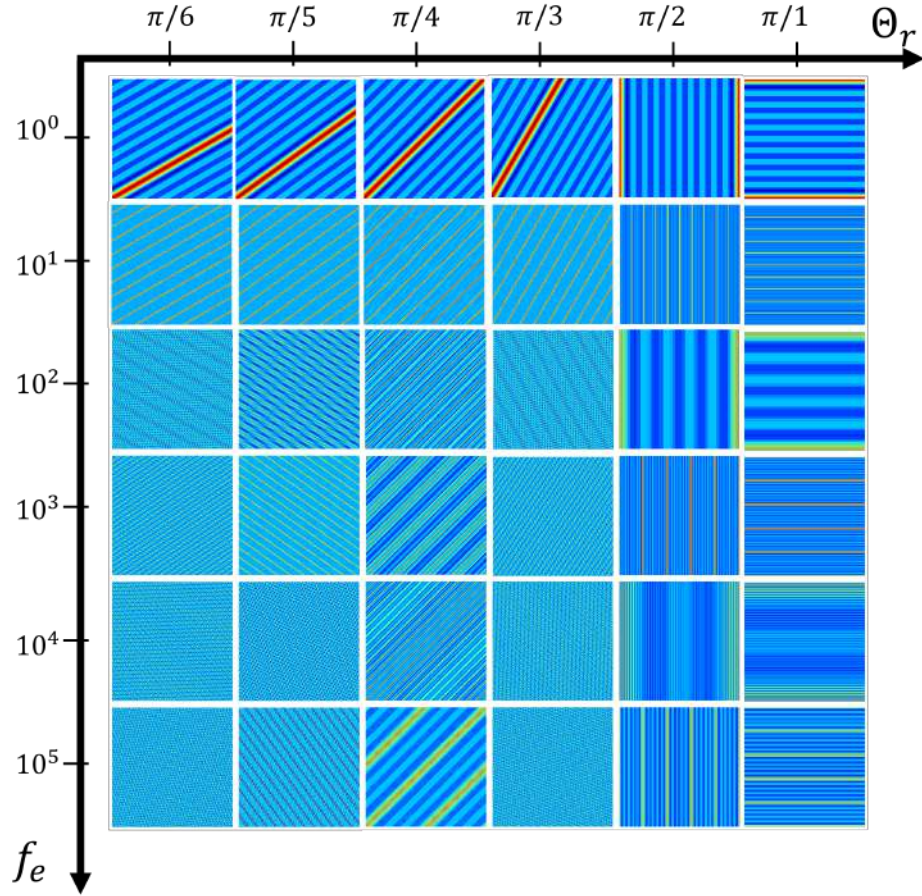


FIGURE 11.2: Simulated Moiré fringes using the Fourier series for Moiré patterns under different parameters of frequency (Which in our EI system may be translated on number of lines) and rotation angle of the pattern as seen on the y axis. These values for the Moiré parameters are used in equation 11.2 and numerically produced using Python.

movement). Then, this can be reduced to.

$$E(x, y) = \sum_{n=-\infty}^{+\infty} a_{nk_1} b_{nk_2} \exp [i2\pi n f_r (x \sin \theta_r - y \cos \theta_r)] \quad (11.2)$$

Where f_r is the joint frequency. Note how the equation $(x \sin \theta_r - y \cos \theta_r)$ is a line parameterization (which will be later resolved using the Hough transform in the next section). Figure 11.2 represents the real space representation of these Fourier series for different f_e and θ_r values. Considering the line parametrization, the reader might already notice how detecting the Moiré patterns can be reduced to detecting periodic lines, which in real space may be represented as lines with the same slope. Figure 11.3 shows this process. Although the direct movement of the mask is done by entering the step values manually, it can be done fully automatically if mask motors can communicate directly with the algorithm by following the sequential instructions in figure 11.4. These instructions have an algorithm that comprises the following functions.

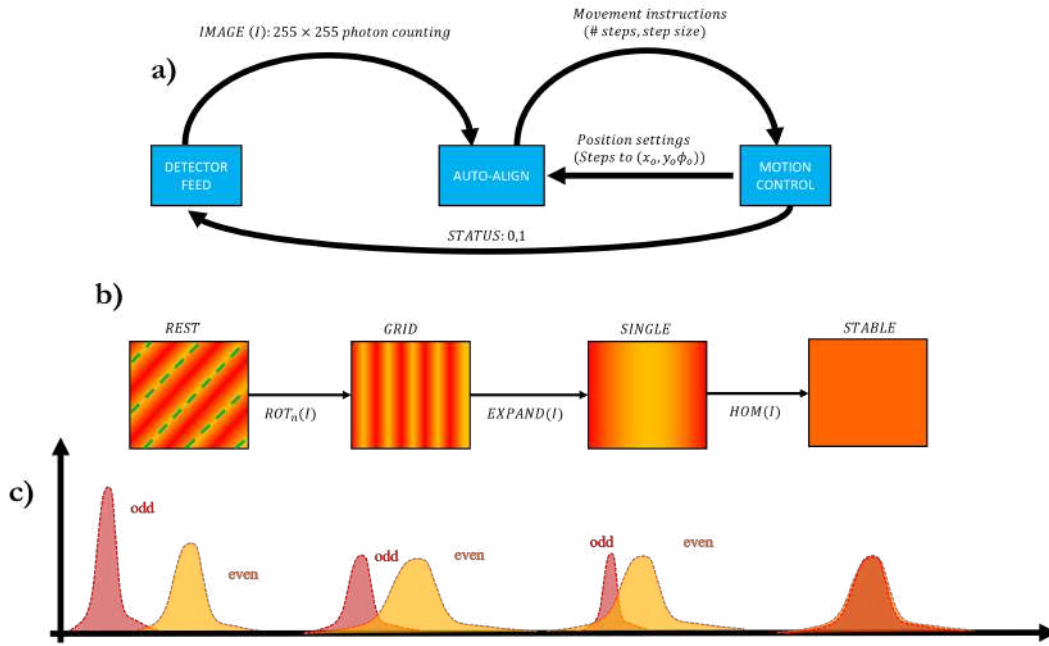


FIGURE 11.3: Iterative align process. a) shows the software communication and feedback of an iterative process whereby the Moiré patterns seen in the detector, the diffractive mask knows it's real-time position on the EI system. b) Process statuses that may be found, REST implies a 2 freedom coordinate movement while GRID uses just one which is Δx . Finally when the algorithm detects uneven illumination in SINGLE, moves only the Δy coordinate. c) Representative histogram evolution over this process.

1. $ROT_n(O) : REST \rightarrow GRID$ Where O is the image input array. Iteratively (until it reaches n threshold steps), the detector feeds a live image to the software. AUTO-ALIGN uses line Hough transform and canny ($\sigma \approx 6$) Edge detection to parametrize the lines. Depending on the $\Delta\phi$ parameter of the lines detected, AUTO-ALIGN feeds the rotation direction and steps (gradient descent) to the motor control system until it reaches GRID status.
2. $EXPAND_n(O) : GRID \rightarrow SINGLE$ Moves Δx parameter of the lines detected iteratively using the control system until AUTO-ALIGN detects a single line. AUTO-ALIGN feeds the motion direction on Δx and steps (gradient descent) to the motor control system until it reaches the single line condition.
3. $HOM_n(O) : SINGLE \rightarrow STABLE$ Moves Δy parameter of the lines detected iteratively using the control system, extracts the image histogram and AUTO-ALIGN checks the condition of whether the histogram mean value of odd and even pixels fits in between a tolerance value. When the system arrives at STABLE status, the system is aligned.

Similarly, the iterative process of dithering capture follows the algorithmic phases shown in figure 11.4.

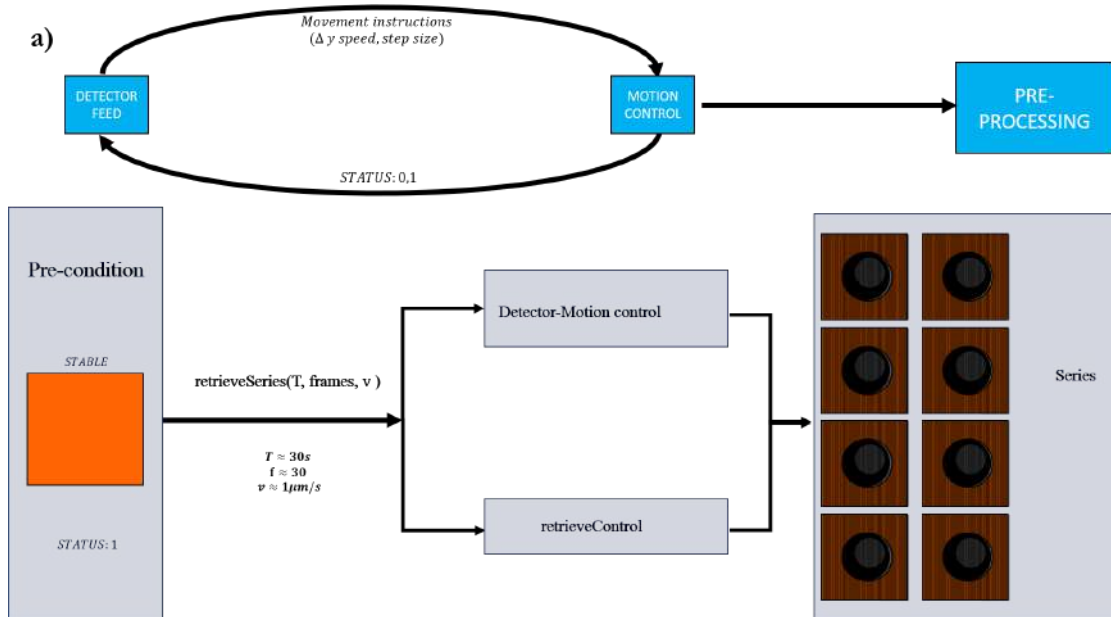


FIGURE 11.4: Recovers one frame per second, 30 frames of 1 second for a series, each series is captured at $10\mu m$ distance. Saves the detector array as a .txt file per frame, which are correctly labeled for later reconstruction. Integrates over the frame files for each dithering step (8 total) giving a total of 8 files one for each integration which corresponds to a whole series

11.2 Pre-processing

The pre-processing phase comprehends a set of algorithms that are crucial to the imaging process. These guarantee a minimal quality standard and do not directly affect statistical data. Images retrieved from all modalities are stored as .txt data grids of 256×256 dimension, where each value represents the photon counting on that position at the pixel grid.

11.2.1 Dead-pixel interpolation

The first step on preparing images for data analysis is to perform a dead-hot pixel correction, which interpolates the counting values that are on the low and high-end of the detector counting capabilities.

Hot Pixels are sensor pixels that appear significantly brighter than surrounding pixels. They are caused by electronic noise or defects in the detector. Conversely, dead pixels are detector pixels that do not respond to light or produce no signal. They appear as black or dark spots in the image. They are interpolated whenever the count value on the pixel reaches the saturation value count (4096) or registers no counts (0). In those cases, a new value is assigned by an interpolation of the average value of neighbor pixels.

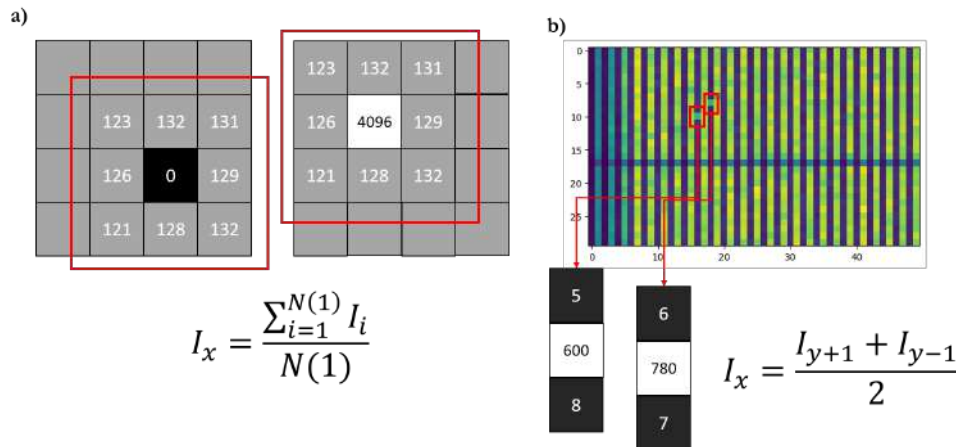


FIGURE 11.5: a) Dead-hot pixel interpolation for saturated and zero values, the interpolation is done over the first-like neighbors. b) Mask density interpolation. High values are replaced by the average intensity of the top and bottom pixels.

By correcting hot and dead pixels, this process reduces visual noise and artifacts in images. Correcting these pixels can lead to a more accurate representation of the samples especially when low-dimension objects have to be resolved. If hot and dead pixels are not corrected before performing flat field correction, these defects could be wrongly interpreted as variations in the detector's sensitivity. This would lead to inaccurate corrections and potentially introduce new artifacts into the image. As well as giving asymptotical values in the flat-field quotient [104].

An additional correction is done for 100% – 0% images for the mask values, this is due to photolithographic issues on the mask production, where some region do not present high attenuation, figure 11.5 shows this issue. The interpolation on these values is done only considering the vertical neighbors.

11.2.2 Flat-field correction

Flat-field correction is used to correct variations in sensitivity across the detector and for imperfections in the optical path. This ensures that each pixel accurately represents the intensity of the the X-rays it captures, unaffected by systemic biases and permanent objects in the imaging frame. In practice, flat-field correction involves capturing a reference image of a uniformly illuminated field. This image is used to identify variations in pixel sensitivity or other elements in the imaging frame, such as visible structures that are part of the diffraction mask in the case of Edge-Illumination. The flat-field image is then used to normalize subsequent images, effectively removing the systemic variations [105].

The exposure time for a flat-field image needs to be long enough to ensure that the image statistics are not dominated by noise. It should be similar to the exposure times used for the actual imaging to ensure the correction is accurate. Table 13.2 shows how the time exposure in this case is five times the total imaging time for each frame.

In X-ray imaging, like in medical diagnostics or material analysis, flat-field correction is vital for ensuring the uniformity and accuracy of the image. It is essential for correctly interpreting the X-ray images, as variations in detector sensitivity can lead to misinterpretation of the results. X-ray imaging often requires detecting very fine details, especially in medical diagnostics. Without flat-field correction, these details could be obscured or misrepresented due to variations in the imaging system.

Chapter 12

Poecilia Reticulata

This section aims to characterize a sample of guppy fish (*Poecilia reticulata*), focusing on its relevance for successful X-ray imaging studies. The guppy fish, particularly in its alevine stage measuring approximately 0.7 cm, presents an ideal biological sample for exploring the capabilities of phase contrast and dark field imaging techniques. These imaging methods are renowned for enhancing the visibility of soft tissues present in biological samples and fine structural details that are often challenging to capture using traditional radiography. The small size of the guppy fish is particularly advantageous for our laboratory setup, which features a compact detector with a size of just 1.4 cm. This alignment in scale allows for precise imaging and detailed analysis. Key regions of interest in the guppy fish are shown in figure [12.1](#) and might provide valuable insights due to their structural properties.

12.1 Generalities

The guppy is a small, live-bearing fish from the Poeciliidae family, originally from Trinidad and Tobago, Venezuela, and Guyana but globally spread out, primarily through intentional releases for mosquito control, aquarium trade and widely used as a model organism for studies in neurobiology and evolutionary biology [[106](#), [107](#)]. Guppies reproduce quickly, with females giving birth to up to 40 individuals every 4 to 6 weeks and reaching reproductive maturity in 3-4 months. Additionally, they are adaptable, thriving in diverse aquatic conditions and rapidly adjusting to new environments, food sources, and predators, making them ideal for controlled environments. However, their artificial introduction can negatively impact native ecosystems and species [[108](#)].

Guppies exhibit a high degree of genetic variation, particularly in traits like coloration and size. This diversity, coupled with their adaptability to various environmental conditions, makes them an excellent subject for studying evolutionary processes, sexual selection, and adaptation. As live-bearing fish with short gestation periods and the ability to produce multiple broods, guppies offer a rapid turnover for generational studies. Guppies are small, easy to maintain in laboratory settings, and can thrive in controlled conditions. This makes them a practical choice for long-term and controlled experiments.

Guppies are specifically chosen for this study due to several advantages that can be benefited from. Young guppies are small and relatively transparent, especially in their alevin stage. This makes them ideal for imaging techniques that require penetration of tissues with minimal obstruction and comparative anatomy studies in different imaging systems [108]. Specific anatomical features of guppies, such as the spine, otoliths, and other skeletal structures, are of interest in X-ray imaging as a reference. These features can be effectively studied using phase contrast and dark field imaging, which enhance the visibility of soft tissues and fine structural details. Image 12.1 shows which parts of the Guppy fish are aimed to be studied.

As technical advantages, the small size of the guppies aligns well with the technical limitations of the detector with a small field of view. This compatibility ensures high-resolution images and detailed analysis of anatomical and physiological features.

12.2 Guppy fish anatomy

Image 12.1 shows a general view of the sample used for this study. This individual has a sagittal length of $0.67\text{cm} \pm 0.01$ and a transversal width of approximately 0.17cm for the widest section. The transversal width of the fish will also be a determinant of whether X-rays are attenuated, deflected, or scattered.

12.2.1 Otoliths

Otoliths, also known as ear stones, are small calcified structures found in the inner ears of fish, including guppies. They play a crucial role in the fish's ability to sense gravity and acceleration, as well as in hearing and detecting mechanical waves in water [109]. The primary component of otoliths is calcium carbonate (CaCO_3), which is present in two crystalline forms: aragonite and vaterite. Aragonite is the most common form found in otoliths [110].

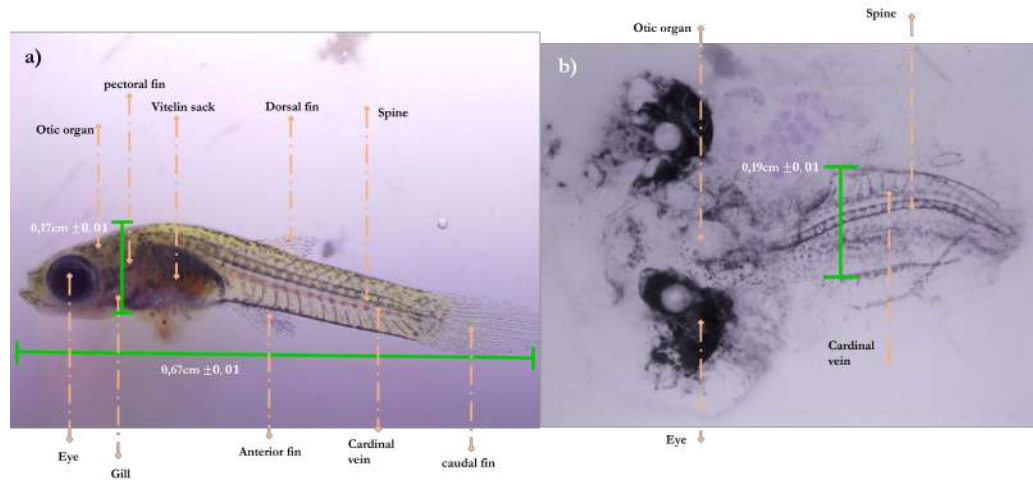


FIGURE 12.1: a) Lateral view of a *Poecilia Reticulata* alevine fish with its respective parts. PhD. Zayra Garavito kindly helped with the identification of visible anatomy as well as the estimation of age of the fish (2 weeks). b) Superior view of the fish after X-ray radiation. Otoliths located in the Otic organ are visible but have low contrast due to their distinctive white color

Due to their high calcium content, otoliths typically appear as bright, distinct structures in X-ray imaging. The density and crystalline nature of the calcium carbonate make them readily distinguishable from the surrounding softer tissues [111]. In phase contrast and dark field imaging, otoliths may be imaged with even greater clarity. Phase contrast imaging may enhance the edges and boundaries of structures, making the otoliths' shapes more distinct. Figure 12.2 shows the relationship between the photon energy and the light-matter interaction process associated with β and δ .

12.2.2 Nasal sacs

Nasal sacs are specialized structures responsible for the sense of smell. They play a crucial role in various behaviors, including locating food, detecting predators, navigating, and recognizing mating cues. Fish have one or two pairs of nostrils (nares) on their heads, leading to the nasal sacs. These structures have bone-like structures composed mainly of Hydroxyapatite and are developed at early stages

12.2.3 Fins

Regarding visibility under X-ray imaging, the bony or cartilaginous structures (like fin rays and lepidotrichia) are more readily visible due to their higher density. The fin membrane, muscles, and connective tissues are less dense and appear less prominently on standard X-ray images. The main component present in fin structures is collagen, which has a low attenuation under X-ray imaging.

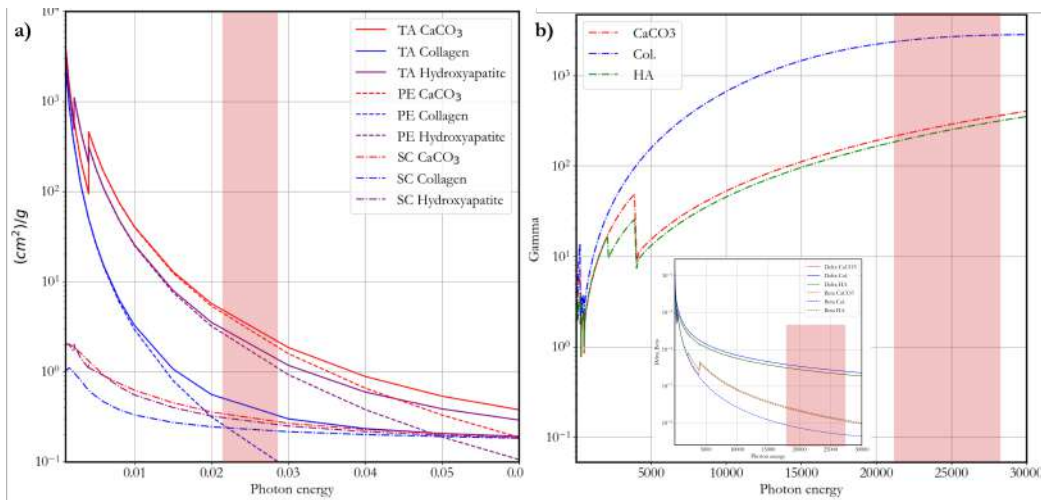


FIGURE 12.2: a) Total contribution of the attenuation coefficient given by the three main materials found on the fish' anatomy composition which include CaCO₃, Collagen and Hydroxyapatite. Each value labelled is either TA (Total Attenuation), PE (Photoelectric Effect) or SC (Scattering). The red zone represents the range of energies used during the imaging process. b) Gamma value calculated using CaCO₃, Collagen and Hydroxyapatite δ, β values found in the subplot [19].

12.2.4 Spine

The spine is composed of numerous small vertebrae. These vertebrae are structured to allow a significant range of motion, contributing to the overall flexibility of the spine. Guppy fish have a highly flexible spine, which aids in their swift and agile movements in the water. This flexibility is crucial for their swimming patterns and for evading predators. The guppy's spine, like that of many fish, is adapted for life in water. Its structure supports efficient locomotion in a three-dimensional aquatic environment. In the early stages of development, the spine undergoes rapid growth and changes, which are crucial for the survival of the fish in its juvenile stages.

12.3 Experimental specifications

In this research, the utilized samples comprised guppy alevins (*Poecilia reticulata*) that were fixed at 13 days post-fertilization, aligning with standard ethical practices in animal research. Sedation prior to fixation was achieved using tricaine (MS-222), a commonly used anesthetic in aquatic research, ensuring minimal stress and discomfort to the subjects. These guppy specimens were originally part of a different project, for which animal use was already approved through an ethical review process. This ensures compliance with regulations on the reuse of animal material in scientific studies, emphasizing responsible and ethical research practices. Post-fixation, the fishes

were preserved at a low temperature in an LV (low-viscosity) solution for 3 hours before their use in the study. This preservation method is designed to maintain the integrity of the tissues and is critical for the quality of the subsequent analyses. The total number of alevins used for the data acquisition is 2 and the date of the fixation is the 25th of October of 2023.

Later sample imaging was done using an Optika SLX-2 stereoscope that uses an OPTIKA C-B10 camera. The camera is equipped with a 1/2.3" APTINA CMOS sensor, providing a resolution of 3584x2748 pixels, and offers a color depth of 1, 4, 8, 24 bits. The device has a high signal-to-noise ratio of 34 dB and a dynamic range of 65.2 dB. It includes a long-life LED illumination system with over 20 years of usage and is capable of cordless operation. Images taken at [12.1](#) were taken using 4.5X magnification.

Part IV

Results and Remarks

Chapter 13

Results and discussion

This chapter discusses in detail the results obtained for the exploration of a multi-modal X-ray imaging system as described in the previous part. First, the Moiré pattern characterization algorithm is tested for multiple misalignment patterns at specific distances for the general setup. Later, the absorption, phase contrast, and dark field signals are effectively recovered using the proposed imaging system for a *Poecilia reticulata* ex-vivo specimen for the two illumination modalities (50%-50% and 0%-100%). Using a segmentation algorithm over structures visible on all images, the CNR figure of merit is calculated to study the behavior of multi-modal signals concerning absorption imaging techniques. Additionally, speckle-based phase contrast imaging is done for the same specimen for qualitative study. Using the software MIST, it is possible to retrieve phase, dark-field, and Laplacian signals.

13.1 In-line feasibility: conditions over the Fresnel number

In-line illumination images were produced using the setup distances shown in section 10.6.1. However, the distance between the sample and the detector is changed to calculate the Contrast-to-noise ratio (CNR) as well as the Signal-to-noise ratio (SNR) while the Fresnel number varies. This was done by using the PEPI simulation software based on Geant4 [112]. By varying z_2 and fixing the distance between the source and detector at $z_{sd} = 1m$, the magnification of the object also changes, producing the images seen in figure 13.1. The sample used to measure phase effects is a PMMA rod with a diameter of 0.5mm. The source and detector simulate the laboratory environment and conditions. Hence, the source is set at a kVp of 28kV with a Tungsten anode, an angle aperture of 0.02rad, and a focal spot of $10\mu m$, the energy spectrum of the source is exported from the TASMICS dataset with an air kerma (kinetic energy released per

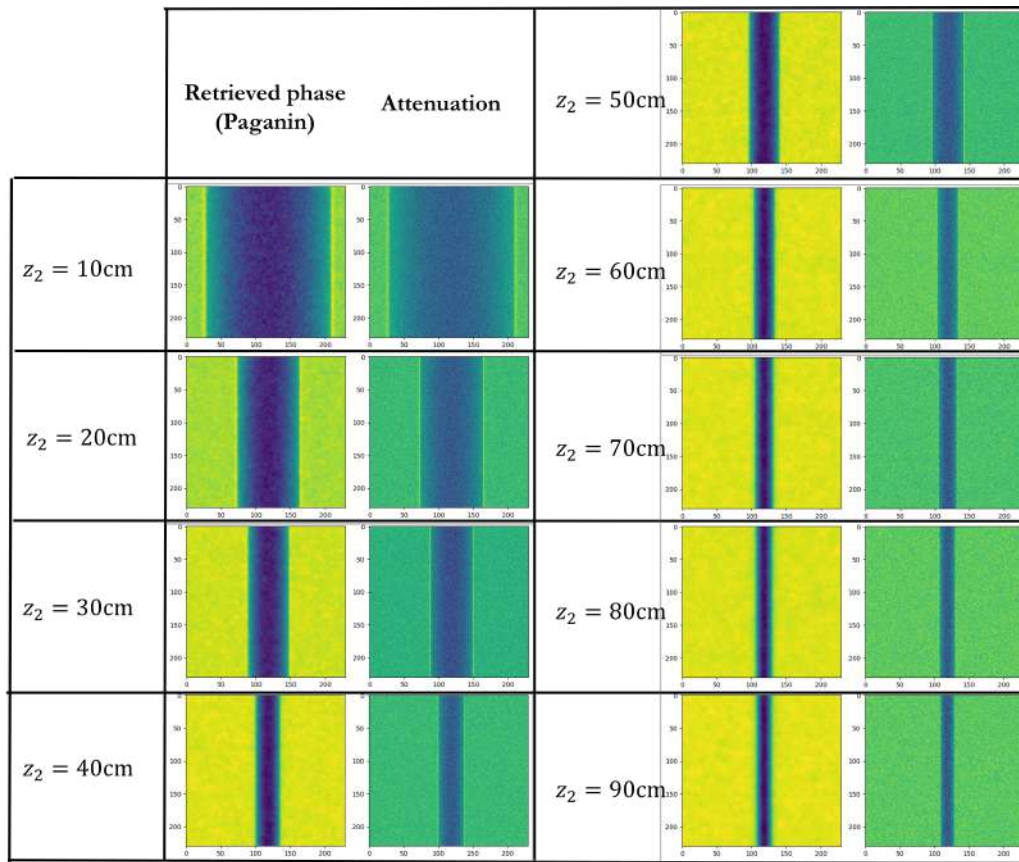


FIGURE 13.1: Simulated images for a 0.5mm width PMMA rod at different distances L from the sample and constant source-detector distance of 1m. $z_2 = 1m - L$. At the left the retrieved phase contrast image can be found, the differential phase signal is extracted using the paganin algorithm explored in chapter 8. At the right, the attenuation image directly retrieved from the simulation with no processing can be found.

unit mass) of 1 Gy. Each simulation has a total of 1×10^9 events, giving enough statistics for noise redundancy. Profiles are then extracted using the column image average values, figure 13.2 shows the normalized intensity profile plots for each imaging distance. Then, the phase signal is extracted using the Paganin algorithm. Which results in the set of images shown in figure 13.1 a) with the profile plots at 13.3

Finally, the images' gradient is calculated to automatically segment the edges by thresholding over the absorption and absolute phase images (See figure 13.4 and 13.5). This automatic thresholding is successfully implemented for the full set of images, but the thresholding range is more lenient in the phase signal profile. Mainly due to the edge enhancing of sample deflection of X-rays which is measured in phase contrast (See figure 13.5). The next section will describe the expected and observed effects due to phase contrast imaging on the cylindrical geometry of the PMMA capillars

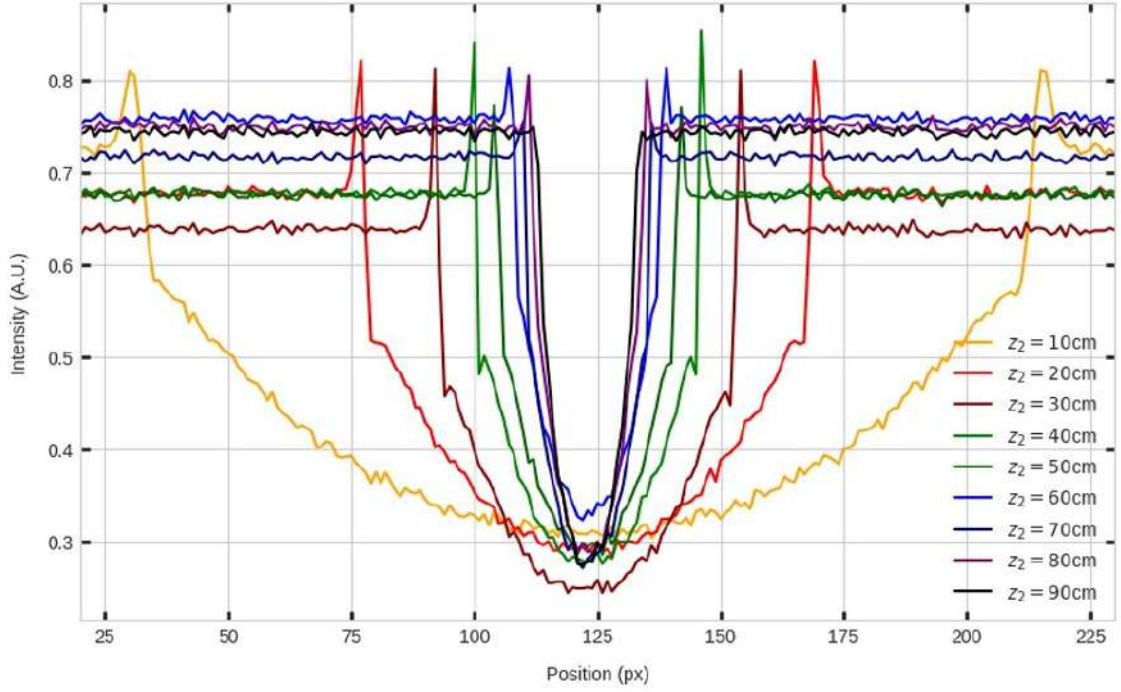


FIGURE 13.2: normalized profile intensity for each raw attenuation image simulation. Each line represents the PMMA rod at a different position in the simulation. Edges on the attenuation image retrieved by the profile plot are sharp. This is mainly due to the effect that propagation-based imaging attenuation image provides also a convoluted phase signal which contributes to the total intensity in the edges and is maximum on places where the structure gradient is also maximum by the TIE equation.

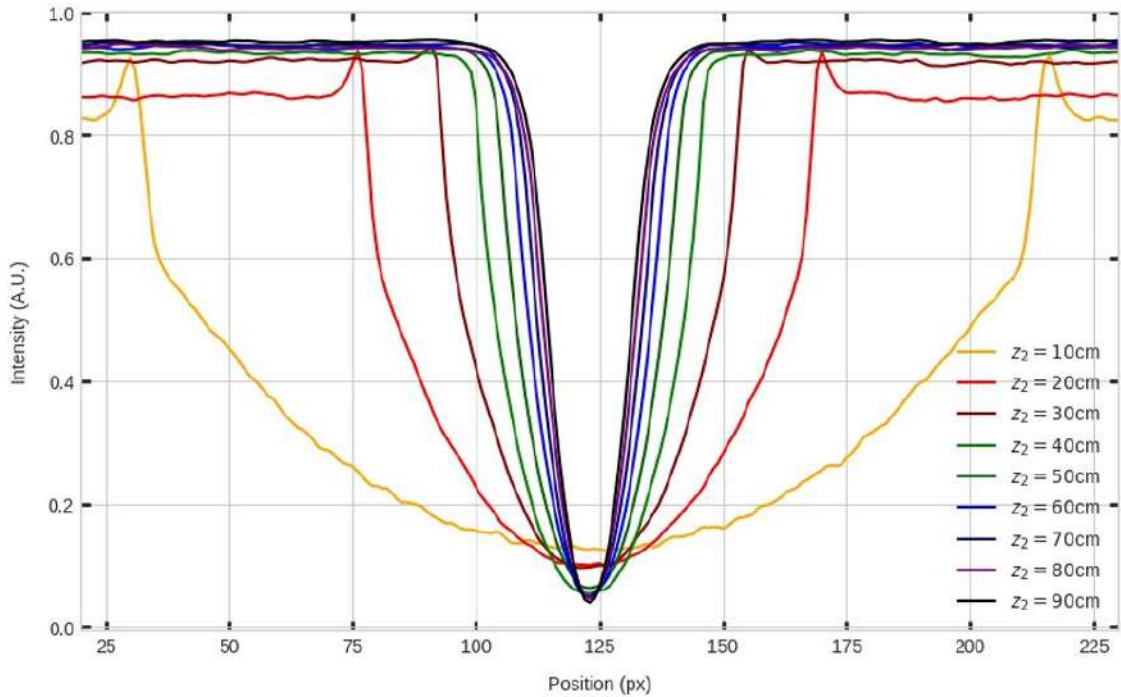


FIGURE 13.3: normalized profile intensity for each processed phase retrieval image simulation. Each line represents the PMMA rod at a different position in the simulation. Edges on the attenuation image retrieved by the profile plot are smooth mainly due to ignoring the contribution of the attenuation signal.

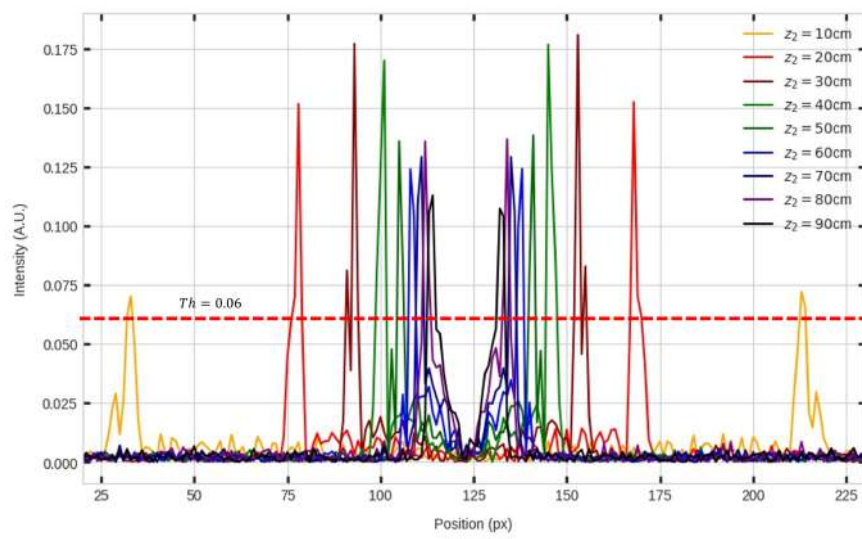


FIGURE 13.4: Profile plot of the gradient for the attenuation images. As expected, the gradient is maximum on the edges and some of the edges present two peaks. The threshold for the automatic segmentation of background noise and signal is chosen to be $Th = 0.06$ on the gradient values.

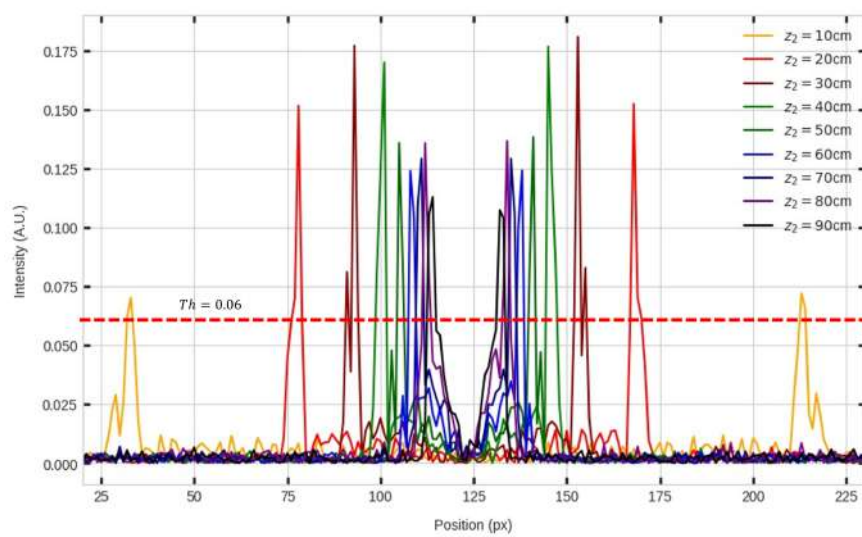


FIGURE 13.5: Profile plot of the gradient for the phase images after phase retrieval algorithm is processed. The gradient is again maximum on the edges and some of the edges present two peaks. The threshold for the automatic segmentation of background noise and signal is chosen to be $Th = 0.06$ on the gradient values. Although the same value was chosen, it is clear that this gradient is more decidable on the edge sections than the gradients seen at figure 13.4.

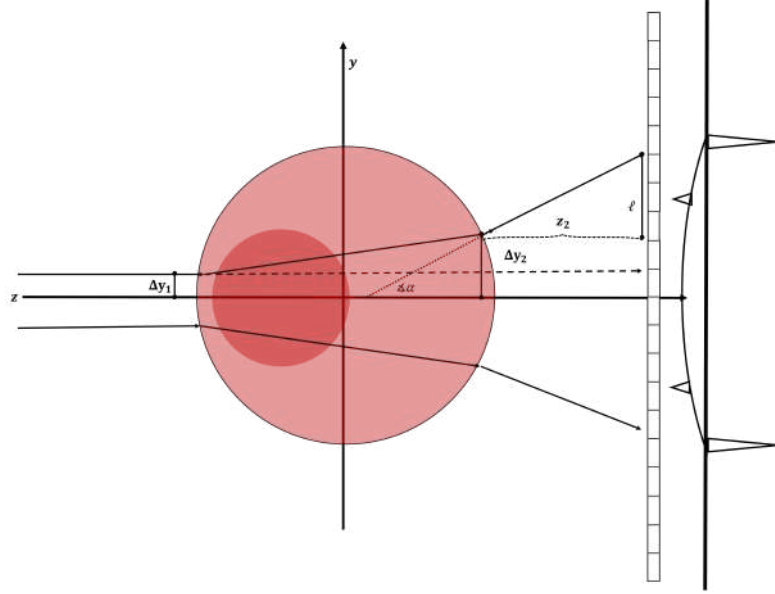


FIGURE 13.6: Ray-tracing geometry of the trajectory of a photon that crosses a cylindrical geometry unabsorbed. Two processes of refraction can be seen due to the entering and exit of the curved geometry. This is expressed as a major concentration of intensity in the edges of this geometry, which is an effect seen in the simulations.

13.1.1 Cylindrical effect of phase contrast imaging

The particular case of Cylindrical geometry angle refraction amplifies phase contrast signal due to rapid variations in the boundary of an object, recall from the Transport of Intensity Equation that the projected intensity signal of the object will be given by the spatial derivative of the phase and the signal attenuation (Equation 4.201). Applying this equation to the interaction of a cylindrical geometry with the X-ray trajectories results in the following.

$$\Delta\alpha \approx \frac{1}{k} |\nabla_{x,y}\phi| = \frac{1}{k} |\nabla_{x,y}\phi \left(2(\delta) + \int_{z_2} \beta dz \right)| \quad (13.1)$$

Assuming $\delta \gg \beta$ we may ignore the attenuation effects. Hence the angular deviation is given by

$$\Delta\alpha \approx \frac{1}{k} |\nabla_{x,y}\phi (2\delta(k))| \quad (13.2)$$

Where the phase for an incident wave to a cylindrical object is given by

$$\nabla_{x,y}\phi = 2k\delta(k)\nabla_{\perp} 2\sqrt{R^2 - x^2 - y^2} \quad (13.3)$$

Resulting in

$$\Delta\alpha \approx 2\delta(k) \frac{\sqrt{x^2 + y^2}}{\sqrt{R^2 - x^2 - y^2}} \quad (13.4)$$

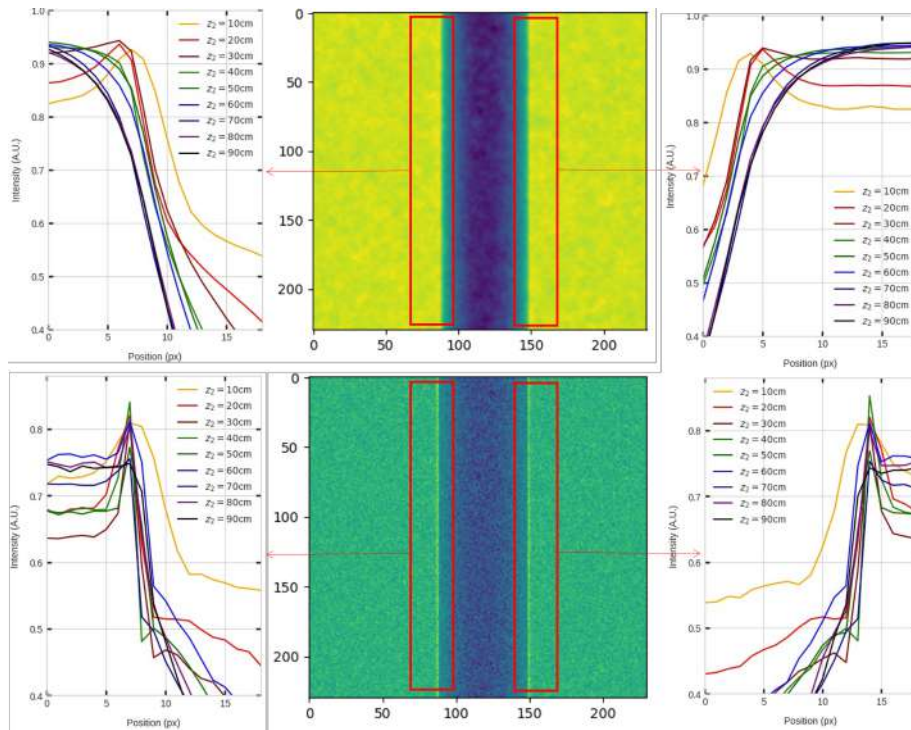


FIGURE 13.7: Edge-specific figure of the aligned profiles over the edge. Note how when the Fresnel condition that depends on L and inversely on z_2 is reduced, the sensitivity over the edge regions is lost and the profile adapts a curved nature on this region, hence implying a resolution loss on low Fresnel number conditions as predicted on the phase contrast theory of this work.

Note the asymptotical behavior whenever the coordinates are on the edge of the transverse area of the cylinder ($x^2 + y^2 = R^2$) which explains the natural amplification of phase contrast on edges even when δ is not significantly higher than β . Figure 13.6 shows this case. The intensity of course is not asymptotical on the edges due to the sampling limitations and the discrete nature of photon counting. Recalling the TIE equation, it is clear that the total intensity that the detector receives comprehends both differential phase contrast (sharp edges) and attenuation signal without the necessity of retrieving the phase signal. Figure 13.7 shows the specific regions where the cylindrical geometry amplifies the effects of phase.

The Full-Width Half-Minimum of the profile distribution can resolve the rod width as the deconvolution of the object with the source's point-spread function (PSF). The resolution in the in-line approach is mainly determined by the source's focal spot and pixel size. A measure of the estimate FWHM that varies over the distance z_2 is shown in figure 13.8. Giving a precise measure of the mean and variance of the segmented regions by using the thresholded regions shown in the gradient graphs allows the calculation of the SNR and CNR for each image at different distances z_2 . The results of the CNR and SNR vs. distance are shown in figure 13.9.

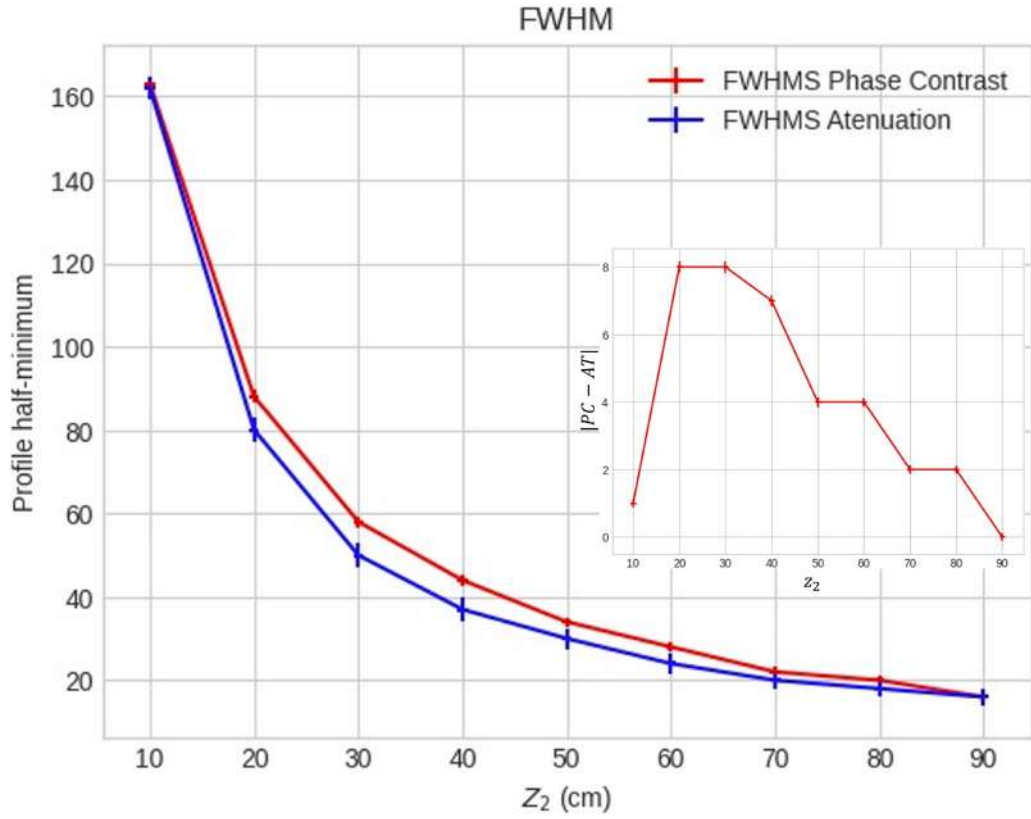


FIGURE 13.8: Calculated FWHM of the intensity profile given both measured widths. The sub-plot represents the discrepancy of the FWHMS calculated using the different signals.

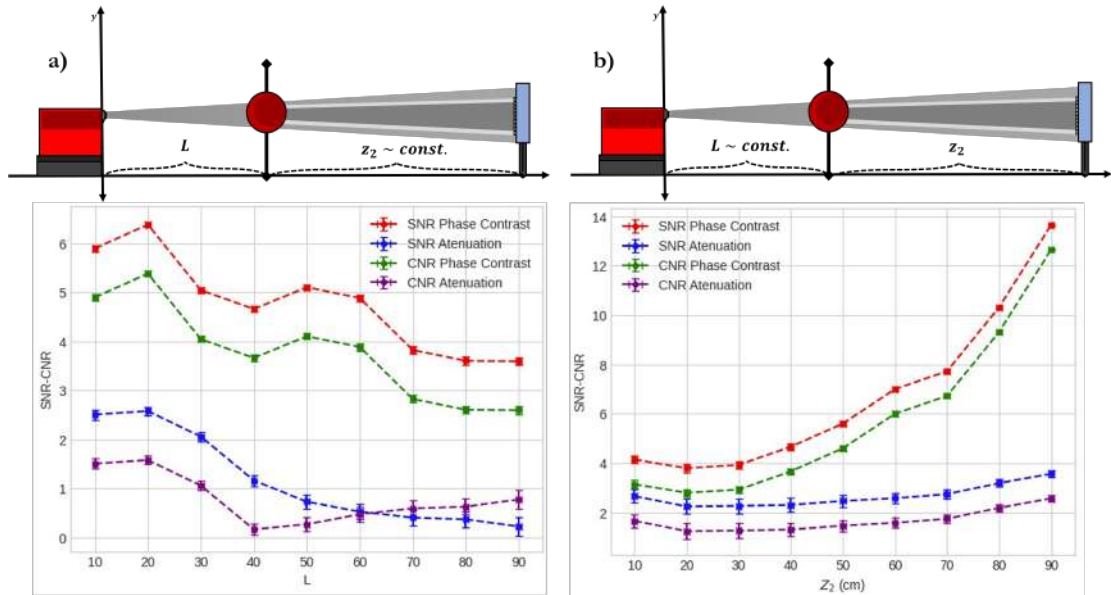


FIGURE 13.9: Contrast-to-Noise ratio and Signal-to-Noise ratio of phase contrast and attenuation images over the reference frame of a) z_2 while the distance between the object and the source varies (Hence a variation of the magnification) b) reference frame of L where the z_2 value increases and magnification remains constant, hence increasing the Fresnel number.

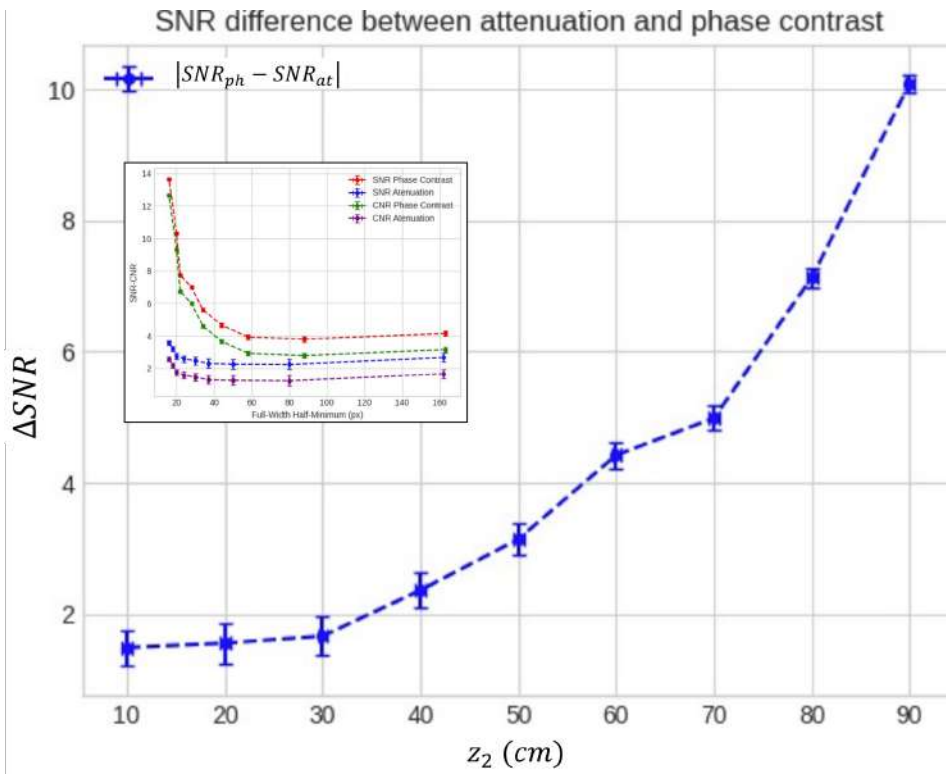


FIGURE 13.10: Signal-to-noise ratio difference between both techniques. As z_2 increases, the difference between the SNRs also increases as a direct consequence of graph 13.9 where attenuation remains constant while phase contrast increases.

CNR and SNR vs. distance in phase contrast and attenuation have drastically different behavior as represented in figure 13.9. While for attenuation both figures of merit remain almost constant, in phase contrast this number radically changes, phase contrast CNR and SNR are always higher than attenuation CNR and SNR. this inflection point is more evident in the difference subplot. Note how the SNR,CNR of the phase contrast in this case rapidly increase while the attenuation remains almost constant. This is a direct consequence of the application of the TIE principle where the wave-field element has more room to propagate over space After this point, z_2 distances will enhance phase contrast even further, which directly translates to increasing the Fresnel number of the system. This is already a major drawback, since as we may see in figure 13.9 a), using phase contrast by an in-line setup is advantageous only after this Fresnel number limit is broken. Smaller diffraction such as microcalcifications, fibers, and veins may show phase contrast effects at even further distances. Henceforth, since medical systems usually use a small aperture field to avoid residual radiation and unnecessary magnification effects, propagation-based phase contrast imaging is not suitable especially for fixed-setup systems such as mammographs and full-body CT scanners. This result aligns with the expected findings in literature [113] on the characterization of in-line propagation-based phase contrast imaging, where the propagation distance

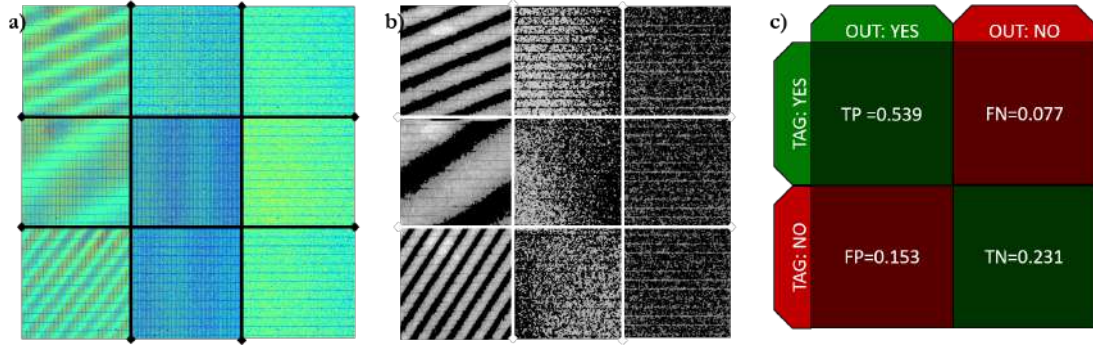


FIGURE 13.11: a) Moiré pattern flat-fields provided to the algorithm for characterization, each column represents a case where the algorithm is whether decidable and can characterize the pattern (left), undecidable and cannot classify the flat-field as aligned or misaligned (centre), and when the algorithm can decide that the flat-field is aligned (right). b) processed images of the Moiré patterns seen in a), these are the images that are submitted to the binary k-means segmentation. c) Confusion matrix of the total cases where the algorithm could successfully classify the flat-field. This algorithm was tested with a total of 26 flat-fields acquired during this work.

that the diffracted wave travels will increasingly improve the SNR and CNR of the differential phase signal. This has a clear relation with the transport of intensity equation where the gradient of the phase signal has a multiplicative factor that depends on the distance of the object to the detector. While propagation-based techniques may be useful especially for micro-resolution applications, the effect on the magnification on the field-of-view may not be suitable for general medical applications such as mammography and computed tomography which is the focus of this work. We dwell on other techniques that may be more consistent for medical applications over the later part of this section.

13.2 Moiré pattern recognition and processing

By using the algorithm introduced in section 11.1. It is possible to automatically identify Moiré interference patterns in the imaging system. This was done for a set of misaligned images. The parameters translated to goniometer distance in full-step modality.

Unlike direct Fourier treatment, this algorithm is consistent even when the number of fringes $M_T < 3$. Using the distances shown at figure 10.13, the system is fully aligned for the two illumination modalities of 50% – 50% and $\sim 100\% - 0\%$ as shown on Flat-fields at figure 13.11. Figure 13.11 also shows cases where the algorithm may not be decidable. The results on whether the algorithm effectively aligns the Moiré pattern is depicted as a confusion matrix, where the algorithm deterministically calculates the necessary steps for the $\Delta\phi$ and Δx motor movements. Table 13.1 shows the result for

performance metrics. Accuracy, although is considerably higher than a random guess (which would be around 0.5 in a balanced binary classification). An accuracy of 0.77 implies that the classifier correctly predicts the outcome (both true positives and true negatives) in 77% of the cases. Fine-tuning is required for the algorithm in hand and a solution for better classification and decidability is proposed in the next chapter.

TABLA 13.1: Performance Metrics Derived from the Confusion Matrix

| Metric | Formula | Value |
|-------------|---|-------|
| Accuracy | $\frac{TP+TN}{TP+TN+FP+FN}$ | 0.770 |
| Precision | $\frac{TP}{TP+FP}$ | 0.779 |
| Recall | $\frac{TP}{TP+FN}$ | 0.875 |
| Specificity | $\frac{TN}{TN+FP}$ | 0.602 |
| F1 Score | $2 \times \frac{\text{Precision} \times \text{Recall}}{\text{Precision} + \text{Recall}}$ | 0.824 |
| MCC | $\frac{TP \times TN - FP \times FN}{\sqrt{(TP+FP)(TP+FN)(TN+FP)(TN+FN)}}$ | 0.502 |

The F1 score indicates a strong balance between precision and recall. This suggests that the classifier is robust in scenarios where it's important to maintain a balance between not missing positive cases (high recall) and maintaining a high accuracy of positive predictions (high precision). However, F1 score can also be fine-tuned by improving the decidability on undecidable images, which mostly occur where the fringing is close to alignment and the number of peaks in the Moiré pattern is low.

13.3 Edge-Illumination: *Poecilla Reticulata*

The system will undergo a full imaging sequence as depicted in figure 13.12, where first a $\sim 100\% - 0\%$ alignment is performed using the mask motion system. After the alignment is correct, the PMMA capillary rod where the fish will be located is moved to the imaging frame for flat-field extraction. This flat-field requires eight dithering steps in the Δx direction which will be also done over the imaging process with the sample present, each dithering step has a total of $10\mu m$ distance corresponding to 8 minimal sample motor steps. Immediately after this, the system will be aligned in $50\% - 50\%$ for the second flat-field which also consists of eight dithering steps of the same distance each. Once the second flat-field dithering is done, the sample is carefully placed in the capillary without altering its position so the dithering will be consistent with the image. As soon as the sample is placed, a reverse dithering

images by dithering frame. Table 13.2 has the imaging specifications and describes how data is saved for later processing. Dithering measurements were performed over a similar sample

TABLA 13.2: X-Ray Capture Specifications

| SOURCE CONDITIONS & SENSOR CONFIGURATION | | | |
|--|------------------|--|---|
| Source Conditions | | Sensor Config | |
| Brand | Hamamatsu | Type | MPX3RXV1, fine pitch (55um pixel pitch) |
| Model | L6620-01 | Operation Mode | SPM |
| Anode | W | Preamp Gain | 1 - High Gain Mode |
| Window | Beryllium 200 um | Serial No. | W108.I4 |
| Filter | None | Sensor Polarity | N-on-P |
| Source Voltage | 28 kV | Sensor Material | Si, 300um |
| Source Current | 50μA | Vsensor | 100V |
| Collimator: D = 2 mm, FPD = 5.5 cm | | Isensor | < 10μA |
| CAPTURE TIMES & EXPOSURE | | | |
| Capture per dith: 30 seconds | | Flat field: 300 seconds | |
| CAPTURES PERFORMED | | | |
| dithering_01: 10 um 9 steps dithering 50%-50% Alignment | | dithering_02: 10 um 9 steps dithering 100%-0% Alignment | |

13.4 Reconstruction of dithered attenuation-based imaging

The previous section highlighted the Edge-illumination imaging process for multi-modal imaging. Now a reconstruction over pixel-parity is performed following mainly the concepts introduced in chapter 7. Column pixel pairs provide the full information to retrieve the signals shown in this and subsequent sections, figure 13.13 illustrates this process. Since the sum of positive and negative fringing for the same beamlet results on the total signal, from now on we define column pixel pairs as $I_p = (I^+, I^-)$ where $I_p \in \text{Dith}_8(I)$. Reconstructed images will be the result of direct operations of each pair to produce a new element I_p that reconstructs the new image. As it may be expected, intensity values are compressed by half the full image resolution in the dithering and pairing direction (Δx). The operation pair that reconstructs the absorption image is the following.

$$I_p = I_+ + I_- \quad (13.5)$$

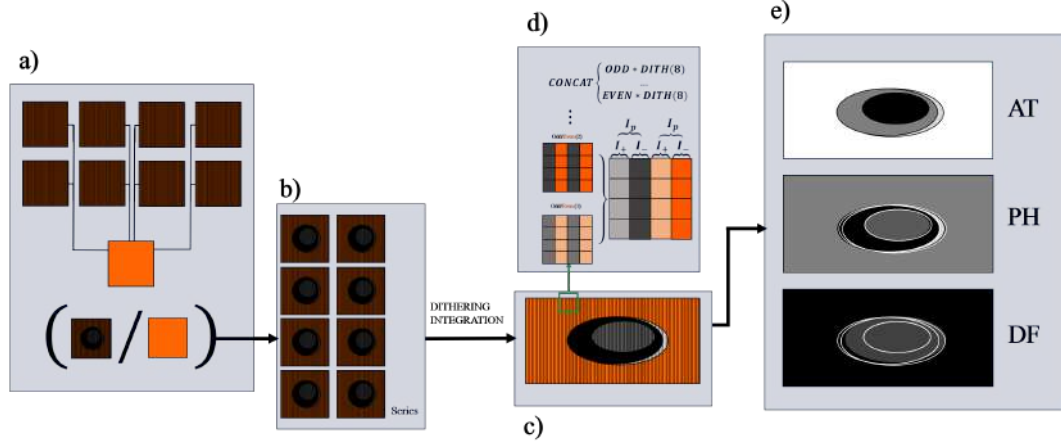


FIGURE 13.13: Diagram of the dithering integration and the reconstruction of images with augmented resolution, phase contrast, and dark-field. a) The pairs of images that coincide in the x direction and illumination modality are pre-processed by a flat-field correction, which consists of the pixel-wise quotient of intensities. b) a pixel column-wise operation is performed over the images according to the signal that needs to be retrieved. d) Each signal has a pair-wise operation that can be used to retrieve said signal. This however reduces the spatial resolution to half the original resolution in the direction where the dithering was performed. A column-wise concatenation will correct this. c) eight total corrected images are then concatenated in dither order, this means the first column of each image of the eight ordered dithers are concatenated, then the second column until the final resolution of 256×1024 is reached. This is done for the full set of images that were obtained from the column-wise operations. e) The output shows the three (or more) signals retrieved (AT,PH,DF) with the augmented resolution.

The total attenuation signal may be also interpreted as the zeroth-momentum of the intensity distribution, which is just the I_p values of the intensity distribution (See section 9). Due to dithering, the total image resolution is $256 \times 128 \cdot 8 = 256 \times 1024$.

A total of 34 images are taken using this sequence, 17 for each illumination configuration, each configuration has a set of eight dithered flat-field images and nine dithered sample images, the extra image on the sample images is taken to study the effect of extra stepping on dithering imaging, changing the total dithering movement distance. The images are then corrected and concatenated following the process in figure 13.13. Then using the operation for attenuation reconstruction, the final image set at 13.14 is obtained for the four different cases.

As figure 13.14 shows, there is almost no visible difference between the imaging alignments aside from the background in the 5050 case, which presents more texture that might be due to an increment in the pixel-wise phase intensities, hence, it does look more noisy. Additionally, the extra dithering imaging reconstruction $8\mu m$ shows artifacts in the sample tail and an edge effect around the fish, where a white contour is visible.

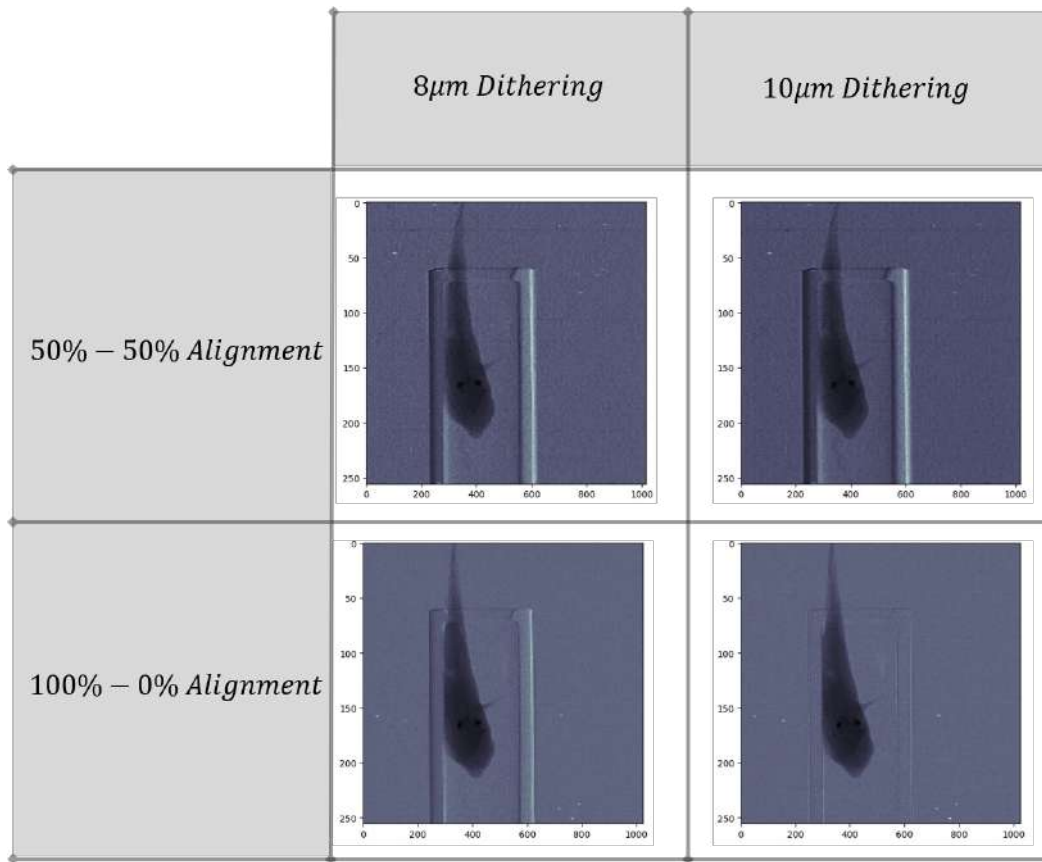


FIGURE 13.14: Attenuation images for a Guppy fish with differences in the number of dithering steps and alignment system used. Image is re-escalated on the x axis for a better fitting and representation of the actual dimensions of the sample

13.5 Reconstruction of dithered differential phase imaging

Using the set of images extracted on the full imaging sequence, a reconstruction of the differential phase image is also performed. As previously mentioned, phase information describes the refraction of resolved structures, and the refraction angle projected on the detector is given by the relation with the phase shift associated with the transport-of-intensity equation.

$$\alpha(x, y) = \frac{1}{k} \nabla_{\perp} \phi(x, y) \quad (13.6)$$

X-ray refraction angles are minimal, often only a few micro-radians, which poses significant challenges in their observation. However, the refractive index for materials composed of light elements is typically a thousand times greater than their absorption factor, especially at wavelengths employed in radiology. This results in significantly enhanced contrast for soft tissues when using X-ray imaging techniques that focus

on detecting light refraction or employ a wave-based approach to interpret phase differences. A clear advantage of EI XPCI is that edge systems are considerably more sensitive to refraction over short field distances due to beamlets that can detect micro-radian deviations which are then represented as positive and negative fringing on the detector. Most of the current works on the topic work with the illumination curve (IC) and the object scattering curve (O) to reconstruct the differential phase signal and the dark field signal [114, 115], by estimating the parameters of a new distribution μ_n, σ_n^2 which describes the IC and the O curve convolution, given by the formula.

$$IC_p(z)/I_o = (IC * O)(x - \Delta x_R)T(z) \quad (13.7)$$

Where Δx_R is the dithering displacement and $T(z)$ is the transmission function given by the attenuation. If an object is placed in the beamlet path, the IC shape will change due to the three effects described above. Attenuation will reduce the area under the IC (T), while refraction ($\Delta\phi$) will shift the position of the IC center. Small-angle scatter due to microstructures broadens the IC , as the spatial spread of the beamlet intensity increases. In practice, the IC is usually modeled with a Gaussian function which by the section 9 makes sense even when the pixel intensity distribution switches due to the presence of a sample (IC_p). Other works have also deduced the relationship between positive and negative fringing on the distinction of odd and even pixels as a local retrieval method applied pixel-by-pixel [116]. This pixel-by-pixel deduction follows the deduction constructed in section 9. Where the differential phase is given by the following pixel-to-pixel operation.

$$I_p = \frac{M}{2z_2} \frac{I_+ - I_-}{I_+ + I_-} \quad (13.8)$$

Similar works interpret the differential phase signal as the distribution resulting from the subtraction of the mean value of the normal distributions that describe the IC and the IC_p . This is also equivalent to the subtraction of the first momentum of both intensity distributions. The phase contrast reconstruction of each image reconstructed as shown in the attenuation case is shown in figure 13.16 Note how the background of the 50% – 50% shows non-homogeneity and noise, this may be due the flat-field imaging process. However, edges and structures not visible on the absorption image emerge in the differential phase contrast image, especially in the 50%-50% (5050) image where the edges are clearly visible. Further discussion on the signal will be done on section 13.9. Later specific measurements over the 5050 case will support this statement where the phase signal is actually amplified and better retrieved than in 0%-100% (0100)

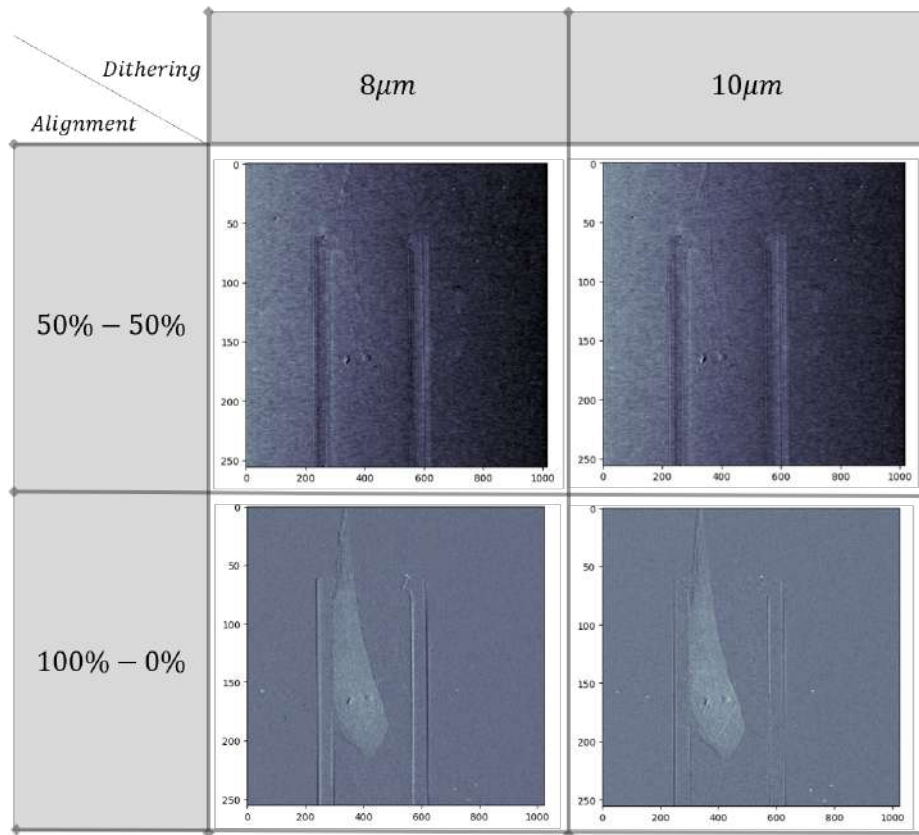


FIGURE 13.15: Differential phase images for a Guppy fish with differences in the number of dithering steps and alignment system used. Image is re-escalated on the x axis for a better fitting and representation of the actual dimensions of the sample

13.6 Reconstruction of dithered phase retrieval imaging

While the differential phase contrast image maps the directional change of phase through the fringing direction Δx , the direct phase retrieval can also be reconstructed by using the Paganin algorithm. By using the imaging parameters such as $\gamma \approx 4.67 \times 10^3$, dither step $\Delta x \approx 1.25\mu m$ and the pixel size $x_p = 55\mu m$ along with the differential phase contrast images, the phase signal is finally obtained and retrieved as shown in figure 13.16.

The noisy nature of phase signal may be mostly related to the estimated γ value. Paganin algorithm may result limited mostly due to the assumption that the sample on the imaging system is assumed to have the same β, δ material. The effect on dither distance is also amplified since the additional frames add to the total phase even in background pixels.

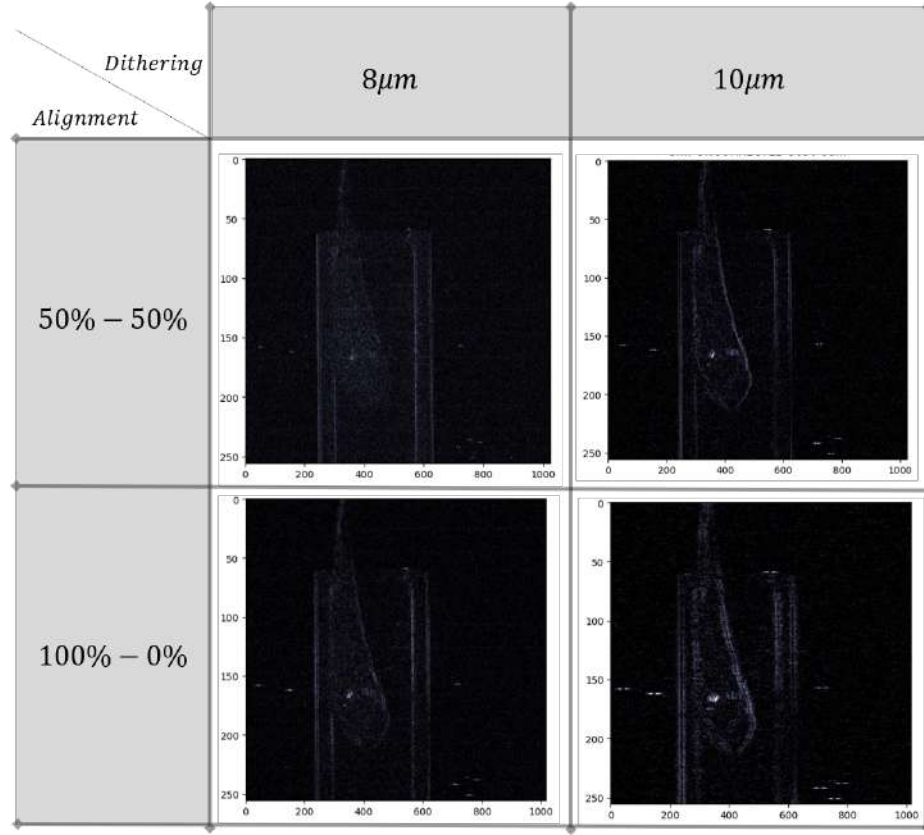


FIGURE 13.16: Retrieved phase images for a Guppy fish with differences in the number of dithering steps and alignment system used. Image is re-scaled on the x axis for a better fitting and representation of the actual dimensions of the sample

13.7 Reconstruction of Dark field (scatter) imaging

The multi-modal proposal of this work comprehends three main signals that can be retrieved by the edge illumination method, each one directly related to a light-matter interaction phenomenon. Dark-field imaging signal is related to small-angle scattering due to numerous unresolved structures that are composed of atoms light enough to not be able to absorb most of the radiation. The deflection cone angular aperture is given mainly by the cross-section of Compton scattering (Small angle scattering) and Rayleigh (Ultra small angle scattering), other phenomena may contribute in a lesser fraction.

$$\sigma_{scatter} = \sigma_{compton} + \sigma_{pp(2)} + \sigma_{rayleigh} \quad (13.9)$$

In average, the total scattered angle is given by the following expression

$$\alpha(x, y) = \sqrt{4\delta^2\rho \cdot w \left(\log \frac{2}{\delta} + 1 \right)} \quad (13.10)$$

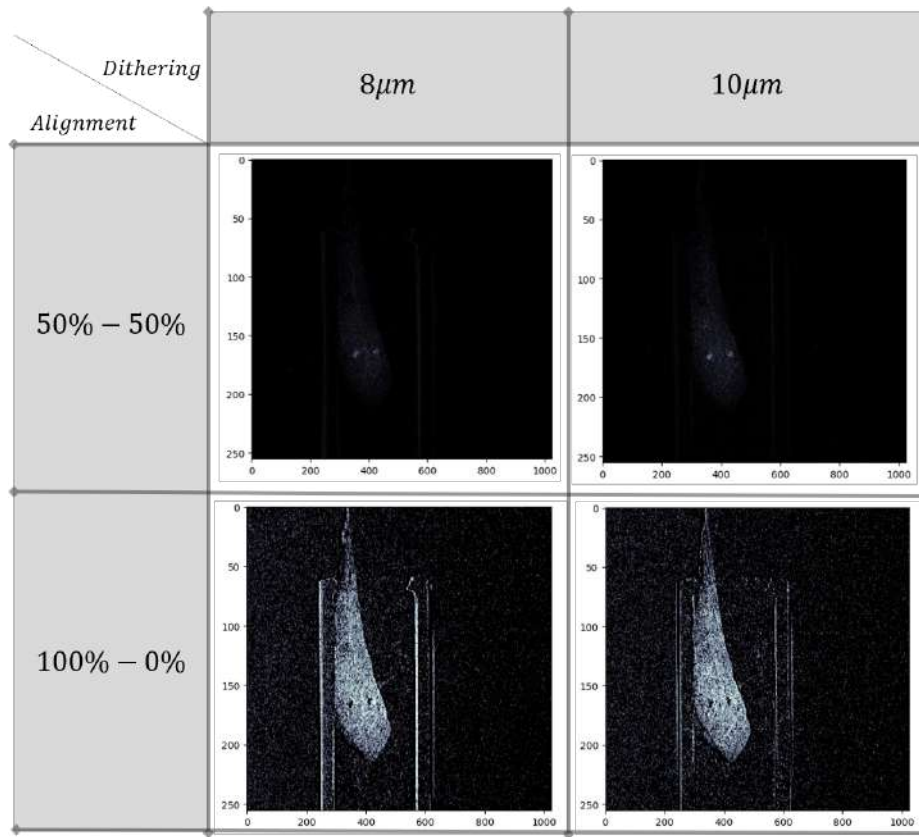


FIGURE 13.17: Dark-field images for a Guppy fish with differences in the number of dithering steps and alignment system used. Image is re-scaled on the x axis for a better fitting and representation of the actual dimensions of the sample

Where ρ is the projected material density and w is the width of the sample [117]. Under the distribution interpretation seen in the phase contrast section, quantifying the dark-field intensity from the ultra-small angle x-ray scattering signal involves measuring the broadening of the IC at the presence of the sample. Other dark-field retrieval methods revolve over the quantification of the scatter itself, solving for the small angles α the photon trajectories before and after the IC is deformed by the object [118] This is often measured as the difference of the variance distribution of intensities with and without the sample [119], which are the second distribution momentum of the gaussian intensity values. Under the pixel-to-pixel interpretation built in this work, the resulting operation over the positive and negative fringing pixels is given by the following result of section 9.

$$I_p = \left(\frac{kxM}{z_2} \right) \left(\frac{I_+^2 - I_-^2}{I_+ + I_-} - 2 \left(\frac{I_+ - I_-}{I_+ + I_-} \right)^2 \right) \quad (13.11)$$

From which the dark-field signal is reconstructed in figure 13.17

As expected, while the phase signal is maximum on the 50% – 50% system, the dark-field is resolved for the 100% – 0% configuration and the signal is maximized.

13.8 Additional imaging for further momenta: Skewness

Under the proposed pixel-to-pixel interpretation of intensity distributions, it is possible to calculate further distribution momenta under the premise that the Gaussian distribution given by the IC and the IC_p has a noisy discrete nature, hence, further momenta residuals are not zero which is the case for a perfectly defined Gaussian. This allows the calculation of the skewness γ_{IC} . Which by an induction argument the residual.

$$\gamma_p = \gamma_{IC} - \gamma_{IC_p} \quad (13.12)$$

It is not zero. The pixel-by-pixel relationship can be calculated directly by expanding the expected value polynomial which gives

$$I_p = \left(\frac{kxM}{z_2} \right) \left[\frac{I_+^3 - I_-^3}{(I_+ + I_-)\Delta\sigma^3} - 3\mu \left(\frac{I_+^2 - I_-^2}{(I_+ + I_-)\Delta\sigma^3} + \frac{\Delta\mu}{\Delta\sigma^3} \right) \right] \quad (13.13)$$

Where $\Delta\mu$ and $\Delta\sigma^2$ are the phase and dark-field signals respectively. A simplified relationship can be found using Pearson's skewness definition [], the following relationship is then deduced

$$I_p = \left(\frac{kxM}{z_2} \right) \left[\left(\frac{\Delta\mu(m_+ - m_-)}{\Delta\mu - \Delta\mu \left(1 - \frac{1}{I_+ + I_-} \right)} \right) \right] \quad (13.14)$$

$$= \left(\frac{kxM}{z_2} \right) \left(\frac{(m_+ - m_-)}{\frac{1}{I_+ + I_-}} \right) \quad (13.15)$$

Which results in the following images An important remark here is mention how the following momenta can be interpreted as light terms of the distribution expansion. For a perfect Gaussian $\gamma_p = 0$ and this remains true even for the real image, the shadows and bright sections of the skew images are located almost near zero and fluctuate positively or negatively according mostly to the geometry of the sample. Further momenta residuals may act as de-noisers for the three main signals (Abs, DP, DF).

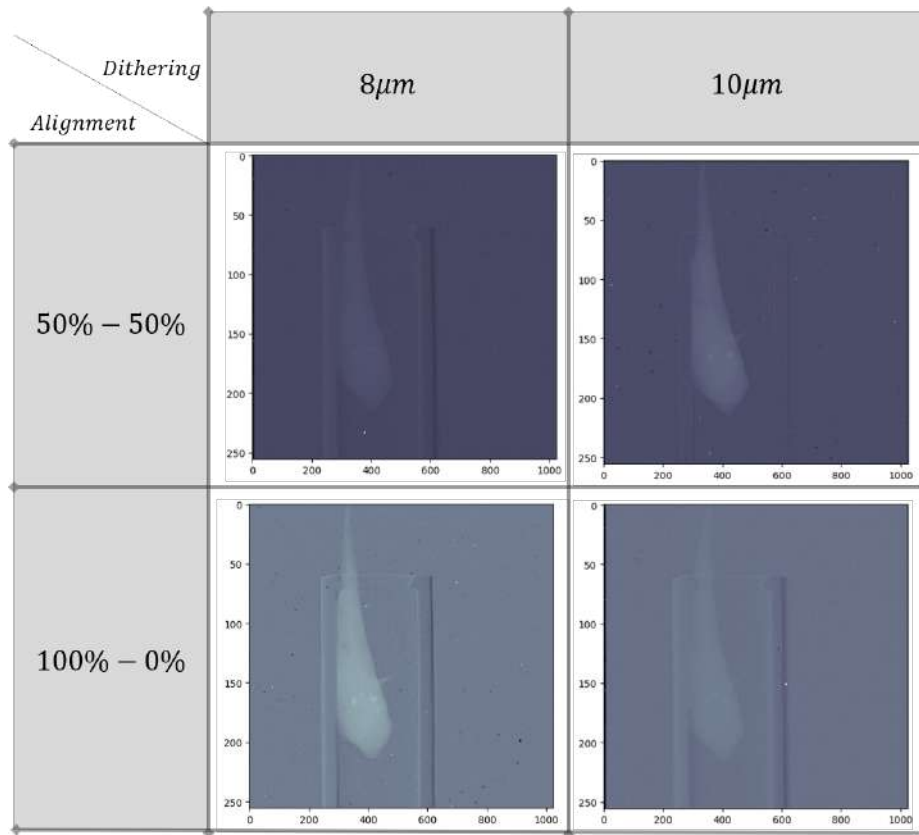


FIGURE 13.18: Dark-field images for a Guppy fish with differences in the number of dithering steps and alignment system used. Image is re-scaled on the x axis for a better fitting and representation of the actual dimensions of the sample

13.9 Automatic segmentation of fish sections

To characterize the technique and the impact of the signals in the contrast metric for object detection, it is necessary to quantify each signal over a region of the image. In this case, the region of interest taken for the metrics will be the otolith nodes present on the fish's lower head. Figure 13.19 shows the masking procedure. The fish's otoliths will be measured compared to the embedded material signal which is the fish's skull and head tissue. The masking process is successfully done for the three signals using 12 kernel distances. Figure 13.20 shows the segmentation results for each signal.

13.10 Visible structures

Under phase contrast and dark-field imaging, some structures that were not visible emerge or are enhanced, but some others disappear, in figure 13.21 a quick exploration of the results for dark-field, phase contrast, and attenuation signals. The signal for all the structures is enhanced by the dark field or the differential phase signal. The

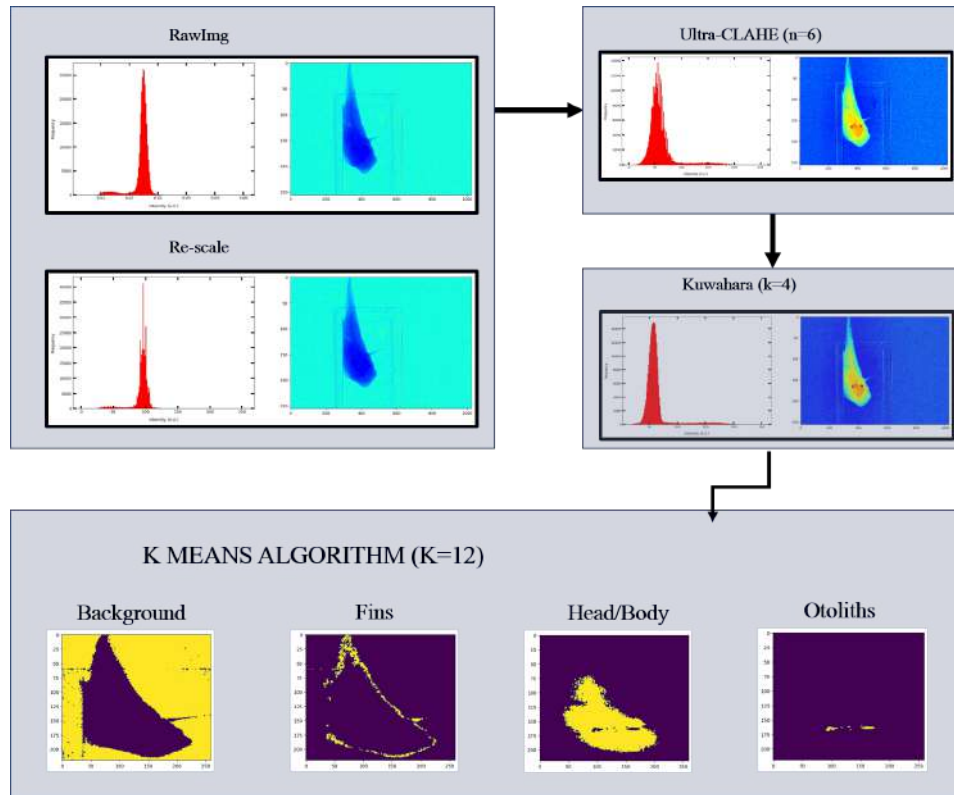


FIGURE 13.19: Masking process to determine the regions of interest (ROIs) of the Guppy fish. First, the already processed, augmented, and reconstructed image output from 13.13 of the three signals goes through an image processing algorithm. Where the image goes through a re-scale process that ignores pixels on the limit values. Then a ULTRA-CLAHE (See section 12) is performed to the image with a $\sigma = 6$ enhancement parameter. This algorithm will improve the distribution of intensities over the whole image, making a dynamic contrast enhancement. Finally, an image smoothing using Kuwahara kerneling with $k = 4$ is performed. This smooth uses a dynamic window where the kernel changes its size and factors depending on the previous average values of intensity, hence minimizing the gradient loss which translates into less edge smoothing. When the processing is over, a k-means algorithm is performed to extract specific regions of the fish as masks that will be operated later on. The number of kernels used was 12 although multiple kernels correspond to the same region. The four final regions chosen are shown on the last step, this includes the background signal, fins and fish edges, head and body section, and otoliths which are high contrast

structure of the neural tubes emerges in between the otoliths and is especially visible in the dark field signal. The lateral fin on the other hand may seem less visible in both signals.

13.11 Figures of merit over ROIs

As previously mentioned, the Fish's otoliths are used to measure the multi-modal signal and how effective is each signal in resolving embedded objects in a biological

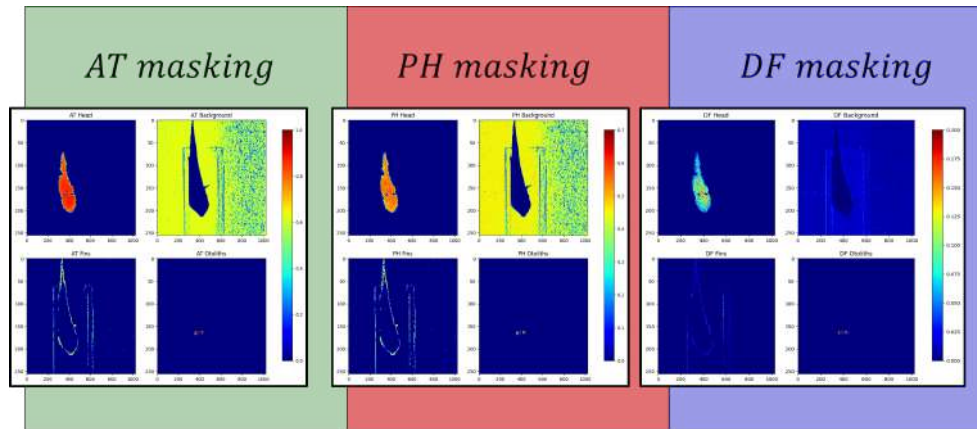


FIGURE 13.20: Masking result for each of the signals, the masks are directly multiplied to each signal image, giving an intensity distribution on the ROI and zero elsewhere.

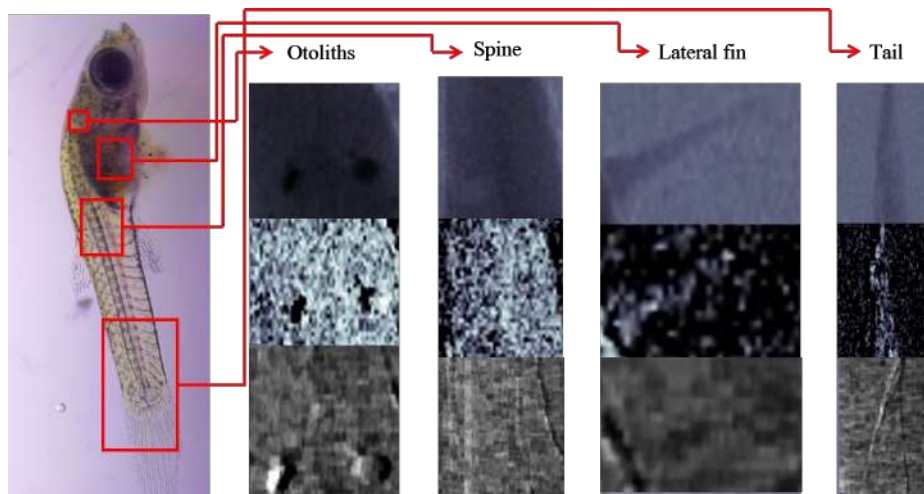


FIGURE 13.21: Qualitative selection of regions that were enhanced by the phase contrast or dark field signal. The four selected structures are the Otoliths, the neck region where the spine is located, the lateral fin visible on the x-ray images, and the tail.

sample. By using the masking algorithm shown in figure 13.19, it is possible to separate signal pixels (otolith mask) from background pixels (Head/body mask). First, an intensity profile of the same region is extracted for each of the signals which is shown in figure 13.22. The regions corresponding to each of the otoliths are clearly visible on the profile. Additionally, the center region shown in figure 13.22 belongs to soft tissue that is not visible on the attenuation profile (Region II, manual SNR ~ 1.37) [120] which belongs to neural tubes that bifurcate from the spine to the otoliths. Neural tubes are soft, compact tissue that contains nerves as well as veins packaged in a single structure Data over otoliths will be used later on to define the system's resolution. The SNR and CNR of signals corresponding to the sections presented in figure 13.21 and masked as seen in figure 13.23 are presented in table 13.3.

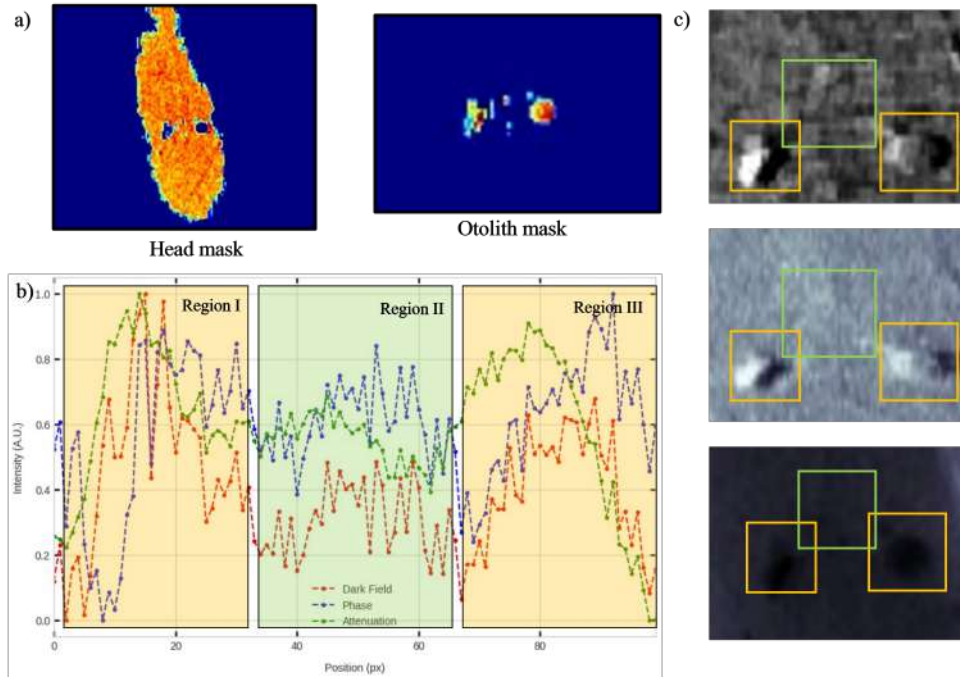


FIGURE 13.22: a) Selected region masks that were used to calculate the figures of merit of the profile plot at b). Otoliths are compared to the head to give a more specific contrast metric since otoliths are embedded in the head tissue. b) Profile plot of the three signals, the three curves seen in the profile plot correspond to a specific structure seen also in the images at c) for each signal. Region I, II and III correspond to the left otolith, the neural tubes and the right otolith of the fish respectively.

TABLA 13.3: Signal Analysis in Different Regions

| Signal Type | OT | | SP | | LF | | TL | |
|-------------|-------|-------|-------|------|-------|------|-------|-------|
| | SNR | CNR | SNR | CNR | SNR | CNR | SNR | CNR |
| AT | 52.84 | 6.84 | 41.89 | 5.32 | 8.82 | 6.76 | 76.57 | 14.97 |
| PH | 17.58 | 6.79 | 24.51 | 7.89 | 5.36 | 1.93 | 29.36 | 11.42 |
| DF | 26.58 | 11.27 | 7.58 | 2.42 | 12.63 | 9.59 | 68.34 | 21.36 |

13.12 Signal resolution for AT, PH, DF signals

Recall figure 13.22 profile for the three signals. Brombal et al. [121] And other works [122] have calculated the resolution of different phase contrast systems (Speckle-based and In-line) by fitting an error function to the corresponding increasing curve of the intensity profile of a high-contrast region. In this case, take Otoliths as a reference. Hence the profile is given by the selected region in figure 13.22 and an error function of the form.

$$\text{Erf}(x, \bar{w}) = \frac{2A}{\sqrt{\pi}} \int_0^{B(x-C)} e^{-k^2} dk + D \quad (13.16)$$

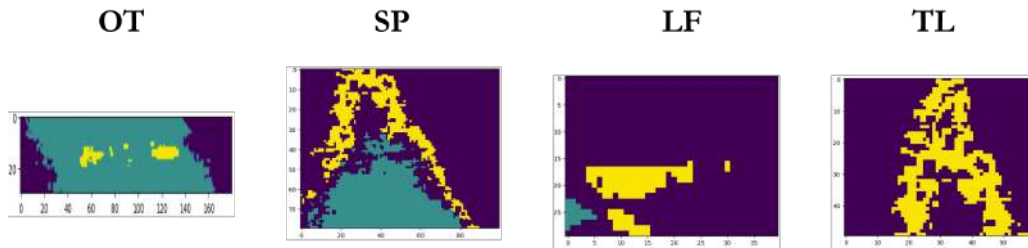


FIGURE 13.23: Compared regions for the CNR and SNR metrics, in some cases three regions were used to compare the total signal to the background.

Where $\bar{w} = [A, B, C, D]$ is a set of fittable parameters. What is of most interest here is the derivative of $\text{Erf}(x, \bar{w})$. Which describes a normal distribution fitted to the set of parameters \bar{w} . Hence

$$g(x, A, B, C, D) = \frac{2AB}{\sqrt{\pi}} e^{-B(x-C)^2} \quad (13.17)$$

Here it might be noticed that the value associated to the variance of this pseudo-distribution is given by the fitted parameter $\sigma^2 = B$. Then the Full-Width Half-Maximum (FWHM) of $g(x, \bar{w})$ is

$$\text{FWHM} = \frac{2\sqrt{2\log 2}}{B} \quad (13.18)$$

Which results in the distributions shown in figure 13.24. Which also shows the process just described. The final fitting parameters for each signal are finally shown in table 13.4 and the unnormalized distribution plot is shown in figure 13.24. According to the FWHM, the best resolution is provided by the DF signal, following the PH signal, and finally the AT signal for this specific section. As the reader may have already noted on the numerical results for the three signals, there is not a single dominant signal on quality and resolution although DF, AT, PH may have advantages over different tissue densities and regions as seen in the results at 13.3. The proposal of a multi-modal system then makes sense for applications that involve multiple materials and low-resolving structures on conventional X-ray imaging. Section 13.15 will make a further proposal for the integration of the three signals into channel codification as RGB X-ray images. Table 13.4 shows the resolution of each region depicted in figure 13.22 for each signal.

13.13 Estimation of the Entrance Surface Dose

Under the purpose of a full characterization of this multi-modal technique, it is necessary to proceed with a characterization of the Entrance Surface Dose (ESD) that enters

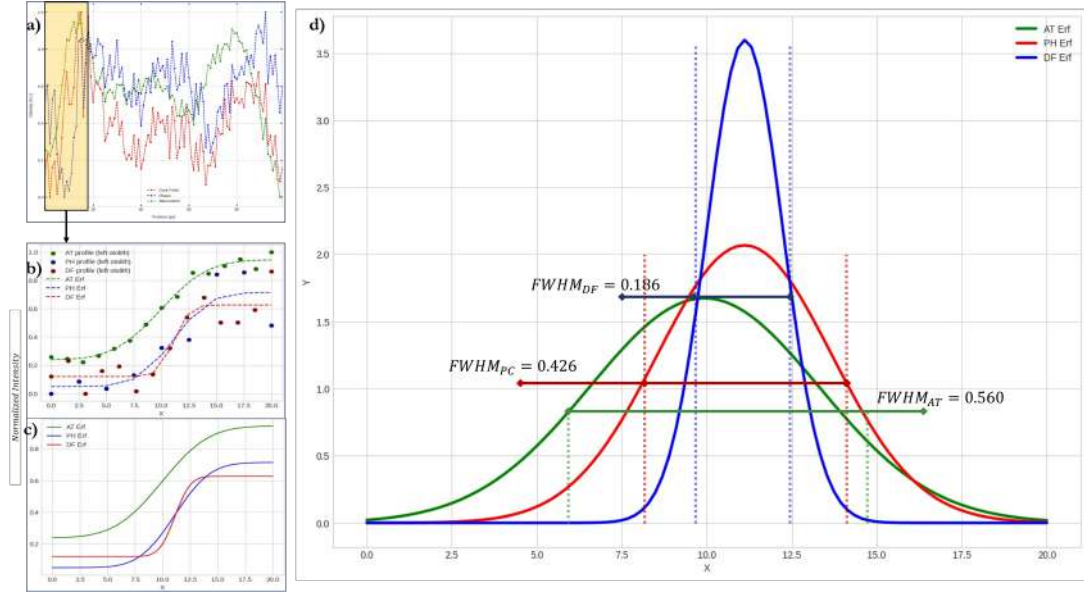


FIGURE 13.24: a) Selected region for the resolution numerical result, this region corresponds to the left otolith at the leftmost edge, which in all curves will represent an increase in intensity. The trimmed data is represented in b) where is fitted to an Erf, this Erf is shown with better numeric stepping in c). The derivative of said Erf is a normal distribution given by d) which has an associated FWHM that corresponds to the resolution of that signal in the image.

TABLA 13.4: Parameter Fitting and FWHM in Different Regions. OT1 corresponds to the first otolith, while NT corresponds to the neural tube region. NA values are in place where the fitting could not be done

| Signal | FWHM | OT1 | | | | FWHM | NTs | | | |
|--------|------|------|-------|------|------|------|------|------|------|------|
| | | A | B | C | D | | A | B | C | D |
| AT | 0.56 | 0.35 | 4.19 | 0.49 | 0.59 | NA | NA | NA | NA | NA |
| PH | 0.42 | 0.36 | 5.51 | 0.48 | 0.52 | 0.72 | 0.36 | 3.23 | 0.62 | 0.12 |
| DF | 0.18 | 0.25 | 12.61 | 0.55 | 0.37 | 1.00 | 0.28 | 2.35 | 0.32 | 0.10 |

the sample. For this purpose, we make use of a previous dosimetry measurement performed in the same setup and described in the next article [123]. The setup has to be switched to carry a Rh filter with a width $w = 50\mu m$ for the results to be comparable. By a geometrical analysis of the photon aperture, the dose over time will be given by the following.

$$\xi_{EI}(T) = \beta_{(Mask)} \frac{A_R}{A_{EI}} \int_{\lambda} \int_0^T \xi_R(t, \lambda) dt d\lambda \quad (13.19)$$

Where A_R, A_{EI} are the transverse area of the cone on both configurations, given by the aperture angle and magnification, $\beta_{(Mask)}$ is the absorption factor introduced by the mask, which corresponds to the reason between the mask period and aperture size and $\int_0^T \xi_R(t, \lambda)$ is the dose calibration factor given by Roque et. Al. This gives the following ESD map (figure 13.26) where the 100% calibrated dose corresponds to 0.388 mGy. The behavior of the graph remains linear due to ESD being in the lower

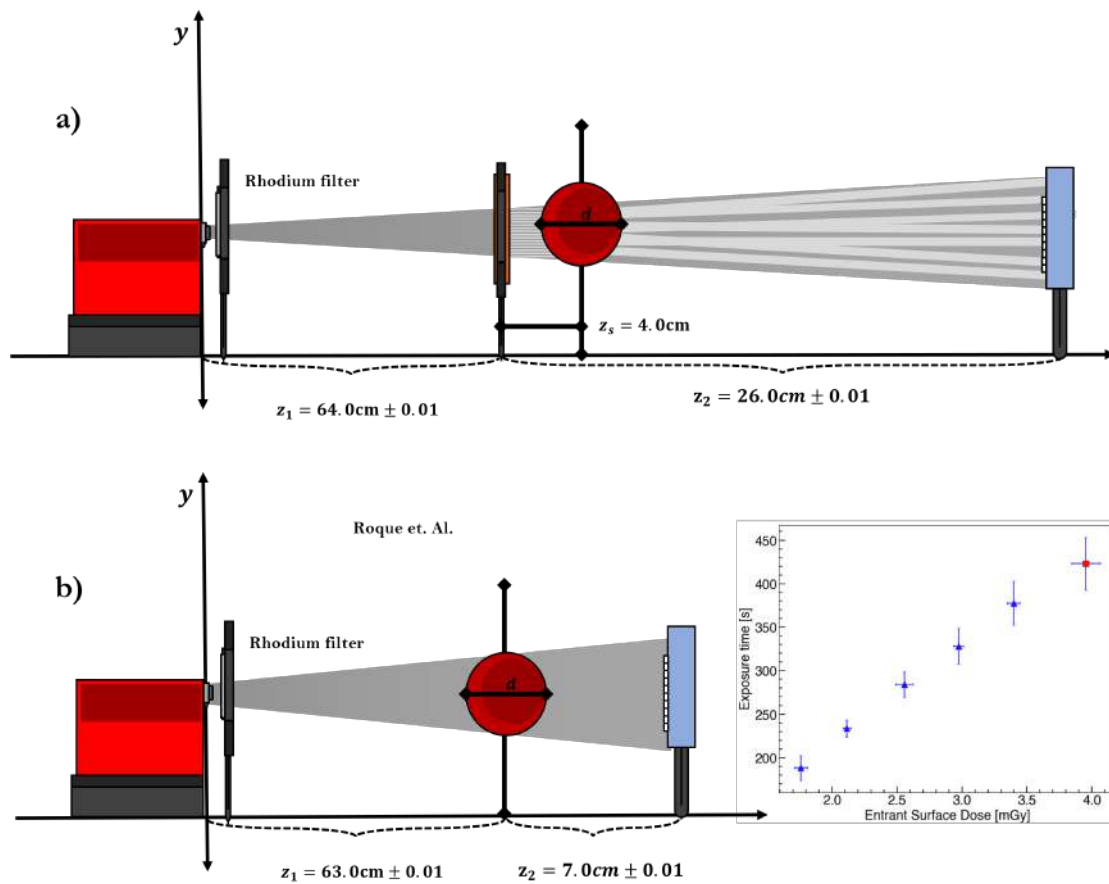


FIGURE 13.25: a) Additional flat-field with a modified EI setup. the setup has now a Rhodium filter at the exit of the X-ray source to equalize the energy spectrum as the one used in Roque et. al. b) X ray imaging setup from Roque et. al. with a Rhodium filter and modified distances, along with the dosimetry measurements of the ESD

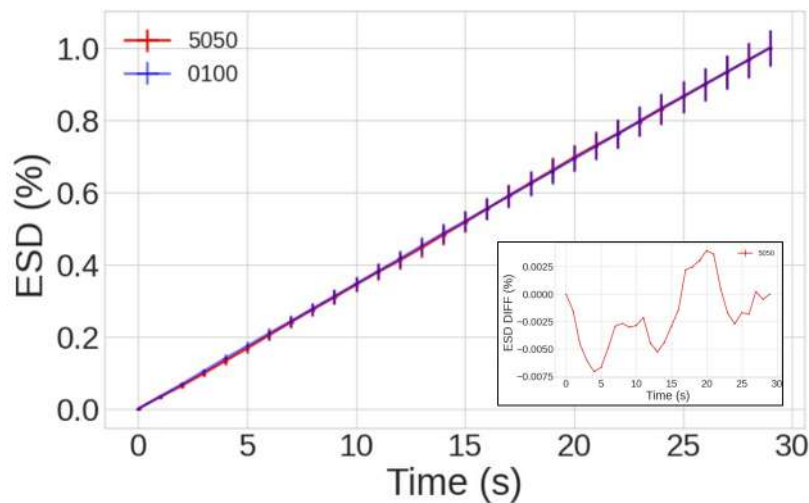


FIGURE 13.26: Estimated ESD on the fish region normalized over the total dose, by the geometrical effects as well as the presence of the mask, the estimated ESD corresponds to 0.388 mGy per dithering frame. For a full imaging set the total estimate is 3.11 mGy per 240 seconds. The subplot is the difference between the 5050 and 0100 alignment systems, as expected, both systems preserve the ESD value

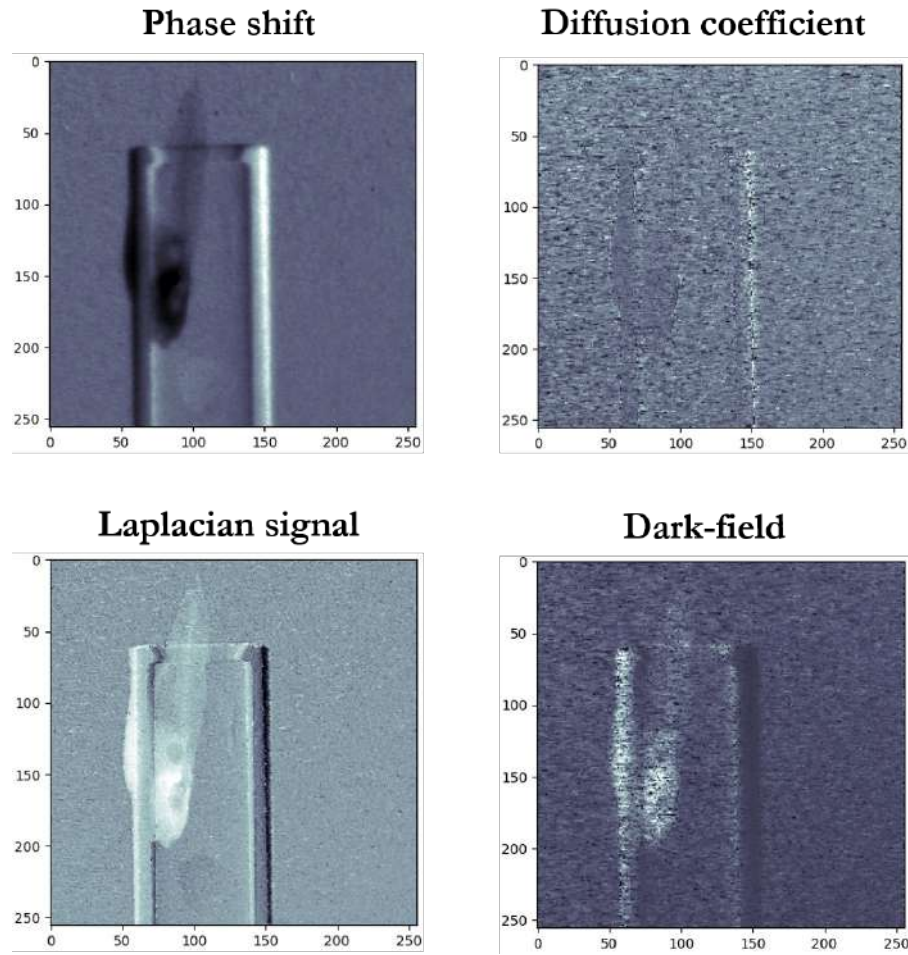


FIGURE 13.27: Speckle-based phase contrast, dark-field, Laplacian signal reconstruction, and attenuation images

regime. For a longer time exposure, it is expected that the tendency has a $x^{1/a}$, $a > 1$ shape.

13.14 Speckle imaging and retrieval using MIST

After the imaging system completes the process of EI imaging shown in section 13.3, the setup is modified to now perform a speckle-based illumination imaging as shown in the experimental preliminaries in figure 13.27. As noted, the Guppy fish does not remain in the same position. mainly due to the necessity of disarming the sample placing to change the set-up to speckle-based imaging. Additionally, a new signal is added which contains the laplacian signal. Dark-field turns back into a noisy image while EI remains consistent on the dark-field signal. The visibility of the speckles

during the pathing with and without the sample was stable at $\mathcal{V} \approx 0.20$. The conditions for effective signal retrieval rely especially in how effective is the speckle tracking throughout the image

13.15 A first exploration of triple-channel X-ray imaging using colormap representation

The multi-modal signal has a potential use individually since each signal can directly represent a property of materials with higher and lower intensities. Nonetheless, one of the greatest challenges especially in medical institutions is to optimize the radiological reading of diagnosis, especially in saturated healthcare systems. A proposal included in this work is to combine the multi-modal signals into one single image, this can be done by different means but one attractive alternative is to use RGB channels for X-ray imaging, where each color of the channel represents either the attenuation, phase or dark-field signal. The results of the six possible combinations of RGB channels into the AT, PH, DF channels are as seen in figure [13.28](#)

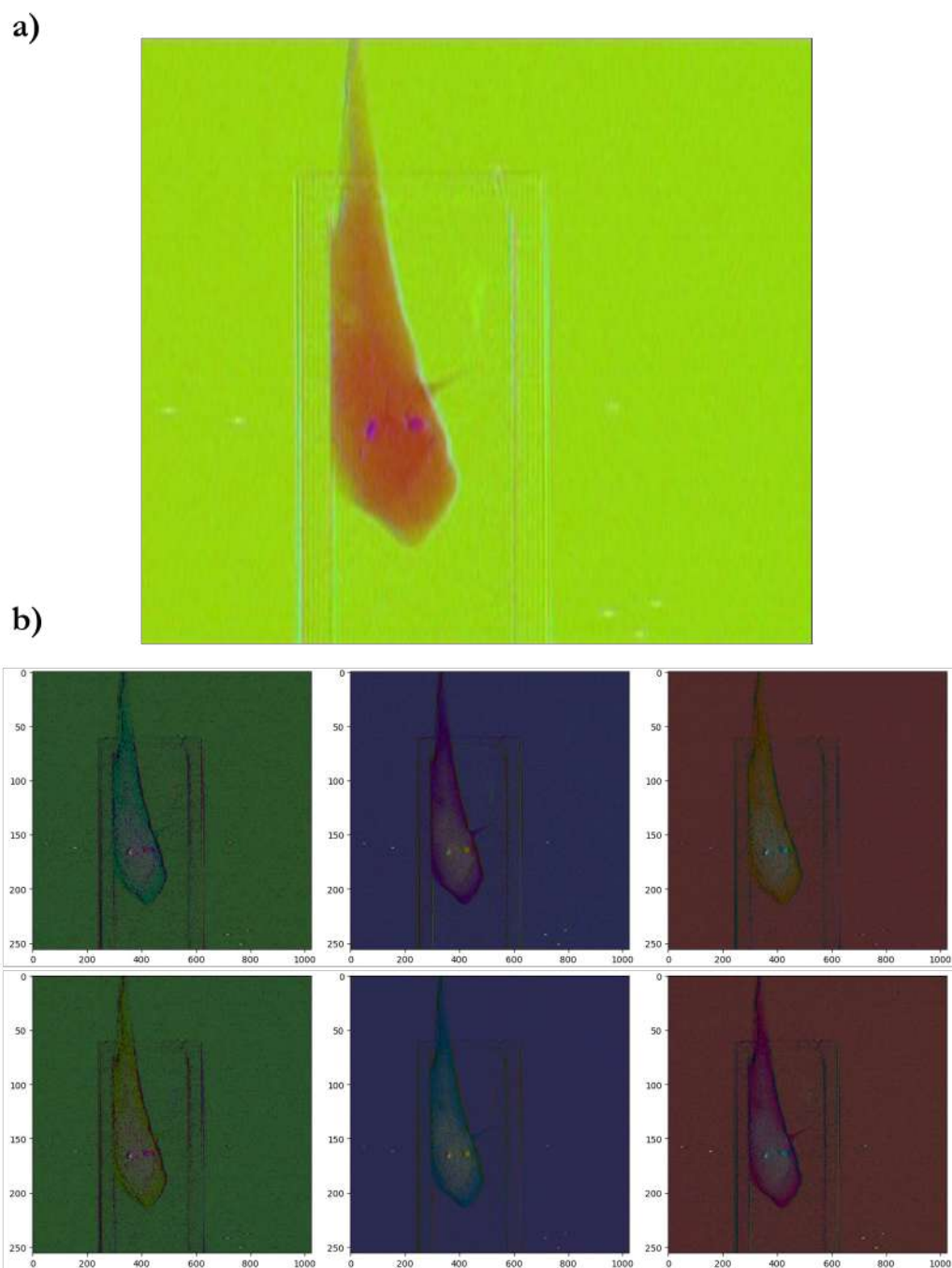


FIGURE 13.28: a) An example of normalizing AT-PH-DF channels into R-G-B color channels. These may give more insights about the contrast over the sample using multi-modal signal integration. b) Possible combinations between color channels and signal channels for the integration of single image reading PH/DF/AT imaging, in some of the images there is a clear highlighting of zones that are not visible in the individual signals, such as a better visibility of the spine, a clear visualization of the skull and edge enhancement.

Chapter 14

Conclusions and further remarks

In this comprehensive work, a multi-modal imaging system was implemented and characterized under the use of a biological sample for the study of the feasibility in the use of X-ray phase contrast and X-ray dark-field imaging as empowering tools for the diagnosis of different structures of soft and hard tissue. During this work, a theoretical model to explain and compute the differential phase, dark-field, and skew signals on the modality of edge-illumination (EI) phase contrast imaging was formalized and tested, successfully retrieving the expected signals by using probability theory of the stochastic nature in photon detection and photon counting statistics. A standardized experimental step-by-step procedure for EI imaging using dithering was proposed, in which the radiation dose and the total time exposure of the sample were successfully reduced, as well as a partially automatized model for the diffraction mask alignment, which might save crucial minutes on the use of this technique. The multi-modal imaging process successfully retrieved the necessary data for the reconstruction of three main signals of interest. Attenuation, differential phase, and dark-field imaging for a biological sample, which was previously characterized. The imaging data was successfully analyzed and the advantages of the use of a multi-modal signal were highlighted on the figures of merit used to compare the attenuation signal with the complementary signals (PH, DF) where all the signals have a better performance on resolving different structures of the sample. Despite no signal dominating in performance, the importance and performance of each may be remarkable for different materials and applications that are more signal-sensitive, highlighting the hypothesis of a multi-modal imaging system being more effective in medical imaging.

The evaluation of the in-line feasibility in the application of medical imaging brings a new hypothesis. Although propagation-based techniques are often easier to implement and apply, they also come with several critical drawbacks. First of all, the

flexibility and freedom of imaging devices to change dimensions and distances must exist. The sensibility of this technique relies on a minimal propagation quota, which also depends on how small are scatterers present in the sample. For example, in the case of mammography, detecting microcalcifications as a warning signal of an early-stage cancer is of utmost importance. However, these structures are scatterers where the imaging system may be insensitive to them especially due to their size. In this case, propagation-based phase contrast loses all its importance due to its fundamental limitations, which were evaluated during this work.

An important part of the scalability of the multi-modal EI technique falls in the temporal resolution. Besides the complexity of the technique is a major disadvantage compared to propagation-based techniques. This limitation however can be overcome by the optimization of steps. One big challenge that is normally presented during EI imaging is the successful alignment which also affects the overall image quality. The solution proposed in this work is a powerful tool that might optimize the alignment process by the use of an algorithmic approach. The results of the confusion matrix and the performance metrics suggest that fine-tuning in undecidable cases is required. However, consider that false positive occurrences may be easily assessed by the user, so further analysis is required.

The imaging process proposed in figure 13.12 shows a simple and straightforward method for multi-modal imaging which is especially optimized for low-time exposure and to minimize artifacts due to micro-motor dead movement caused by frequent direction switches. However, this iterative process is specifically adapted to address a particular laboratory environment. Further testing on more general setup conditions may be necessary for a conclusive remark on the generalization of the methodology used.

The attenuation, phase, and dark field imaging signals were successfully retrieved by making use of an algorithmic road map that allows the efficient reconstruction a processing of the signals. The increase of CNR/SNR on phase and dark-field signals over regions of interest that had limited or no information under the attenuation signal suggests that these signals provide additional information that is potentially useful in the assistance of upholding decisive diagnostics and reducing the number of false negatives. Although qualitative and quantitative characterizations of the ROIs suggest that phase contrast and dark field signals provide better contrast and supporting information to the image, further study is necessary to fully quantify the net benefit of the additional information that provides phase contrast and dark-field imaging. It might be of interest to study the real effect of further momenta-like skewness.

The estimate on the ESD and the total dose deposited to the patient is lower under edge-illumination as expected since most of the dose is continuously deposited in the diffracting mask. Overall optimization on time exposure implies a drastic reduction in the total dose induced to the sample, which is of great interest for medical application and validation. Nonetheless, the total use of the X-ray tube significantly increases but this drawback is shadowed by the benefit of dose reduction considering the medical interests.

A strong alternative for EI is the use of speckle-based techniques, which were shallowly explored in a qualitative manner. Further exploration of speckle-based techniques as an alternative for medical imaging is ideal. However, just like EI systems, it can be predicted that speckle-based systems have similar disadvantages, especially in temporal resolution and energy (tube) usage.

Finally, a proposal of the recreation for a single image that comprises the information of the three signals was tested by means of an RGB channel image, this proposal might be of great value, especially in medical imaging, where it might save crucial time on radiology readings. The optimization for the proper channel assignation that maximizes joint contrast and the actual role of color in highlighting regions of the sample can be a powerful tool even in applications outside medical imaging. The use of individual channels may also be of great use, especially in the real of artificial intelligence. Predictive models for convolutional neural networks focused on diagnostic images may also be able to use the additional signals as training data for a wider volume and possibly better insights and performance.

Bibliography

- [1] N. Prize, *Philipp Lenard – Nobel Lecture*. NobelPrize.org, 2023.
- [2] K. Simonyi, *Kulturgeschichte der Physik: Von den Anfängen bis heute*. Deutsch (Harri), 2001.
- [3] J. D. McCoy, *Dental and oral radiography; A textbook for students and practitioners of dentistry*. Andesite Press, Aug. 2015.
- [4] W. C. Rontgen, “First x-ray image of a human hand,” Dec. 1895.
- [5] A. Feldman, “A sketch of the technical history of radiology from 1896 to 1920.,” *RadioGraphics*, vol. 9, pp. 1113–1128, Nov. 1989.
- [6] W. D. Coolidge, “X-ray tube,” May 1915. US3233115A.
- [7] G. EASTMAN, “Method and apparatus for coating plates for use in photography,” 1897. US226503A.
- [8] E. J. Calabrese and P. B. Selby, “Muller mistakes: The linear no-threshold (LNT) dose response and US EPA’s cancer risk assessment policies and practices,” *Chemico-Biological Interactions*, vol. 383, p. 110653, Sept. 2023.
- [9] P. Müller, M. Schürmann, and J. Guck, “The theory of diffraction tomography,” 2015.
- [10] S. Seltzer, “Xcom-photon cross sections database, nist standard reference database 8,” 1987.
- [11] P. Müller, M. Schürmann, and J. Guck, “The theory of diffraction tomography,” 2015.
- [12] A. W. Greaves, “Phase contrast in x-ray imaging,” 2011.
- [13] P. Irrera, *Low dose x-ray image processing : Joint denoising and contrast enhancement, and automatic detection of anatomical landmarks for image quality estimation*. Theses, Télécom ParisTech, June 2015.

- [14] P. R. T. Munro, K. Ignatyev, R. D. Speller, and A. Olivo, "Source size and temporal coherence requirements of coded aperture type x-ray phase contrast imaging systems," *Optics Express*, vol. 18, p. 19681, Sept. 2010.
- [15] HAMAMATSU, "Hamamatsu microfocus x-ray source l6622-01," Jan. 2002.
- [16] P. Modregger, M. Kagias, S. C. Irvine, R. Brönnimann, K. Jefimovs, M. Endrizzi, and A. Olivo, "Interpretation and utility of the moments of small-angle x-ray scattering distributions," *Physical Review Letters*, vol. 118, June 2017.
- [17] "Medipix3 technology brief." The Medipix Collaboration. Accessed on November 20, 2023.
- [18] M. F. Walsh, S. J. Nik, S. Procz, M. Pichotka, S. T. Bell, C. J. Bateman, R. M. N. Doesburg, N. D. Ruiter, A. I. Chernoglazov, R. K. Panta, A. P. H. Butler, and P. H. Butler, "Spectral ct data acquisition with medipix3.1," *Journal of Instrumentation*, vol. 8, p. P10012–P10012, Oct. 2013.
- [19] B. Henke, E. Gullikson, and J. Davis, "X-ray interactions: photoabsorption, scattering, transmission, and reflection at $e=50\text{--}30000$ eV, $z=1\text{--}92$," *Atomic Data and Nuclear Data Tables*, vol. 54, pp. 181–342, Jul 1993.
- [20] R. Behling, "X-ray sources: 125 years of developments of this intriguing technology," *Physica Medica*, vol. 79, pp. 162–187, Nov. 2020.
- [21] N. Lossau, *Röntgen*. VGS, 1995.
- [22] P. M. Dunn, "Wilhelm conrad roentgen (1845-1923), the discovery of x rays and perinatal diagnosis," *Archives of Disease in Childhood - Fetal and Neonatal Edition*, vol. 84, pp. 138F–139, Mar. 2001.
- [23] D. L. Crandall and A. C. Barger, "Henry p. bowditch's forgotten contributions to radiology.," *American Journal of Roentgenology*, vol. 161, pp. 1105–1108, Nov. 1993.
- [24] H. Kogelnik, "Inauguration of radiotherapy as a new scientific speciality by leopold freund 100 years ago," *Radiotherapy and Oncology*, vol. 42, pp. 203–211, Mar. 1997.
- [25] P. K. Spiegel, "The first clinical x-ray made in america–100 years.," *American Journal of Roentgenology*, vol. 164, pp. 241–243, Jan. 1995.
- [26] R. Wilks, *Principles of Radiological Physics*. Modern Practical Nursing, Churchill Livingstone, 1987.

- [27] A. B. Partridge, "The rays: A history of radiology in the united states and canada," *Medical History*, vol. 15, no. 2, p. 201–202, 1971.
- [28] J. J. Corn, ed., *Imagining tomorrow*. The MIT Press, London, England: MIT Press, Jan. 1988.
- [29] H. K. Pancoast, "The american congress of radiology," *Radiology*, vol. 20, pp. 231–232, Mar. 1933.
- [30] J. Ulicný, "Lorenz-Mie light scattering in cellular biology," *Gen. Physiol. Biophys.*, vol. 11, pp. 133–151, Apr. 1992.
- [31] H. J. Muller, "The production of mutations by x-rays," *Proceedings of the National Academy of Sciences*, vol. 14, pp. 714–726, Sept. 1928.
- [32] H. J. Muller, "THE MEASUREMENT OF GENE MUTATION RATE IN DROSOPHILA, ITS HIGH VARIABILITY, AND ITS DEPENDENCE UPON TEMPERATURE," *Genetics*, vol. 13, pp. 279–357, July 1928.
- [33] N. Prize, *Hermann J. Muller – Nobel Lecture*. NobelPrize.org, 2023.
- [34] Y. Sung, R. Gupta, B. Nelson, S. Leng, C. H. McCollough, and W. S. Graves, "Phase-contrast imaging with a compact x-ray light source: system design," *Journal of Medical Imaging*, vol. 4, p. 1, Nov. 2017.
- [35] M. Born, E. Wolf, A. B. Bhatia, P. C. Clemmow, D. Gabor, A. R. Stokes, A. M. Taylor, P. A. Wayman, and W. L. Wilcock, *Principles of Optics: Electromagnetic Theory of Propagation, Interference and Diffraction of Light*. Cambridge University Press, Oct. 1999.
- [36] T. Young and T. Young, *A course of lectures on natural philosophy and the mechanical arts*. Printed for J. Johnson, 1807.
- [37] F. Zernike, "The concept of degree of coherence and its application to optical problems," *Physica*, vol. 5, p. 785–795, Aug. 1938.
- [38] D. Mengu, E. Ulusoy, and H. Urey, "Non-iterative phase hologram computation for low speckle holographic image projection," *Optics Express*, vol. 24, p. 4462, Feb. 2016.
- [39] B. L. van der Waerden, ed., *Sources of Quantum Mechanics*. Dover Books on Physics, Mineola, NY: Dover Publications, Feb. 2007.
- [40] S. de Chadarevian, "John kendrew and myoglobin: Protein structure determination in the 1950s," *Protein Science*, vol. 27, p. 1136–1143, May 2018.

- [41] M. H. De la Torre I., F. Mendoza Santoyo, J. M. Flores M., and M. d. S. Hernandez-M., "Gabor's holography: seven decades influencing optics [invited]," *Applied Optics*, vol. 61, p. B225, Dec. 2021.
- [42] I. M. Fodchuk, S. M. Novikov, and I. V. Yaremchuk, "Direct and inverse problems in x-ray three-crystal triple laue case interferometry," *Applied Optics*, vol. 55, p. B120, Mar. 2016.
- [43] A. P. Petrakov, "X-ray phase-contrast method and its application to the study of blood vessels with a model object," *Technical Physics*, vol. 48, p. 607–611, May 2003.
- [44] A.-L. Robisch, J. Wallentin, A. Pacureanu, P. Cloetens, and T. Salditt, "Holographic imaging with a hard x-ray nanoprobe: ptychographic versus conventional phase retrieval," *Optics Letters*, vol. 41, p. 5519, Nov. 2016.
- [45] Z. Qi, J. Zambelli, N. Bevins, and G.-H. Chen, "Quantitative imaging of electron density and effective atomic number using phase contrast ct," *Physics in Medicine and Biology*, vol. 55, p. 2669–2677, Apr. 2010.
- [46] M. Fiddy and U. Shahid, "Legacies of the gerchberg–saxton algorithm," *Ultra-microscopy*, vol. 134, p. 48–54, Nov. 2013.
- [47] C. Zuo, J. Li, J. Sun, Y. Fan, J. Zhang, L. Lu, R. Zhang, B. Wang, L. Huang, and Q. Chen, "Transport of intensity equation: a tutorial," *Optics and Lasers in Engineering*, vol. 135, p. 106187, Dec. 2020.
- [48] J. D. Jackson, *Classical Electrodynamics*. Nashville, TN: John Wiley & Sons, 3 ed., July 1998.
- [49] B. H. Bransden and C. J. Joachain, *Physics of atoms and molecules*. London, England: Prentice-Hall, Dec. 1982.
- [50] D. GABOR, "A new microscopic principle," *Nature*, vol. 161, p. 777–778, May 1948.
- [51] W. Xu, M. H. Jericho, I. A. Meinertzhagen, and H. J. Kreuzer, "Digital in-line holography for biological applications," *Proceedings of the National Academy of Sciences*, vol. 98, p. 11301–11305, Sept. 2001.
- [52] M. Endo, S. Mori, T. Tsunoo, and H. Miyazaki, "Magnitude and effects of x-ray scatter in a 256-slice ct scanner: X-ray scatter in a 256-slice ct," *Medical Physics*, vol. 33, p. 3359–3368, Aug. 2006.

- [53] D. M. Paganin and D. Pelliccia, "X-ray phase-contrast imaging: a broad overview of some fundamentals," 2020.
- [54] L. T. Ikelle, "On elastic-electromagnetic mathematical equivalences: Elastic-electromagnetic equivalences," *Geophysical Journal International*, vol. 189, p. 1771–1780, Apr. 2012.
- [55] S. Harutyunyan and R. B. Davis, "Magnon-phonon interactions in a ferromagnetic media: Reflection and refraction of magneto-elastic waves," in *Volume 15: Sound, Vibration and Design*, IMECE2009, ASMEDC, Jan. 2009.
- [56] M. R. Teague, "Deterministic phase retrieval: a green's function solution," *Journal of the Optical Society of America*, vol. 73, p. 1434, Nov. 1983.
- [57] D. M. Paganin and D. Pelliccia, "Tutorials on x-ray phase contrast imaging: Some fundamentals and some conjectures on future developments," 2019.
- [58] E. J. Lee CI, *Breast Cancer Screening*. Philadelphia, Pa:Lippincott Williams & Wilkins, fifth ed., 2014.
- [59] B. E. A. Saleh and M. C. Teich, *Fundamentals of Photonics*. Wiley, Aug. 1991.
- [60] O. Oltulu, Z. Zhong, M. Hasnah, M. N. Wernick, and D. Chapman, "Extraction of extinction, refraction and absorption properties in diffraction enhanced imaging," *Journal of Physics D: Applied Physics*, vol. 36, p. 2152–2156, Aug. 2003.
- [61] J. H. Hubbell, "Photon cross sections, attenuation coefficients, and energy absorption coefficients from 10 keV to 100 GeV," 1970.
- [62] E. National Academies of Sciences and Medicine, *Airport Passenger Screening Using Backscatter X-Ray Machines*. 2015.
- [63] J. R. C. Harold Elford Johns, *Physics of Radiology*. Charles C Thomas Pub Ltd, fourth ed., 1983.
- [64] L. T. Niklason, J. A. Sorenson, and J. A. Nelson, "Scattered radiation in chest radiography," *Medical Physics*, vol. 8, p. 677–681, Sept. 1981.
- [65] J. Kosanetzky, B. Knoerr, G. Harding, and U. Neitzel, "X-ray diffraction measurements of some plastic materials and body tissues: X-ray diffraction in plastics and tissues," *Medical Physics*, vol. 14, p. 526–532, July 1987.
- [66] J. M. COWLEY, "Chapter 1 - fresnel and fraunhofer diffraction," in *Diffraction Physics (Third Edition)* (J. M. COWLEY, ed.), North-Holland Personal Library, pp. 3–24, Amsterdam: North-Holland, third edition ed., 1995.

- [67] M. Bettmann, "Angiographic contrast agents: conventional and new media compared," *American Journal of Roentgenology*, vol. 139, p. 787–794, Oct. 1982.
- [68] P. B. Denis G. Pelli, *Measuring contrast sensitivity*, vol. 90. Vision research, fifth ed., 2013.
- [69] S. P. Venkataraman S, "Breast imaging for cancer screening: Mammography andultrasonography," *UpToDate*, 2019.
- [70] G. Margaritondo, "Spectromicroscopy and internal photoemission spectroscopy of semiconductor interfaces," *Progress in Surface Science*, vol. 56, p. 311–346, Dec. 1997.
- [71] Y. Chen, C. K. Hagen, A. Olivo, and M. A. Anastasio, "A partial-dithering strategy for edge-illumination x-ray phase-contrast tomography enabled by a joint reconstruction method," *Physics in Medicine and Biology*, vol. 65, p. 105007, May 2020.
- [72] A. Olivo, F. Arfelli, G. Cantatore, R. Longo, R. H. Menk, S. Pani, M. Prest, P. Poropat, L. Rigon, G. Tromba, E. Vallazza, and E. Castelli, "An innovative digital imaging set-up allowing a low-dose approach to phase contrast applications in the medical field," *Medical Physics*, vol. 28, p. 1610–1619, Aug. 2001.
- [73] M. Endrizzi, P. C. Diemoz, T. P. Millard, J. Louise Jones, R. D. Speller, I. K. Robinson, and A. Olivo, "Hard x-ray dark-field imaging with incoherent sample illumination," *Applied Physics Letters*, vol. 104, Jan. 2014.
- [74] P. C. Diémoz, F. A. Vittoria, C. K. Hagen, M. Endrizzi, P. Coan, A. Bravin, U. H. Wagner, C. Rau, I. K. Robinson, and A. Olivo, "A single-image retrieval method for edge illumination x-ray phase-contrast imaging: Application and noise analysis," *Physica Medica*, vol. 32, p. 1759–1764, Dec. 2016.
- [75] F. A. Vittoria, P. C. Diemoz, M. Endrizzi, L. Rigon, F. C. Lopez, D. Dreossi, P. R. T. Munro, and A. Olivo, "Strategies for efficient and fast wave optics simulation of coded-aperture and other x-ray phase-contrast imaging methods," *Applied Optics*, vol. 52, p. 6940, Sept. 2013.
- [76] D. Paganin, S. C. Mayo, T. E. Gureyev, P. R. Miller, and S. W. Wilkins, "Simultaneous phase and amplitude extraction from a single defocused image of a homogeneous object," *Journal of Microscopy*, vol. 206, p. 33–40, Apr. 2002.
- [77] A. Barty, K. A. Nugent, D. Paganin, and A. Roberts, "Quantitative optical phase microscopy," *Optics Letters*, vol. 23, p. 817, June 1998.

- [78] M. De Graef and Y. Zhu, "Quantitative noninterferometric lorentz microscopy," *Journal of Applied Physics*, vol. 89, p. 7177–7179, June 2001.
- [79] T. E. Gureyev, S. Mayo, S. W. Wilkins, D. Paganin, and A. W. Stevenson, "Quantitative in-line phase-contrast imaging with multienergy x rays," *Physical Review Letters*, vol. 86, p. 5827–5830, June 2001.
- [80] A. Doherty, S. Savvidis, C. Navarrete-León, M. F. Gerli, A. Olivo, and M. En-drizzi, "Edge-illumination x-ray dark-field tomography," *Physical Review Applied*, vol. 19, May 2023.
- [81] K. Ignatyev, P. R. T. Munro, R. D. Speller, and A. Olivo, "Effects of signal diffusion on x-ray phase contrast images," *Review of Scientific Instruments*, vol. 82, July 2011.
- [82] O. Aumala and J. Holub, "Dithering design for measurement of slowly varying signals," *Measurement*, vol. 23, p. 271–276, June 1998.
- [83] Y. Chen, C. K. Hagen, A. Olivo, and M. A. Anastasio, "A partial-dithering strategy for edge-illumination x-ray phase-contrast tomography enabled by a joint reconstruction method," *Physics in Medicine and Biology*, vol. 65, p. 105007, May 2020.
- [84] J. Javh, J. Slavič, and M. Boltežar, "The subpixel resolution of optical-flow-based modal analysis," *Mechanical Systems and Signal Processing*, vol. 88, p. 89–99, May 2017.
- [85] P. C. Diemoz, F. A. Vittoria, and A. Olivo, "Spatial resolution of edge illumination x-ray phase-contrast imaging," *Optics Express*, vol. 22, p. 15514, June 2014.
- [86] J. Javh, J. Slavič, and M. Boltežar, "The subpixel resolution of optical-flow-based modal analysis," *Mechanical Systems and Signal Processing*, vol. 88, p. 89–99, May 2017.
- [87] C. Degen, F. Reinhard, and P. Cappellaro, "Quantum sensing," *Reviews of Modern Physics*, vol. 89, July 2017.
- [88] J. Thim, B. Norlin, M. O'Nils, S. Abdalla, and B. Oelmann, "Realizing increased sub-pixel spatial resolution in x-ray imaging using displaced multiple images," *Nuclear Instruments and Methods in Physics Research Section A: Accelerators, Spectrometers, Detectors and Associated Equipment*, vol. 633, p. S247–S249, May 2011.
- [89] D. Jurado Romero, "Dithering and superresolution in x-ray pci," in *VI uniandes particle physics school*, (Universidad de los Andes), 2023.

- [90] A. Zamir, M. Endrizzi, C. K. Hagen, F. A. Vittoria, L. Urbani, P. De Coppi, and A. Olivo, "Robust phase retrieval for high resolution edge illumination x-ray phase-contrast computed tomography in non-ideal environments," *Scientific Reports*, vol. 6, Aug. 2016.
- [91] N. C. and Ávila C., "Optimization of an x-ray system for free-space propagation and single mask edge illumination phase contrast imaging," *Bacheloir thesis, Universidad de los Andes*, 2019.
- [92] G. K. Kallon, M. Wesolowski, F. A. Vittoria, M. Endrizzi, D. Basta, T. P. Millard, P. C. Diemoz, and A. Olivo, "A laboratory based edge-illumination x-ray phase-contrast imaging setup with two-directional sensitivity," *Applied Physics Letters*, vol. 107, Nov. 2015.
- [93] R. B. Suñé, *Spectral CT data acquisition with Medipix3.1*. PhD thesis, CERN, Geneva, Switzerland, 2010. Accessed on November 20, 2023.
- [94] E. N. Gimenez, R. Ballabriga, G. Blaj, M. Campbell, I. Dolbnya, E. Frodjh, I. Horswell, X. Llopart, J. Marchal, J. McGrath, D. Omar, R. Plackett, K. Sawhney, and N. Tartoni, "Medipix3rx: Characterizing the medipix3 redesign with synchrotron radiation," *IEEE Transactions on Nuclear Science*, vol. 62, no. 3, pp. 1413–1421, 2015.
- [95] J. Mir, R. Clough, R. MacInnes, C. Gough, R. Plackett, I. Shipsey, H. Sawada, I. MacLaren, R. Ballabriga, D. Maneuski, V. O'Shea, D. McGrouther, and A. Kirkland, "Characterisation of the medipix3 detector for 60 and 80 kev electrons," *Ultramicroscopy*, vol. 182, p. 44–53, Nov. 2017.
- [96] G. Roque, C. Avila, M. L. Pérez-Lara, L. Mendoza, and S. Procz, "Study of contrast-to-noise ratio performance of a medipix3rx cdte detector for low dose mammography imaging," *Nuclear Instruments and Methods in Physics Research*, vol. 992, p. 165000, Mar. 2021.
- [97] B. Pfau and S. Eisebitt, *X-Ray Holography*, pp. 1093–1133. Cham: Springer International Publishing, 2016.
- [98] A. Burvall, U. Lundström, P. A. C. Takman, D. H. Larsson, and H. M. Hertz, "Phase retrieval in x-ray phase-contrast imaging suitable for tomography," *Optics Express*, vol. 19, p. 10359, May 2011.
- [99] H. Wang, Y. Kashyap, and K. Sawhney, "From synchrotron radiation to lab source: advanced speckle-based x-ray imaging using abrasive paper," *Scientific Reports*, vol. 6, Feb. 2016.

- [100] M.-C. Zdora, “State of the art of x-ray speckle-based phase-contrast and dark-field imaging,” *Journal of Imaging*, vol. 4, p. 60, Apr. 2018.
- [101] J. E. D. Thomas S. Curry, *Christensen’s Physics of Diagnostic Radiology*, vol. 1. Williams & Wilkins, fourth ed., 1990.
- [102] R. S. Ayyala, M. Chorlton, R. H. Behrman, P. J. Kornguth, and P. J. Slanetz, “Digital mammographic artifacts on full-field systems: What are they and how do i fix them?,” *RadioGraphics*, vol. 28, no. 7, pp. 1999–2008, 2008. PMID: 19001654.
- [103] J. D., “Davidjhub’s github repository.” <https://github.com/DavidJHub>. Accessed on: June 17, 2024.
- [104] I. Rutel, M. Yester, and G. Barnes, “Tu-ff-a4-03: Post-processing dead pixel evaluation for digital detectors,” *Medical Physics*, vol. 33, p. 2222–2223, June 2006.
- [105] A. L. C. Kwan, J. A. Seibert, and J. M. Boone, “An improved method for flat-field correction of flat panel x-ray detector,” *Medical Physics*, vol. 33, p. 391–393, Jan. 2006.
- [106] A. S. Reyes, A. Bittar, L. C. Ávila, C. Botia, N. P. Esmeral, and N. I. Bloch, “Divergence in brain size and brain region volumes across wild guppy populations,” *Proceedings of the Royal Society B: Biological Sciences*, vol. 289, Aug. 2022.
- [107] A. Corral-Lopez, N. I. Bloch, W. van der Bijl, M. Cortazar-Chinarro, A. Szorkovszky, A. Kotrschal, I. Darolti, S. D. Buechel, M. Romensky, N. Kolm, and J. E. Mank, “Functional convergence of genomic and transcriptomic architecture underlies schooling behaviour in a live-bearing fish,” *Nature Ecology and Evolution*, Nov. 2023.
- [108] A. Deacon, “*Poecilia reticulata* (guppy),” Jan. 2022.
- [109] S. Sahney and M. V. H. Wilson, “Extrinsic labyrinth infillings imply open endolymphatic ducts in lower devonian osteostracans, acanthodians, and putative chondrichthyans,” *Journal of Vertebrate Paleontology*, vol. 21, p. 660–669, Dec. 2001.
- [110] R. W. Gauldie, “Polymorphic crystalline structure of fish otoliths,” *Journal of Morphology*, vol. 218, p. 1–28, Oct. 1993.
- [111] R. J. Bryson-Richardson, S. Berger, T. F. Schilling, T. E. Hall, N. J. Cole, A. J. Gibson, J. Sharpe, and P. D. Currie, “Fishnet: an online database of zebrafish anatomy,” *BMC Biology*, vol. 5, Aug. 2007.
- [112] L. Brombal, F. Arfelli, R. H. Menk, L. Rigon, and F. Brun, “Pepi lab: a flexible compact multi-modal setup for x-ray phase-contrast and spectral imaging,” *Scientific Reports*, vol. 13, Mar. 2023.

- [113] L. Brombal, S. Donato, D. Dreossi, F. Arfelli, D. Bonazza, A. Contillo, P. Delogu, V. Di Trapani, B. Golosio, G. Mettievier, P. Oliva, L. Rigon, A. Taibi, and R. Longo, "Phase-contrast breast ct: the effect of propagation distance," *Physics in Medicine and Biology*, vol. 63, p. 24NT03, Dec. 2018.
- [114] P. C. Diemoz and A. Olivo, "On the origin of contrast in edge illumination x-ray phase-contrast imaging," *Optics Express*, vol. 22, p. 28199, Nov. 2014.
- [115] K. S. Morgan, D. M. Paganin, and K. K. W. Siu, "Quantitative single-exposure x-ray phase contrast imaging using a single attenuation grid," *Optics Express*, vol. 19, p. 19781, Sept. 2011.
- [116] P. R. Munro, L. Rigon, K. Ignatyev, F. C. Lopez, D. Dreossi, R. D. Speller, and A. Olivo, "A quantitative, non-interferometric x-ray phase contrast imaging technique," *Optics Express*, vol. 21, p. 647, Jan. 2013.
- [117] R. von Nardroff, "Refraction of x-rays by small particles," *Physical Review*, vol. 28, p. 240–246, Aug. 1926.
- [118] M. Ando, R. Gupta, A. Iwakoshi, J.-K. Kim, D. Shimao, H. Sugiyama, N. Sunaguchi, T. Yuasa, and S. Ichihara, "X-ray dark-field phase-contrast imaging: Origins of the concept to practical implementation and applications," *Physica Medica*, vol. 79, p. 188–208, Nov. 2020.
- [119] A. Doherty, S. Savvidis, C. Navarrete-León, M. F. Gerli, A. Olivo, and M. Endrizzi, "Edge-illumination x-ray dark-field tomography," *Physical Review Applied*, vol. 19, May 2023.
- [120] R. J. Bryson-Richardson, S. Berger, T. F. Schilling, T. E. Hall, N. J. Cole, A. J. Gibson, J. Sharpe, and P. D. Currie, "Fishnet: an online database of zebrafish anatomy," *BMC Biology*, vol. 5, Aug. 2007.
- [121] L. Brombal, S. Donato, D. Dreossi, F. Arfelli, D. Bonazza, A. Contillo, P. Delogu, V. Di Trapani, B. Golosio, G. Mettievier, P. Oliva, L. Rigon, A. Taibi, and R. Longo, "Phase-contrast breast ct: the effect of propagation distance," *Physics in Medicine and Biology*, vol. 63, p. 24NT03, Dec. 2018.
- [122] L. Brombal, F. Arfelli, P. Delogu, S. Donato, G. Mettievier, K. Michielsen, P. Oliva, A. Taibi, I. Sechopoulos, R. Longo, and C. Fedon, "Image quality comparison between a phase-contrast synchrotron radiation breast ct and a clinical breast ct: a phantom based study," *Scientific Reports*, vol. 9, Nov. 2019.
- [123] G. Roque, C. Avila, M. L. Pérez-Lara, L. Mendoza, and S. Procz, "Study of contrast-to-noise ratio performance of a medipix3rx cdte detector for low dose

mammography imaging,” *Nuclear Instruments and Methods in Physics Research Section A: Accelerators, Spectrometers, Detectors and Associated Equipment*, vol. 992, p. 165000, Mar. 2021.

Appendix A

Feynman rules for QED

The Feynman rules, as the name implies, is a set of rules that provide the probability of a quantum mechanical process occurring. Feynman diagrams are a graphical representation of these rules and are used to depict all types of particle interactions, Feynman diagrams are used extensively in particle physics to visualize and calculate the behavior and interaction of subatomic particles. To set the rules used in the derivation of photon-matter interactions under a Quantum Electrodynamics (QED) representation, we may represent particle entities by their wave functions

$$\begin{array}{ccc} \text{1/2 Spin} & \text{1 Spin} & \text{Anti 1/2 Spin} \\ \psi(x) = ae^{-i/\hbar p \cdot x} u^{(s)}(p) & A^\mu(x) = ae^{-(i/\hbar) p \cdot x} \epsilon_{(s)}^\mu & \psi(x) = ae^{i/\hbar p \cdot x} v^{(s)}(p) \end{array} \quad (\text{A.1})$$

Where spinors $u^{(s)}$ and $v^{(s)}$ satisfy the Dirac equations.

$$(\gamma^\mu p_\mu - mc)u = 0 \qquad (\gamma^\mu p_\mu + mc)v = 0 \quad (\text{A.2})$$

and the orthogonal adjoints are normalized so

$$\bar{u}u = 2mc \qquad \bar{v}v = -2mc \quad (\text{A.3})$$

Similarly for the photon, the polarization vectors are orthonormal and normalized

$$\epsilon^\mu \epsilon_\mu^* = 1 \quad (\text{A.4})$$

And satisfy the momentum space Lorentz equation

$$\epsilon^\mu p_\mu = 0 \quad (\text{A.5})$$

Now to calculate the associated amplitude \mathcal{M} associated with a particular diagram, we may follow a recipe:

1. **Quantum number labeling** Each interacting particle may have their defined quantum numbers such as the outgoing four-momenta p_n , spin s_n and internal four momenta q_n where n is the number of particles.
2. **External lines** Arrows in the Feynman diagram point in the direction of the process propagation. Inward lines point to the process. Outward lines point outside the process, vertices must enforce four-momentum conservation
3. **Vertex factors** For every j -th vertex, there is a contribution factor given by

$$C_j = ig_e \gamma^\mu \quad (\text{A.6})$$

Where g_e is a dimensionless coupling constant related to the fine-structure constant by $\alpha = g_e^2/4\pi$.

4. **Propagators** Each internal line contributes a factor related to the particle propagator, which for half-spin particles (fermions) it may be.

$$K_j = \frac{(\not{q} + mc)}{q^2 - m^2 c^2} \quad (\text{A.7})$$

And integer spin (photons)

$$K_j = \frac{-ig_{\mu\nu}}{q^2} \quad (\text{A.8})$$

5. **Conservation laws** For each vertex and phase coordinate, define the delta factor

$$(2\pi)^2 \delta^4(k_1 + k_2 + k_3) \quad (\text{A.9})$$

Where k_j is the inwards four-momenta of each vertex if the direction is outwards, the sign changes for the specific k

6. **Integration over internal momenta** The differential for each internal momentum q is given by

$$D\Delta = \frac{d^4 q}{(2\pi)^4} \quad (\text{A.10})$$

Which is the total phase space for the internal momenta. Integrating over the total space and applying the inverse delta operator will finally produce the complex amplitude term $-i\mathcal{M}$

Appendix B

Auto-movement imaging flux diagram

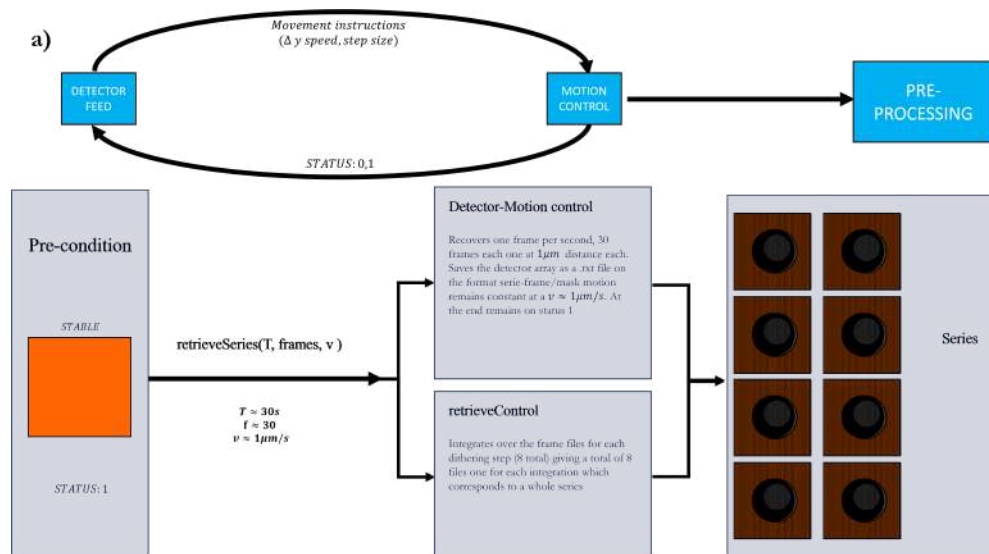


FIGURE B.1: Single Flat-Field correction processing a) Flux diagram for alignment pre-condition

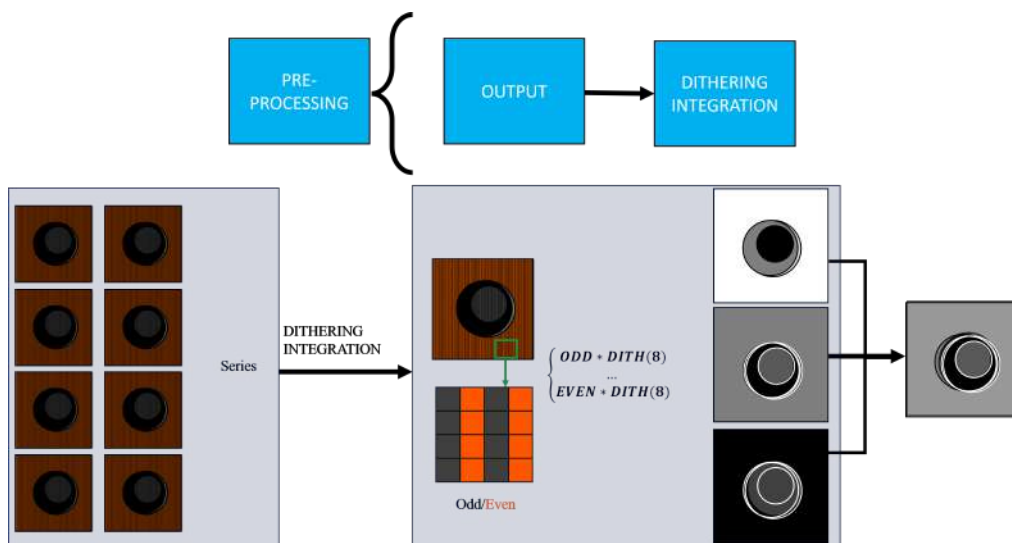


FIGURE B.2: Image integration process